Alma Mater studiorum - Università di Bologna

DOTTORATO DI RICERCA
Ingegneria Chimica dell'Ambiente e della Sicurezza
XXIII Ciclo
Settore scientifico disciplinare di afferenza: ING-IND/25

Fluid Dynamic Analysis and Modelling of Industrial Chemical Equipment

Mirella Coroneo

Coordinatore Dottorato
Prof. Giulio Cesare Sarti

Relatore
Prof. Alessandro Paglianti
Correlatore
Prof. Giuseppina Montante

Esame finale anno 2011

A mio marito

Acknowledgements

I would like to express my deep and sincere gratitude to my thesis supervisor, Prof. Alessandro Paglianti, for his excellent scientific guidance and for all the hope he has put on me, before I thought I could do any research at all. His ideas and support had a major influence on this thesis, while the joy and enthusiasm he has for research were extremely important for my scientific education.

I would like also to thank Prof. Giuseppina Montante, for her precious supervising during my work and for her endless support. Her wide knowledge, useful comments and friendly advices have been of great value for me.

I am also indebted to all the professors, researchers and students, whom I had the honours to collaborate with, all the members of the laboratory of the Department of Chemical Mining and Environmental Engineering and all the friends and the very good friends that I met in this great experience. All of them provided a stimulating and fun environment in which to learn and grow.

Lastly, and most importantly, I am infinitely indebted to my husband, Alessandro Minisgallo, for his extraordinary patience, encouragement and never-ending support, to my younger sister, Federica Coroneo, for her infinite support and unreserved high regard for me, and to my elder sister, Laura Coroneo, for showing the way for a research career. Without their encouragement and understanding this period would have been more hard then it was.

Contents

Chapter 1

General Introduction

1.1 Computational Fluid Dynamics

The flow of fluids is one of the most important phenomenon in many physical fields and in different engineering processes. Any fluid flow is governed by three fundamental principles: the conservation of mass, momentum and energy. These fundamental physical principles can be expressed in terms of basic mathematical equations, which in their most general form are either integral equations or partial differential equations (Anderson, 1995).

Due to the mathematical complexity of these equations, that form a set of non-linear equations, no analytical solution is known except for very simple geometries. Moreover, when turbulent flows are involved the problem becomes even more complex as the set of equations usually needs a suitable turbulence model for closure.

Computational Fluid Dynamics, or CFD for short, is based on a translation of the original physical problem to be solved in a system of algebraic equations. Their resolution yield the values of the physical variables (i.e. pressure, velocity and temperature) in a set of previously defined discrete points in time and/or space. As a result, CFD is the science that replaces the integrals or the partial derivatives in conservation equations with discretized algebraic forms, which are solved to obtain a collection of values of all variables in all the domain under investigation. Hence it deals with the resolution of fluid flow problems by means of a computer machine (Anderson, 1995).

The history of Computational Fluid Dynamics started as a combination of physics, numerical mathematics, and, to some extent, computer sciences employed to simulate fluid flows (Blazek, 2001). It is a branch of the Computational Mechanics field and has been subject to a continuous implementation of new mathematical models, since the computational resources available have always been the most

important limiting factor. As a result, historically, advancements in the computational power have almost always been spent to improve the physical description of the flow with more accurate and computationally demanding models.

In the past few decades Computational Fluid Dynamic has become a very powerful tool for the analysis of fluid flow and related phenomena, as for example single phase and multiphase mixing, mass transfer and chemical reaction. Actually, today CFD methodologies are routinely employed in many different fields (such as for example turbomachinery, aerospace engineering, automotive, etc.) and are becoming an essential part of the design process of several equipments and also a substantial research tool in certain physical sciences (Blazek, 2001). However, it would be completely wrong to consider CFD a mature technology. There are still many open questions like turbulence and multiphase flows modelling, robust but accurate discretisation methods, etc. Also the connection of CFD with other disciplines (like structural mechanics or heat conduction) requires further research.

1.2 CFD and Chemical Engineering

Nowadays many process industries are taking full advantage of CFD technologies such as mixing, oil & gas, food processing, polymer and mineral industries (Fouhy and Parkinson, 1995; Trambouze, 1996).

Generally, a typical chemical process plant usually involves:

- fluid flow devices such as pipes and valves;
- fluid transport equipment such as compressors and pumps;
- drying equipment such as fluidized beds, cyclone driers and spray driers;
- dynamic and static mixing equipment;
- mass transfer units;
- reaction units;
- heat generation and heat transfer units such as furnaces, boilers, burners, process heaters, heat exchangers, condensers and evaporators;
- separation equipment such as cyclones, hydro-cyclones, electro-static precipitators, gravity separators and centrifuge separators.

The flow field in most of these units is very complex and difficult to measure, making trouble-shooting and efficiency improvements very difficult. However, failure of a chemical process equipment can result in undesirable downtime and loss

of revenue. For these reasons, reliable methods of analysis and trouble shooting of equipment are very important (Brenner, 2009).

A strategic innovation tool is represented by CFD, that the chemical industry has come to rely on to maintain and foster technology to meet economic challenges. Nowadays, CFD is applied to a number of unit operations in the chemical and process industries (Birtigh et al. 2000; Brenner, 2009). It can be applied for diagnosis, analysis, troubleshooting and prototyping of process equipments. It is also applied to examine configuration changes and thus minimize risk and avoid unnecessary downtime during testing, to compare performance under different operating conditions, to examine the influence of various parameters on flow behaviour and hence performance without actually building a real model (Anderson, 1995; Fouhy and Parkinson, 1995). Equipment at its full-scale can also be analysed, eliminating scale-up related issues.

Furthermore, these methods provide an inside look into the function and operation devices and can help identify areas for improvement. In chemical process industries small increments in efficiency lead to large increments in product cost savings, since unit operations usually handle large amounts of fluid. At this regard, CFD permits to analyse the performance of an equipment in advance for making major structural changes, minimizing the risk of lost profit during changeover.

The number of processes that can be improved with the aid of CFD techniques are a lot. However, the potential for process improvements using CFD solutions is yet to be realized and yet to be fully integrated in chemical process industries.

In any case, the range of applications where CFD is accepted as an essential engineering and innovation tool include, among others, batch and in-line mixers, bubble column reactors, fluidized bed reactors, all separation processes, classifiers, spray dryers, scrubbers, fuel cells, furnaces and heat exchangers (Birtigh et al. 2000).

1.3 Commercial Computational Fluid Dynamics

Nowadays some Commercial Computational Fluid Dynamics (CCFD) codes exist, which are used both in the industrial and in the academic field. Commercial CFD codes, for their general purpose nature, are complex instruments from the modelling and numerical point of view. They are built in order to solve a myriad of thermal fluid dynamics problems, with a lot of different added models, but they are also developed in order to produce always *a* solution, which is not always *the* solution of the problem under investigation. This occurs because in commercial CFD codes algorithms and techniques finalized to the robustness and convergence of the calculus are used (Barozzi et al., 2008).

The easiness to find a solution of a problem through commercial computational

fluid dynamics usually brings scarce consciousness, false sense of simplicity and excessive confidence in the solution results. However the modelling and numerical complexity need the choice of a lot of different parameters (model equations, grid size, time step, numerical and modelling constants, etc.) necessary to the simulation setting, and depending on the different settings infinite solutions to the problem can be reached. Therefore, the user has to be conscious of the analysis objective and proceed accordingly, since the research activity through commercial CFD does not require neither less time, effort or study than the traditional research tools, while requiring experience and consciousness (Barozzi et al., 2008).

Actually CFD is no more than an aid to engineers with the skill and knowledge to apply it (Fouhy and Parkinson, 1995).

1.4 Research objectives

This research is aimed at investigating the capability of fully predictive Computational Fluid Dynamics approaches to reliably predict the fluid dynamic behaviour of different industrial chemical equipment, specifically membrane modules, stirred vessels and fluidized beds.

Objective of the work is to identify suitable simulation strategies for the abovementioned apparatuses, to indicate or develop the more appropriate models and finally to understand the effect of numerical issues on simulation results, thus assessing the appropriateness of CFD methods for the design and geometry optimization, as well as for trouble-shooting purposes.

In particular:

- the effect of mathematical modelling and numerical issues on the RANS-based predictions of the main features of single-phase and two-phase turbulent flow in stirred vessels is verified, by comparison with experimental data, with particular attention to the effect of grid size and discretization schemes. Numerical uncertainties effects are also investigated for the prediction of gas fluidized beds behaviour under different operating conditions.

- the capability of an original CFD approach to reliably predict the flow dynamic behaviour and the separation performances of a membrane modules for hydrogen purification is investigated through a strict comparison with experimental data under different operating conditions.

- CFD approach appropriateness for the membrane module geometrical optimization is also investigated.

1.5 Thesis outline

The thesis is organized as follows.

In Chapter 2 the mathematical modelling adopted in this work for single and multi phase laminar and turbulent flow is presented together with a brief introduction to numerical modelling and to the experimental optical techniques adopted for validation purposes.

Then in Chapter 3 a novel approach for modelling membrane modules for hydrogen purification is presented. Different lab-scale modules equipped with ceramic and metallic membranes and a pilot module equipped with three Pd-Ag membranes are considered. The geometrical optimization of these modules is also discussed.

Chapter 4 refers to the modelling of stirred vessels, with particular attention to the influence of numerical settings on the prediction of fluid flow and mixing, and to the hydrodynamics of immiscible liquid-liquid dispersions.

In Chapter 5 the CFD modelling of homogeneous bed expansion and of segregating fluidized bi-disperse mixtures of particles differing in size and density in gas-solid fluidized beds is proposed.

Finally in Chapter 6 all the results obtained in the present thesis are summarised and possible future developments are outlined.

1.6 Bibliography

Anderson, J.D., (1995) Computational fluid dynamics, the basics with applications, McGraw-Hill, New York;

Barozzi, G.S., Corticelli, M.A., Levoni, P., (2008) I codici commerciali per la termofluidodinamica computazionale, in Fondamenti di termofluidodinamica computazionale, Servizi grafici editoriali, Padova;

Birtigh, A., Lauschke, G., Schierholz, W.F., Beck, D., Maul, C., Gilbert, N., Wagner, H., Werninger, C.Y., CFD in Chemical Engineering from an industrial perspective (2000) Chemie Ingenieur Technik, 72, pp. 175-193;

Blazek, J., (2001) Computational fluid dynamics: principles and applications, Elsevier, Oxford;

Brenner, G., CFD in process engineering (2009) Notes on Num. Fluid. Mech, 100, pp. 351-359;

Fouhy, K., Parkinson, G., CPI Design Engineers Go with the Flow (1995) Chemical Engineering, 102, pp. 28-31;

Trambouze, P., CFD applied to process engineering. An introduction (1996) Rev. I. Fr. Petrol, 51, pp. 199-203;

Chapter 2

Models and Instrumentations

2.1 Mathematical modelling

It is well known that the equations lying at the basis of fluid dynamic science are the conservation of mass, momentum and energy. The conservation of a certain flow quantity means that its total variation inside an arbitrary volume can be expressed as the net effect of the amount of the quantity being transported across the boundary, any internal forces and sources, and external forces acting on the volume. The amount of the quantity crossing the boundary (usually referred to as flux) can be in general decomposed into two different parts: one due to the convective transport and the other one due to the molecular motion present in the fluid at rest. This second contribution is of a diffusive nature and is proportional to the gradient of the quantity considered.

The conservation equations for laminar and turbulent, single and multi-phase flows are presented in the following.

2.1.1 Laminar single-phase flows

The governing equations of an isothermal fluid flow are the well-known continuity and momentum equations. They can be derived by mass and momentum balances on a stationary element (Bird et al., 1979) and for a single phase system are:

$$\frac{\partial \rho}{\partial t} = -\nabla \cdot (\rho \boldsymbol{u}) \tag{2.1}$$

$$\frac{\partial}{\partial t}\rho \boldsymbol{u} = -\nabla \cdot \rho \boldsymbol{u}\boldsymbol{u} - \nabla p - \nabla \cdot \tau + \rho \boldsymbol{g} \tag{2.2}$$

where the fluid density, ρ, the velocity vector, $\boldsymbol{u}$, and the pressure, p, are in general functions of space and time and the viscous stress tensor, τ, depends from the fluid fields characteristics.

In the case of an incompressible fluid, the density can be assumed constant with respect to space and time, and the continuity equation (2.1) simplifies to:

$$\nabla \cdot \boldsymbol{u} = 0 \tag{2.3}$$

The solution of this last equation together with the momentum equation (2.2) gives the flow and pressure fields of the incompressible fluid once the six components of the viscous stress tensor τ are specified. To this end, a suitable constitutive equation for τ has to be introduced.

When dealing with compressible fluid problems the continuity (2.3) and momentum (2.2) equations must be coupled with proper thermodynamic equation of state in order to close the problem.

In the case of an incompressible fluid exhibiting a Newtonian behaviour the viscous stress tensor can be expressed as:

$$\tau = -\mu \left(\nabla \boldsymbol{u} + (\nabla \boldsymbol{u})^T \right) \tag{2.4}$$

Substituting the continuity equation (2.3) and Newton equation (2.4) in the momentum equation (2.2), the well-known Navier-Stokes equation is obtained:

$$\rho \frac{\partial \boldsymbol{u}}{\partial t} = -\rho \nabla \cdot \boldsymbol{u}\boldsymbol{u} - \nabla p + \mu \nabla^2 \boldsymbol{u} + \rho \boldsymbol{g} \tag{2.5}$$

The problem appears now mathematically closed. The solution of the set of four equations (2.3) and (2.5) gives the four unknowns of the problem: the three components of the fluid velocity, u_1, u_2, u_3, and the fluid pressure p, but apart from few extremely simple cases, no analytical solution is known and the only possible way to obtain the flow field from the equation set is by means of numerical methods.

2.1.2 Turbulent single-phase flows

In principle, the numerical solution of equations (2.3) and (2.5) provides the time-dependent, three-dimensional flow field both for laminar and for turbulent flows. However, in the case of turbulent flow, usually it is not possible to properly resolve in space and time all the energy-containing turbulence structures, leading to one of two undesirable outcomes (Micale et al., 2001):

- For accurate and not dissipative numerical schemes, the solution will exhibit unrealistically large oscillations and will possibly diverge. In this case, the

large scales of the motion are well resolved and the energy cascade correctly transfer kinetic energy from larger to smaller scales down to the grid size. However, a build-up of fluctuations at this end of the spectrum will result, since direct viscous dissipation from these smallest resolved scales will not be sufficient to match the energy input from larger scales. The result will be unrealistic, with the possibility of numerical divergence (Micale et al., 2001).

- If the numerical scheme implies a sufficient amount of numerical viscosity, a stable and even realistic time-dependent solution can be obtained. However, a grid-dependent energy dissipation will replace the complex effects of small-scale fluid dynamics and the solution will be globally inaccurate, since the small scales inaccuracy will propagate up to the large scales (Micale et al., 2001).

Actually, the extremely complex and apparently stochastic nature of turbulence is not due to external sources (i.e. fluctuations in the boundary conditions) neither to an inadequate mathematical formulation of the problem, but it is an intrinsic property of some solutions of the equations. When turbulent fluid flow is involved, the numerical solution of the above set of equations should result into the instantaneous values of the velocity and pressure fields in the whole system. This approach, known as Direct Numerical Simulation (DNS), is possible with presently available computers only for rather simple flow cases. It is impossible for the description of high Reynolds number turbulent flow as the full spectrum of time and length scale must be examined (since the time scale is proportional to $Re^{-5/2}$ and the length scale to $Re^{5/4}$). This implies that higher the Reynolds number is the finer should be the grid and the smaller the time step, in order to capture all the features of the turbulent flow field. In any case, DNS is an important tool for understanding the turbulent structures and the laminar-turbulent transition. It also plays a vital role in the development and calibration of new and/or improved turbulence models. However in engineering applications, the effects of turbulence can be taken into account only approximately, using models of various complexities. Applying a turbulence model to a physical problem practically means to renounce to study the real behaviour of the fluid, substituting it with an equivalent fluid, which can be described with constitutive equations which behaves in a sufficiently regular and predictable way.

The first level of approximation is reached by the Large-Eddy Simulation (LES) approach. The development of LES is founded on the observation that the small scales of turbulent motion posses a more universal character than the large scales, which transport the turbulent energy. Thus the idea is to resolve only the large eddies accurately and to approximate the effects of the small scales by relatively simple subgrid-scales models. Since LES requires significantly less grid points than

DNS, the investigation of turbulent flows at much higher Reynolds numbers become feasible. However since LES is inherently three-dimensional and unsteady, it is still computationally very demanding and LES is still far from becoming an engineering tool.

The next level of approximation is represented by the so-called Reynolds Averaged Navier-Stokes equations (RANS). It is based on the decomposition of the flow variables into a mean and a fluctuating part followed by time or ensemble averaging. In all engineering applications, information on the mean value of the physical quantities of interest is usually more useful then the huge amount of instantaneous values that would be produced by DNS. It is therefore reasonable to rewrite the flow equations in time averaged form and then attempt to solve the resulting equations set in order to directly obtain the time averaged values of the quantities of interest.

The RANS approach

The Reynolds averaging procedure is based on the time mean of the generic flow quantity Φ:

$$\overline{\Phi} = \frac{1}{T}\int_T \Phi dt \tag{2.6}$$

in which T is defined as an interval simultaneously long with respect to the time scale of the turbulent fluctuations, but short with respect to the time constants characteristic of the long-term variation of Φ. This definition is actually ambiguous in the case of time-dependent flows, where it is meaningful only if a clear gap exists between the time scale of the true turbulent fluctuations and that of the long-term changes. It is conceptually more sound to think of $\overline{\Phi}$ as an ensemble average over the set of all realizations of the flow. Φ is formally splitted into mean and fluctuating components:

$$\Phi = \overline{\Phi} + \Phi' \tag{2.7}$$

Representing each variables as the sum of its time-averaged mean value and a fluctuating component (Tennekes and Lumely, 1977), the resulting averaged equations are:

$$\nabla \cdot \bar{\boldsymbol{u}} = 0 \tag{2.8}$$

$$\rho\frac{\partial \bar{\boldsymbol{u}}}{\partial t} = -\rho\nabla\cdot\bar{\boldsymbol{u}}\bar{\boldsymbol{u}} - \nabla\bar{p} - \left[\nabla\cdot\boldsymbol{\tau}^{(t)}\right] + \mu\nabla^2\bar{\boldsymbol{u}} + \rho\boldsymbol{g} \tag{2.9}$$

that are commonly known as Reynolds equations.

As a result, equations formally similar to (2.3) and (2.2) are obtained, but they govern the space and time behaviour of mean quantities $\bar{p}$ and $\bar{\boldsymbol{u}}$ rather than of instantaneous values p and $\boldsymbol{u}$ and they contain extra terms.

For incompressible flows, the only extra terms are turbulent stresses $\tau^{(t)}$, whose physical origin can be related to the interaction among the fluctuating fluid motion with the time-averaged fluid motion. The presence of these extra terms introduces the so-called *closure problem*. In fact six more unknowns are now involved and to close the problem six more equations are therefore required.

The set of equations that gives the Reynolds stresses as a function of the time-averaged variables is called *turbulence model*. Once the Reynolds equations are coupled with a suitable turbulence model, a mathematically closed set of equations is obtained, that can be solved by numerical strategies.

Considerable efforts in developing turbulence models have been made in the last decades, as the accuracy of the fluid flow solution strongly depends on the modelling of the new unknowns, i.e. the components of the Reynolds stress tensor.

The $\kappa - \epsilon$ model

The most successful and widely validated turbulence model is the $\kappa - \epsilon$ model (Launder and Spalding, 1974). It is most often used in engineering applications, since it offers a reasonable compromise between computational effort and accuracy. It is based on the Boussinesq eddy viscosity hypothesis to link the Reynolds stress components to the mean velocity gradient. A new unknown is introduced in place of the six Reynolds stresses: the turbulence viscosity. It relies on the Boussinesq assumption that an analogy exists among the viscous stresses and the Reynolds stresses relationships with the instantaneous and mean velocity respectively. According to this analogy the Reynolds stress tensor, $\tau^{(t)}$, can be modelled in a similar way as the Newton law for the viscous stresses (2.4). The resulting constitutive equation in the case of incompressible fluid is:

$$\tau_{ij}^{(t)} = \tau_{ji}^{(t)} = -\mu_t \left(\frac{\partial \overline{u_i}}{\partial x_j} + \frac{\partial \overline{u_j}}{\partial x_i} \right) \tag{2.10}$$

where μ_t $[Pa\ s]$ is the eddy (or turbulent) viscosity. It is worth noting that the Boussinesq hypothesis implies the isotropy of the turbulent viscosity, i.e. the ratio between the Reynolds stresses components and the corresponding mean deformation rate is constant. This assumption is not verified in many turbulent flows and therefore, in particular for flows characterised by a strong stress anisotropy, the closure based on it cannot lead to accurate prediction of the fluid flow characteristics.

In order to close the problem in the $\kappa - \epsilon$ model a new equation for μ_t is introduced that relates it to other quantities, i.e. the turbulent kinetic energy, κ, and the dissipation of the turbulent kinetic energy, ϵ, that are defined in the following way:

$$\kappa = \frac{1}{2}\left(\overline{u_1'^2} + \overline{u_2'^2} + \overline{u_3'^2}\right) = \frac{1}{2}\sum_i \overline{u_i'^2} \tag{2.11}$$

$$\epsilon = \sum_{ij} \frac{\mu}{\rho}\overline{\frac{\partial u_i'}{\partial x_j}\frac{\partial u_i'}{\partial x_j}} \tag{2.12}$$

From the dimensionless analysis, μ_t can be expressed as the product of a velocity scale θ and a length scale l:

$$\mu_t = C_\mu \rho \theta l \tag{2.13}$$

where C_μ is an empirical dimensionless constant.

If κ and ϵ are adopted to define θ and l:

$$\theta = \kappa^{1/2} \tag{2.14}$$

$$l = \frac{\kappa^{3/2}}{\epsilon} \tag{2.15}$$

substituting eqns. (2.14) and (2.15) in eqn. (2.13), it follows that:

$$\mu_t = C_\mu \rho \frac{\kappa^2}{\epsilon} \tag{2.16}$$

At this point one equation for μ_t has been added (2.16) but two more unknowns (κ and ϵ) have been introduced, and in order to close the problem two more equations are needed. These are the transport equation for κ and ϵ that are derived in the following way.

The turbulent kinetic energy transport equation can be derived by the difference between the instantaneous kinetic energy and mean kinetic energy transport equations. The first can be easily obtained from the Navier-Stokes equation adding together each of its three components respectively multiplied by the corresponding mean velocity component, while the latter can be obtained by a similar procedure from the Reynolds averaged equation.

The resulting κ transport equation is:

$$\frac{\partial \rho\kappa}{\partial t} + \frac{\partial \rho\overline{u_j}\kappa}{\partial x_j} = \frac{\partial}{\partial x_j}\left(\mu\frac{\partial \kappa}{\partial x_j}\right) - \frac{\partial}{\partial x_j}\left(\frac{1}{2}\rho\overline{u_j' u_i' u_i'}\right) - \rho\overline{u_i' u_i'}\frac{\partial \overline{u_i}}{\partial x_j} - \mu\overline{\frac{\partial u_i'}{\partial x_j}\frac{\partial u_i'}{\partial x_j}} \tag{2.17}$$

where the first and second term at the left-hand side represents the accumulation rate and the mean flow transport, respectively. The terms at the right-hand side represent the molecular transport, the turbulent transport, T_κ, the production term, P_κ, and the dissipation. All of them can be written in the exact form except for T_κ and P_κ, which need to be modelled.

The production rate term can be modelled through the *generalized Boussinesq hypothesis*, i.e.:

$$\tau_{ij}^{(t)} = \rho\overline{u_i' u_j'} = -\mu_t \left(\frac{\partial \overline{u_i}}{\partial x_j} + \frac{\partial \overline{u_j}}{\partial x_i} \right) + \frac{2}{3}\rho\kappa\delta_{ij} \tag{2.18}$$

where δ_{ij} is the Kronecker delta. This generalized hypothesis (2.18) is adopted (instead of (2.10)) in order to ensures that the sum of the normal Reynolds stress components gives always a physically correct result.

Actually, the normal components of the Reynolds stresses are, by definition, given by:

$$\tau_{x_1x_1} = \rho\overline{u_1'^2}; \qquad \tau_{x_2x_2} = \rho\overline{u_2'^2}; \qquad \tau_{x_3x_3} = \rho\overline{u_3'^2} \tag{2.19}$$

from which clearly results that:

$$\rho\overline{u_1'^2} + \rho\overline{u_2'^2} + \rho\overline{u_3'^2} = 2\rho\kappa \tag{2.20}$$

substituting eqn. (2.10) and the continuity equation for incompressible fluids eqn. (2.3) into eqn.(2.20) the following clearly impossible result is obtained:

$$\kappa = \frac{-\mu_t \nabla \boldsymbol{u}}{\rho} = 0 \tag{2.21}$$

The adoption of the generalised Boussinesq hypothesis avoids this discrepancy. It is worth however observing that a further assumption is involved in eqn. (2.18), i.e. that the κ total value is equally subdivided among the normal stresses.

Finally the production rate term is modelled as:

$$P_\kappa = -\rho\overline{u_i' u_j'}\frac{\partial \overline{u_i}}{\partial x_j} \approx \mu_t \left(\frac{\partial \overline{u_i}}{\partial x_j} + \frac{\partial \overline{u_j}}{\partial x_i} \right) \frac{\partial \overline{u_i}}{\partial x_j} - \frac{2}{3}\rho\kappa\delta_{ij}\frac{\partial \overline{u_i}}{\partial x_j} \tag{2.22}$$

For incompressible fluids:

$$\frac{2}{3}\rho\kappa\delta_{ij}\frac{\partial \overline{u_i}}{\partial x_j} = 0 \tag{2.23}$$

and then:

$$P_\kappa \approx \mu_t \left(\frac{\partial \overline{u_i}}{\partial x_j} + \frac{\partial \overline{u_j}}{\partial x_i} \right) \frac{\partial \overline{u_i}}{\partial x_j} \tag{2.24}$$

The turbulent transport term of κ, T_κ, can be modelled with an expression similar to the turbulent momentum transport equation:

$$T_\kappa = \frac{1}{2}\rho\overline{u_j' u_i' u_i'} + \overline{\rho u_j'} \approx \frac{\mu_t}{\sigma_k}\frac{\partial \kappa_i}{\partial x_j} \tag{2.25}$$

where the value of the empirical constant σ_κ is expected to be close to 1.

Substituting the modelled terms in the exact κ transport equation (2.17) the modelled κ equation can be obtained:

$$\frac{\partial \rho\kappa}{\partial t} + \frac{\partial \rho\kappa\overline{u_i}}{\partial x_i} = \frac{\partial}{\partial x_j}\left[\left(\mu + \frac{\mu_t}{\sigma_k}\right)\frac{\partial \kappa}{\partial x_j}\right] + \mu_t\left(\frac{\partial \overline{u_i}}{\partial x_j} + \frac{\partial \overline{u_j}}{\partial x_i}\right)\frac{\partial \overline{u_i}}{\partial x_j} - \rho\epsilon \tag{2.26}$$

In a similar way, the transport equation for ϵ can be derived from the Navier-Stokes equation. It has the same form of the transport equation for κ and it also has some terms that needs to be modelled, such as the production, P_ϵ, and dissipation, D_ϵ, terms, which are assumed to be proportional to the corresponding terms in the κ equation. This assumption ensures that ϵ decreases in such a way that it is always positive even when κ decreases.

Under this assumption the production term is given by:

$$P_\epsilon = C_{\epsilon 1}\frac{\epsilon}{\kappa}P_\kappa \tag{2.27}$$

and the dissipation term is:

$$D_\epsilon = C_{\epsilon 2}\rho\frac{\epsilon^2}{\kappa} \tag{2.28}$$

Finally employing the generalised gradient diffusion hypothesis, the turbulent transport term can be written as:

$$T_\epsilon = \frac{\partial}{\partial x_j}\left(\frac{\mu_t}{\sigma_\epsilon}\frac{\partial \epsilon}{\partial x_j}\right) \tag{2.29}$$

The resulting modelled ϵ transport equation is:

$$\frac{\partial \rho\epsilon}{\partial t} + \frac{\partial \rho\overline{u_j}\epsilon}{\partial x_j} = \frac{\partial}{\partial x_j}\left[\left(\mu + \frac{\mu_t}{\sigma_\epsilon}\right)\frac{\partial \epsilon}{\partial x_k}\right] + C_{\epsilon 1}\frac{\epsilon}{\kappa}P_\kappa - C_{\epsilon 2}\rho\frac{\epsilon^2}{\kappa} \tag{2.30}$$

The modelled ϵ transport equation (2.30) coupled with the modelled κ transport equation (2.26) finally leads to the mathematical closure of the problem.

The five empirical constants appearing in the equations have to be derived by comparison of the predicted flow fields with experimental values. Among the values reported in the literature those leading to the most reliable results and that have been validated in a number of relevant cases are those proposed by Launder and Spalding (1974). These emphstandard $\kappa - \epsilon$ constants values are:

$$C_\mu = 0.09$$
$$C_{\epsilon 1} = 1.44$$
$$C_{\epsilon 2} = 1.92$$
$$\sigma_\kappa = 1.0$$
$$\sigma_\epsilon = 1.3$$

The $\kappa - \epsilon$ model has given excellent results in the modelling of many industrial problems of fluid flow and up to now is the most widely validated turbulence model. Moreover it is mathematically robust and it is a simple model, as it requires only initial and boundary conditions. For these reason the $\kappa - \epsilon$ model has become the standard in most CFD applications and will be selected in the following turbulence flow problems.

2.1.3 Laminar multi-phase flows

Multi-phase problems are widely present in nature and industrial equipment. Their modelling is usually faced through two different modelling approaches. In all cases, for the continuous phase an Eulerian formulation is adopted while the dispersed phase is treated by either a discrete model or a continuum model.

In the former case, namely the Eulerian-Lagrangian approach, the equations of motion for each particle are solved taking into account the forces acting on the discrete phase and the collisions between them, while with the continuum model, referred to as Eulerian-Eulerian approach, the solids are considered as fully interpenetrating continua subject to continuity and momentum equations.

The Eulerian-Lagrangian approach is a powerful tool, because it permits to obtain detailed information on the motion of particles and it may be used to develop or test constitutive relations for particle-particle interactions, for example. However, this is also an expensive tool, because the computational time step has to be set close to the time scale of the particle-particle interactions, which is much less than the macroscopic flow time scale. Also the limitations, due to computational power requirements, on the particle number make the Lagrangian approach unsuitable for the simulation of dense fluid-solid (two-phase) systems. For these reasons, the computational time necessary in Eulerian-Lagrangian simulations can be orders of magnitude higher than that needed for Eulerian-Eulerian ones. In any case, researchers adopted both the discrete and continuum approaches for different equipment simulation with a certain degree of success (van den Akker, 2006).

In this work the Eulerian-Eulerian approach will be followed and thus the two phases are treated as separate fluids, occupying disconnected regions of space. In this model the continuity and momentum equations for a generic multi-phase system are solved and therefore separate flow fields for each phase are determined simultaneously.

The continuity and momentum equations for the multi-phase system are similar to the single-phase equations. The continuity equation for a generic phase k, based on the Eulerian treatment, is:

$$\frac{\partial \rho_k \phi_k}{\partial t} = -\nabla \cdot (\rho_k \phi_k \boldsymbol{u}_k) \tag{2.31}$$

where ϕ is the volumetric fraction.

The momentum equation for the continuous phase is expressed as:

$$\frac{\partial (\rho_c \phi_c \boldsymbol{u}_c)}{\partial t} + \nabla \cdot (\rho_c \phi_c \boldsymbol{u}_c \boldsymbol{u}_c) + \nabla \cdot \rho_c \tau_c = -\phi_c \nabla \boldsymbol{p}_c + \phi_c \rho_c \boldsymbol{g} + \sum_{d_i} F^{d_i c} \tag{2.32}$$

and for the i-th discrete phase as:

$$\frac{\partial (\rho_{d_i} \phi_{d_i} \boldsymbol{u}_{d_i})}{\partial t} + \nabla \cdot (\rho_{d_i} \phi_{d_i} \boldsymbol{u}_{d_i} \boldsymbol{u}_{d_i}) + \nabla \cdot \rho_{d_i} \tau_{d_i} = -\phi_{d_i} \nabla \boldsymbol{p}_{d_i} + \phi_{d_i} \rho_c \boldsymbol{g} + F^{c d_i} + \sum_{d_k} F^{d_k d_i} \tag{2.33}$$

where c refers to the continuous phase, while d_i and d_k to the generic dispersed phase.

The volume balance on all the phases is:

$$\sum_k \phi_k = 1 \tag{2.34}$$

It can be observed that in the momentum balance equations new terms appear with respect to the single phase equation. They are the momentum exchange terms between the different phases. These terms are given by the linear combination of the mechanisms that contribute to momentum exchange between the phases, i.e. drag force, added mass, lift and Basset terms.

Under the hypothesis that all phases share the same pressure field, substituting the modelled momentum transfer terms and a suitable constitutive equation for the viscous stress tensor, τ, in the momentum equations, the above equations constitute a set of $4 \times N + 1$ equations, equal to the total number of unknowns, which are the pressure, the N volumetric fractions and the $3 \times N$ velocity components.

2.1.4 Turbulent multi-phase flows

In the case of turbulent flows, again conservation equations need to be time averaged and in the momentum equation new unknown terms arise that involve the fluctuating velocity of both phases and of the volume fraction fluctuation. These

terms are usually modelled by substituting the fluctuations of the dispersed phases with the corresponding quantities of the continuous phase (Gosman et al., 1992).

As in the case of turbulent single-phase flows, for modelling the Reynolds stress tensor a turbulence model has to be devised, but as a difference, no well-tested turbulence models are available for turbulent multiphase problems.

A possible solution is to employ an extension of the standard $\kappa - \epsilon$ model. In this case the modelling of the κ and ϵ transport equations is more complicated, as new unknown *interphase transfer terms* arise. These terms allows, in principle, to account for turbulence promotion or damping due to the presence of the dispersed phases. In absence of reliable information on these terms, the simple *homogeneous* approach can be employed, where both phases are assumed to share the same values of κ and ϵ and the inter-phase turbulence transfer is not considered. In this case the above equations for κ and ϵ simplifies to:

$$\frac{\partial}{\partial t}(\rho\kappa) + \nabla\left(\rho\overline{\boldsymbol{u}}\kappa - \left(\mu + \frac{\mu_t}{\sigma_k}\right)\nabla\kappa\right) = S_\kappa \tag{2.35}$$

$$\frac{\partial}{\partial t}(\rho\epsilon) + \nabla\left(\rho\overline{\boldsymbol{u}}\epsilon - \left(\mu + \frac{\mu_t}{\sigma_\epsilon}\right)\nabla\epsilon\right) = S_\epsilon \tag{2.36}$$

where:

$$\rho = \sum_k \phi_k \rho_k \tag{2.37}$$

$$\overline{\boldsymbol{u}} = \frac{1}{\rho}\sum_k \phi_k \rho_k \overline{\boldsymbol{u}_k} \tag{2.38}$$

$$\mu_t = \sum_k \rho_k \mu_{t,k} = \rho c_\mu \frac{\kappa^2}{\epsilon} \tag{2.39}$$

$$S_\kappa = \sum_k \phi_k S_{\kappa k} \tag{2.40}$$

$$S_\epsilon = \sum_k \phi_k S_{\epsilon k} \tag{2.41}$$

With this model the different inertia of phases is taken into account and, at least in principle, flow fields involving higher particle concentration can be dealt with.

2.2 Numerical techniques

2.2.1 Discretization procedure

The motion of fluids is governed by a closed set of equations, whose solution leads to the determination of the fluid velocity and pressure fields. Unfortunately analytical methods are applicable only to simplified flow problems and nearly all solution strategies adopt numerical methods.

The first step of a numerical approach is to devide the physical space where the flow is to be computed into a large number of geometrical elements called grid cells. The grid normally consists in two dimensions of triangles or quadrilaterals, and in three dimensions of tetrahedra, hexaedra, prisms or pyramids. The most important requirements for a grid is that there must not be any holes between the grid cells and that grid cells do not overlap. The grid should be smooth, i.e. there should be no abrupt changes in the volume of the grid cells or in the stretching ratio and the elements should be as regular as possible (Blazek, 2001). The grid is used either to construct control volumes and to evaluate the flux integrals, or to approximate the spatial derivatives of the flow quantities.

Basically two types of grids exist (Blazek, 2001):

- Structured grids, where each grid point is uniquely identified by the indices i, j, k and the corresponding Cartesian coordinates. The grid cells are quadrilateral in 2D and hexaedra in 3D.

- Unstructured grids, where grid cells as well as grid points have no particular ordering, i.e. neighbouring cells or grid points cannot be directly identified by their indices. Unstructured grids usually consist of a mix of quadrilaterals and triangles in 2D and of hexaedra, tetrahedra, prisms and pyramids in 3D.

The main advantage of structured grids is that computer memory can access the neighbours of a grid point very quickly and easily and the evaluation of gradients, fluxes and also the treatment of boundary conditions is greatly simplified, however for complex geometries the generation of structured grids is complex. On the other side, unstructured grids offer the largest flexibility and can be generated automatically, independent of the complexity of the domain (Blazek, 2001).

Having generated the grid, the next step is to discretise the governing equations into a set of algebraic equations that can be solved by a suitable iterative procedure. The accuracy of the solution therefore depends on the grid choice, as the smaller are the computational cells the closer it is to the exact solution. For transient problems the accuracy of the solution will depend also on the time interval size. This step can been accomplished with different methodologies, among which only the finite volume method will be discussed in the present work. This method directly utilises

the conservation laws, discretising them on each control volume (grid cells) and approximating the surface integral by the sum of the fluxes crossing the individual faces of the control volume.

The transport equation of the generic variable Φ is:

$$\frac{\partial \rho \Phi}{\partial t} + \nabla \cdot (\rho \Phi \boldsymbol{u}) = \nabla \cdot (\Gamma \nabla \Phi) + S_\Phi \tag{2.42}$$

where S_Φ is a source term that includes the contributions of pressure and body forces. When integrated on a volume ΔV and on a time interval Δt it becomes:

$$\int_{\Delta t}\int_{\Delta V} \frac{\partial \rho \Phi}{\partial t} dV dt + \int_{\Delta t}\int_{\Delta V} \nabla \cdot (\rho \Phi \boldsymbol{u})\, dV dt = \\ = \int_{\Delta t}\int_{\Delta V} \nabla \cdot (\Gamma \nabla \Phi)\, dV dt + \int_{\Delta t}\int_{\Delta V} S_\Phi dV dt \tag{2.43}$$

Applying the Gauss theorem one obtains:

$$\int_{\Delta t} \frac{\partial}{\partial t} \int_{\Delta V} (\rho \Phi)\, dV dt + \int_{\Delta t}\int_{A_V} (\rho \Phi \boldsymbol{u}) \cdot \boldsymbol{n} dA dt = \\ = \int_{\Delta t}\int_{A_V} (\Gamma \nabla \Phi) \cdot \boldsymbol{n} dA dt + \int_{\Delta t}\int_{\Delta V} S_\Phi dV dt \tag{2.44}$$

that in a stedy-state problem can be simplified as:

$$\int_{A_V} (\rho \Phi \boldsymbol{u}) \cdot \boldsymbol{n} dA = \int_{A_V} (\Gamma \nabla \Phi) \cdot \boldsymbol{n} dA + \int_{\Delta V} S_\Phi dV \tag{2.45}$$

Equations' spatial discretization

In this context, it is convenient to differentiate between the discretization of the convective and the viscous fluxes. Because of the physical nature of the viscous fluxes, the only reasonable way to discretize them is to employ central differences. However CFD codes can store discrete values of the scalar Φ at the cell centres, while face values Φ_f are required for the convection terms and must be interpolated from the cell centre values. This is usually accomplished using an upwind scheme. This method takes into account the flow direction when determining the value of Φ at the cell face. Upwinding means that the face value Φ_f is derived from quantities in the cell upstream, or upwind, relative to the direction of the normal velocity. It is possible to choose from several upwind schemes, for example first-order upwind, second-order upwind and QUICK. Different discretization scheme can be applied to the integrated equations and in the following a brief description of the features of the principal ones will be given.

Central Differencing Scheme The principle is to average the conservative variables to the left and right cells faces in order to evaluate the flux at a side of a control volume. Let's consider the cell volume of centre P. In the following the subscript e, w, s, n, b, t are referred to the face centres in the directions est, west, south, north, bottom and top respectively. Capital letters E, W, S, N, B, T are referred to the centres of the adjacent cells volumes in the corresponding directions.

Considering for simplicity the steady state integrated equation (2.45), the convective and diffusive fluxes through the cell faces can be approximated by values of the flow variables in the cell central points. When applying this approximation and assuming that the source terms are linearly approximated as:

$$S_\Phi \nabla V = S_u + S_p \Phi_P \tag{2.46}$$

the general discretized expression becomes:

$$a_p \Phi_P = a_w \Phi_W + a_e \Phi_E + a_s \Phi_S + a_n \Phi_N + a_b \Phi_B + a_t \Phi_T + S_u + S_p \Phi_P \tag{2.47}$$

where the coefficients are a function of the diffusive coefficients, of the convective fluxes and of the size of the cell. This scheme is second order accurate and is well suited for dicretising the diffusive flux terms, but cannot take into account the flux directionality, thus it does not properly dicretize the convective flux terms and can lead to oscillations. For this reason, it is necessary to employ an alternative method for the discretization of the convective terms.

First-Order Upwind Scheme When first-order accuracy is desired, quantities at cell faces are determined by assuming that the cell-centre values of any field variable represent a cell-average value and hold throughout the entire cell (i.e. the face quantities are identical to the cell quantities). Thus when first-order upwinding is selected, the face value Φ_f is set equal to the cell-centre value of Φ in the upstream cell. The accuracy in this case is only first order and when the flow is not aligned with the grid lines the method leads to severe *numerical diffusion* problems.

Second-Order Upwind Scheme When second-order accuracy is desired, quantities at cell faces are computed using a multidimensional linear reconstruction approach (Barth and Jespersen, 1989). In this approach, higher-order accuracy is achieved at cell faces through a Taylor series expansion of the cell-centred solution about the cell centroid. The face value Φ_f is computed using the following expression:

$$\phi_f = \Phi + \nabla\Phi \cdot \boldsymbol{r} \tag{2.48}$$

where Φ and $\nabla\Phi$ are the cell-centred value and its gradient in the upstream cell, and $\boldsymbol{r}$ is the displacement vector from the upstream cell centroid to the face centroid.

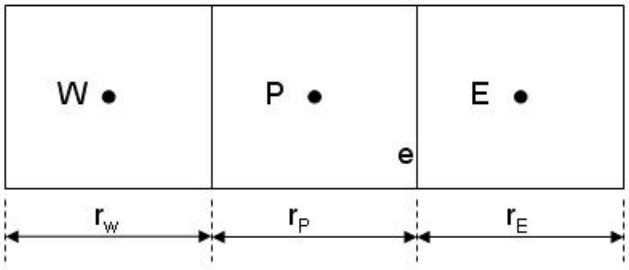

Figure 2.1: Face e and its neighbour cells

QUICK Scheme The QUICK scheme permits to compute a higher-order value of the convected variable Φ at a face. QUICK-type schemes are based on a weighted average of second-order-upwind and central interpolations of the variable. For the face e (see Figure 2.1), if the flow is from left to right, such a value can be written as:

$$\Phi_e = \varphi \left[\frac{r_E}{r_P + r_E} \Phi_P + \frac{r_P}{r_P + r_E} \Phi_E \right] + (1 - \varphi) \left[\frac{r_W + 2r_P}{r_W + r_P} \Phi_P + \frac{r_P}{r_W + r_P} \Phi_W \right] \quad (2.49)$$

Equations' temporal discretization

Usually a separate discretization in space and time is adopted, permitting in this way a large flexibility, since different levels of approximation can be selected for the convective and the viscous fluxes, as well as for the time integration.

A generic expression for the time evolution of a variable Φ is given by:

$$\frac{\partial \Phi}{\partial t} = f(\Phi) \quad (2.50)$$

where the function f incorporates any spatial discretization. If the time derivative is discretized using backward differences, the first-order accurate temporal discretization is given by:

$$\frac{\Phi^{n+1} - \Phi^n}{\Delta t} = f(\Phi) \quad (2.51)$$

and the second-order discretization is given by:

$$\frac{3\Phi^{n+1} - 4\Phi^n + \Phi^{n-1}}{2\Delta t} = f(\Phi) \quad (2.52)$$

Once the time derivative has been discretized, a choice remains on how to evaluate $f(\Phi)$, in particular at which time level.

One method is to evaluate $f(\Phi)$ at the future time level:

$$\frac{\Phi^{n+1} - \Phi^n}{\Delta t} = f\left(\Phi^{n+1}\right) \tag{2.53}$$

This is referred to as *implicit* integration since Φ^{n+1} in a given cell is related to Φ^{n+1} in neighbouring cells through $f(\Phi^{n+1})$:

$$\Phi^{n+1} = \Phi^n + \Delta t f\left(\Phi^{n+1}\right) \tag{2.54}$$

This implicit equation can be solved iteratively at each time level before moving to the next time step. The advantage of the fully implicit scheme is that it is unconditionally stable with respect to time step size.

2.2.2 Pressure-velocity coupling algorithms

The fluid flow equations are basically conservation equations for mass and momentum. No analogous equation can be written for the pressure p, that is implicitly contained in the momentum equation. When dealing with compressible fluid flows, the equation of state, that links density to pressure, allows to explicitly derive the pressure. In the case of incompressible flow, as the density is constant and by definition not linked to p, it is necessary to introduce pressure-velocity coupling methods that allows using the continuity equations to determine the correct pressure and velocity fields by iterative procedures.

SIMPLE algorithm The simplest coupling algorithm is the SIMPLE method (Semi-Implicit Method for Pressure Linked Equations) proposed by Patankar and Spalding (1972). The discretized continuity and Navier-Stokes in a centred Cartesian grid are:

$$\sum u_{i,f} A_f = 0 \tag{2.55}$$

$$a_p u_{i,P} - \sum a_f u_{i,f} - A_f p + S_p = 0 \tag{2.56}$$

where the subscript f is referred to the values in the cell faces and the pressure term contribution has been extracted from the source term. If the fluxes through the faces are taken equal to the mean between the values in centres of the adjacent cells, the continuity equation (2.55) can be written as:

$$A_f\left(u_{1,E} - u_{1,W}\right) + A_f\left(u_{2,N} - u_{2,S}\right) + A_f\left(u_{3,T} - u_{3,B}\right) = 0 \tag{2.57}$$

or in compact form:

$$\sum A_i u_i = 0 \tag{2.58}$$

The SIMPLE algorithm consists in the following steps:

- if p^k is the pressure field at the generic iteration k, the velocity field obtained from the momentum equation $u^*_{i,P}$ must clearly satisfy eqn. (2.56):

$$a_p u^*_{i,P} - \sum a_f u^*_{i,f} - A_f p^k + S_P = 0 \tag{2.59}$$

- If $u^*_{i,P}$ was the correct velocity field it should satisfy also the continuity equation (2.58), if not, a mass source will appear:

$$\sum A_p u^*_{i,P} = \dot{m}_p \neq 0 \tag{2.60}$$

Naming p and u_i the correct pressure and velocities values that contemporary satisfy the continuity and momentum equations, they can be expressed as:

$$p = p^k + p^{corr} \tag{2.61}$$

$$u_i = u^*_i + u^{corr}_i \tag{2.62}$$

and the problem becomes that of determining the corrective terms p^{corr} and u^{corr}_i. A correlation between p^{corr} and u^{corr}_i can be obtained by subtracting eqn. (2.59) and eqn. (2.56):

$$a_p u^{corr}_{i,p} - \sum a_f u^{corr}_i - A_f p^{corr} = 0 \tag{2.63}$$

By neglecting the second term in eqn. (2.63) and substituting the u^{corr} value obtained from eqn. (2.62), one obtains:

$$u_{i,P} = u^*_{i,P} + a_P^{-1} A_f p^{corr} \tag{2.64}$$

Substituting it in eqn. (2.58):

$$\sum A_i u^*_{i,p} + \sum A_i \left(a_p^{-1} A_f p^{corr}\right) = 0 \tag{2.65}$$

which, considering eqn. (2.60), can be written as:

$$\dot{m}_p + \sum A_i \left(a_p^{-1} A_f p^{corr}\right) = 0 \tag{2.66}$$

From this last equation the pressure correction can be obtained.

- At this point the pressure and velocity fields can be adjusted through the relevant equations (2.61) and (2.62) and the resulting new values can be adopted to iterate the procedure till a sufficient degree of convergence is achieved.

The main inconsistency of the SIMPLE method is the assumption that in eqn. (2.63) the second term can be neglected. This introduces an error in the pressure correction equation and, even though the term p^{corr} is reduced to zero when the iteration procedure converges, it may cause a very slow convergence or even divergence of the algorithm. A solution could be introducing suitable under-relaxation factors in the momentum and pressure correction equations. To under-relax a generic variable Φ means that the value to be considered at the iteration $k+1$ is:

$$\left\{ \Phi^{k+1} = \alpha \Phi^{new} + (1-\alpha)\,\Phi^{k} \quad 0 < \alpha < 1 \right. \tag{2.67}$$

where Φ^{new} is the new Φ value obtained at the end of the $k+1$ iteration, while α is the under-relaxation factor and its value depends on the specific problem.

SIMPLEC algorithm A better coupling algorithm is a modification of the SIMPLE, the so-called SIMPLEC (VanDoormal and Raithby, 1984). In this method a better approximation in eqn. (2.63) is applied. If p varies by the amount p^{corr}, this leads to variations of the velocity at the point P, $u_{i,p}$, and in the neighbour point, u_i. This variations are of the same order and therefore neglecting u_i in eqn. (2.63) without neglecting $u_{i,P}$ is not a consistent approximation. The SIMPLEC algorithm improves this approximation by adding and subtracting the term $\sum a_f u_{i,p}^{corr}$ in eqn. (2.63):

$$a_p u_{i,p}^{corr} - \sum a_f u_i^{corr} - A_f p^{corr} + \sum a_f u_{i,p}^{corr} - \sum a_f u_{i,p}^{corr} = 0 \tag{2.68}$$

and rearranging:

$$a_p u_{i,p}^{corr} - \sum \left(a_f u_i^{corr} + a_f u_{i,p}^{corr} \right) - A_f p^{corr} - \sum a_f u_{i,p}^{corr} = 0 \tag{2.69}$$

The neglected term is now the second one in eqn. (2.69).

The iterative procedure is analogous to the SIMPLE one, but this method does not require to under-relax the pressure term and it leads to a faster convergence in a large number of problems. It is adopted as a standard pressure-velocity algorithm in most of the CFD codes.

2.2.3 Solution algorithm of the discretized equations

The set of linear algebraic equations, that results from the discretisation process, consist of N equations for N unknowns for each variable of the problem, with N being the total number of control volumes of the computational domain. There are two families of solution technique for this kind of equation sets: direct and iterative methods.

In order to solve the equations with a direct method, as for example the standard Gauss elimination, the number of operations, and consequently the CPU time required, is proportional to N^3. Typically the number of cells N is very large in CFD simulations and the direct approaches are therefore usually not suitable.

Iterative methods are based on the repeated applications of algorithms that leads to convergence after a certain number of iterations. If the convergence rate is good enough, the iterative methods are often faster than the direct methods.

The main difference among the two methods is that the latter does never give an exact solution, while in principle the former can. However, in practice the truncation errors involved in the direct method calculations may never allow to reach the true solution.

2.2.4 CFD approach

As a result, the solution of a fluid flow problem by means of a CFD approach involves the followings steps:

1. Pre-processing, in which the specific problem to be solved needs to be specified. This means providing the geometry of the computational domain, its subdivision into discrete control volumes (computational grid), the physical and chemical phenomena involved and the related model equations, the fluid properties and the boundary conditions on the boundary cells.

2. Solving, in which step model equations are solved in the computational domain usually employing Finite Volume Methods (FVM), which is the numerical solution technique employed in most of CFD codes. It requires:

    - integration of the governing equations on the individual control volumes;
    - conversion of the integral equations in a set of algebraic equations by mean of a suitable discretization technique;
    - linearization of the discretized equations;
    - solution of the resultant linear equations system to yield updated values of the dependent variables through an iterative solution method of the resulting algebraic equations.

3. Post-processing, which is needed in order to display and analyse the simulation results.

2.3 Optical techniques

2.3.1 Particle Image Velocimetry

Particle Image Velocimetry (PIV) is a widely used measurement technique, which permits to collect accurate information of a large part of a flow field of an equipment, in a fast and not intrusive way and with a good repeatability. The result is the instantaneous velocity of a fluid throughout a region illuminated by a two-dimensional light sheet.

PIV measures the velocity of the fluid by means of the measurement of the velocity of tracer particles within the flow, which in most applications have to be purposely added to the flow. These particles, referred to as seeding, are illuminated in a plane of the flow at least twice within a short time interval. The light scattered by the particles is recorded either on a single frame or on a sequence of frames and the displacement of the particle images between the light pulses is determined through evaluation of the PIV recordings. In order to be able to handle the great amount of data which can be collected employing the PIV technique, sophisticated post-processing is required (Raffel et al., 1998).

The particles are chosen to be near neutrally buoyant and to efficiently scatter light, while the illumination is most commonly provided by a laser, shaped into a planar sheet using cylindrical lenses (Grant, 1997). An advantage of using a laser is that many lasers have a pulsed output with a pulse duration and a repetition rate making them suitable as a stroboscopic illumination source (Grant, 1997). The time delay between pulses depends on the mean flow velocity and the magnification at imaging.

The light scattered by the added particles is detected by a camera which is synchronised with the laser to open shutter simultaneously with the laser pulses using an external hub.

The accuracy of the results depends from the quantity of seeding particles, since a small number of particles are not able to highlight the details of the flow field, while a large number of particles can overload the camera and decreases the results accuracy (Raffel et al., 1998). However, even if the seeding particles quantity is optimal, it is not possible to identify and follow each single particle and the reconstruction of the flow field is done in a statistical way (via auto- and cross-correlation). The recorded images are divided into smaller sub-regions called interrogation areas. These sub-regions are chosen small enough to consider that the velocity inside each interrogation area is constant and uniform (Raffel et al.,

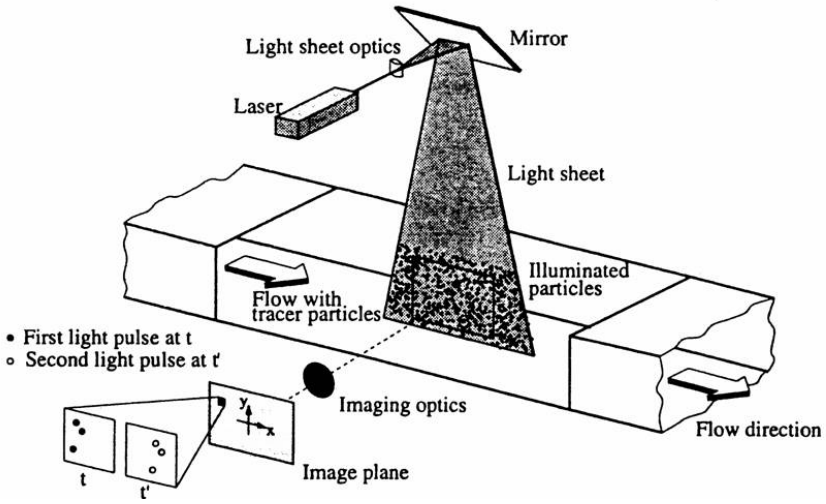

Figure 2.2: Typical experimental arrangement for particle image velocimetry (Raffel et al. 1998)

1998).

The projection of the vector of the local flow velocity into the plane of the light sheet (2-component velocity vector) is calculated taking into account the time delay between the two illuminations and the magnification at imaging. The process of interrogation is repeated for all interrogation areas of the PIV recordings. In this way it is possible to obtain good spatial and temporal details of the average as well as of the fluctuating velocity (Raffel et al., 1998).

Figure 2.2 briefly explain a typical set-up for PIV recording. It needs (Raffel et al. 1998):

- a light source at high power (laser);
- a lens system, which permits to have a light sheet;
- appropriate seeding particles;
- a digital high velocity and high definition camera;
- an appropriate software for the post-processing.

PIV is being successfully used to aid, both qualitatively and quantitatively, the understanding of fluid dynamic phenomena (Grant, 1997) and an important supporting relationship has developed between CFD and PIV. The provision of velocity data, obtained simultaneously, on a distributed spatial grid from PIV studies has led to considerable interest in using the data to validate CFD codes (Collicott,

1993). For this purpose carefully designed experiments are also performed (Raffel et al. 1998).

In a reciprocating manner, many investigators developing PIV analysis systems have looked to CFD as a means of calibrating and validating their analysis software by introducing virtual particles into a numerical flow model and attempting to reconstruct the flow from the resulting trajectories or images (Collicott, 1993).

2.3.2 Planar Laser Induced Fluorescence

Planar Laser Induced Fluorescence (PLIF) is a non-intrusive technique for measuring scalar concentrations in fluid flows. It has been employed in a wide range of experimental configurations, with the sole limitation being a requirement for optical access to the measurement region (Crimaldi, 2008).

The principle of PLIF measurements is to use a substance that has fluorescent properties which can be detected by a camera with an appropriate light filter and to relate the local fluorescence to dye concentration (Crimaldi, 2008).

Typically, the tracer is an organic fluorescent dye such as fluorescein or rhodamine and its local fluorescence is caused by excitation obtained from a thin laser sheet. The dye absorbs a portion of the excitation energy and spontaneously re-emits a portion of the absorbed energy as fluorescence (Crimaldi, 2008). By using a filter, the camera can only pick up light reflected from the dye flowing through the equipment and this fluorescence is used to infer the local concentration of the dye (Crimaldi, 2008). Conversely to PIV, single laser pulses are used instead of two, as it is not the movement of the particles which is being measured but the fluorescent tracer concentration.

2.4 Notation

A:	area, m^2
$C_\mu, C_{\epsilon 1}, C_{\epsilon 2}$:	constant, dimensionless
F:	interphase exchange term, $kgm^{-2}s^{-2}$
$\boldsymbol{g}$:	gravity acceleration, ms^2
l:	length scale, m
p:	pressure, Pa
$\overline{p}$:	mean pressure, Pa
$\boldsymbol{r}$:	displacement vector, m
$S_\kappa, S_\epsilon, S_\Phi$:	source term
t:	time, s
T:	time interval, s
$\boldsymbol{u}$:	velocity vector, $m\ s^{-1}$
$\overline{\boldsymbol{u}}$:	mean velocity vector, $m\ s^1$
$\boldsymbol{u}'$:	velocity fluctuation, $m\ s^{-1}$
V:	volume, m^3

Greek letters

α:	under-relaxation factor, dimensionless
δ_{ij}:	Kronecker delta, dimensionless
ϵ:	turbulent dissipation, m^2s^{-3}
ϕ:	volumetric fraction, dimensionless
φ:	under-relaxation factor, dimensionless
Φ:	generic flow quantity
$\overline{\Phi}$:	generic mean flow quantity
Φ':	generic fluctuating flow quantity
Γ:	diffusivity, m^2s^{-1}
κ:	turbulent kinetic energy, m^2s^{-2}
μ:	dynamic viscosity, $Pa\ s$
μ_t:	turbulent viscosity, $Pa\ s$
θ:	velocity scale, ms^{-1}
ρ:	density, $kg\ m^3$
$\sigma_\epsilon, \sigma_\kappa$:	constant, dimensionless
$\boldsymbol{\tau}$:	viscous stress tensor, $kg\ m^{-1}s^{-2}$
$\boldsymbol{\tau}^{(t)}$:	turbulent stress tensor, $kg\ m^{-1}s^{-2}$

Subscript

c:	continuous phase
d_i, d_k:	dispersed phase

e, w, s, n, b, t:	face centres value in direction est, west, south, north, bottom and top
E, W, S, N, B, T, P:	values at the centres of the corresponding cell volume
f:	face value
i, j:	axis direction
k:	generic phase

Superscript

$corr$:	corrective value
n:	generic time step
k:	generic iteration

2.5 Bibliography

Barth, T.J., Jespersen, D., (1989) The design and application of upwind schemes on unstructured meshes. Technical Report AIAA-89-0366, AIAA 27th Aerospace Sciences Meeting, Reno, Nevada;

Bird, R.B., Stewart, W.E., Lightfoot, E.N., (1960) Transport Phenomena, Wiley, New York;

Blazek, J., (2001) Computational fluid dynamics: principles and applications, Elsevier, Oxford;

Collicott, S. H., (1993) Transition from particle image velocimetry to laser speckle velocimetry with increasing density. In Applications of Laser Techniques to Fluid Mechanics (Ed. R. J. Adrian), pp. 181-194, Springer-Verlag, Berlin;

Crimaldi, J.P., Planar laser induced fluorescence in aqueous flows (2008) Exp. Fluids, 44, pp. 851-863;

Gosman, A.D., Issa, R.I., Lekakou, C., Looney, M.K., Politis, S., Multidimensional modelling of turbulent two-phase flows in stirred vessels (1192) AIChE J., 38, pp. 1946-1956;

Grant, I., Particle image velocimetry: a review (1997) Proc. Instn. Mech. Engrs, part C, 211, pp. 55-76;

Launder, B. E., Spalding, D. B., The numerical computation of turbulent flows (1974) Comput. Meth. Appl. Mech. Eng., 3, pp. 269-289;

Micale, G., Montante, G., Grisafi, F., Brucato A., Ciofalo, M., (2001) CFD Prediction of Turbulent Flow and Mixing in Stirred Vessels: Single- and Two-Phase Flow, Department of Nuclear Engineering, University of Palermo, Res. Memo No. 2/2001, Palermo, Italy (Abbreviated version for MixNet).

Pantankar, S. V., Spalding, D. B., A calculation procedure for the heat mass and momentum transfer in three dimensional parabolic flows, Int. J. heat mass transfer, 15, p. 1787, 1972;

Raffel, M., Willert, C., Kompenhans, J., (1998) Particle Image Velocimetry, A practical guide, Springer, Berlin;

Tennekes, H., Lumely, J.L., (1977) A first course on turbulence, The MIT press, Cambridge, Massachusetts;

van den Akker, H. E. A., The details of turbulent mixing process and their simulation (2006) Adv. Chem. Eng., 31, pp. 151-229, Marin G.B. (Ed), Academic Press;

VanDoormal, J. P., Raithby, G. D., Enhancements of the SIMPLE method for predicting incompressible fluid flows (1984) Numer. Heat Transfer, 7, pp. 147-163;

Chapter 3

Membrane Separation Modules

3.1 Abstract

In this part of the work a novel modelling approach based on Computational Fluid Dynamics for the prediction of the gas separation process in membrane modules for hydrogen purification is developed.

With this approach, the pressure and velocity flow fields of the gas mixture and the species concentration distribution in the selected three-dimensional domain, representing quite closely the selected module geometry, are simultaneously and numerically computed by solving the continuity, momentum and species transport equations, including a gas-through-gas diffusion term derived from the Stefan-Maxwell formulation. As a result, the hydrogen permeation calculations depend on the local determination of the mass transfer resistances offered by the gas phase and by the membrane, which is modelled as a permeable surface of known characteristics and which allows the permeation of different components as a function of the transport mechanisms and of the local driving force.

The reliability of the gas velocity field calculated numerically is assessed by comparison of the predictions with experimental velocity fields collected by Particle Image Velocimetry (PIV).

The applicability of the model to properly predict the separation process under a wide range of pressure, feed flow rate, temperature and gas mixtures composition is assessed through a strict comparison with permeation experimental data, collected from the Membrane Separation research group of DICMA and reported in Pizzi et al. (2008) and Catalano et al. (2009). The influence of inhibitor species on the module performance, that is obtained by implementing in the CFD model a suitable literature correlation, is also discussed.

Finally, the case of a pilot scale module equipped with three Pd-Ag membranes, that are well-suited for the separation of H_2 from methane steam reforming gas

mixtures, is considered. The appropriateness of the selected CFD method for the design and the geometrical optimization of membrane modules of pilot size is demonstrated.

3.2 Outline of the chapter

The present chapter is organised as follows:

- first of all the objective of this research are highlighted (paragraph 3.3);
- then in section 3.4 a brief literature review on the CFD modelling of membrane separation process with particular attention to gas membrane separation modelling by CFD is highlighted;
- in section 3.7 the experimental set-up for Particle Imaging Velocimetry (PIV) experiments is described;
- then the modelling approach devised in this work for the transport through the gas phase (paragraph 3.5.1), a ceramic (paragraph 3.5.2) and a metallic membrane (paragraph 3.5.3) are presented;
- in paragraph 3.6 and 3.8 the different simulated geometry and their operating conditions are presented;
- while in paragraph 3.9 the parameters of each membrane are calculated and in paragraph 3.10 the computational details are described;
- at this point the results for all the different membrane modules are discussed (paragraph 3.11);
- finally the main conclusions are summarized (paragraph 3.12).

3.3 Research objectives

This work is aimed at providing a CFD simulation strategy for inorganic membrane apparatuses adopted in gas mixture separation operations without introducing any simplifying hypothesis on the velocity field and on the concentration distribution of the species flowing in the module. Simulations will be run under a number of different operating conditions, predicting the effect of working temperature variations, tackling multi-component mixtures and including also the cases of inert and inhibitor species. This last aspects of estimating the effects of gas inhibitors have never been performed thorough CFD so far.

Particular attention will be devoted also to the effects of non ideal flow on the module separation performances and the capability of the CFD simulations to accurately predict such flow features will be assessed by comparison of the simulation results with mass transfer experimental data and with original experimental data collected by particle image velocimetry (PIV) in a laboratory scale membrane unit.

Finally, the design and the geometric optimization of a pilot membrane module adopted for hydrogen purification from steam reforming gas will be considered and the possibility to determine the usefulness of purposely designed geometric variations for improving the module performance will also be discussed.

3.4 Literature review on CFD modelling of hydrogen membrane separation

The adoption of palladium-based membranes modules for the separation of hydrogen from other gaseous products, as is required in the case of hydrogen production by hydrocarbon reforming, appears to be particularly significant for industrial application (Lin and Rei, 2001). These types of membranes are characterized by a high capability to separate hydrogen from gaseous mixtures and are particularly significant for industrial applications aimed at the production of ultra-pure hydrogen.

Among the possible applications, Pd-based membranes are well-suited for being adopted in reforming reactors devoted to converting natural gas into hydrogen. Although the combination of hydrogen separation through a selective membrane and the steam reforming reaction into one unit is extremely promising, since the removal of hydrogen from the reaction mixtures allows shifting equilibriums toward the right-hand side of the reaction, the control of the membrane operating conditions and the monitoring of the behaviour of the most delicate components of the system are difficult to achieve (De Falco et al. 2008). For these reasons, in recent studies hydrogen separation in membrane modules placed outside the reaction environment has been suggested (De Falco et al., 2008; Iaquaniello et al., 2008; Barba et al., 2008; Li et al., 2008) and it will be considered in this work.

Among the critical issues of membrane modules for gas mixture separations, apart from the membrane properties, concentration polarization and non-ideal flow effects have been identified in previous works (He et al., 1999; Zhang et al., 2006; Mori et al., 2007; Koukou et al., 1996; Koukou et al., 1999; Takaba and Nakao, 2005). Actually, for these types of membranes, which ensures high hydrogen permeance and practically infinite selectivity, the influence of the convective resistance to the overall mass transfer process and, consequently, to the module separation performances can be significant.

The importance of concentration polarization in membrane separation of gas has been identified only in the late 1990s (He et al., 1999) and its effect on the hydrogen permeation through metallic membrane modules has been reported in several recent works, as e.g. Zhang et al. (2006), Mori et al. (2007) and Nair and Harold (2008). As a result, proper module design and optimization are expected from the development of modelling approaches in which the real fluid dynamic conditions can be coupled with the membrane mass transport properties (Takaba and Nakao, 2005). To this purpose, Computational Fluid Dynamics techniques appear to be very promising because they allow to tackle the membrane module separation process by distributed-parameter simulations, thus replacing the usually adopted spatially averaged or lumped parameter models. As a result, the application of CFD techniques might lead to a detailed understanding of the membrane separation operations in any operating condition, geometrical configuration and scale of the module. Nevertheless, to date, development of proper modelling strategies and strict tests on their predictive capabilities are still required in order to reliable adopt CFD codes as a design tool in this field.

One of the first application of CFD methods to membranes was devoted to the fluid dynamic analysis and geometrical optimisation of turbulence promoters (Cao et al., 2001). Afterwards, De Pinho et al. (2002) and Wiley and Fletcher (2003) performed initial attempts to couple simplified flow equations with mass transport mechanism models, focusing their attention on the concentration polarization phenomenon. Recently, a similar approach was adopted to desalination membranes by Ahmad et al. (2005). Liu et al. (2004, 2005) have modelled the mass transport across a pervaporation membrane as a pseudo-first-order chemical reaction, putting attention to the concentration polarization (Liu et al., 2004) and to the baffle effects on the membrane separation efficiency (Liu et al., 2005).

To date, CFD methods have been applied to the simulation of gas mixture membrane separation processes only in a few cases (Koukou et al., 1996; Koukou et al., 1999; Takaba and Nakao, 2005; Abdel-jawad et al., 2007; Chasanis et al., 2008; Kawachale et al., 2008; Kawachale et al., 2009), while a wider range of applications can be found in the field of liquid separation (Ghidossi et al., 2006). The importance of abandon the ideal flow assumption in the modelling of gas mixture separation by ceramic membranes has been demonstrated by Koukou et al. (1996, 1999), who presented a mathematical model based on the finite volume method which was aimed at predicting the performance of the reactors removing the usually strongly simplified plug flow hypothesis, and by Takaba and Nakao (2005), who have shown that the concentration polarization is more important when membrane permeability and selectivity are increased and that the Reynolds number decrease, due to a reduction of the feed flow rate, worsens the mass fraction of the desired product in the permeate gas. Abdel-jawad et al. (2007) have investigated the effect of the velocity field and of the gas species diffusion on the spatial distribution of

partial pressure across a inorganic molecular sieve silica membrane. Chasanis et al. (2008) have assessed the effect of scale on the performances of a water gas shift membrane microreactor and Kawachale et al. (2008) have focused on the species distribution close to a polymeric membrane for VOC separations. Very recently Kawachale et al. (2009) have pointed out the importance of paying attention to unfavourable hydrodynamics conditions in the realm of gas separation by CFD simulations, improving the design of laboratory membrane test cells.

The CFD models developed so far have been validated by comparison with gas permeation experimental data in a few cases (Koukou et al., 1996 and 1999; Zhang et al., 2006; Abdel-jawad et al., 2007), while a strict evaluation of predicted local fluid dynamic features of membrane modules for gas separation is still lacking in the literature, probably due to the lack of relevant experimental data, which to date have been presented in a few preliminary studies only (Chen et al., 1998; Yoon et al., 2006).

Overall, the simulations strategies developed up to now have shown that, although they still require deep and broad validation tests, CFD methods are potentially very useful for overcoming the usually adopted simplified hypotheses on the apparatuses fluid dynamic behaviour and they can provide detailed local information on the velocity and concentration distributions of the processed fluid mixtures, thus drawing attention on important aspects affecting the separation performances and tracking the way for the adoption of CFD methods to the study, the design and the optimization of membrane modules of industrial interest.

3.5 The model equations

For a proper modelling of the membrane module behaviour, the fluid dynamic study was addressed considering the influence of the permeation process on the gas velocity field and on species concentration distribution. Actually the distribution of hydrogen partial pressure in the module is responsible of the driving force through the membrane and as a consequence of the permeate flow rate. However it does not have a constant value in the different part of the module and its trend is represented in Figure 3.1. Actually hydrogen permeation involves different phenomena. From the retentate side to the permeate side, it is possible to recognise the following steps:

- Diffusive and convective transport from the bulk of the phase to the surface of the membrane;

- Dissociative adsorption of hydrogen molecules on the surface of the metallic layer;

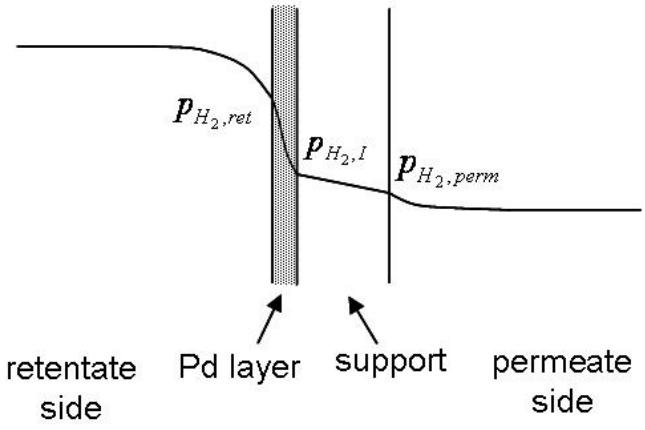

Figure 3.1: Effective total permeance for case I, II, III

- Penetration of the atomic hydrogen from the surface of the metallic layer to its bulk;

- Diffusive transport inside the metallic layer;

- Transition of the atomic hydrogen from the bulk of the metallic layer to its surface;

- Desorption of molecular hydrogen;

- Mass transport through the porous support;

- Diffusive and convective transport from the support surface to the bulk phase of the permeate side.

Obviously, depending on the membrane under consideration, some of these steps my not be present. In any case, in order to couple the transport phenomena in the bulk of the phase and the permeation through the membrane a CFD approach was used. One of the main advantages of the present modelling strategy is the possibility to adopt local, rather than mean, values of the driving forces, which feature should ensure a better accuracy and a deeper knowledge of the module behaviour, permitting to evaluate the weight of gas resistance in the separation process efficiency.

3.5.1 Mass transport in the gas phase

The numerical simulations were based on a method developed in the realm of a finite volume CFD code. With this method, the velocity and the pressure fields of the gas mixture are obtained from the numerical solution of the mass and momentum conservation equations, while the species concentration distribution and the relevant permeate and retentate fluxes are obtained from a scalar convection-diffusion equation including a source term to tackle the mass flow of the species across the membrane. Actually, a detailed description of the membrane structure and the consequent attempt to predict its permeability characteristics is not feasible, while investigating the full module fluid dynamic and transport behaviour; therefore, in this approach the transport mechanisms which take place in the membrane and the relevant permeability coefficients have to be known in advance. Clearly, a common model for describing the membranes mass transfer behaviour cannot be devised and an optimization procedure for calculating the model parameters is generally necessary in order to describe the permeation through each specific membrane (Caravella et al., 2008). Actually, the permeance of the membrane is the only unpredictable variable of the model.

Depending on the flow regime, the instantaneous conservation equations or their Reynolds averaged counterparts were considered for laminar and turbulent conditions, respectively. For all the selected cases, the Mach number was well below 0.1; therefore, the compressibility effects were negligible and the incompressible form of the equations was adopted.

Specifically, for laminar fluid flow, the steady-state mass (eqn. 2.3), momentum (eqn. 2.5), and species conservation equations for incompressible Newtonian fluids were determined over the three-dimensional domain reproducing fairly faithfully the experimental module geometrical details. In particular, the following set of equations was considered:

$$\nabla \cdot (\rho \boldsymbol{u}) = \sum_i S_i \tag{3.1}$$

$$\nabla \cdot (\rho \boldsymbol{u}\boldsymbol{u}) = -\nabla p + \mu \nabla^2 \boldsymbol{u} \tag{3.2}$$

$$\nabla \cdot (\rho \boldsymbol{u} Y_i + J_i) = S_i \tag{3.3}$$

where ρ is the fluid density, $\boldsymbol{u}$ is the velocity vector, p is the static pressure, μ is the dynamic viscosity, Y_i is the mass fraction of the species i, J is its diffusive flux and S_i is a source/sink term to account for the mass flow of the species across the membrane.

For the turbulent regime, the Reynolds averaged Navier-Stokes equations (RANS) have been solved (eqns. 2.8 and 2.9). The RANS equations are obtained from the instantaneous conservation equations splitting the variables ($\boldsymbol{u}$, Y_i) into their mean ($\bar{\boldsymbol{u}}$, $\bar{Y_i}$) and fluctuating parts ($\boldsymbol{u'}$, Y_i'):

$$\nabla \cdot (\rho \bar{\boldsymbol{u}}) = \sum_i S_i \tag{3.4}$$

$$\nabla \cdot (\rho \bar{\boldsymbol{u}} \bar{\boldsymbol{u}}) = -\nabla p + \mu \nabla^2 \bar{\boldsymbol{u}} - \nabla \cdot \left(\rho \overline{\boldsymbol{u'u'}}\right) \tag{3.5}$$

$$\nabla \cdot \left(\rho \bar{\boldsymbol{u}} Y_i + J_i + \rho \overline{\boldsymbol{u'Y'}}\right) = S_i \tag{3.6}$$

The resulting set of equations is not mathematically closed, because not only $\bar{\boldsymbol{u}}$ and $\bar{Y_i}$ but also $\boldsymbol{u'}$ and $\boldsymbol{Y'}$ are unknowns. In order to close the problem, the Reynolds stresses, $\rho\overline{\boldsymbol{u'u'}}$, and the Reynolds flux, $\rho\overline{\boldsymbol{u'Y'}}$, have both been modelled using the eddy viscosity hypothesis. In particular, the standard $\kappa - \epsilon$ model (Launder and Spalding, 1974) was selected for the former, while the latter was considered equal to the mean scalar gradient times turbulent diffusivity, given by the ratio between the turbulent viscosity and the turbulent Schmidt number.

As pertains the diffusive flux, J_i, since the molecular transport in the bulk might significantly affect the overall model results, the dilute approximation was abandoned and the interaction among the gas species was considered (Bird et al., 1960). The diffusive mass flux of the i species, J_i, was modelled as:

$$J_i = -\sum_{j=1, j\neq i}^{N} \rho \boldsymbol{D}_{i,j} \nabla Y_i \tag{3.7}$$

where N is the number of gas species in the mixture and $\boldsymbol{D}_{i,j}$ is the mass diffusion coefficient of the $i-j$ components in a multicomponent mixture and the other symbols have the usual meaning. Since $\boldsymbol{D}_{i,j}$ depends on the species concentration, the Maxwell-Stefan formulation has been adopted (Taylor and Krishna, 1993). Finally, the diffusion coefficient square matrix, $\boldsymbol{D}_{i,j}$, has been calculated as

$$\boldsymbol{D}_{i,j} = [G]^{-1}[H] \tag{3.8}$$

The $(N-1) \times (N-1)$ matrices, $[G]$ and $[H]$, are defined as

$$G_{i,i} = -\left(\frac{\phi_i}{D_{i,N}}\frac{M}{M_N} + \sum_{j=1, j\neq i}^{N} \frac{\phi_j}{D_{i,j}}\frac{M}{M_i}\right) \tag{3.9}$$

$$G_{i,j} = \phi_i \left(\frac{1}{D_{i,j}} \frac{M}{M_j} - \frac{1}{D_{i,N}} \frac{M}{M_N} \right) \tag{3.10}$$

$$H_{i,i} = - \left(\phi_i \frac{M}{M_N} + (1 - \phi_i) \frac{M}{M_i} \right) \tag{3.11}$$

$$H_{i,j} = \phi_i \left(\frac{M}{M_j} - \frac{M}{M_N} \right) \tag{3.12}$$

where M is the mixture molecular weight and $D_{i,j}$ is the binary mass diffusion coefficient.

In all cases, the source/sink terms, S_i, permit taking into account the mass flow of the species across the membrane, which is described as a zero-thickness wall. The transport through it is modelled by means of the source term, S_i, introduced in eqns. (3.3) and (3.6), which is nil in all the module except in the region near the membrane. As a result, source and sink terms are introduced at the two sides of the membrane by means of S_i, permitting the species i to disappear from one of the membrane sides and to come out on the other side. As a consequence, a source term equal to the sum of the source terms of all the permeable species is added at the right side of the continuity eqns. (3.1) and (3.4) only to those cells.

Clearly, the method requires the preliminary knowledge of the permeability characteristics of the membrane, which determine the formulation of the source term. In the case of Pd-Ag membranes, which are permeable to hydrogen only, the source term takes in account only the hydrogen permeation. Depending on each specific membrane, any mechanism can be included in the model by means of eqns. (3.1, 3.2, 3.3) or eqns. (3.4, 3.5, 3.6).

Simulation results are the permeate and retentate flow rate and compositions, which can be easily compared with the experimental data, as well as the three-dimensional distributions of all gas species velocity and concentration, which permit to fully understand the fluid dynamic behaviour of the module.

3.5.2 Mass transport through a ceramic membrane

In order to model the mass transfer across a ceramic membrane, the following form of the source term has been considered:

$$S_i = \frac{A_c}{V_c} Q_{i,tot} \left(p_{ret} \phi_{i,ret} - p_{perm} \phi_{i,perm} \right) \tag{3.13}$$

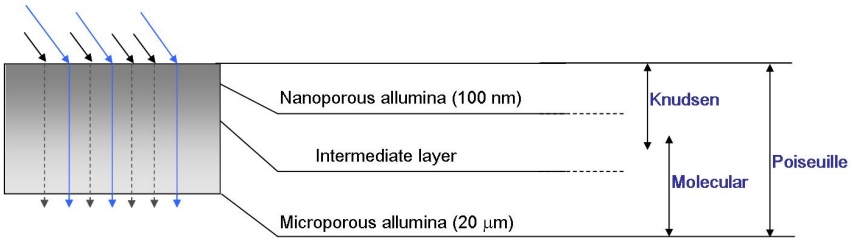

Figure 3.2: Characteristics of the ceramic membrane and transport mechanisms through it

where A_c is the cell mass transfer area and V_c is its volume, ϕ_i is the i species molar fraction and p_{ret} and p_{perm} are the total pressure at the retentate and permeate side, respectively. The overall transport properties of the membrane have been taken into account by a total permeance coefficient, $Q_{i,tot}$, defined as the ratio between the flux and the pressure gradient for each species.

Depending on the type of membrane, different transport mechanisms can be present and in the present case (see Figure 3.2) the expected transport mechanisms for the gas molecules across the porous medium are the molecular diffusion (self or mutual diffusion), the Knudsen diffusion and the viscous (Poiseuille) flow. In this work, a modified Bosanquet equation (Karger and Ruthven, 1992; Pollard and Present, 1948) including the Poiseuille flow has been formulated. It is worth observing that since the Poiseuille flow transport mechanism takes place only in the membrane holes, it has to be summed to the flow through the membrane pores (Karger and Ruthven, 1992). Therefore, in our model, which is schematically shown in Figure 3.3, the total diffusion coefficient is due to the Knudsen and molecular diffusion mechanisms acting in series, and to the Poiseuille flow, which is in parallel with the other two all together. Under these conditions, the total permeance of the i species through the porous ceramic membrane is given by:

$$Q_{i,tot} = \frac{1}{\frac{1}{Q_{i,M}} + \frac{1}{Q_{i,K}}} + Q_{i,P} \tag{3.14}$$

where the subscripts M, K and P refer to molecular diffusion, Knudsen diffusion and Poiseuille flow, respectively. In the following, depending on the number of components of the gas stream, the term $Q_{i,M}$ will be replaced with $Q_{i,s}$ or with $Q_{i,m}$ referring to the self-diffusivity (for the case of one component) and to the mutual diffusivity (for two or more components), respectively. The permeance of the species i relevant to the j transport mechanism depends on the corresponding

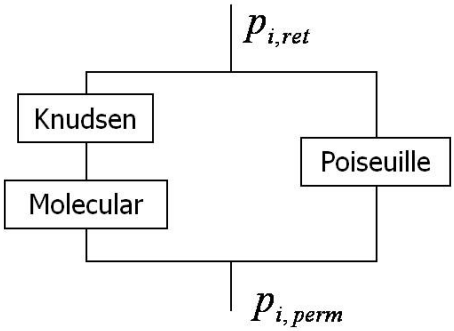

Figure 3.3: Schematisation of the mass transport mechanisms through a porous membrane

species diffusion coefficient, $D_{i,j}$, as:

$$Q_{i,j} = \frac{M_i}{1000}\frac{D_{i,j}}{RTl} \tag{3.15}$$

where R is the ideal gas constant, T the operating temperature, M_i the molecular mass of the species i and l a characteristic length for mass transfer.

As pertain the diffusion coefficients, literature correlations, for each of the above mentioned transfer mechanism, are available (Karger and Ruthven, 1992). In particular, the effective mutual diffusion coefficient, $D_{i,m}$, is given by:

$$D_{i,m} = \frac{\epsilon}{\tau}\frac{3}{8\sqrt{2}\sigma_{i,j}^2}\left(\frac{kT}{p}\right)\left(\frac{kT}{\pi M^*}\right)^{1/2} \tag{3.16}$$

where ϵ and τ are the membrane porosity and tortuosity, respectively, p is the total pressure, k is the Boltzmann's constant, $\sigma_{i,j}$ is the arithmetic mean of the i and j gas species molecular diameters and M^* depends on the molecular mass of the two species. For fixed membrane type, the values of the membrane geometrical properties in eqn. (3.16) can be grouped in a single constant value, A, and the resulting expression of the permeance for mutual diffusion is:

$$Q_{i,m} = A\frac{M_i\sqrt{T}}{\sqrt{2}\sigma_{in}^2 p\sqrt{M^*}} \tag{3.17}$$

Similarly, for the effective self-diffusivity, $D_{i,s}$, Knudsen diffusivity, $D_{i,K}$, and Poiseuille diffusivity, $D_{i,P}$, the following simplified expressions derived from the selected literature correlations are adopted:

$$Q_{i,s} = \frac{M_i}{1000RTl}\frac{\epsilon}{\tau}\frac{3}{8\sigma_i^2}\left(\frac{kT}{p}\right)\left(\frac{kT}{\pi M_i}\right)^{1/2} = A\frac{\sqrt{M_i T}}{\sigma_i^2 p} \tag{3.18}$$

$$Q_{i,K} = \frac{M_i}{1000RTl}\frac{\epsilon}{\tau}970000r\sqrt{\frac{T}{M_i}} = B\sqrt{\frac{M_i}{T}} \tag{3.19}$$

$$Q_{i,P} = \frac{M_i}{1000RTl}\frac{\epsilon}{\tau}\frac{r^2 p}{8\mu_i} = C\frac{M_i}{T}\frac{p}{\mu_i} \tag{3.20}$$

where, similarly to A, B and C are constant values specific for each membrane type. In this work, a single value of the permeability coefficients for each mechanism and gas species was adopted.

3.5.3 Mass transport through a metallic membrane

The hydrogen mass flux in a palladium-silver membrane is strictly related to its dissociation/diffusion mechanism in the metallic layer (Sieverts, 1929; Holleck, 1970; Ward and Dao, 1999), and is usually described through the Sieverts' law which states that for dense and defect free Pd membranes the flux is proportional to the difference of the square root of hydrogen partial pressure at the two sides of the membrane. On the other hand, the mass transfer mechanism through the inorganic support of the metallic layer, clearly depends on the specific characteristics of the selected material. Theoretically, the resistance offered by the ceramic support to the flux cannot be considered negligible (Goto et al., 2000; Caravella et al., 2008) and it was assumed as a part of the membrane, although its effect is generally much less important with respect to that of the Pd-Ag layer. The inclusion of the support resistance in the model equations is aimed to make the approach as general as possible and to broaden its applicability. Nevertheless, if the support does not give any significant mass transfer resistance, it is worth and straightforward simplifying the model.

Under the assumption that the membrane metallic layer is defect free (Catalano et al., 2009), the only permeable species is H_2, and the source term is nil for all other species. The mass flux through the Pd-Ag layer has to be equal to the mass flux through the membrane support and as a result, S_{H_2} reads as:

$$S_{H_2} = \frac{A_c}{V_c}Q_{H_2,Pd}\left[\left(p_{ret}\phi_{H_2,ret}\right)^{0.5} - \left(p_I\phi_{H_2,I}\right)^{0.5}\right] \tag{3.21}$$

$$S_{H_2} = \frac{A_c}{V_c}Q_{H_2,sup}\left[p_I\phi_{H_2,I} - p_{perm}\phi_{H_2,perm}\right] \tag{3.22}$$

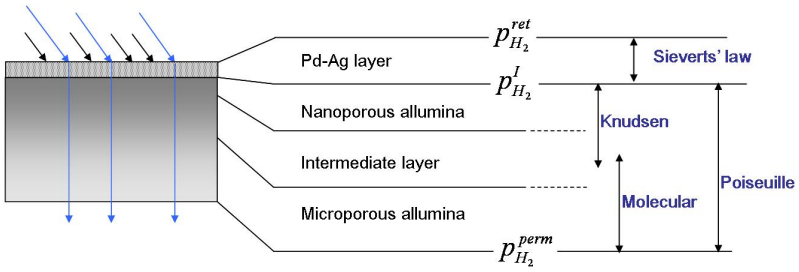

Figure 3.4: Characteristics of the metallic membrane and transport mechanisms through it

where the subscript I identify the interface between the support and the metallic layer (see Figure 3.4), while Q_{sup} is the total permeance of the support and Q_{Pd} is the permeance of the Pd-Ag layer.

The unknown value of the hydrogen partial pressure at the interface between the metallic layer and the support, $p_{H_2,I}$, is obtained by locally solving the set of equations resulting from the equality of the H_2 mass flux through the support (term on the right end side of Eq. (3.22)) and through the metallic layer (term on the right end side of Eq. (3.21)). It is worth observing that the driving force in the source term is evaluated adopting local values, thus removing the assumption adopted in lumped parameters models. In order to describe the permeance of the porous support two different transport mechanisms, molecular diffusion and Knudsen diffusion, were taken in account, while the viscous (Poiseuille) flow has been neglected due to the small diameter of the support pores. Then on the basis of the Bosanquet equation (Karger and Ruthven, 1992; Pollard and Present, 1948), the total permeance of the support, Q_{sup}, was written as:

$$Q_{sup} = \frac{1}{\frac{1}{Q_{H_2,M}} + \frac{1}{Q_{H_2,K}}} \tag{3.23}$$

where the effective molecular self-diffusion permeance, Q_M, and the effective Knudsen permeance, Q_K, are evaluated as indicated for the ceramic membrane.

In order to calculate the permeance of the Pd-Ag layer, Q_{Pd}, and to model its dependency from temperature, an Arrhenius relationship was assumed (Holleck, 1970). As a result, Q_{Pd} was written as:

$$Q_{Pd} = Fe^{-E/RT} \tag{3.24}$$

where R is the universal gas constant, F is the pre-exponential factor and E is the Sieverts activation energy for H_2 permeation through the membrane metallic layer.

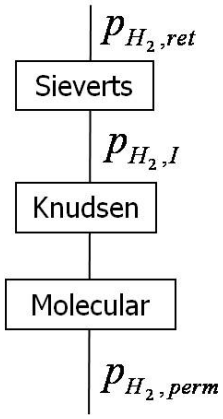

Figure 3.5: Schematisation of the mass transport mechanisms through a Pd-Ag membrane

The transport mechanisms in the Pd-Ag layer and in the inorganic support have been considered in series, as schematised in Figure 3.5.

Overall, four constants have been introduced for the source term formulation. Therefore, in order to run the simulations, their values have to be known in advance and they have been obtained on the basis of experimental data of pure H_2 tests carried out at different temperatures by a minimized error procedure, then the same set of constants was always used for all the simulations at different operating conditions.

The approach applies not only if the feed stream is composed by hydrogen and inert gas species (e.g. N_2, CH_4, He, etc.), but it is suitable also in the case of gas mixtures containing inhibitors of known behaviour (e.g. CO) provided that a suitable modification for eqn. (3.24) is available. Carbon monoxide is an inhibitor for the Pd metallic layer because it affects the hydrogen dissociation path. Barbieri et al. (2008) have shown that the effect of CO can be predicted introducing the inverse of a Langmuirs isotherm for correcting the Sieverts permeance. Following this suggestion, the local effective Q_{Pd} term has to be evaluated as:

$$Q_{Pd} = F\left(1 - \alpha\left(T\right)\frac{K_{CO}p_{ret}\phi_{CO,ret}}{1 + K_{CO}p_{ret}\phi_{CO,ret}}\right)e^{-E/RT} \tag{3.25}$$

where $\alpha(T)$ and K_{CO} have to be experimentally evaluated. In the present work, the values suggested by Barbieri et al. (2008) have been used.

Table 3.1: Different membrane modules

Modules	scale	Type of membrane	Internals
LC	laboratory	ceramic	-
LM1	laboratory	metallic - a	-
LM2	laboratory	metallic - b	-
LM2*	laboratory	metallic - b	2 perforated plates
PM0	pilot	metallic - c	-
PM2	pilot	metallic - c	2 baffles
PM3	pilot	metallic - c	3 baffles

3.6 Geometrical details

Different module geometries and membranes were investigated in the present work and are summarised in Table 3.1. The geometrical configuration of the first simulated lab-scale apparatus corresponds to the lab-scale membrane module experimentally investigated by Pizzi et al. (2008) and by Catalano et al. (2009). It consists of a cylindrical shell with a length of 185 mm and a diameter of 54 mm, equipped with inlet and outlet pipes having a diameter of 4 mm, and of an internal tube, containing the tubular membrane.

The tube-in-shell apparatus was equipped with different membranes, and in particular with a ceramic membrane and with two different Pd-Ag membranes, named LC, LM1 and LM2 respectively in the following.

The ceramic membrane is 90 mm long and has an external diameter of 10 mm. It consists of a support of asymmetric $\alpha - Al_2O_3$ and of a ceramic coating with high selectivity to hydrogen. The two metallic membranes have a support of $\alpha - Al_2O_3$ and deposited on it a Pd-Ag layer (80%w Pd - 20%w Ag). The membrane of the first metallic module (namely LM1) was 100 mm long and had an active diameter of 7 mm. The support had a top layer of 70 nm and a Pd-Ag layer of 12 μm deposited by electroless deposition on the inner surface of the membrane. LM2 module is equipped with a blind membrane, 90 mm long and with a diameter of 11 mm. The support consists of a top layer of 100 nm while the metallic layer deposited on the outer surface by a two-step electroless deposition was 2.5 μm.

On a module of the same geometry of LM2, PIV measurements were conducted. The effect of flow distribution on the membrane performance was also investigated by the simulations of an additional laboratory scale module, LM2*, which is similar to LM2 apart from the gas inlet and outlet regions, which were equipped with two perforated plates aimed at improving the fluid dynamic behaviour of the module. The plates have diameters equal to the shell internal diameter and eight circular holes of 4 mm distributed at a distance of 20 mm from the module axis. The

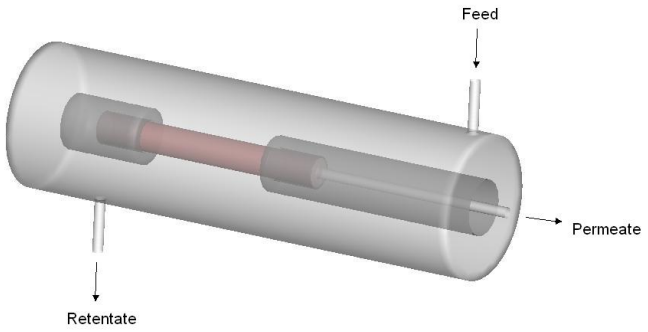

Figure 3.6: Geometric configuration of the LM2 module

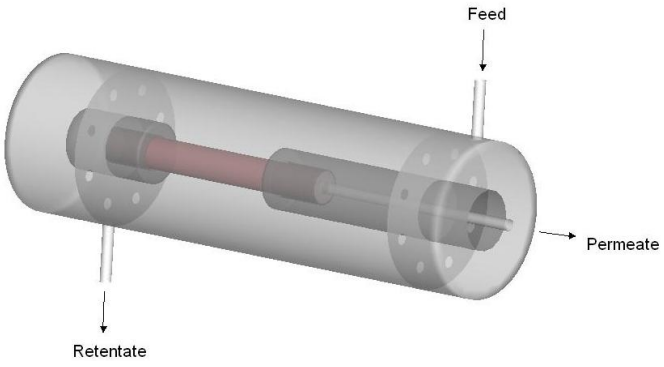

Figure 3.7: Geometric configuration of the LM2* module

geometric features of LM2 and LM2* computational domains are depicted, respectively, in Figure 3.6 and 3.7.

For the pilot membrane module, which is depicted in Figure 3.8 and will be referred to as PM0 in the following, a simple shell and tube geometry was selected, as suggested by Barba et al. (2008). It consists of three tubular membranes (length $L = 446\ mm$ and diameter $D = 30\ mm$), placed inside a cylindrical elliptical-bottomed shell of length and diameter equal to 883 mm and 162 mm, respectively. In particular, Pd-Ag membranes with a metallic layer 3 μm thick deposited on the tube outer surface were selected.

Modified geometries of PM0 were also considered. In particular, in order to investigate the effect of fluid flow on the module separation performances, two or three purposely designed baffles were inserted in the module geometry (Figure 3.9). In the following, the pilot modules equipped with two and three baffles will be referred to as PM2 and PM3, respectively. The baffles consist of circular plates of diameter equal to the shell internal diameter and three circular holes of 48 mm for not interfering with the membrane housing.

3.7 PIV experimental set-up

The experimental investigation of the fluid dynamic behaviour was carried out in the cylindrical laboratory scale membrane module indicated as LM2 (length $L = 184\ mm$ and diameter $D = 55\ mm$), and depicted in Figure 3.10, similar to that investigated by Pizzi et al. (2008) and Catalano et al. (2009) for measuring the permeation of Pd-based hydrogen selective membranes. It consists of a cylindrical shell made of Perspex for allowing optical access, equipped with inlet and outlet pipes (diameter $D_{pipes} = 4\ mm$) and of an internal tube, supporting a tubular membrane. All the module internals including the membrane were painted matte black to minimize laser light reflection, while the refractive effects at the curved external surface could not be entirely eliminated. The experiments were aimed at determining the gas phase velocity field only, since the permeation behaviour of the module was already obtained in the above-mentioned previous works (Pizzi et al., 2008; Catalano et al., 2009).

Air was used as the gas phase; the flow rate was measured by a rotameter and fixed at 100 lh^{-1}, corresponding to an inlet velocity of 2.2 $m\ s^{-1}$ and resulting in a shell Reynolds number, Re, equal to 45.0.

The measurements were performed using the PIV technique, whose main elements are shown in Figure 3.11. The laser sheet source adopted was a pulsed New Wave Nd:YAG laser, emitting light at 532 nm with a maximum frequency of 15

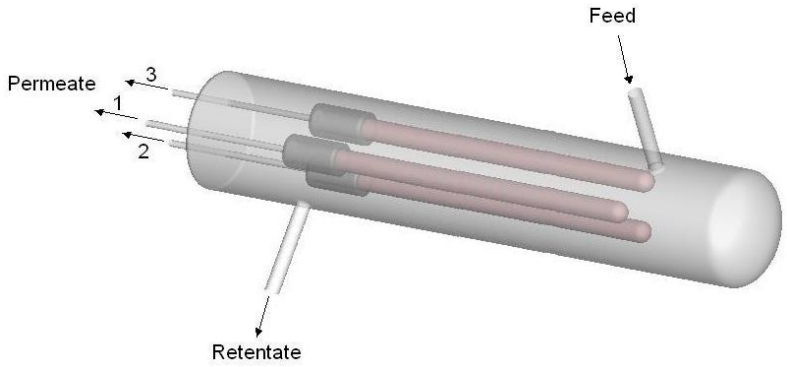

Figure 3.8: Geometric configuration of the PM0 module

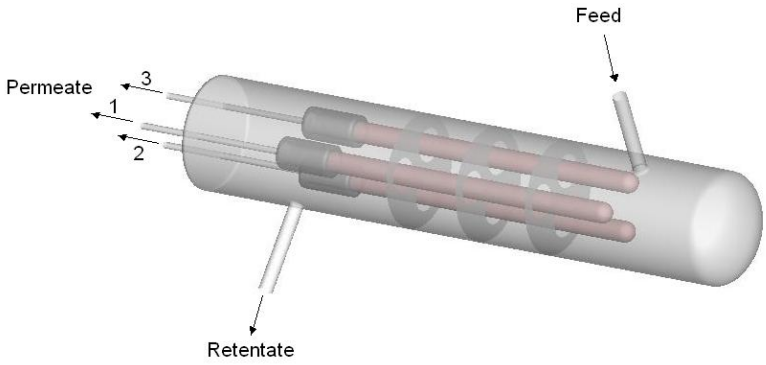

Figure 3.9: Geometric configuration of the PM3 module

Table 3.2: Details of the simulated cases

Module	Case	Shell IN ($\%mol\ H_2$)	$N_{shell,IN}$ $[Nl\ min^{-1}]$	Tube IN ($\%mol\ H_2$)	$N_{tube,IN}$ $[Nl\ min^{-1}]$	p_{tube} $[bar]$	p_{shell} $[bar]$	T $[K]$
LC	I	H_2 or N_2	1.05	-	-	1.05	2.0-5.0	773.15
	II	H_2	1.05	N_2	1.03	1.6-5	1.6-5.0	773.15
	III	H_2 - N_2 (50%)	1	-	-	1.2	2.0-4.0	773.15
LM1	IV	N_2	1.03	H_2	1.04	2-10	2.0-10.0	678.15
	V	N_2	1.03-15	H_2 - N_2 (30-90%)	1.04-10	2-10	2.0-10.0	678.15
LM2	VI	H_2	1-3	-	-	1.05	1.2-2.3	673.15
	VII	H_2 - N_2(50-88%)	1-20	-	-	1.05	1.5-6.0	673.15
	VIII	H_2 - CH_4(50%)	1-2	-	-	1.05	3.0-6.0	673.15
	IX	H_2 - N_2 - CH_4(50%)	1-2	-	-	1.05	3.0-6.0	673.15
	X	H_2	1-2	-	-	1.05	1.2-1.4	723.15
	XI	H_2 - N_2(50-88%)	1-20	-	-	1.05	1.5-6.0	723.15
	XII	H_2	1-3	-	-	1.05	1.1-1.9	773.15
	XIII	H_2 - N_2(50%)	1-20	-	-	1.05	3.0-6.0	773.15
	XIV	H_2 - CO(80-88%)	3	-	-	1.05	3.0-7.0	647.00
	XV	H_2 - N_2(80-88%)	3	-	-	1.05	3.0-7.0	647.00
	XVI	H_2 - N_2 - CO(80-88%)	3	-	-	1.05	3.0-7.0	647.00
LM2*	XVII	H_2 - N_2(50 - 88%)	1-20	-	-	1.05	2.3 - 6	673.15

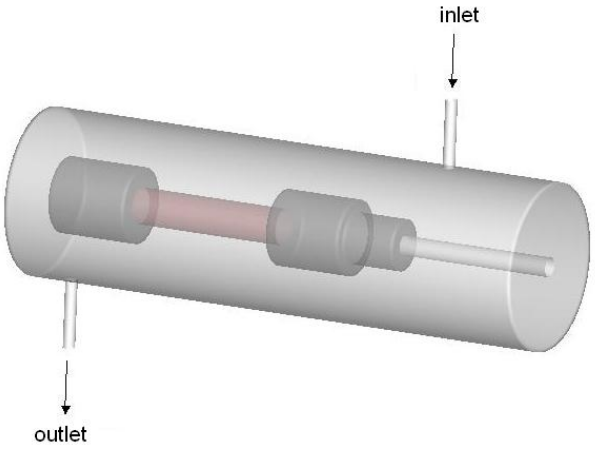

Figure 3.10: Geometry of the PIV module

Hz. The image capturing was performed by a PCO camera (1280×1024 pixels CCD) cooled by a Peltier module to improve the signal-to-noise ratio. The laser control, the laser/camera synchronization, and the data acquisition and processing were handled by a Dantec Dynamics system (a FlowMap System Hub unit and FlowManager software).

The gas was seeded with water droplets of a few micrometers in diameter obtained by a nebulizer. The droplets concentration adequacy was preliminary checked, and a satisfactory number of droplets, that is about 5-10, for each interrogation area was found in almost all locations of the illuminated plane. The measurements were performed in different portions of the plane crossing the shell inlet and outlet tube centres. Up to 1000 images were found to be required for obtaining a sample-independent time averaged flow field. The time between two laser pulses, Δt, was equal to 800 μs, and that going from a pulse couple to another was equal to 1 s. It is worth observing that, due to the big velocity variations inside the module, the selected Δt value could not ensure a uniform accuracy of the velocity data. The cross-correlation of the image pairs was performed on a rectangular grid with 50% overlap between adjacent cells; the interrogation area was set at 32×32 pixels, corresponding to about 0.88×0.88 mm. In order to reduce the measuring error sources, the average pixel intensity was subtracted from each single image pair for reducing noise and the velocity vectors of magnitude bigger than the gas inlet velocity were discarded.

In the following, the origin of the coordinate system is located at the beginning of the membrane at the side closer to the outlet, and z and x are the axial and radial coordinates, respectively, as shown in Figure 3.11. The mean axial velocity, V_z, is positive if directed upward from the inlet toward the outlet sections, and

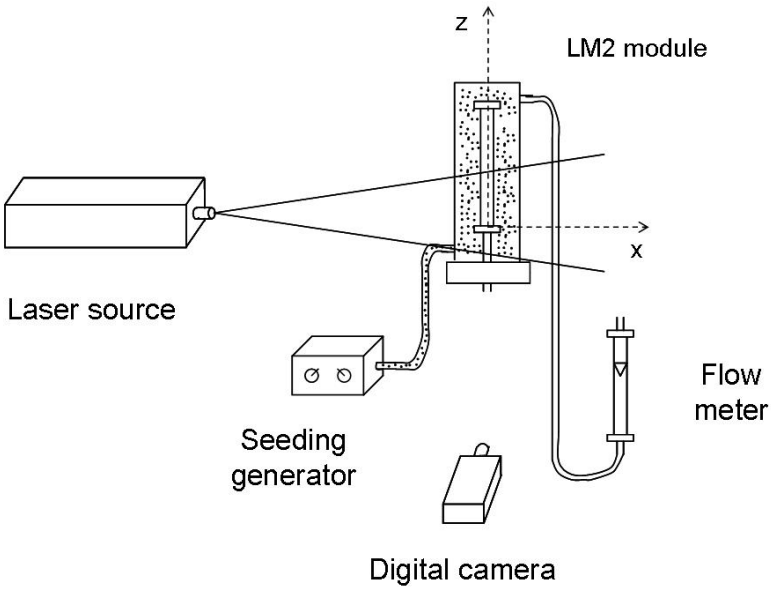

Figure 3.11: PIV set-up

the mean radial velocity, V_x, is positive if directed from the inlet toward the shell opposite wall.

3.8 Operating conditions

The operating conditions adopted in the simulations of permeation experiments of the lab-scales modules are summarised in Table 3.2. Permeation experimental data in the same conditions were collected from the Membrane Separation group. Permeation data for characterising the H_2 purification performances of the membranes under variable operating conditions, have provided the gas flow rates and the composition information required to strictly evaluate the CFD model accuracy. The ceramic membrane performances were firstly investigated by feeding pure gases to the module shell side and measuring the gas flow rate at the shell and tube exit sections (case I). In particular, the permeation of pure N_2 and H_2 was evaluated at fixed temperature and fixed downstream total pressure, while varying the pressure in the shell side. In case II, the experimental data were collected by feeding pure H_2 to the shell side and pure N_2 to the tube inlet and by maintaining an equal total pressure at both module sides. Further tests were subsequently performed by feeding a mixture of H_2 and N_2 (50% mol) at the shell side only (case III). As highlighted in Figure 3.12, different mass transfer mechanisms across the membrane are

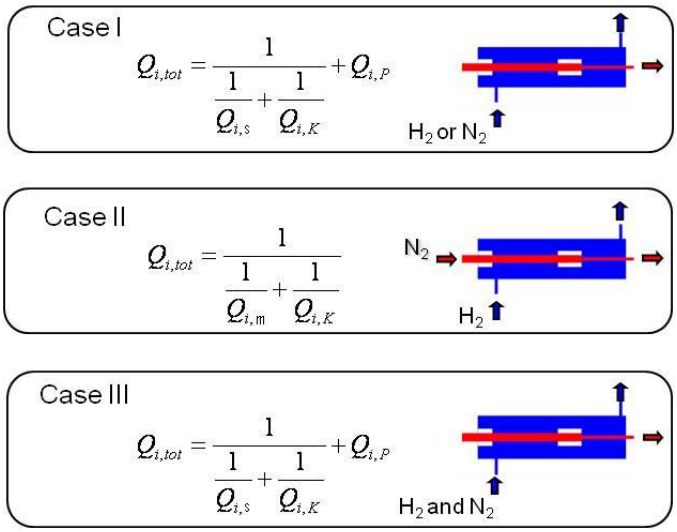

Figure 3.12: Effective total permeance for case I, II, III

involved in each of the three cases and consequently different form of eqn. (3.14) can be considered. In particular, for a pure gas feed stream (case I) self-diffusion, Knudsen and Poiseuille flow take place, in case III due to the presence of different gases the self-diffusion is substituted by the mutual diffusion. Finally, if the pressure gradient is nil, as in case II, the contribution of the Poiseuille flow can be neglected.

For the LM1 module, the gas stream was fed to the tube side co-currently with the N_2 sweep stream and the total pressure was maintained equal at the two module sides. Pure H_2 and a mixture of H_2 and N_2, at different molar fractions, were fed to the tube side in case IV and V, respectively. As concerns the mass transfer in the Pd-Ag support, Knudsen and Sieverts mechanisms are present in the two cases and the molecular diffusivity is always the mutual diffusivity.

The LM2 module was tested in counter-current flow with the feed stream flowing in the shell side and without any sweep flow. In particular, in cases VI, X and XII, a pure H_2 gas stream was fed on the module outer side at fixed downstream total pressure, while varying the pressure in the shell side, at a temperature equal to 673.15 K, 723.15 K and 773.15 K, respectively. In cases VII, XI and XIII (at temperature of 673.15 K, 723.15 K and 773.15 K, respectively), a mixture of H_2 and N_2, at different concentrations, was considered and the effect of the shell pressure and of the feed flow rate was tested. As for the mass transfer mechanisms, since inside the support only hydrogen is present, the contribution to molecular diffusion is always given by the self-diffusion. In cases VIII and IX, a mixture of $H_2 - CH_4$ and of $H_2 - N_2 - CH_4$, respectively, was fed to the module at $T = 673.15$

K and at different retentate pressure and feed flow rate.

As a result, the permeation of H_2 at fixed downstream total pressure of 1.05 *bar* was investigated varying temperature, shell-side pressure, flow rate and composition of the feed gas mixture. Initially, the same conditions of the permeation experiments performed by Pizzi et al. (2008) and by Catalano et al. (2009) were purposely selected (case I - XIII), in order to perform a rigorous model validation. Afterwards, the number of simulations was expanded, thus allowing to get insight on the effect of a wide range of different operating parameters on the module separation features. Consequently a feed flow rate up to 20 $Nl\ min^{-1}$ was simulated for an inlet gas stream of $H_2 - N_2$ (cases VII, XI and XIII) and different inlet composition were considered in order to test carbon monoxide inhibition (cases XIV, XV, XVI).

The simulations on the pilot modules were performed considering a typical methane steam reforming gas stream at temperature $T = 723.15\ K$. In particular, a pressure of 21 *bar* and 1.5 *bar* were considered at shell and tube side, respectively. The module was fed from the shell inlet tube, since the Pd selective layer was assumed to be deposited on the tube external surface, while no sweeping stream was considered to flow inside the tube. A feeding flow rate of 95.04 Nm^3h^{-1} was considered with the following composition:

CH_4 : 22% *mol*
CO_2 : 4% *mol*
H_2 : 18% *mol*
H_2O : 56% *mol*

The CO contribution was neglected as the specific problem of including in the CFD model a suitable correlation for taking into account the interaction of CO with the membrane metallic layer has been tackled for LM2 module.

3.9 Calculation of the permeance coefficients

As far as the ceramic membrane is concerned, the total permeance coefficient adopted in the simulations was obtained by determining the A, B and C constant values in the simpler case I, defined above, for which two different data sets were available, one collected with pure hydrogen and the other with pure nitrogen as the feed gas streams. The three unknown constants were obtained using eqns.(3.18 3.19 3.20) combined with the equations of flux for H_2 and N_2 to best fit the experimental permeate fluxes in the cases of pure gas feed streams. The calculated constants are reported in Table 3.3: A and C are practically coincident in the two cases, while a not negligible difference was obtained for B. In this situation, only the values obtained from the H_2 feed data were used for all the simulations;

Table 3.3: Values of the model constants: A $[kg^{0.5}kmol^{0.5}K^{-0.5}s^{-1}]$, B $[kg^{-0.5}kmol^{0.5}K^{0.5}s\ m^{-1}]$, C $[kmolKPa^{-1}m^{-2}]$, Q_{Pd} $[kg\ Pa^{-0.5}m^{-2}s^{-1}]$, F $[kgPa^{-0.5}m^{-2}s^{-1}]$ and E $[kJ\ kmol^{-1}]$

		A	B	C	Q_{Pd}	F	E
LC	H_2	$1.22 \cdot 10^{-6}$	$4.99 \cdot 10^{-9}$	$2.08 \cdot 10^{-18}$	-	-	-
	N_2	$1.21 \cdot 10^{-6}$	$3.75 \cdot 10^{-9}$	$2.08 \cdot 10^{-18}$	-	-	-
LM1		0.09	82.7	-	$1.61 \cdot 10^{-6}$	-	-
LM2		14.5	$3.7 \cdot 10^{4}$	-	Q_{Pd}(F,E)	$2.7 \cdot 10^{-4}$	$17.7 \cdot 10^{3}$
PM		-	-	-	$7.21 \cdot 10^{-6}$	-	-

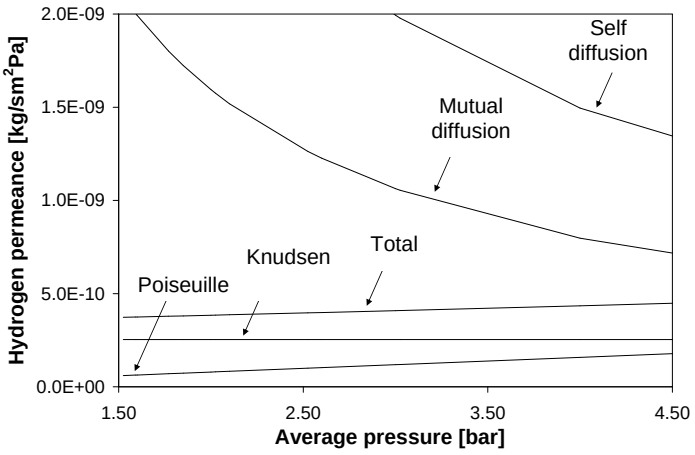

Figure 3.13: Variation of the H_2 permeance coefficients with pressure (LC module)

indeed, they were considered more accurate than those deduced from the N_2 data, as a higher number of experimental data, collected in a wider range of experimental conditions, were available for the H_2 case.

The computed permeance coefficients of H_2 show different values and also significantly different behaviours at variable pressure conditions (Figure 3.13). It is worth observing that the self and mutual permeance resistances are almost negligible at low pressure as compared with the Knudsen and the Poiseuille flow ones, while their contribution is somewhat more visible when the pressure is higher.

Moreover, the two main resistances are those related to the Knudsen diffusion and the Poiseuille flow, the former does not depend from pressure, while the latter decreases increasing the pressure value. Since the two resistances act in parallel, the value of the total permeance increases increasing the working pressure. This behaviour matches the trends observed in the experimental data confirming that in

the modelling, consideration of all the possible transport mechanisms through the ceramic membrane should be preferred to simpler approaches, such as those based on the Knudsen transport mechanism only.

The permeance coefficients for the LM1 membrane were obtained considering the experimental data relevant to case IV, while for calculating the permeance coefficients for LM2, cases VI, X and XII had to be considered, since in this case it was necessary to calculate the influence of temperature and the coefficients D and E has to be calculated separately. The unknown constants, obtained with a method similar to that adopted for the ceramic module, are shown in Table 3.3. For the LM2 module Q_{Pd} depends on temperature and values of $2.7 \cdot 10^{-4} [kgPa^{-0.5}m^{-2}s^{-1}]$ and of $17.7 \cdot 10^{3} [kJkmol^{-1}]$ were obtained respectively for F and E. It is worth mentioning that the constant E is within the literature range for membranes of similar alloy compositions (20% of Ag by weight) (Gallucci et al., 2007).

As for the the pilot modules, a metallic layer thickness of 3 μm was assumed and the value of $1.2 \cdot 10^{-8}$ $mol\ s^{-1}\ m^{-1}\ Pa^{-0.5}$ was selected, on the basis of laboratory tests on LM2 module. This value is within the range of various available experimental data (Basile et al., 2001; Guo et al., 2003; Rothenberger et al., 2004; Basile et al., 2005).

Therefore the modelling approach was based on the following procedure:

- analysis of the membrane under consideration and definition of the important transport mechanisms to be considered;
- definition of the most suitable transport resistance scheme in order to describe the overall permeability of the membrane;
- evaluation of the effective permeability of the membrane through pure components permeation experiments provided by the Membrane Separation group;
- implementation of the information in the CFD algorithm;
- simulation of the module behaviour at the same conditions of the pure permeation experiments to test the reliability of the procedure;
- simulation of the module behaviour at the same condition as the mixture experiments to test the model as a predicting tool (without introducing any variation of the model parameters).

3.10 Computational details

The general-purpose commercial CFD code Fluent 6.3 was selected for the solution of the steady-state conservation equations adopting either the laminar or the

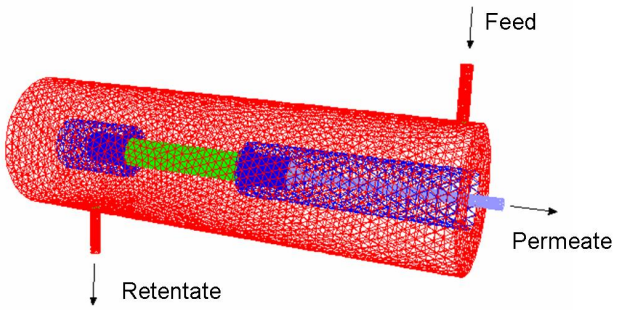

Figure 3.14: Mesh on the computational domain of the LM2 module

turbulent formulation depending on the specific flow regime. The equations were numerically solved in a Cartesian coordinate system and the mass source terms (e.g. eqn. 3.13) were implemented through a purposely written user-defined function provided by Ansys Inc, which was suitably modified. The convective terms were discretized by a second order upwind scheme, while the SIMPLEC algorithm (VanDoormal and Raithby, 1984) was used in all cases to couple the continuity and Navier-Stokes equations, due to its stability and accurateness.

The computational grids cover the full three dimensional domains and reproduce quite closely the real modules geometrical details, apart from the membrane that was always assumed to be a zero-thickness wall. For the ceramic membrane module (LC), the computational domain consisted of a total of about 434 000 cells, while 457 000 and 734 000 cells for the LM1 and for the LM2/LM2* modules, respectively, were selected. An accurate grid refinement in the boundary layers close to the membrane in both shell and tube side was performed, because in these regions the biggest variable gradients were expected. A finer mesh was also required for the LM2/LM2* modules in the small cylindrical gaps, globally long 37 mm and of about 0.5 mm in thickness, enclosed by the fitting accessories and the membrane. The computational domain of the LM2 module is depicted in Figure 3.14.

The computational domain of the PIV laboratory scale simulations was built reproducing as close as possible the experimental module adopted for the PIV measurements. Nevertheless, small differences due to possible defects and imperfect positioning of the experimental module must be considered as sources of differences between the simulated and the experimental geometries. The spatial discretization of the domain was performed adopting about 940 000 unstructured cells.

The gas flow and pressure fields for all the lab-scale modules were calculated by solving the laminar Navier-Stokes equations.

The unstructured grid employed for the simulations of the pilot PM0 and of

the two baffled PM2 and PM3 modules consisted of about 740 000 cells, over the full three-dimensional domain. An additional simulation of PM3 was also run on a grid of about 2 000 000 cells, in order to test the grid sensitivity of the results, and small differences were found with respect to the coarser grid for the flow rates and the compositions of the permeate and retentate flux. Therefore, the coarser discretization was selected as the standard grid for all the simulations. The pilot modules were assumed to operate in turbulent regime, since for the selected operating conditions the shell Reynolds number ranges from $6 \cdot 10^4$ close to the inlet to $5 \cdot 10^3$ toward the shell outlet and the calculations were all performed by the RANS-based approach described above.

The solution convergence was carefully checked by monitoring the residuals of all variables as well as the species mass flow rate. The solution was considered achieved when the residuals were dropped to the order of 10^{-5} or less, which is at least 2 orders of magnitude tighter than Fluents default criteria, and unchangeable values of the mass flow rate were attained.

The solution of the model set of equations is a three-dimensional map of all of the gas species velocity and concentration in each of the computational cell. The origin of the coordinate system (x, y, z) in the computational domain was always located on the axis of the module, which coincides with the z direction, at the membrane cross section closest to the shell outlet.

In the following, the numerical results will be compared with the available experimental data for a detailed and quantitative analysis and evaluation of the simulation strategy.

3.11 Results

3.11.1 Lab-scale ceramic membrane module LC

A first indication of the computational approach effectiveness can be obtained by the comparison of the experimental and computed permeate flow rate relevant to the pure gas feeds (case I), depicted in Figure 3.15

Generally, the CFD predictions accuracy is high, being the error lower than 6% in most cases. Large deviations from the average error are obtained in two cases only, probably due to experimental uncertainties. The accuracy of the simulations is mainly due to the selected method for evaluating the permeance coefficients, while a more significant benchmark for the simulation strategy is offered from case II, for which the calculations were carried out without any variation of the calculated constants A, B, C with respect to case I. In this case, the permeation performances of the membrane also allow to evaluate the appropriateness of adopting eqn.(3.14), instead of simply considering the main mechanism only, i.e. the Knudsen diffusion.

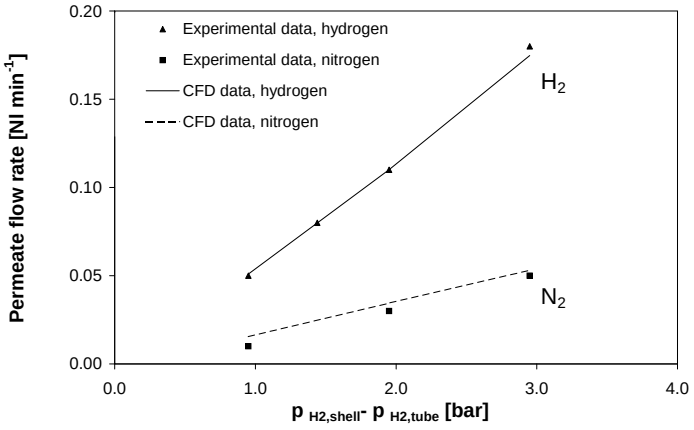

Figure 3.15: Experimental and computed permeate flow rate (LC module, case I)

It is worth specifying that in this particular case, the contribution of the Poiseuille flow vanishes due to the absence of pressure gradient between the outer and the inner side of the membrane.

However, in order to evaluate the sensitivity of the proposed approach to the choice of different transport mechanisms in the membrane, for each of the experimental conditions relevant to case II, the simulations were repeated adopting the following forms for eqn. (3.14):

(a) The constant B has been evaluated from the experimental data relevant to case I considering only the Knudsen mechanism. $Q_{i,tot}$ has been computed neglecting $Q_{i,M}$ and ignoring $Q_{i,P}$ because the pressure difference is nil.

(b) The constant B was calculated from the case I data considering both the Knudsen and the Poiseuille flow.

(c) Finally the constant A and B were evaluated from the case I data considering Knudsen, Poiseuille flow and molecular diffusion mechanisms. $Q_{i,tot}$ has been computed ignoring $Q_{i,P}$ only.

The resulting flow rates of hydrogen and nitrogen permeate are compared with the corresponding experimental data in Figure 3.16. It is apparent that different accuracy levels are obtained with the three models. It is worth noting that when the molecular diffusion is neglected, the experimental effect of the working pressure is not correctly predicted by the CFD simulations. As can be observed, fairly accurate predictions of the H_2 permeate flow rate are obtained with the more complex of

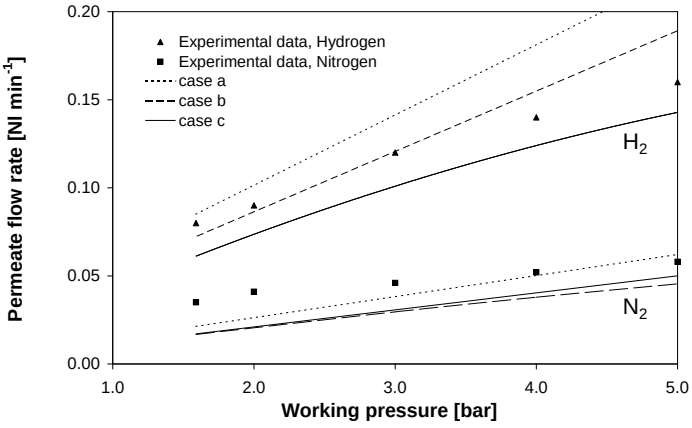

Figure 3.16: Comparison between the experimental flow rate of H_2 and N_2 permeate and the CFD results obtained with different models at different operating conditions (LC module, case II)

the three models, which leads to a slight and constant underestimation of the predicted flows being the computed trend parallel to experimental one. The accuracy of the predictions is worst in the other two cases of simplified transport equation, the discrepancy being more marked increasing the pressure. As pertain the nitrogen results obtained by the more complex model, the absolute error between the computed and the experimental flow rates is the same as for the hydrogen case and the predicted data trend is again parallel to the experimental one, although the relative error is more significant. Since nitrogen flows in the reverse direction with respect to hydrogen, i.e. from tube to shell side, geometrical differences, which were not taken into account, could be responsible for the lost of modelling accuracy. Overall, the predicted H_2 and N_2 permeate flow rates show a reasonable agreement with the relevant experimental data.

When a gas mixture is fed in the module (case III), the predicted H_2 and N_2 permeate flow rates, calculated considering the complete form of eqn. (3.14), show a very good agreement with the experimental data (see Figure 3.17), thus further confirming the suitability of the modelling approach to fairly predict the membrane separation features. Overall, a realistic prevision of the ceramic membrane behaviour can be obtained with the developed CFD approach. Its applicability to any ceramic membrane system is expected to be straightforward at the condition that the mass transfer mechanisms and the relevant diffusivity coefficients of the membrane are known.

After assessing the reliability of the simulation strategy, a deeper analysis of

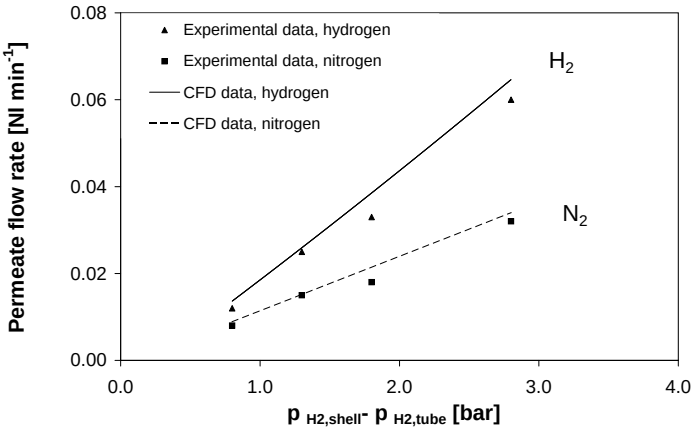

Figure 3.17: Experimental and computed permeate flow rate (LC module, case III)

the local fluid dynamic features of the module, which may importantly affect the overall mass transfer performances of the membrane, can be confidently performed. The effect of a full coupling of the fluid dynamic and the mass transfer modelling can be estimated from the analysis of the velocity vector plots shown in Figure 3.18, where a particular shell portion in the case of the ceramic membrane is considered and the two different results obtained considering (Figure 3.18a) or neglecting (Figure 3.18b) the mass transfer across the membrane are shown. As can be observed, a different shape of the velocity vectors is predicted by the two simulations, thus proving that the mass transfer produces visible effects on the present module hydrodynamics. Therefore, a simplified purely fluid dynamic modelling strategy is not viable for obtaining accurate predictions. Moreover, the gas velocity vectors clearly indicate that the effect of the inlet geometry of the module shell cannot be disregarded. Indeed, the presence of the strong gas jet produced from the shell feed stream entrance confirms that, although over all the flow regime is laminar, the flow close to the initial membrane portion is significantly different with respect to the rest of its surface.

3.11.2 Lab-scale metallic membrane module LM1

The effectiveness of the modelling approach to the prediction of Pd-Ag membranes behaviour has been evaluated for the LM1 module first. As said before, the experimental data relevant to the case IV have been used to calculate the model parameters; as it can be seen in Figure 3.19, the experimental behaviour is well described by the CFD simulations, thus validating the adopted procedure. The

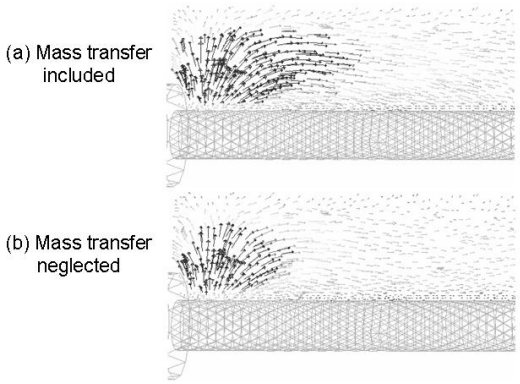

Figure 3.18: Velocity vector plots with species transport model included (a) and neglected (b). Shell side, portion of a plane orthogonal to that containing the shell inlet and outlet tubes (LC module)

same model constants were adopted also for case V which therefore was described without the help of any adjustable parameter; the predicted H_2 molar fraction in the permeate flow (Figure 3.19) shows also in this case a remarkable agreement with experimental data, thus confirming that the CFD procedure can be confidently applied also to this membrane type. Indeed, the root mean square error of prediction obtained for case V is equal to 5.58% which is only slightly higher to that of 5.29% obtained for case IV, which was used to tune the model.

The present simulations provide also detailed information on the species distribution in the whole volume of the module. As an example, the predicted H_2 concentration profiles along the membrane axis on the shell side is shown in Figure 3.20. It is worth noticing that the H_2 profile outside the membrane is not linear, thus an average driving force for the mass transfer is not easily predictable. Therefore in this case, the usually adopted simplified assumption on the concentration profiles along the module might not closely match the real system behaviour.

Some CFD simulations were performed on LM1 module varying the feed flow rate of a mixture at 50% *mol* of H_2 between 1 and 10 $Nl\ min^{-1}$, the sweep flow rate from 1 to 15 $Nl\ min^{-1}$ and the membrane permeability up to six times the actual permeability. Obviously an increase of the membrane permeability increases the permeate flux, but this is not the only resistance present in the module. As it can be observed in Figure 3.21, the feed flow rate (which is fed tube side, in this case) has negligible influence on the permeate flux, while the sweep flow rate permits to change considerably the permeate flux, proving that even the gas transport shell side gives an important contribution to the permeation process.

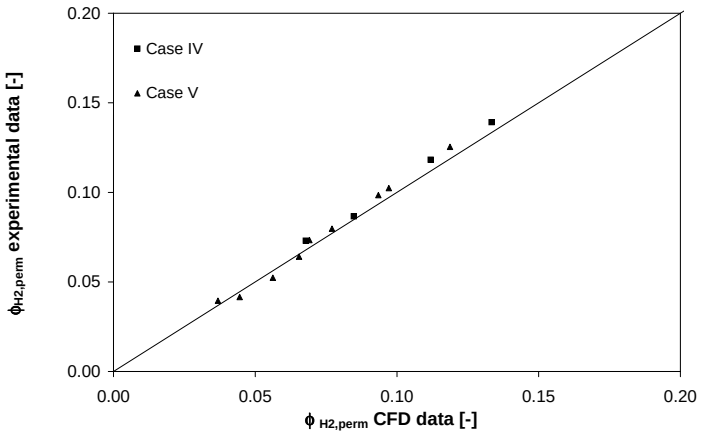

Figure 3.19: Comparison between the experimental molar fraction of H_2 permeate and the CFD results at different operating conditions (LM1 module, cases IV and V)

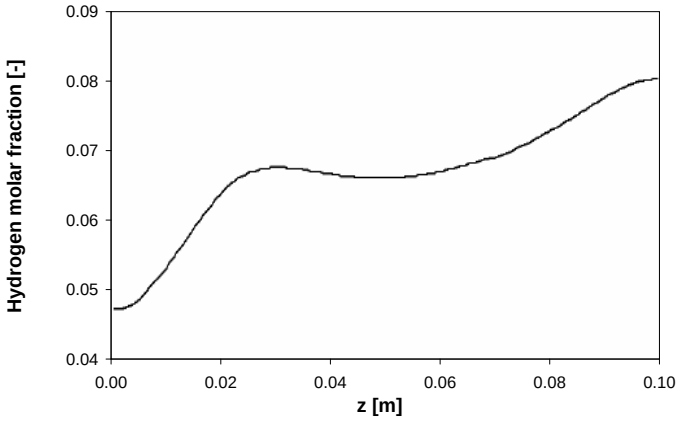

Figure 3.20: H_2 molar fraction along the LM1 module in the shell side (Case V)

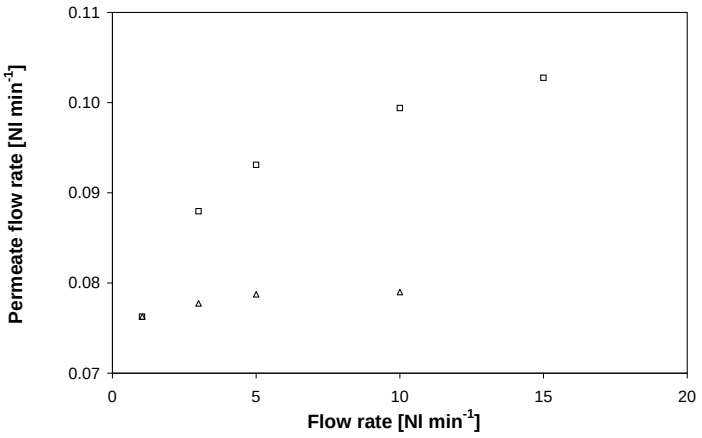

Figure 3.21: Permeate flow rates at different feed flux (Triangles) and sweep flux (Squares). (LM1 module, case V)

3.11.3 Lab-scale metallic membrane module LM2

Prediction of experimental permeation performances

The diffusion rate constants of the Pd-Ag layer and of the ceramic support of the LM2 module are greater than those of the LM1 one (Table 3.3). As a result, the influence of the convective resistances in the LM2 module is expected to be more important, due to the low value of the mass transfer resistance. In this case, a local and accurate evaluation of the convective resistance is crucial and significant improvements of the permeate flow rates predictions are expected with the CFD approach with respect to lumped parameters models.

As already mentioned above, the experimental data of cases VI, X and XII, that are all relevant to pure gas permeation conditions, were adopted beforehand for determining the model constants. Afterwards, the same cases have been simulated providing accurate results, being the root mean square error between the experimental and the computed permeate flow rates lower than 5%, except a couple of cases, thus confirming the appropriateness of the coupling between the fluid dynamics and mass transfer equations.

The benchmark for the fully predictive capability of the simulation strategy is offered from all the other cases, for which the calculations were carried out without any variation of the calculated constants A, B, F and E with respect to the former cases. In particular, the simulation results of cases VII and XI, relevant to mixtures of H_2-N_2 at 50% *mol* and 88% *mol* of H_2 at different temperatures, are particularly important for assessing the model capability in predicting the temperature effect

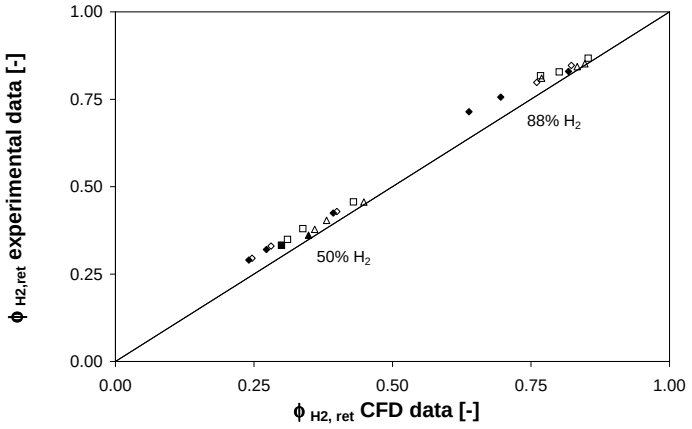

Figure 3.22: Comparison between experimental and computed H_2 molar fraction in the retentate stream at different operating pressures and at temperature T = 673.15 K (open symbols) and T = 723.15 K (solid symbols). Diamonds: 1 $Nl\ min^{-1}$, Squares: 2 $Nl\ min^{-1}$, Triangles: 3 $Nl\ min^{-1}$ (LM2 module, case VI)

on the gas mixture separation. The results can be observed in Figure 3.22, where the agreement of the computed retentate H_2 molar fractions with the experimental data at two different temperatures is apparent. In Figure 3.23, a similar plot is reported comparing the behaviour of $H_2 - N_2$ and $H_2 - CH_4$ mixture at 50% *mol* of H_2 at a fixed temperature (cases VII and VIII). As can be observed, the present CFD model predictions are accurate for different binary mixtures as well as for the case of ternary mixtures, that are depicted in Figure 3.24, where the computed and the experimental results relevant to a $H_2 - N_2 - CH_4$ gas stream are shown.

Overall, the accuracy of the predicted H_2 molar fraction in the retentate flow demonstrates that the present CFD model can be confidently adopted for predicting the membrane separation features at different operating conditions, i.e. temperature, pressure, feed flow rate and compositions in binary and ternary mixtures. Its applicability to any Pd-Ag membrane system is expected to be straightforward at the condition that the mass transfer mechanisms and the relevant diffusivity coefficients of the membrane are known.

Comparison with PIV data

The PIV data collected in the plane crossing the shell inlet and outlet tube axis confirm the complex fluid dynamic behaviour of LM2 membrane module, found in

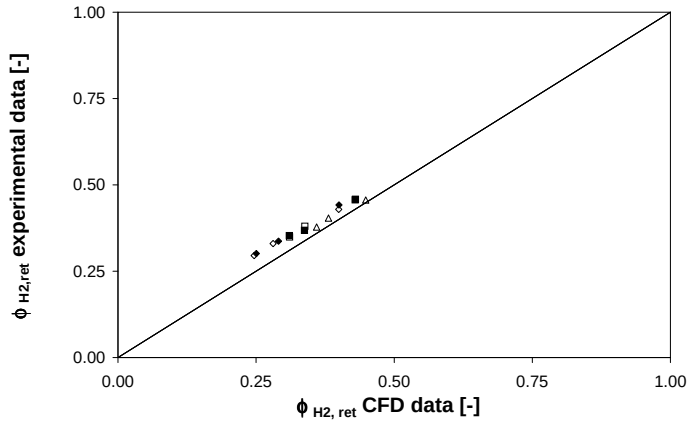

Figure 3.23: Comparison between experimental and computed H_2 molar fraction in the retentate stream at different operating pressures and compositions for case VII (open symbols) and case VIII (solid symbols). Diamonds: 1 $Nl\ min^{-1}$, Squares: 2 $Nl\ min^{-1}$, Triangles: 3 $Nl\ min^{-1}$ (LM2 module)

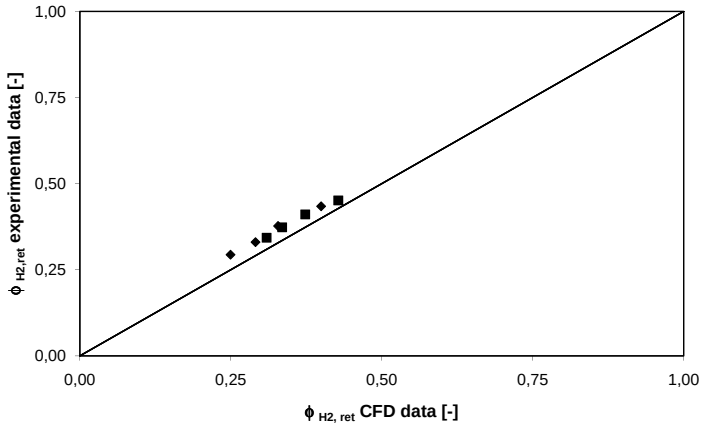

Figure 3.24: Comparison between experimental and computed H_2 molar fraction in the retentate stream at different operating pressures. Diamonds: 1 $Nl\ min^{-1}$, Squares: 2 $Nl\ min^{-1}$ (LM2 module, case IX)

the simulations. As can be observed in Figure 3.25a, where the air velocity vectors and the corresponding magnitude colour map in a measurement plane portion close to the gas inlet of the PIV module are depicted, the air jet induced by the entrance tube moves much faster than the surrounding fluid; the velocity magnitude in the inlet jet region is an order of magnitude higher than in the upper module portion. The air jet impinges on the shell wall opposite the inlet tube side, and it is split into two streams which produce two recirculation loops, one above and one below the impingement section. As a result, the velocity field is more complex and irregular in one side of the shell, which is opposite the inlet side, than in the inlet side itself and this feature reflects also on the flow distribution around the membrane, thus affecting the separation step.

Both the PIV vector plot and the color map compare fairly well with the CFD results (Figure 3.25b); the flow features and the velocity magnitude are well predicted from the calculation. The major differences between measurements and calculations can be noticed close to the lower tube and they must be associated with the measurement uncertainties due to light reflection and positioning errors.

Overall, although the important flow regime variation goes from fully turbulent in the inlet tube to laminar in the shell, the CFD simulation catches fairly well the fluid dynamic behaviour of the module. A quantitative evaluation of the reliability of the CFD results can be performed comparing the two velocity components, u_x and u_z, at a selected elevation (fixed z coordinate) as obtained from PIV and CFD. The results shown in Figures 3.26 and 3.27 reveal that for both velocity components the computed velocity profiles follow quite closely the experimental data; the discrepancies are mainly due to the geometric and positioning differences between the real module and the modelled module. For a comprehensive evaluation of the prediction accuracy with respect to the experimental data, the PIV measurement error of 2.5%, which has been estimated following Westerweel (1997), must be considered. Overall, the PIV measurements confirm the reliability of the CFD simulations in predicting the module fluid dynamics behaviour.

Effect of operating conditions and analysis of the local features

Since the model has provided reliable predictions as compared with the available experimental data, the local information obtained by the simulations can be adopted for evaluating the module behaviour and the influence of the operating conditions on the separation performances. A particular feature of the flow field in the shell section is shown in Figure 3.28, relevant to the LM2 membrane module, where the maps of the gas velocity component along the axis at three different sections close to the gas entrance are depicted. In the lower part of the outer tube, the feed gas moves from the inlet pipe towards the membrane active surface, while a stream with a lower H_2 concentration moves in the opposite direction toward the

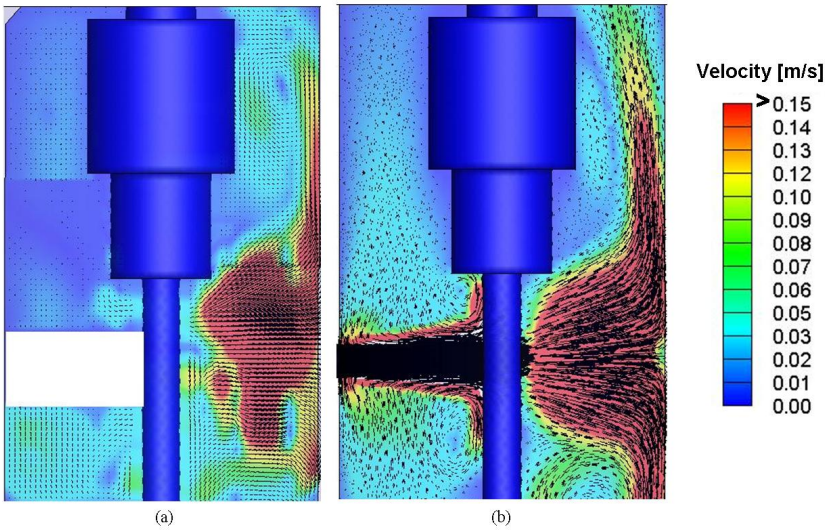

Figure 3.25: Vector plot and contour map of the gas velocity field on a portion of the measurement plane of the LM2 module; (a) PIV data, (b) CFD results

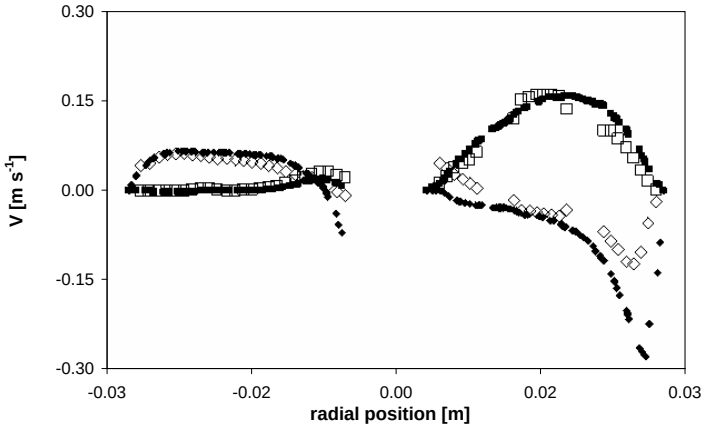

Figure 3.26: Velocity profiles of CFD results (solid symbols) and PIV data (open symbols) at $z = -0.072\ m$. Squares: u_x, Diamonds: u_z

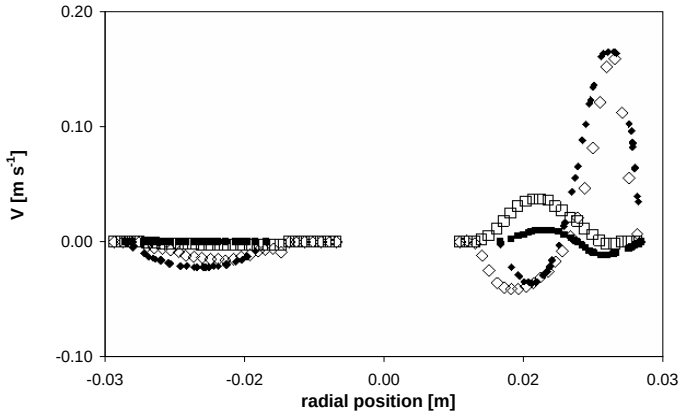

Figure 3.27: Velocity profiles of CFD results (solid symbols) and PIV data (open symbols) at $z = -0.021\ m$. Squares: u_x, Diamonds: u_z

feed stream, in the upper part of the shell. As a result, where the two streams come across, a dilution of the feed in H_2 is obtained.

The dilution effect and the concentration polarization phenomena are also visible in Figures 3.29 and 3.30. The hydrogen concentration on the membrane surface can be up to 40% lower than the bulk concentration, as shown in Figure 3.30, where the H_2 molar fraction profiles on two lines parallel to the module axis, the former close to the membrane (line 3) and the latter in the phase bulk (line 1), are plotted. In Figure 3.29, it is reported the H_2 molar fraction on lines 1 and 2, which are parallel to the axis of the module and equidistant from it. Hydrogen molar fraction is higher along line 2 than along line 1 (note that the latter line is an expansion of the same line plotted in Figure 3.30). The reason is that the feed inlet causes a recirculation inside the module: the feed stream goes from the inlet pipe to the opposite side of the module and then, after having crossed the membrane and lowered its hydrogen content, it returns back near the feed inlet.

Apart from this critical section of the membrane, it is important to observe that whatever stream line is considered, the stream reaches the membrane with a poorer H_2 concentration, confirming a lower membrane module efficiency with respect to the ideal case.

An overall picture of the H_2 molar fraction map for the LM2 module is shown in Figure 3.32. At the operating conditions considered in this work, radial and axial gradients for the species molar fraction and relevant polarisation effects can be observed which also confirm the results obtained by other researchers on similar membranes (Pizzi et al., 2008; Mori et al., 2007) tested in analogous experimental

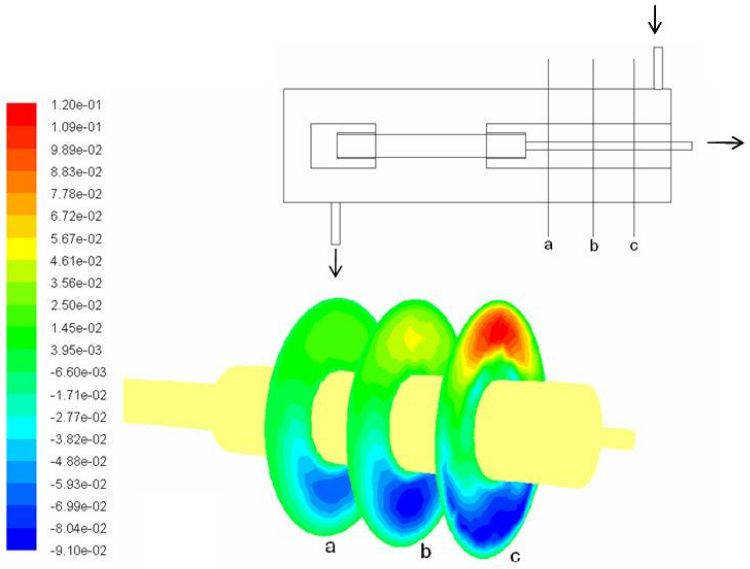

Figure 3.28: Axial velocity maps near the shell inlet at different positions (LM2 module)

conditions. In the small gaps between the fitting and the membrane the H_2 partial pressure is the same as in the inner tube (Figure 3.31) and the membrane active surface available for the hydrogen permeation is reduced (this effect is not present when pure hydrogen is fed). Since the overall membrane efficiency can be affected by these features, preliminarily knowledge could be very beneficial for efficient design and scale-up of industrial separation apparatuses. It is worth mentioning that the hydrogen penetration depth in the fitting zone depends on the feed stream composition, being it bigger the higher the H_2 feed concentration is. In any case, when a mixture is fed, the hydrogen flux entering the gaps can be considered nil.

The capability of the CFD approach to investigate the polarisation effect is apparent from the analysis of the radial profiles of H_2 molar fraction at different cross sections, shown in Figure 3.33. As can be observed, the profiles are unexpectedly not symmetric, because of the entrance effects previously shown in Figure 3.28. Besides, the bulk concentration in each section is largely greater than the concentration at the membrane wall. Therefore, neglecting the convective resistance might induce a wrong estimation of the membrane permeability, especially for membranes characterised by low mass transfer resistances.

The influence of temperature on permeate flow is clearly visible in Figure 3.34. As it was expected, the higher the temperature is, the higher the permeate flow

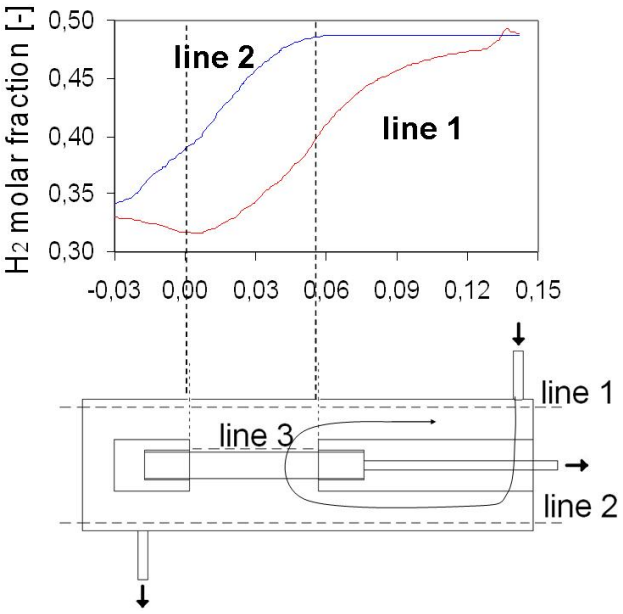

Figure 3.29: Hydrogen molar fraction along a line in the bulk of the phase close to the inlet section (line 1) and a line on the opposite side (line 2) in the LM2 module

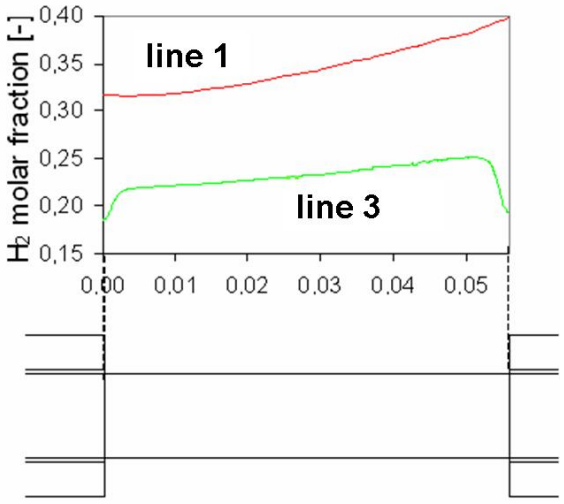

Figure 3.30: Hydrogen molar fraction along a line in the bulk phase (line 1) and a line close to the membrane (line 3) in the LM2 module

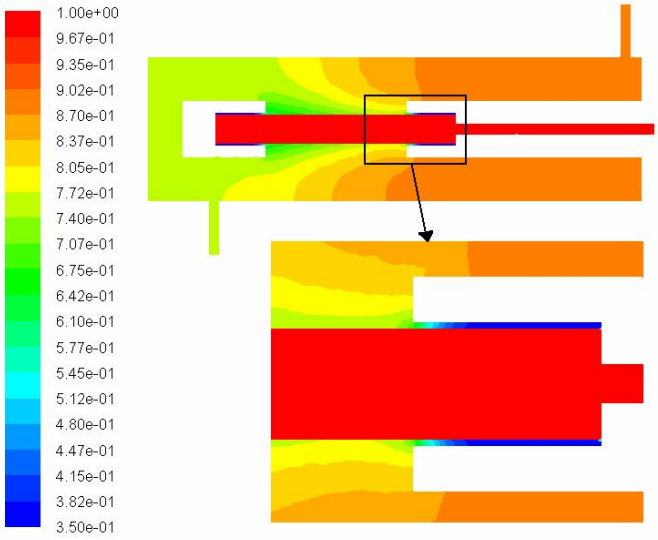

Figure 3.31: H_2 mole fraction map in a plane containing the shell inlet and outlet tubes (LM2 module, case VII, $88\% mol\ H_2$, $p_{ret} = 3bar$)

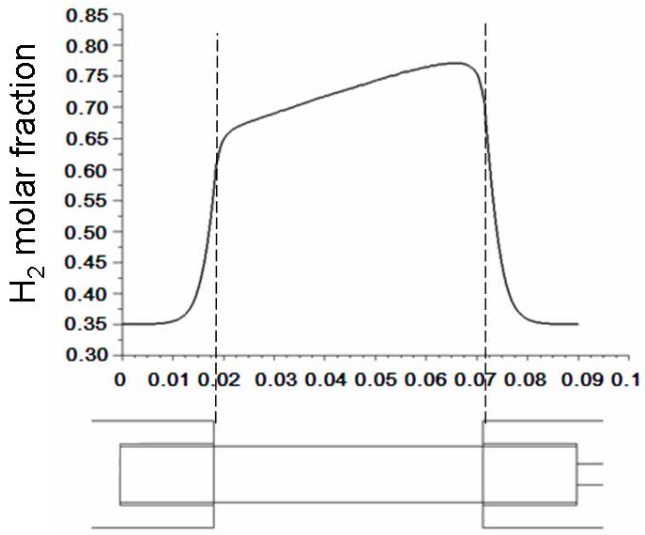

Figure 3.32: H_2 mole fraction on a line close to the membrane (LM2 module, case VII)

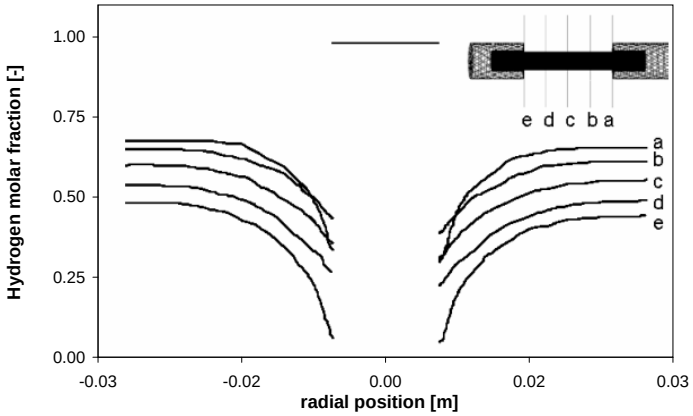

Figure 3.33: Radial H_2 mole fraction at different axial position (LM2 module, case VII, 88% mol H_2)

is. The results agree well with the analysis performed by Catalano et al. (2009) and with the experimental trend reported by Pizzi et al. (2008), who working on a membrane with the same characteristics as the present one measured a reduction of the permeate flow rate of about 31% for a temperature decreases from $773.15K$ to $673.15K$, while with our computational approach, a depletion of about 30% is predicted for the same temperature change.

For the case of gas mixtures, the analysis of the CFD results also allows to evaluate the effect of the temperature on the gas species distribution inside the separation module. The H_2 molar fraction maps, when an equimolecular mixture of $H_2 - N_2$ is fed to the module, for working temperatures of 673K and 773K are shown in Figures 3.35 and 3.36, respectively. In both cases, large radial gradients of the hydrogen concentration take place indicating that the polarization phenomenon cannot be neglected. It is interesting to notice that the temperature rise results in a decrease of the outlet molar fraction in the retentate stream and in the extension of the zone with a value lower than 29%. Actually, if the temperature increases, the membrane permeance increases, and as a result the membrane resistance becomes less important with respect to the convective mass transfer resistance. For both cases, the axial profile of the hydrogen concentration is not symmetric, thus simplified fluid-dynamic models cannot be used for predicting the behaviour of the present separation unit.

The non-symmetric distribution of the hydrogen is due to the effects of the inlet stream. The velocity vector plot shown in Figure 3.37 highlights that a clear recirculation loop develops between the inlet nozzle and the active part of the

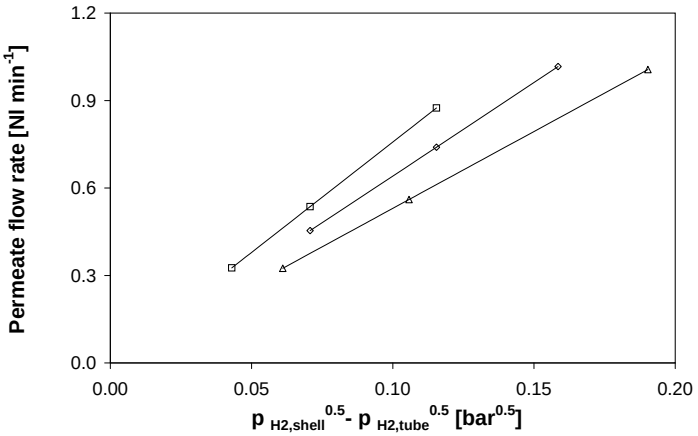

Figure 3.34: Computed H_2 permeate flow rate at different operating temperatures. Feed flow rate: 1 $Nl\ min^{-1}$, pure H_2; Triangles: T=673.15K, Diamonds: T=723.15K, Squares: T=773.15K (LM2 module, cases VI, X, XII)

membrane. The flow loop induces a non-symmetric distribution and dilutes the hydrogen mole fraction from the value of 0.5 in the feed stream to an average value of about 0.44 in the starting section of the active part of the membrane. The velocity vectors magnitude is quite small all over the module apart from the inlet and outlet regions, correspondently the Reynolds number in the tube reaches the maximum value of 116 and in the shell region of the membrane it ranges from about 1 to 35 in this specific case and anyhow it remains close to these values at the other operative conditions. The flow regime is responsible for the concentration polarization phenomenon revealed by the concentration maps.

The value of the permeate flow rate at several operating temperatures, shown in Figure 3.38, helps to quantify the composition effect predicted computationally. As can be observed, increasing the temperature at fixed H_2 partial pressure, the permeate flow rate of pure H_2 increases sharply, while the increment is fairly small for mixtures of H_2 and N_2 feed streams. The physical reason for this behaviour may be found in the different mass transfer resistance in the two cases. In particular, for the case of pure H_2 feed stream, only the membrane mass resistance is present, while in the case of gas mixtures, the convective mass transfer resistance is comparable with the resistance of the membrane. Therefore, the permeate flow rate is only slightly influenced by a change in the working temperature of the membrane, at least in the range of temperature analysed in this work.

Finally, Figure 3.38 shows that the effect of the temperature on the permeate flow could be overestimated if the analysis is restricted only to the pure H_2 feed

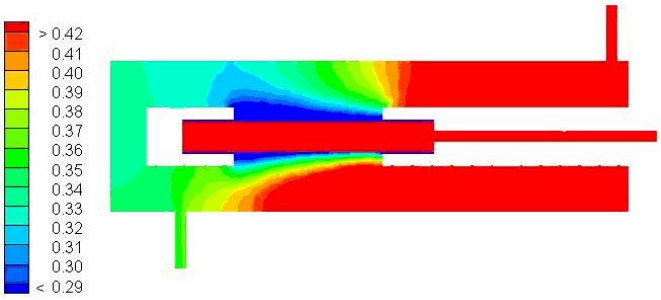

Figure 3.35: Map of H_2 mole fraction at $T = 623\ K$ (LM2 module, case VII, feed flow rate: 3 $Nl\ min^{-1}$, 50% $mol\ H_2$, p_{ret}= 6 bar)

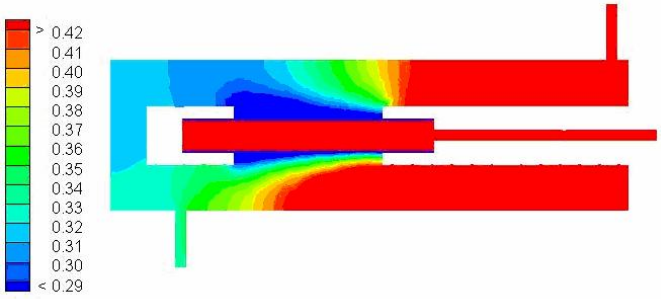

Figure 3.36: Map of H_2 mole fraction at $T = 723\ K$ (LM2 module, case XI, feed flow rate: 3 $Nl\ min^{-1}$, 50% $mol\ H_2$, p_{ret}= 6 bar)

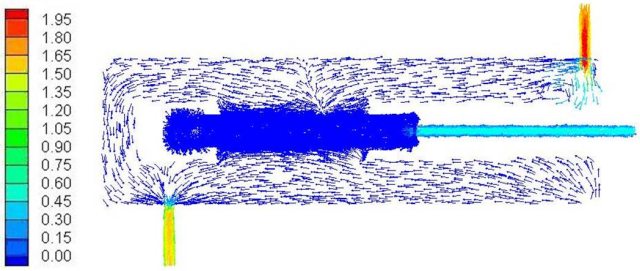

Figure 3.37: Map of velocity vectors [m s^{-1}] at $T = 623\ K$ (LM2 module, case VII. Feed flow rate: 3 $Nl\ min^{-1}$, 50% $mol\ H_2$, p_{ret}= 6 bar)

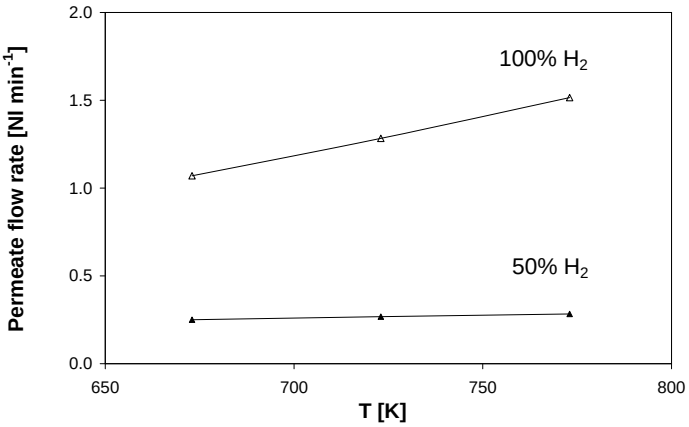

Figure 3.38: Total permeate flow rate at various operating temperatures. Feed flow rate: 2 $Nl\ min^{-1}$. Open symbols: pure H_2, Solid symbols: $H_2 - N_2$ mixture (LM2 module)

stream. For a correct design of the equipment, the mass transfer resistance due to the polarization effect, that can be easily estimated if the fluid dynamic of the module is known, has to be taken into account.

The effect of the feed stream composition is clear from Figure 3.39, where the predicted permeate flow rate against the Sieverts driving force is presented at different feed stream compositions. The driving force is evaluated from the H_2 partial pressure at the outlet sections of the shell, $p_{H_2,ret}$, and of the tube, $p_{H_2,perm}$. The results reveal that the H_2 permeate flux is much lower for gas mixtures permeation than for the pure H_2 case, although the two systems apparently work with the same driving force. Also this computational result agrees with the experimental data by Pizzi et al. (2008), who measured a permeate flow reduction of 60.4% when pure hydrogen feed stream was replaced with a equimolecular mixture of $N_2 - H_2$, while in our predictions the reduction has been estimated to be equal to 57.2%. Therefore, the inert gas is responsible of dilution, that decreases the driving force, and of an additional resistance to the mass transfer, that have both to be taken into account for the correct design of the module.

The presence of a significant effect of the concentration polarization phenomenon is also confirmed by the increase in the H_2 permeate flux obtained for increasing the flow rate of the feed gas mixtures (Figure 3.40). As can be observed, the beneficial effect of the increased flow rate becomes smaller and smaller, while increasing the feed flux. An interesting information is also given by the efficiency, defined as the ratio between the H_2 permeate and the H_2 feed to the module. As it is shown

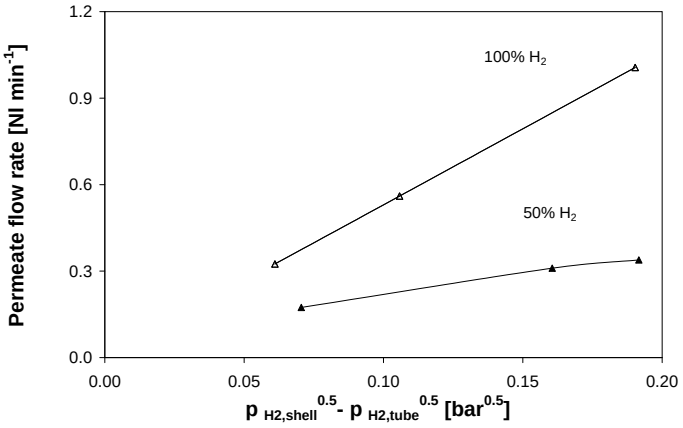

Figure 3.39: Total permeate flow rate at different feed stream compositions vs Sieverts driving force. Feed flow rate: 1 $Nl\ min^{-1}$, T=673.15K. Open symbols: pure H_2, solid symbols: $H_2 - N_2$ mixture (LM2 modules, cases VI-VII)

in Figure 3.40, the efficiency decreases drastically when the feed flux is increased. As a result, the increase of the feed flux might not be a solution for reducing the concentration polarization effect. Instead, geometrical optimization of the module for reducing the H_2 concentration difference between the bulk and the membrane zone can be attempted.

The model improvement based on the inclusion of the multi-component diffusion allows to evaluate how the mixture components are distributed over the whole module volume. In Figure 3.41, relevant to the simulation of case IX, the dilution effect of the H_2 molar fraction induced by the recirculation loop can be clearly noticed again. Moreover, a contribution to the reduction of the permeate flow is also given by the presence of the fitting accessories, which extend over a portion of the membrane and does not allow to that part of the surface to contribute to the hydrogen permeation, as a difference with respect to the case of pure H_2. From Figure 3.41, it is apparent that the small gaps are filled with CH_4 while they are poor of N_2, as a result of the different diffusivity coefficients of the two species in the mixture: N_2 diffuses faster than CH_4.

The model capability to determine the concentration of each component on the membrane surface, has lead to predict a slight difference between the CH_4 and the N_2 molar fraction on the membrane, but in the particular case of inert gas mixtures the difference is not expected to affect the membrane separation properties. Generally, the asset of the CFD model in the prediction of local concentration of multi-component mixtures may be significant, as in the case of species interacting

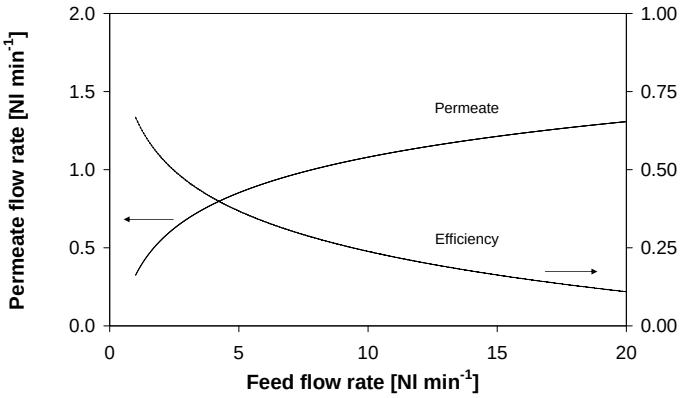

Figure 3.40: Computed H_2 permeate flow rate and efficiency, T=673.15K (case VII, 50% *mol* H_2, $p_{ret} = 6$ *bar*)

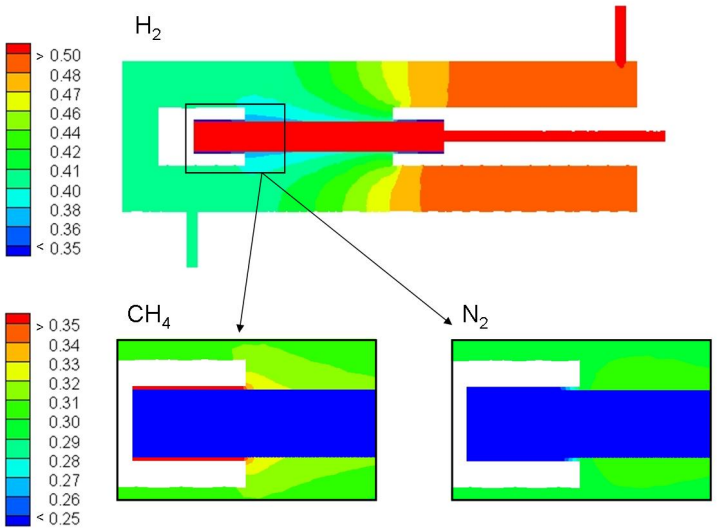

Figure 3.41: Maps of species mole fraction in a plane containing the shell inlet and outlet tubes (LM2 module, case IX, 1 $Nl\ min^{-1}$)

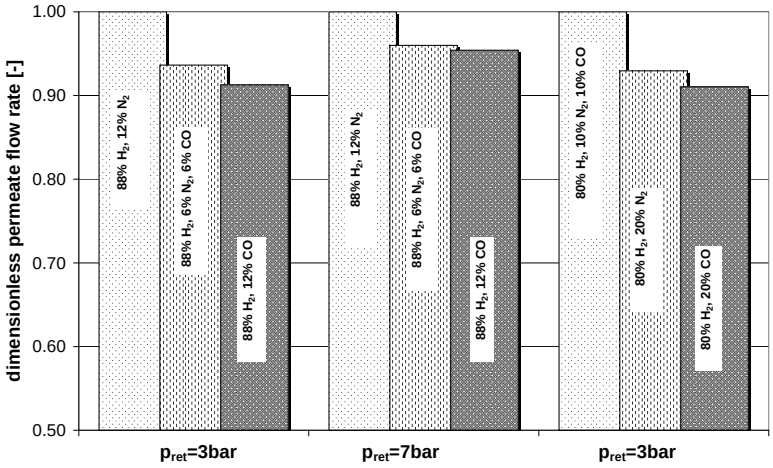

Figure 3.42: Computed dimensionless H_2 permeate flow rate at different operating conditions (LM2 module, cases XIV, XV, XVI)

with the membrane surface and inhibiting the H_2 mass transfer (Gallucci et al., 2007; Peters et al., 2008). Indeed, the correct evaluation of the effects of inhibitors strictly depends on the estimation of the species concentration on the membrane surface (eqn. 3.25), it is strongly influenced by the membrane permeance and by the fluid-dynamic behaviour of the retentate stream and it can change from the inlet section to the outlet ones. As an example, the predicted effect of carbon monoxide on the module permeation can be observed in Figure 3.42 (cases XIV, XV and XVI) where dimensionless permeate flow rate (permeate flow rate/permeate flow rate in $H_2 - N_2$ mixture) changes depending on the operating conditions and on the non-permeating gas compositions (N_2 only, CO only or a mixture of N_2 and CO). The simulation results show that changing the gas from N_2 to CO, or to an equimolecular mixture of N_2 and CO, the permeate flow rate reduction depends on the operating conditions. Therefore, for a proper estimation of the module performances, the CFD method presented in this work, that is able to tackle the mutual influence of the mass transfer resistances and of the inhibition of the membrane, appears to be particularly suitable.

3.11.4 Lab-scale metallic membrane module LM2*

The importance of reliable predictive methods for taking into account the non ideal flow behaviour of membrane separation units must be related to the impact

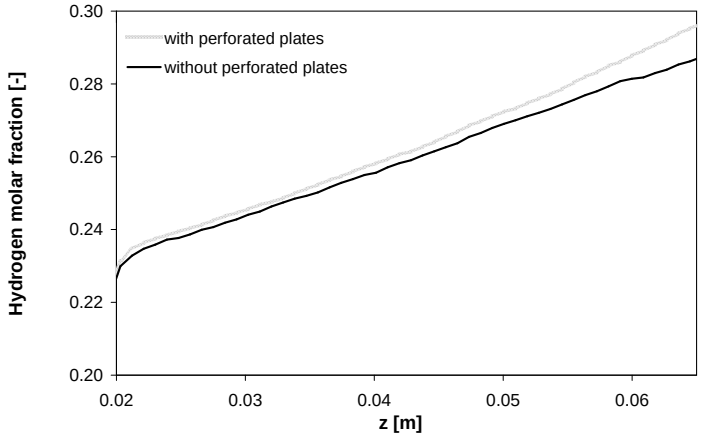

Figure 3.43: H_2 mole fraction along the LM2 and LM2* modules axis obtained as the average on a cylindrical surface very close to the membrane active surface (LM2 module, case VII; LM2* module, case XVII)

of the flow field on the separation performances. For addressing this last aspect, the separation of a binary mixture of H_2 and N_2 in a laboratory scale module (LM2*) differing from LM2 by the presence of two perforated plates was considered. The simulation results reveal that, together with the modification of the fluid flow features due to the introduction of the two perforated plates, a different hydrogen distribution is obtained that affects the separation efficiency.

In order to compare the results of the two simulations, a cylindrical surface wrapping the membrane was considered. The surface has a diameter equal to 11.6 mm, which is slightly bigger than the membrane diameter. In this way, it was possible to compare the species distribution in the shell side region close to the membrane. The calculated average H_2 mole fraction on the cylindrical surface and along the module axial coordinate is depicted in Figure 3.43 for LM2 and LM2*. As can be observed, at the axial coordinates of 0.06-0.065 m, which correspond to the membrane portion closer to the inlet, the feed gas reaches the membrane with higher H_2 content with respect to the original case, since the perforated plate reduces the gas stream recirculation due to the inlet jet. As for the separation efficiency, for the investigated operative conditions (feed flow rate of 3 $Nl\ min^{-1}$, mixture of H_2 and N_2 at 50% mol of H_2, shell and tube side pressures of 6 and 1.05 bar, respectively), the flow field modification has a positive effect on the membrane performances, since the permeate flow rate increases with respect to the original case of about 3.3%.

In any case, it is important to underline that the introduction of perforated

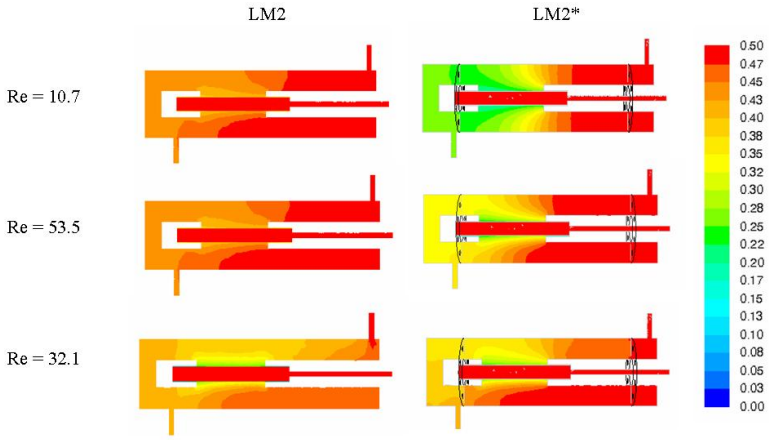

Figure 3.44: H_2 mole fraction maps in the section containing the shell inlet tube for the LM2 and LM2* modules at different Reynolds number (LM2 module, case VII; LM2*, case XVII)

plates gives rise to two contrasting effects on the mass transfer process: the first is positive as it is related to the removal of gas dilution described above; the second effect could be negative, because the reduction of the mean velocity due to the elimination of the recirculation loop might produce an increment of the polarization resistance. As a consequence, the overall action of the perforated plates is given by the balance of these two effects. In order to widen the analysis, different simulations were run on the two modules (LM2 and LM2*), with and without perforated plates, at different shell Reynolds numbers, i.e. changing the feed flow rate from 3 $Nl\ min^{-1}$ to 1 and 5 $Nl\ min^{-1}$. The H_2 concentration maps depicted in Figure 3.44 show that significantly different distributions are obtained depending on the operating conditions that ultimately result in different H_2 permeated fluxes. As a result, although the introduction of perforated plates can be beneficial for improving the module behaviour, quantitative information on the separation performances must be drawn only from dedicated simulations of each specific geometry and operating condition.

3.11.5 Pilot membrane modules PM0, PM2 and PM3

Since the laboratory scale module investigations have shown that the non ideal features of the gas streams flow can be reliably predicted by the CFD method and the same method was shown to be accurate in estimating the separation performances of the membrane modules, its application to the design and optimization of a pilot membrane module will be considered in the following.

All the results reported in this section refer to a computational domain of 740 000 cells, since a grid dependency test performed by an additional simulation of the PM3 module discretized with $2 \cdot 10^6$ cells, reported small differences in the velocity field and a variation of 5% in the H_2 permeate flow rate.

The predicted H_2 concentration distribution on the module cross section containing the shell inlet tube is depicted in Figure 3.45. The H_2 concentration distribution in the simplest unbaffled module PM0 (Figure 3.45a) highlights that, as soon as the inlet stream enters the module, it is quickly diluted by the gas stream recirculated from the centre of the separation module, which can be observed in the mean velocity vectors in the same plane reported in Figure 3.46a. As a consequence of the gas stream mixing, the H_2 mole fraction is reduced from about 0.18 to about 0.14, before reaching the membrane. This concentration drop has a negative effect on mass transfer because the separation driving force is reduced. Moreover, the effect of the above-mentioned stream is not limited to the inlet section, but it affects the behavior of the whole separation module.

Overall, the fluid dynamic behaviour of the module appears to be more similar to that of a continually stirred tank reactor, since the H_2 concentration is almost homogeneous along the membrane and it is almost equal to the outlet value, rather than to that of a plug flow module, where the H_2 concentration should decrease moving from the inlet to the outlet section.

The introduction of baffles in the module shell allows a reduction of the internal mixing and permit to obtain a fluid dynamic behaviour that is closer to the plug flow model, as can be observed in Figure 3.45 b and c relevant to the H_2 molar maps of PM2 (two baffles) and PM3 (three baffles) modules, respectively. It is worth noticing that the geometric change allows to increase the mean driving force for the H_2 separation, since baffles avoid that gas streams coming from regions with low H_2 concentration could come back and dilute the gas streams with the higher H_2 concentration. The compartment due to baffles can be noticed by the analysis of the vector maps shown in Figure 3.46 b and c compared with Figure 3.46 a.

It is also important to point out that in the baffled configurations the gas velocity near the membrane is much higher (0.26-1.7 $m\ s^{-1}$) than that of the unbaffled module (that is in the range 0.26-0.57 $m\ s^{-1}$), due to the cross section restriction, as can be observed in Figure 3.47, where the velocity profiles along the module axis obtained as the average of the velocity values on three cylindrical surfaces very close to the three membranes are depicted. In the PM0 module, the velocity magnitude close to the membrane surface slightly decreases going from the inlet ($z = 0.446\ m$) toward the outlet ($z = 0\ m$) because of the permeation process, while the profiles for the PM2 and PM3 modules show higher velocity magnitude in the baffle regions, due to the fact that all the flow is forced to pass near the membranes. This velocity magnitude change has a positive effect on mass transfer, because it allows reduction of the polarization resistance.

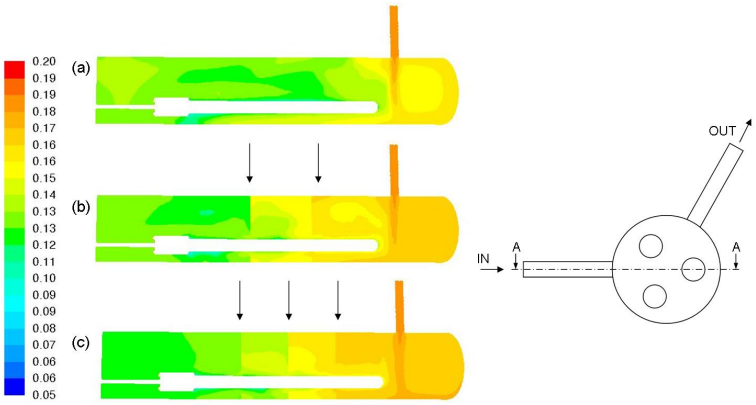

Figure 3.45: H_2 mole fraction maps in the section containing the shell inlet tube (section A-A); (a) PM0, (b) PM2, (c) PM3; arrows indicate the positions of baffles

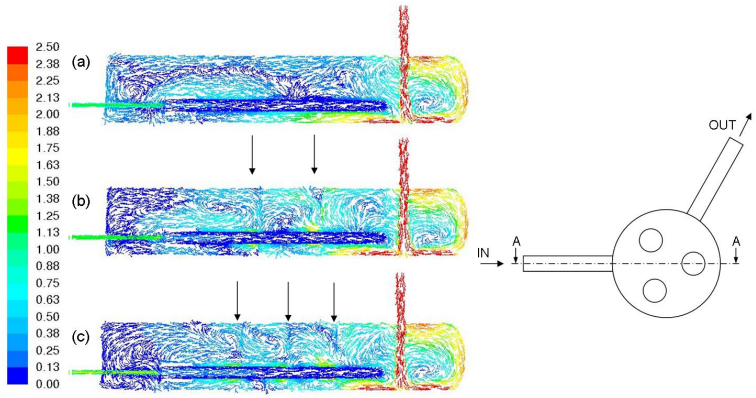

Figure 3.46: Vector plot in the section containing the shell inlet tube (section A-A); (a) PM0, (b) PM2, (c) PM3; arrows indicate the positions of baffles

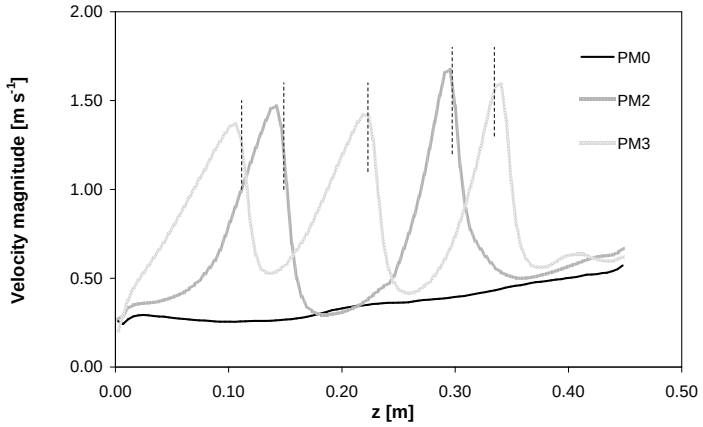

Figure 3.47: Velocity profiles along the module axis obtained as the average of the velocity values on three cylindrical surfaces very close to the membranes (dashed lines represent baffles positions)

The different fluid dynamic behaviour of the module equipped with baffles has a clear impact on the H_2 concentration close to the membrane, as can be noticed comparing the H_2 mole fraction maps on a module cross section at fixed axial position ($z = 0.2\ m$) for the three PM configurations shown in Figure 3.48. It is apparent that the regions of low H_2 concentration close to the membrane surfaces practically disappear with the adoption of three baffles.

Overall, the introduction of baffles resulted to be very beneficial for the fluid dynamics and the separation performances of the module. The baffles permit the division of the module into compartments, avoiding recirculation in the whole module. It is important to observe that recirculation is still present, but only inside each compartment.

Table 3.4: Performance of the three different pilot modules

configuration	permeate flow $[kg\ s^{-1}]$	increase of permeate flow [%]	H_2 retentate mole fraction [%]	decrease of H_2 retentate mole fraction [%]
PM0	$1.00{\cdot}10^{-4}$	-	14.13	-
PM2	$1.39{\cdot}10^{-4}$	38.19	12.62	10.64
PM3	$1.47{\cdot}10^{-4}$	46.40	12.18	13.80

The average H_2 mole fraction on three cylindrical surfaces very close to the

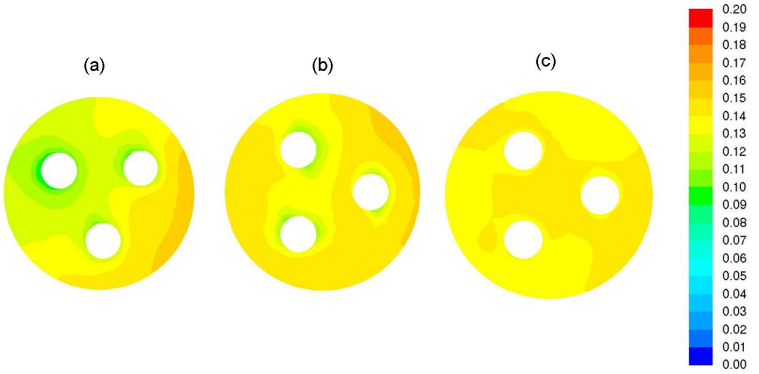

Figure 3.48: H_2 mole fraction at $z = 0.20\ m$; (a) PM0, (b) PM2, (c) PM3

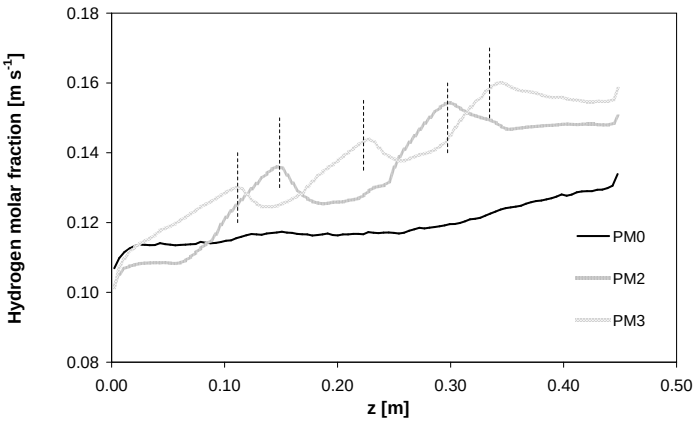

Figure 3.49: H_2 mole fraction along the module axis obtained as the average on three cylindrical surfaces very close to the membranes (dashed lines represent baffles positions)

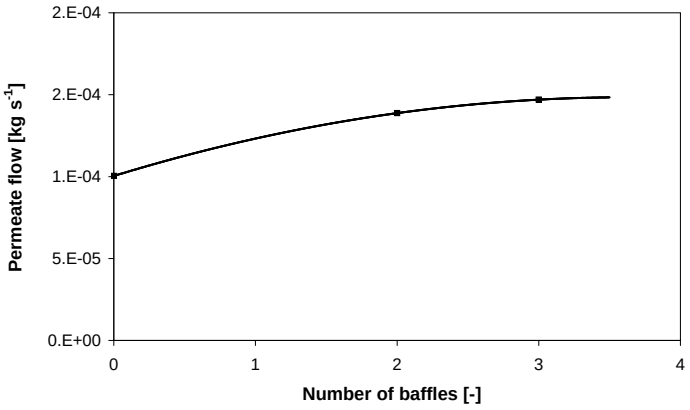

Figure 3.50: Flow rate for the three PM configurations (no baffles, two baffles and three baffles)

membranes along the axis of the module for the three different configurations is compared in Figure 3.49. As a difference from the baffled modules, in the unbaffled PM0 the H_2 mole fraction is almost constant along the membrane and it is always lower than the value predicted with the other two configurations. The presence of these special shaped baffles produce a global and local effect on the module behaviour: first of all, the mean H_2 mole fraction on the membrane becomes higher, due to the absence of recirculation in the whole volume; moreover, baffles permit local removal of inert gases from the surface of the membrane, producing an increase in the local H_2 mole fraction. In this way, when the module is provided with baffles, the driving force is higher in all the module, and it is even higher in the regions near the baffles.

Obviously, an higher driving force produces an increase in permeate flow, as it is possible to observe in Figure 3.50, where permeate flows for the three configurations are reported. Permeate flow rates, H_2 mole fractions in the retentate stream, and the percentage increases of the permeate flow in PM2 and PM3 with respect to PM0 are reported in Table 3.4.

3.12 Conclusions

In the present work, a CFD approach for the simulation of membrane modules for gas mixture separation has been developed and it was demonstrated to be a reliable tool for the description and the prediction of the behaviour of membrane modules

for gas mixtures separation at different operating conditions.

Different membranes have been investigated and since the selected membranes are totally or partially constituted by a porous structure that is extremely complicated to predict theoretically, the diffusion coefficients of all the membranes have been evaluated from experimental data. These characteristics have been fixed on the basis of pure H_2 permeation experimental data and afterwards the effect of several different operating conditions was accurately predicted without introducing any adjustable parameter. The different membranes have been modelled with a simple approach considering four different transport mechanisms: molecular diffusion (self and mutual), Knudsen diffusion, Poiseuille flow and Sieverts' law.

With this approach, the effect of different temperatures, feed flow rates, pressures and compositions of the feed stream in binary and ternary mixtures on the separation performances has been accurately predicted.

The accuracy of the CFD simulations for investigating the non ideal flow of membrane separation modules was also tested by comparison of the simulation results with original PIV data obtained in a laboratory scale module.

The definite decrease of H_2 permeate flux, when mixtures are fed instead of pure gases, has been successfully modelled, confirming the ability of the CFD approach to investigate the flow dynamics of the module and its influence on the membrane separation efficiency. For instance, in the case of LM2 module the results show that the membrane resistance to the mass transfer is low and the convective resistance is not negligible. Actually, the present approach permits to investigate the presence of the gas resistance, which is typically accounted for by lumped parameter models; it provides information on the local concentration distribution of each component in gas mixtures, that are particularly important both in reacting systems and in systems containing permeation inhibitors. The simulations considering the case of membrane inhibition, that have been accounted for in the model by implementing a literature equation, have allowed to estimate the relative importance of concentration polarization and inhibition.

The good agreement between the experimental and the predicted data suggests that CFD can be considered as an useful and reliable tool for designing new modules or optimising existing ones. In practice, a CFD simulation allows to identify the importance of the different mass transfer resistances, thus guiding on the module geometry selection. While the impact of the flow field features in the separation performances was assessed by comparing the separation of a binary mixture of H_2 and N_2 obtained in two modules of different design and equal operating conditions.

Overall, the analysis of the results suggests that the lower is the resistance to the mass transfer across the membrane, the more important are the convective resistances and the improvements of the predictions obtained with the CFD approach with respect to simple models based on lumped parameters. In any case, for industrial applications the CFD simulations may be useful also to identify the

influence of some internals on the mass transfer performances, to correctly estimate the driving force across the membrane taking into account the polarisation effect, and to identify the effect of different working conditions as the adoption of sweep streams.

Actually, the selected modelling method that allows determination of the gas mixture separation in a fully predictive way, requiring only the permeability characteristics of the selected membrane, was adopted to investigate the optimization of a pilot module separation performances by the introduction of novel baffles. The baffles permit production of compartments inside the module, avoiding complete mixing and increasing the driving force. They also permit to reduce the polarization effect, since their particular shape forces the gas species to flow close to the membranes, pushing away all the inert species from the membrane surfaces. It was found that the improvement of the separation performances of the module increases with the number of baffles, although it is expected that an optimum geometric configuration can be identified above which a further baffle addition does not lead to any separation advantage. The number of baffles in the final module design must be selected depending on the required separation efficiency: as a guideline, starting from a single baffle configuration look at the flow and concentration fields and add a new baffle at the location where the washing effect of the first baffle vanishes.

3.13 Notation

A:	area, m^2
$C_\mu, C_{\epsilon 1}, C_{\epsilon 2}$:	constant, dimensionless
F:	interphase exchange term, $kgm^{-2}s^{-2}$
$\boldsymbol{g}$:	gravity acceleration, ms^2
l:	length scale, m
p:	pressure, Pa
$\overline{p}$:	mean pressure, Pa
$\boldsymbol{r}$:	displacement vector, m
$S_\kappa, S_\epsilon, S_\Phi$:	source term
t:	time, s
T:	time interval, s
$\boldsymbol{u}$:	velocity vector, $m\ s^{-1}$
$\overline{\boldsymbol{u}}$:	mean velocity vector, $m\ s^1$
$\boldsymbol{u}'$:	velocity fluctuation, $m\ s^{-1}$
V:	volume, m^3

Greek letters

α:	under-relaxation factor, dimensionless
δ_{ij}:	Kronecker delta, dimensionless
ϵ:	turbulent dissipation, m^2s^{-3}
ϕ:	volumetric fraction, dimensionless
φ:	under-relaxation factor, dimensionless
Φ:	generic flow quantity
$\overline{\Phi}$:	generic mean flow quantity
Φ':	generic fluctuating flow quantity
Γ:	diffusivity, m^2s^{-1}
κ:	turbulent kinetic energy, m^2s^{-2}
μ:	dynamic viscosity, $Pa\ s$
μ_t:	turbulent viscosity, $Pa\ s$
θ:	velocity scale, ms^{-1}
ρ:	density, $kg\ m^3$
$\sigma_\epsilon, \sigma_\kappa$:	constant, dimensionless
$\boldsymbol{\tau}$:	viscous stress tensor, $kg\ m^{-1}s^{-2}$
$\boldsymbol{\tau}^{(t)}$:	turbulent stress tensor, $kg\ m^{-1}s^{-2}$

Subscript

c:	continuous phase
d_i, d_k:	dispersed phase

e, w, s, n, b, t:	face centres value in direction est, west, south, north, bottom and top
E, W, S, N, B, T, P:	values at the centres of the corresponding cell volume
f:	face value
i, j:	axis direction
k:	generic phase

Superscript

$corr$:	corrective value
n:	generic time step
k:	generic iteration

3.14 Bibliography

Abdel-jawad, M.M., Gopalakrishnan, S., Duke, M.C., MacRossan, M.N., Smith Schneider, P., Diniz Da Costa, J.C., Flowfields on feed and permeate sides of tubular molecular sieving silica (MSS) membranes (2007) J. Membr. Sci., 299, pp. 229-235;

Ahmad, A.L., Lau, K.K., Abu Bakar, M.Z., Abd. Shukor, S.R., Integrated CFD simulation of concentration polarization in narrow membrane channel (2005) Comput. Chem. Eng., 29, pp. 2087-2095;

Barba, D., Giacobbe, F., De Cesaris, A., Farace, A., Iaquaniello, G., Pipino, A., Membrane reforming in converting natural gas to hydrogen (part one) (2008) Int. J. Hydrogen Energy, 33, pp. 3700-3709;

Barbieri, G., Scura, F., Lentini, F., De Luca, G., Orioli, E., A novel model equation for the permeation of hydrogen in mixture with carbon monoxide through Pd-Ag membranes (2008) Sep. Purif. Technol., 61, pp. 217-224;

Basile, A., Gallucci, F., Paturzo, L., Hydrogen production from methanol by oxidative steam reforming carried out in a membrane reactor (2005) Catal. Today, 104, pp. 251-269;

Basile, A., Paturzo, L., Lagana, F., The partial oxidation of methane to syngas in a palladium membrane reactor: Simulation and experimental studies (2001) Catal. Today, 67, pp. 65-75;

Bird, R.B., Stewart, W.E., Lightfoot, E.N., (1960) Transport Phenomena, , Wiley, New York;

Cao, Z., Wiley, D.E., Fane, A.G., CFD simulations of net-type turbulence promoters in a narrow channel (2001) J. Membr. Sci., 185, pp. 157-176;

Caravella, A., Barbieri, G., Drioli, E., Modelling and simulation of hydrogen permeation through supported Pd-alloy membranes with a multicomponent approach (2008) Chem. Eng. Sci., 63, pp. 2149-2160;

Catalano, J., Giacinti Baschetti, M., Sarti, G.C., Influence of the gas phase resistance on hydrogen flux through thin palladium-silver membranes (2009) J. Membr. Sci., 339, pp. 57-65;

Chasanis, P., Kenig, E.Y., Hessel, V., Schmitt, S., Modelling and simulation of a membrane microreactor using computational fluid dynamics (2008) Comput. Aided Chem. Eng., 25, pp. 751-756;

Chen, H., Cao, C., Xu, L., Xiao, T., Jiang, G., Experimental velocity measurements and effect of flow maldistribution on predicted permeator performances (1998) J. Membr. Sci., 139, pp. 259-268;

De Falco, M., Barba, D., Cosenza, S., Iaquaniello, G., Marrelli, L., Reformer and membrane modules plant powered by a nuclear reactor or by a solar heated molten salts: Assessment of the design variables and production cost evaluation (2008) Int. J. Hydrogen Energy, 33, pp. 5326-5334;

De Pinho, M.N., Semio, V., Geraldes, V., Integrated modeling of transport processes in fluid/nanofiltration membrane systems (2002) J. Membr. Sci., 206, pp. 189-200;

Gallucci, F., De Falco, M., Tosti, S., Marrelli, L., Basile, A., The effect of hydrogen flux pressure and temperature dependence factors on the membrane reactor performances (2007) Int. J. Hydrogen Energy, 32, pp. 4052-4058;

Ghidossi, R., Veyret, D., Moulin, P., Computational fluid dynamics applied to membranes: state of art and opportunities (2006) Chem. Eng. Process., 45, pp. 437-457;

Goto, S., Assabumrungrat, S., Tagawa, T., Praserthdam, P., The effect of direction of hydrogen permeation on the rate through a composite palladium membrane (2000) J. Membr. Sci., 175, pp. 19-24;

Guo, Y., Lu, G., Wang, Y., Wang, R., Preparation and characterization of Pd/Ag/ ceramic composite membrane and application to enhancement of catalytic dehydrogenation of isobutene (2003) Sep. Purif. Technol., 32, pp. 271-279;

He, G., Mi, Y., Yue, P.L., Chen, G., Theoretical study on concentration polarization in gas separation membrane processes (1999) J. Membr. Sci., 153, pp. 243-258;

Holleck, G.L., Diffusion and solubility of hydrogen in palladium and palladium-silver alloys (1970) J. Phys. Chem., 74, pp. 503-511;

Iaquaniello, G., Giacobbe, F., Morico, B., Cosenza, S., Farace, A., Membrane reforming in converting natural gas to hydrogen: Production costs, Part II (2008) Int. J. Hydrogen Energy, 33, pp. 6595-6601;

Karger, J., Ruthven, D.M., (1992) Diffusion in zeolites and other microporous solids, , Wiley, New York pp. 88-104;

Kawachale, N., Kumar, A., Kirpalani, D.M., Numerical investigation of hydrocarbon enrichment of gas mixtures by permeation through polymeric membranes (2008) Chem. Eng. Technol., 1, pp. 58-65;

Kawachale, N., Kumar, A., Kirpalani, D.M., A flow distribution study of laboratory scale membrane gas separation cells (2009) J. Membr. Sci., 332, pp. 81-88;

Koukou, M.K., Papayannakos, N., Markatos, N.C., Bracht, M., Van Veen, H.M., Roskam, A., Performance of ceramic membranes at elevated pressure and temperatures: effect of non-ideal flow conditions in a pilot scale membrane separator (1999) J. Membr. Sci., 155, pp. 241-259;

Koukou, M.K., Papayannakos, N., Markatos, N.C., Dispersion Effects on Membrane Reactor Performance (1996) AIChE J., 42, pp. 2607-2615;

Koukou, M.K., Papayannakos, N., Markatos, N.C., On the important of non-ideal flow effects in the operation of industrial-scale adiabatic membrane reactors (2001) Chem. Eng. J., 83, pp. 95-105

Launder, B.E., Spalding, D.B., The numerical computation of turbulent (1974) Comput. Methods Appl. Mech. Eng., 3, pp. 269-289;

Li, A., Lim, C.J., Grace, J.R., Staged-separation membrane reactor for steam methane reforming (2008) Chem. Eng. J., 138, pp. 452-459;

Lin, Y.-M., Rei, M.-H., Separation of hydrogen from the gas mixture out of catalytic reformer by using supported palladium membrane (2001) Sep. Purif. Technol., 25, pp. 87-95;

Liu, S.X., Peng, M., Vane, L.M., CFD modeling of pervaporative mass transfer in the boundary layer (2004) Chem. Eng. Sci., 59, pp. 5853-5857;

Liu, S.X., Peng, M., Vane, L.M., CFD simulation of effect of baffle on mass transfer in a slit-type pervaporation module (2005) J. Membr. Sci., 265, pp. 124-136;

Mori, N., Nakamura, T., Noda, K., Sakai, O., Takahashi, A., Sakai, H., Iwamoto, Y., Hattori, T., Reactor configuration and concentration polarization in methane steam reforming by a membrane reactor with a highly hydrogen-permeable membrane (2007) Ind. Eng. Chem. Res. , 46, pp. 1952-1958;

Nair, B.K., Harold, M.P., Experiments and modelling of transport in composite Pd and Pd/Ag coated alumina hollow fibers (2008) J. Membr. Sci., 311, pp. 53-67;

Peters, T.A., Stange, M., Klette, H., Bredesen, R., High pressure performance of thin Pd-23% Ag/stainless steel composite membranes in water gas shift gas mixture; influence of dilution, mass transfer and surface effects on the hydrogen flux (2008) J. Membr. Sci., 316, pp. 119-127;

Pizzi, D., Worth, R., Giacinti Baschetti, M., Sarti, G.C., Noda, K., Hydrogen permeability of 2,5 m palladium-silver membranes deposited on ceramic supports (2008) J. Membr. Sci., 325, pp. 446-774;

Pollard, W.G., Present, R.D., On gaseous self-diffusion in long capillary tubes (1948) Phys. Rev., 73, pp. 762-774;

Rothenberger, K.S., Cugini, A.V., Howard, B.H., Killmeyer, R.P., Ciocco, M.V., Morreale, B.D., Enick, R.M., Ma, Y.H., High pressure hydrogen permeance of porous stainless steel coated with a thin palladium film via electroless plating (2004) J. Membr. Sci., 244, pp. 55-68;

Sieverts, A., Die aufnahme von gasen durch metalle (1929) Z. Metallkd., 21, pp. 37-46;

Takaba, H., Nakao, S., Computational fluid dynamics study on concentration polarization in H_2/CO separation membranes (2005) J. Membr. Sci., 249, pp. 83-88;

Taylor, R., Krishna, R., (1993) Multicomponent Mass Transfer, Wiley, New York;

Vandoormal, J.P., Raithby, G.D., Enhancements of the SIMPLE method for predicting incompressible fluid flows (1984) Numer. Heat Transfer, 7, pp. 147-163;

Ward, T.L., Dao, T., Model of Hydrogen permeation behaviour in palladium membranes (1999) J. Membr. Sci., 153, pp. 211-231;

Westerweel, J., Fundamentals of digital particle image velocimetry (1997) Meas. Sci. Technol., 8, pp. 1379-1392;

Wiley, D.E., Fletcher, D.F., Techniques for computational fluid dynamics modelling of flow in membrane channels (2003) J. Membr. Sci., 211, pp. 127-137;

Yoon, S.Y., Ross, J.W., Mench, M.M., Sharp, K.V., Gas-phase particle image velocimetry (PIV) for application to the design of fuel cell reactant flow channels (2006) J. Power Sources, 160, pp. 1017-1025;

Zhang, J., Liu, D., He, M., Xu, H., Li, W., Experimental and simulation studies on concentration polarization in H_2 enrichment by highly permeable and selective Pd membranes (2006) J. Membr. Sci., 274, pp. 83-91;

Chapter 4

Stirred Vessels

4.1 Abstract

This part of the work deals with CFD modelling of stirred vessels. The homogenisation process and the dispersion of two immiscible liquids are specifically analysed.

The analysis is started verifying the effect of numerical issues on the RANS-based predictions of single phase stirred tanks. In particular, the effect of grid size and discretization schemes on global parameters, mean velocity and turbulent dissipation rate is considered. Although contradictory results have been reported so far on the capability of RANS methods in fluid mixing, the most widely accepted conclusion is that adequate values are generally to be expected for the predicted mean flow quantities, while much less confidence must be put on the calculated turbulent quantities and related phenomena. The results obtained in this work partially revise this last statement and demonstrate that firm conclusions on the limits of RANS simulations can be drawn only after careful verification of numerical uncertainties.

The homogenisation process of a scalar tracer is then investigated and simulation results are compared to original passive tracer homogenisation curves determined with planar laser induced fluorescence.

The capability of a CFD approach based on the solution of Reynolds averaged Navier-Stokes equations is also investigated at the purpose of describing the fluid dynamic characteristics of the dispersion of organics in water. At this purpose an Eulerian-Eulerian description of the two phases is adopted and the capability in catching the dispersion features is critically assessed.

The simulation results are discussed and compared to literature and original experimental data.

4.2 Outline of the chapter

The present chapter is organised as follow:

- in paragraph 4.3 the research objectives of the analysis and modelling of stirred tanks are described;
- while in paragraph 4.4 a brief introduction to stirred tank behaviour, design and simulation strategies is presented;
- then the modelling issues on the determination of the turbulent flow field in stirred tanks are highlighted in paragraph 4.5;
- in paragraph 4.6 the liquid-liquid dispersion is introduced;
- in paragraph 4.7 the experimental set-up for the PLIF measurements and for the determination of the dispersion conditions are presented;
- in paragraph 4.8 the computational approach for the flow field determination, the transport of the scalar and the liquid-liquid dispersion is described;
- then all the results are presented in paragraph 4.9;
- finally in paragraph 4.10 the main conclusions are summarised.

4.3 Research objectives

One of the objectives of this research work is to perform a systematic, much stringent evaluation of the numerical errors with respect to the modelling approximations, focusing the attention on the contribution of numerical issues to the accuracy of the most widespread RANS simulation method for stirred vessels, namely that based on the $\kappa - \epsilon$ model closure and standard wall functions for the treatment of the near wall region. Attention is focused on local and global dissipation rate, local turbulent kinetic energy, impeller pumping capacity, and the homogenisation process of a scalar tracer. For validation, comparison of the computed results with original experimental data will be provided for the last aspect, while literature data for the other parameters were available. The analysis of the results helps to explain most of the discrepancies obtained by different authors.

Moreover, the purpose of the work on liquid-liquid dispersion is to contribute to the study of the fluid dynamics of immiscible liquid-liquid systems. For this reason, the onset of liquid dispersion, N_{id}, and the just dispersed condition, N_{jd}, will be investigated by examining the drawdown of portions of the upper liquid by the stirrer both experimentally and numerically to ascertain whether a RANS-based CFD simulation method is capable to describe these threshold conditions.

4.4 Generalities on stirred vessels

Fluid mixing

Fluid mixing is a unit operation tipically required at several stages of the process industry that leads from raw materials to the final product.

Mixing is required for different purposes (i.e. blending of fluids, solid suspension and dispersion, heat exchange promotion, gas-liquid and liquid-liquid dispersion) and is usually achieved through the employment of stirred vessels, which are widely used in the chemical, pharmaceutical, mineral, biotechnological industries for the mixing of single and multiphase systems. Stirred tanks are usually constituted of a cylindrical vessel equipped with many different types of impellers, depending on the specific required purpose. Obviously, the fluid flow behaviour of a stirred tank depends from fluid characteristics, vessel and impeller geometry.

Stirred tank impellers usually have to contemporary fulfil different duties. For instance in the catalytic hydrogenation of a liquid, the impeller must suspend the solid catalytic particles, disperse the gaseous hydrogen in the liquid phase and promote heat exchange. As a result, the choice of the proper impeller is very important for a successful design.

Impellers can be divided in radial and axial impellers, depending if they generate mainly a radial flow or a flow parallel to the impeller axis. Axial impellers promote high fluid recirculation rate, while radial impellers allow a better turbulence promotion. For this reason radial impellers are preferred for shear rate controlled processes (e.g. liquid-liquid and gas-liquid dispersion), while axial impellers are more appropriate when convective flows are most important, i.e. for bulk motion controlled processes (e.g. liquid blending).

In order to design the apparatus, it is necessary to establish not only the stirrer type and vessel geometry, but also the size of the impeller, its position with respect to the vessel bottom, and the right agitation speed.

The vessel type most commonly employed is a simple cylindrical tank with a flat or dished bottom agitated by single or multiple impellers. Vertical baffles are often required as, if not provided, a strong tangential velocity arises, which gives rise to a deep vortex on the liquid free surface. Moreover, the relative velocities between the impeller and the fluid are small and the impeller is able to induce only little radial and axial flows, resulting in a very low mixing efficiency.

Global parameters

The power requirement of a stirred tank is given through a dimensionless quantity, called power number, defined as:

$$N_P = \frac{P}{\rho N^3 D^5} \tag{4.1}$$

where P is the power supplied to the impeller, ρ is the fluid density, N the agitation speed and D the impeller diameter.

Another dimensionless parameter, the pumping number, is defined in order to highlight the amount of recirculation of fluid through the impeller:

$$N_Q = \frac{Q}{ND^3} \tag{4.2}$$

where Q is the impeller pumped flow rate.

For baffled tanks, both the power number and the pumping number are functions of the Reynolds number, which only in the case of stirred vessels is defined as:

$$Re = \frac{\rho N D^2}{\mu} \tag{4.3}$$

where μ is the fluid viscosity.

Moreover for fully turbulent fluid flow, i.e. when $Re > 10^4$, both N_P and N_Q are practically constant, and their values are fixed for impeller type and geometry.

Impeller simulation strategies

In order to model baffled stirred vessels, proper impeller simulation strategies have to be used, since a computational grid which can remain attached to both the moving impeller and the stationary baffles is required.

There are various strategies that have been devised to overcome this problem. The simplest of these strategies is called Impeller Boundary Conditions Method and consists in imposing suitable velocity and turbulence quantities on the surface swept by impeller blades. However this strategy requires the availability of experimental data for the system under investigation.

Other procedures are more complex but fully predictive. In particular, two different fully predictive procedures can be adopted for the simulations: a time-dependent approach often called *Sliding Mesh* or *Sliding Grid* (Murthy et al., 1994) and a steady approach namely *Multiple Reference Frame* or *Multiple frame of reference* (Luo et al., 1994). In both of these methods the whole tank is subdivided in two non-overlapping computational domains (see Figure 4.1).

The *sliding mesh* approach With the *sliding mesh* approach the external domain is stationary, while the inner domain rotates with the impeller. In this way both the stationary baffles and the rotating impeller can be conveniently incorporated in the grids of the relevant domains. The two regions are implicitly coupled at the interface separating the two blocks via a sliding mesh algorithm, which takes

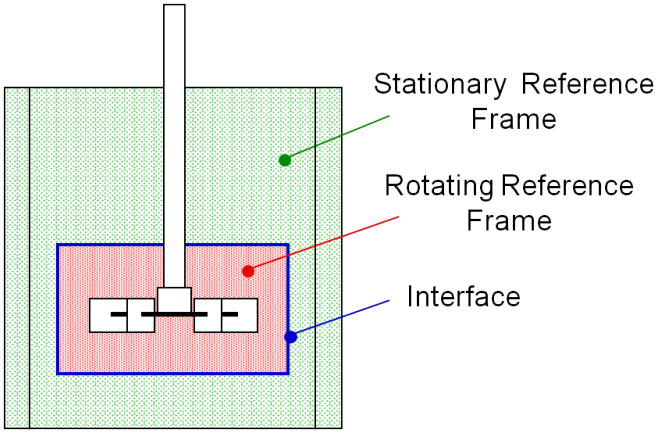

Figure 4.1: Sketch of the subdivision of the computational domain in stationary and rotating frames

into account the relative motion between the two sub-domains and performs the necessary interpolations.

The sliding mesh simulations are conducted as a transient event, and the computation is stopped when converged periodic solution has been attained.

The *multiple reference frame* approach The *multiple reference frame* is a steady-state approximation, since each of the inner and outer simulations is conducted under steady-state assumptions in its own reference frame.

Actually, in the stationary zone, the stationary equations are used, while in the zones containing the moving components equations written for a rotating reference frame are solved. At the interfaces between cell zones, a local reference frame transformation is performed to enable flow variables in one zone to be used to calculate fluxes at the boundary of the adjacent zone.

This approach does not account for the relative motion of a moving zone with respect to adjacent zones (which may be moving or stationary) and the grid remains fixed for the computation. This is analogous to freezing the motion of the moving part in a specific position and observing the instantaneous flow field with the rotor in that position.

It is clearly an approximation, but it can provide a reasonable model of the flow for all that applications in which rotor-stator interaction is relatively weak.

4.5 CFD and stirred vessels

Computational fluid dynamics has emerged as powerful, effective means to predict the local fluid dynamics and associated phenomena such as mass transfer and chemical reactions in the tanks in both fundamental and applied research (Van den Akker, 2006). These tools can alleviate the need for extensive experiments provided that the validity of their response is checked for a broad variety of situations. Three main approaches have been followed in the development of CFD for the modelling of turbulence, namely the Reynolds averaged Navier-Stokes (RANS) simulation, the large eddy simulation (LES) and the direct numerical simulation (DNS).

The RANS approach is the most widespread simulation method used in the field of turbulent fluid mixing since the early 1990s, when fully predictive methods have been developed for tackling the problem of moving boundaries (e.g. Luo et al., 1993, 1994; Brucato et al., 1994; Murthy et al., 1994). In spite of some important intrinsic limitations due to time averaging of the flow variables in a statistical context, to the removal of turbulence unsteadiness and of the inherently transient nature of the flow, in several cases the RANS simulation has so far provided realistic predictions with affordable computer memory and computational times. The results obtained with this method are strictly dependent on the turbulent model adopted for addressing the closure problem (introduced by the six unknown components of the Reynolds stress tensor).

In order to overcome these limitations, growing attention has been devoted in the recent past to the development and application to stirred vessels of LES methods, after the pioneering works of Eggels (1996), Revstedt et al. (1998) and Derksen and Van den Akker (1999) at the expense of more significant computational requirements. Generally, improvement is expected with LES for flows in which the rate-controlling processes occur in the resolved large scales, while the appeal of LES is weak in the case of rate-controlling processes occurring at the smallest scales (Pope, 2004). DNS techniques have been faced only in a very few cases (Bartels et al., 2001; Verzicco et al., 2004) due to huge computer power requirements.

Overall, the comparison of LES and RANS simulations has led to state the superiority of the former, although different specific conclusions have been drawn by various investigators in terms of local turbulent quantities (e.g. Hartmann et al., 2004; Yeoh et al., 2004a,b; Delafosse et al., 2008; Murthy and Joshi, 2008; Guha et al., 2008); diverging conclusions have been obtained for the global turbulent energy dissipation rate with the RANS simulations relative to the same LES cases (namely: under-predicted by 45% by Yeoh et al. (2004a), under-predicted by 20-25% by Murthy and Joshi (2008), well predicted by Delafosse et al. (2008)). Similarly, contradictory results have been obtained for the homogenisation process of a passive tracer and the related mixing time calculated with the RANS method: with respect

to the measured process time, the simulated one has been overestimated by up to two or three times in some cases (Jaworski et al., 2000; Bujalski et al., 2002), of about 30% in other cases (Ochieng et al., 2008), whereas good fit has been documented only after adjusting a simulation parameter (Montante and Magelli, 2004). Generally, more satisfactory agreement between calculated and measured data has always been reported for LES simulations (Yeoh et al., 2005; Hartman et al., 2006; Jahoda et al, 2007). The spread of result quality obtained with RANS simulations is much more important than for LES, ranging from poor predictions of turbulent features in single phase systems to successful simulations of turbulent stirred tanks even in two-phase (e.g. Ghadge et al., 2005; Jahoda et al., 2009; Khopkar and Tanguy, 2008) and three-phase (Murthy et al., 2007) systems.

It is worth observing that these prediction uncertainties and errors are usually attributed to modelling deficiencies only, although the contribution of numerical errors is not to be disregarded in the verification/validation process (Coleman and Stern, 1997). Recently, Laborde-Boutet et al. (2009) have discussed the importance of numerical schemes in the RANS simulation of bubble column flows and reported that artificial match of experimental data can be obtained for numerical reasons. The numerical dependency of RANS results as applied to the simulation of stirred vessels has been systematically faced only in a few cases (Wechsler et al., 1999; Aubin et al., 2004; Deglon and Meyer, 2006). It is finally worth stressing that hardware constraints have not allowed a full investigation of the numerical uncertainties due to the spatial discretization of the computational domain, thus leading to grid independence studies being limited to rather coarse grids or small grid refinements (e.g. Ng et al., 1998; Brucato et al., 1998a; Montante et al., 2001; Ranade et al., 2002; Aubin et al., 2004).

4.6 Fluid dynamics behaviour of liquid-liquid dispersion

The fluid dynamic behaviour of immiscible liquid-liquid dispersion is rather complex due to the occurrence and interaction of several phenomena, namely drop break-up and coalescence, mean flow pattern and turbulence, drop suspension, interfacial area and drop size distribution (DSD), possible phase inversion, the influence of system composition as well as of small amounts of impurities, etc. (Leng and Calabrese, 2004), which make this operation one of the most difficult to deal with.

The fluid dynamic interaction between the two phases plays a significant role in determining the features of the dispersion, but it is far from being fully understood. Average properties over the whole vessel are usually considered for system descrip-

tion and for scale-up. The following main aspects have been studied: minimum agitation speed for complete liquid-liquid dispersion (Armenante and Huang, 1992); correlation of mean drop size and DSD to energy dissipation rate and mixer geometric parameters (Calabrese et al., 1986) as well as to energy dissipation rate and flow in the vessel (Zhu and Kresta, 1998a, 1998b); the influence of various impellers on the dispersion features (Zhu and Kresta, 1998a, 1998b; Pacek et al., 1999; Giapos et al., 2005); description of the interaction between the liquid phases in terms of intermittent turbulence (Baldyga and Bourne, 1993; Baldyga and Podgrska, 1998; Baldyga et al., 2001). Modelling of these systems has also been attempted in recent years by fully-predictive, two-phase CFD techniques coupled with break-up and coalescence models (Alopaeus et al., 2002; Maa et al., 2007; Derksen and van den Akker, 2007), which parallels the analogous efforts to study gas-liquid systems: in spite of the high complexity of the system and the significant simplifications thereof, the first results are encouraging (van den Akker, 2006).

One key issue for broadening the understanding of these systems and allowing CFD code validation is to get more detailed information about their flow structure, namely mean flow and turbulence of both phases and their interaction. This scope is experimentally very difficult as intrusive techniques may disturb the flow, while the dispersed phase limits the optical accessibility of the modern, non-intrusive measuring techniques (LDV and PIV). Recently, Svensson and Rasmuson (2006) studied the effect of the dispersed phase (up to 10 vol. %) on the flow structure of the continuous one by means of the PIV technique combined with refractive index matching; though, no information has been provided about the behaviour of the dispersed phase.

4.7 The experimental set-up

The experimental investigation and all the simulations refer to a stirred tank of standard geometry consisting of a flat bottomed cylindrical vessel (diameter, $T = 23.2\ cm$) equipped with four equally spaced baffles fixed along the internal surface of the vessel, closed with a lid and filled up to a tank height, H, equal to T (see Figure 4.2). Agitation was provided by a six-blade standard Rushton turbine (diameter $D = T/3$, disk and blade thickness equal to 2.0 mm), reported in Figure 4.3, placed at a distance $T/2$ from the vessel base. For avoiding optical distortion, the vessel was contained in a square tank filled with demineralised water, that was the continuous liquid phase adopted in all the experiments.

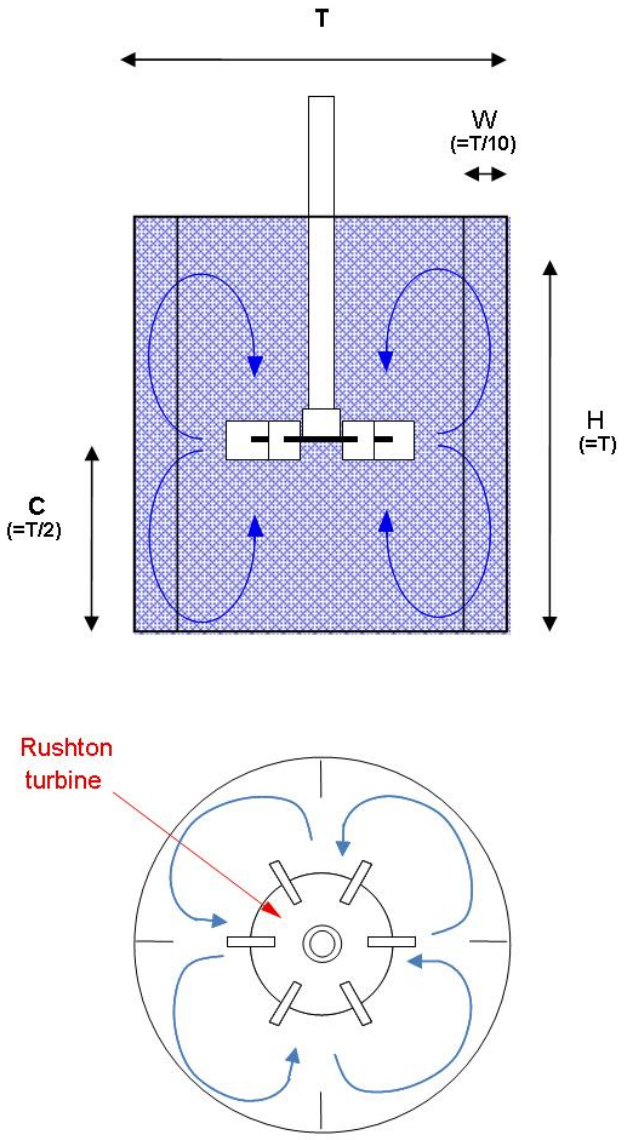

Figure 4.2: Geometry of the stirred tank

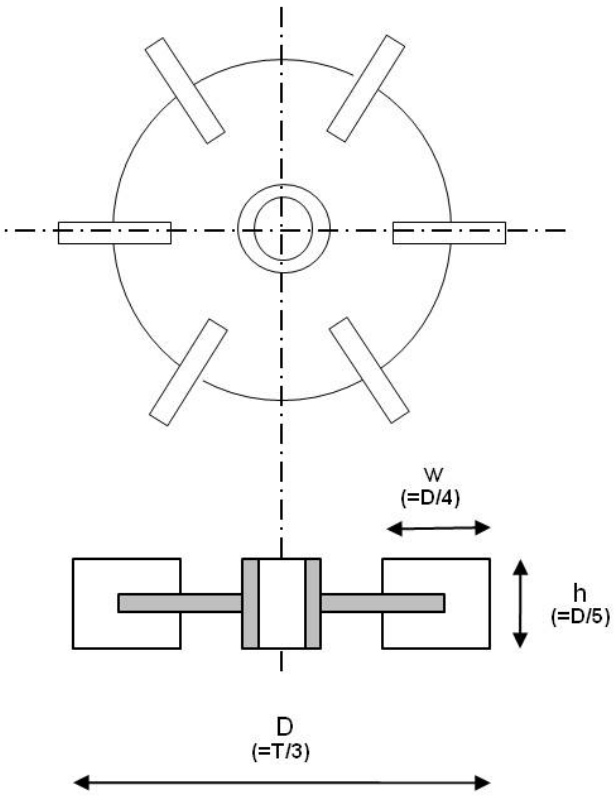

Figure 4.3: Geometry of the Rushton turbine

4.7.1 PLIF measurements

The transient homogenisation process of a passive scalar tracer in water has been studied for impeller rotational speed, N, fixed at 300 rpm, corresponding to a rotational Reynolds number of $2.9{\cdot}10^4$. PLIF experiments were conducted, in which a small amount of a tracer (Rhodamine-6G) solution was injected rapidly (less than 0.5 s) into the liquid batch by means of a small tube positioned axially beneath the turbine, at a distance $T/4$ from the tank bottom. A laser sheet source (Nd:YAG pulsed laser, emitting wavelength of 532 nm, energy of 120 mJ per pulse, pulse width of 10 ns) and a digital camera perpendicular to the laser sheet (1340×1024 pixels CCD) were employed for vessel illumination and detection of the tracer dispersion process, respectively, in the agitated liquid. A high pass wavelength filter was fitted to the camera to allow the passage of the fluorescent light, while blocking scattered and reflected laser light.

Each image was analysed following the method proposed originally by Houcine et al. (1996), which is well suited for the analysis of images obtained with diverging laser sheets and has been frequently adopted for the PLIF characterisation of stirred tanks (e.g. Hall et al., 2004; Fall et al., 2001). The method is based on the measurement of the pixel grey levels of the image background both before the injection of the fluorescent tracer, $\overline{NG}_{bg}(x,y)$, and after the achievement of perfect mixing conditions, $\overline{NG}_{pm}(x,y)$, as well as the instantaneous, local value, $NG(x,y,t)$. The instantaneous, local concentration is finally obtained from these values as:

$$c\left(x,y,t\right) = \frac{NG\left(x,y,t\right) - \overline{NG}_{bg}\left(x,y\right)}{\overline{NG}_{pm}\left(x,y\right) - \overline{NG}_{bg}\left(x,y\right)} c_{pm} \tag{4.4}$$

where $\overline{NG}_{bg}(x,y)$ and $\overline{NG}_{pm}(x,y)$ are obtained by averaging 10 images and c_{pm} is the homogeneous tracer concentration corresponding to perfect mixing conditions.

Clearly, the approach is meaningful only if the emitted fluorescent intensity is linearly dependent on tracer concentration. In our system with Rhodamine 6G as a tracer, this has been checked to be true up to 80 ppm tracer concentration.

Each image was analysed to determine the spatial degree of homogeneity by means of the coefficient of variation:

$$CoV(t) = \sqrt{\frac{\sum_{x=1}^{X}\sum_{y=1}^{Y}\left(\frac{c(x,y,t)}{\bar{c}(t)} - 1\right)^2}{N_{pix} - 1}} \tag{4.5}$$

where N_{pix} is the overall number of pixels, X and Y are the number of pixels along the radial and axial direction, respectively, c is the pixel level concentration and $\bar{c}$ is the average pixel level concentration.

In order to obtain a reliable estimate of the time series of the coefficient of variation up to the condition of almost full homogenization, which corresponds to a CoV value of about 0.01, 4 ml of aqueous tracer solution (204 $mg\ l^{-1}$ of Rhodamine 6G in water), were injected into the stirred tank. For these conditions, the initial Rhodamine 6G concentration was out of the linearity range of the calibration curve and, therefore, the relevant images had to be discarded, thus loosing information during the first second after injection. Also, for CoV equal to about 0.01, the maximum value of the local concentration is about 0.4 $mg\ l^{-1}$ and the measurement accuracy decreases.

4.7.2 Determination of the dispersion conditions

The immiscible liquid-liquid dispersion was investigated using diesel as the dispersed phase. It was chosen for N_{id} and N_{jd} determinations, since it is opaque and clearly distinguishable from water and it is lighter than water (826 $kg\ m^{-3}$ density). For the determination of N_{id} and N_{jd}, the vessel was always entirely filled with the two liquids with 19 vol % of oil and it was closed on top for avoiding air entrainment.

The dispersion regimes as a function of the impeller speed, ranging from 2 to 5 s^{-1} and corresponding to a variation of the rotational Reynolds number of the water phase between $1.24 \cdot 10^4$ and $3.10 \cdot 10^4$, were determined from the analysis of the captured images. Before starting the acquisition, for each agitation condition the two liquids were mixed for about one hour. The appearance of droplets below the impeller was considered as the indicator of N_{id} achievement. On the other hand, N_{jd} has been identified by the visual observation of the lid of the tank and it was considered as achieved when the oil layer almost completely disappeared.

4.8 The computational approach

4.8.1 Numerical determination of the single phase turbulent flow field

The Reynolds-averaged continuity and momentum equations for an incompressible fluid in turbulent motion were solved in a Cartesian coordinate system and, for the turbulence closure, the standard $\kappa - \epsilon$ model (Launder and Spalding, 1974) was selected. The numerical solution of these equations was achieved by a finite-volume method in the realm of the general purpose CFD code FLUENT 6.3. The SIMPLEC algorithm was adopted to couple the continuity and the momentum equations. Different discretization schemes for the convective terms of the momentum and the κ and ϵ equations were adopted, namely first order upwind, second

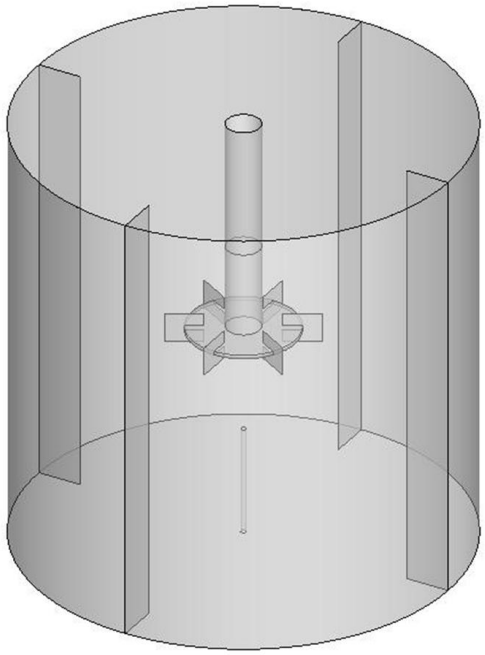

Figure 4.4: Geometry of the stirred tank adopted in the simulations

order upwind and the higher order QUICK schemes (Bakker and Marshall, 2004). The computational domain represented faithfully the geometry of the stirred vessel adopted for the PLIF experiments, the only difference being the description of baffles and blades, which were assumed as zero-thickness walls (see Figure 4.4). As a result, the effect of blade thickness, which together with disk thickness is known to affect the mean and turbulent variables (Rutherford et al., 1996), is not specifically investigated. It is worth observing that in order to make effective the inclusion of any of the vessel internals thickness, an adequate grid refinement is required. Therefore, if included, the effect of blade thickness could have been accounted for only with the finer grids.

Four computational grids were considered, whose features are summarised in Table 4.1 and shown in Figure 4.5. In any case, hexahedral cells over the full 2π three dimensional domain were adopted: indeed, the domain azimuthal limitation over π due to geometrical periodicity is not appropriate for modelling the scalar transport. Wall boundary conditions with conventional linear-logarithmic wall-functions (Launder and Spalding, 1974) were adopted on the solid walls. The consistency of the y^+ values with the log-walls functions was verified for all the grids. The value of y^+ in the first cell was located within the logarithmic law

Table 4.1: Different grids

	n_z	n_r	n_q
Grid 1: $\approx 2.7 \cdot 10^5$ cells	63	36	96
Grid 2: $\approx 1.9 \cdot 10^6$ cells	126	72	192
Grid 3: $\approx 3.6 \cdot 10^6$ cells	156	89	240
Grid 4: $\approx 6.6 \cdot 10^6$ cells	189	108	288

layer in almost all cases ($30 < y^+ < 300$); a linear law was used when $y^+ < 11.225$. The steady-state Multiple Reference Frame (MRF) approach was selected for tackling the steady and the rotating walls in a fully-predictive way, since in previous works the difference between the ensemble averaged flow field calculated with the stationary and the time dependent approaches was found to be negligible (Aubin et al., 2004; Montante et al., 2001) and in this work the angle-resolved features of the flow are not specifically investigated. The vertical extension of the rotating reference frame was limited to the impeller vicinity to about 2.5 times the blade height in order to avoid problems of artificial swirl (Oshinowo et al., 2000), while the diameter was placed midway between the blade tip and the baffle inner edge.

The solution convergence was carefully checked by monitoring the residuals of all the variables and the values of the torque and of the tangential velocity component. Generally, at the end of calculations most of the variables residuals were as low as 10^{-7}. It is worth noting that estimates for grid convergence uncertainty (Coleman and Stern, 1997) were also effected for the four grids considered in this work, based either on the grid convergence metric, e, or on the grid convergence index, GCI (Roache, 1994).

4.8.2 Numerical determination of scalar transport

The dynamics of tracer homogenization were calculated by solving the Reynolds-averaged time-dependent convection-diffusion equation of the scalar:

$$\frac{\partial \rho\phi}{\partial t} + \nabla \rho \bar{\boldsymbol{u}} \phi = \nabla \left(\rho D_m \nabla \phi - \frac{\mu_t}{\sigma_t} \nabla \phi \right) \tag{4.6}$$

where ϕ is the tracer volumetric fraction, $\bar{\boldsymbol{u}}$ is the mean velocity vector, ρ is the fluid density, D_m is the molecular diffusivity, μ_t is the turbulent viscosity and σ_t is the turbulent Schmidt number. The molecular diffusivity was always assumed to be equal to $10^9 m^2 s^{-1}$, though it was not a critical value in any case, since the contribution of molecular diffusion to the overall tracer dispersion process is

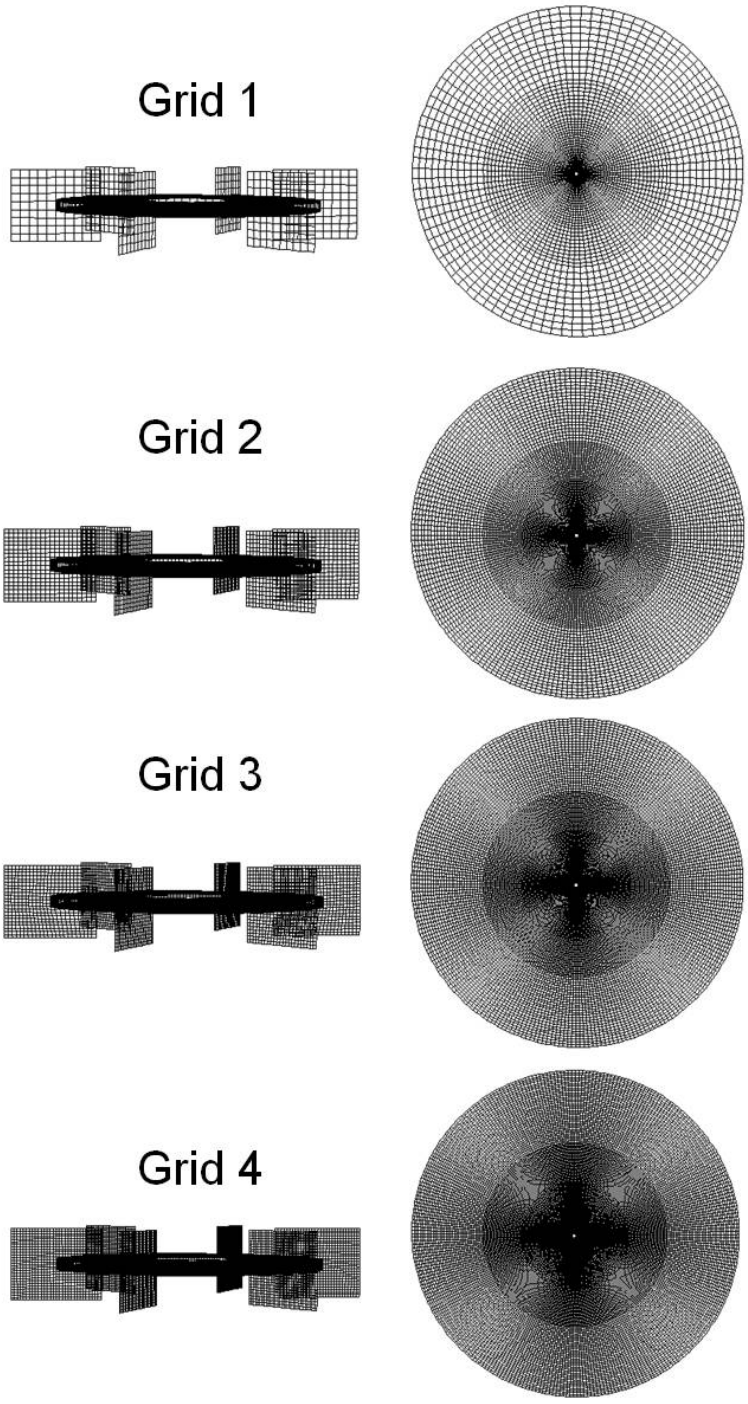

Figure 4.5: Features of different grids

expected to be small with respect to the turbulent diffusion; this last was modelled by the ratio between the turbulent viscosity and the turbulent Schmidt number (Montante et al., 2005). For this last parameter, the commonly suggested value of 0.7 (e.g. Hartmann et al., 2006) has been adopted. In all cases, the second order upwind discretization scheme was adopted for the solution of Equation 4.6. The standard time step for the solution was equal to $2.08 \cdot 10^{-3}$ s, that covers the azimuthal extent of one cell in the coarser grid (i.e. $2\pi/96$), and is much smaller than the experimental data acquisition rate ($8\ Hz$). The standard settings for the time step size and the number of internal iterations for each time step were selected after a sensitivity study, in which the independency of the results with respect to simulation runs with smaller time steps and a bigger number of internal iterations was found. Two different sets of initial and boundary conditions were adopted: one matching as closely as possible the tracer injection of the PLIF experiments, which was not instantaneous, and another simplified and less computationally demanding with respect to the former. In the most realistic and computationally intensive case, a velocity inlet boundary condition was imposed at the upper surface of the injection tube and the tracer injection time interval was explicitly simulated. In the simplified approach, the tracer was released instantaneously in the region between the injection tube and the impeller, i.e. the volume fraction of the tracer was fixed to 1 in a number of computational cells whose total volume was equal to the tracer experimental volume. In order to assess whether the selection of the tracer initial position affected the results in any critical way, five different initial conditions for the tracer instantaneous injection were considered, namely:

- a reference initial condition (case 1), corresponding to a cylinder of tracer moving at a velocity equal to 0.057 $m\ s^{-1}$ (that is equal to the experimental injection velocity);

- a shorter and thicker shape cylinder, obtained by halving the height of the injected volume (case 2);

- an eccentric position, obtained by placing the cylinder base centre 0.0028 m apart from the center of the tube inlet surface (case 3);

- a cylinder of the same shape as case 3 and doubled velocity (case 4);

- an eccentric cylinder, with a base centre placed 0.0035 m apart from the centre of the tube inlet surface, and a radial and tangential velocity component of 0.028 $m\ s^{-1}$ (case 5).

In any case, the tube was explicitly included in the computational domain and the injection was assumed to take place after the attainment of a fully developed

velocity field, as in the experiments, which means adopting the solution of the flow equations obtained previously as the initial condition for the solution of the scalar transport equation.

4.8.3 Numerical determination of liquid-liquid dispersion

The CFD simulation approach for the determination of liquid-liquid dispersion was similar to that adopted for the simulation of solid-liquid and gas-liquid systems (Montante and Magelli, 2005; Montante et al., 2007).

It was based on the solution of the Reynolds averaged Navier-Stokes (RANS) equations for each phase in a Eulerian framework under steady-state assumptions. The Reynolds averaged continuity and momentum equations for the phase c read as:

$$\nabla \cdot (\phi_c \bar{\boldsymbol{u}}_c) = 0 \tag{4.7}$$

$$\nabla \cdot (\phi_c \rho_c \bar{\boldsymbol{u}}_c \bar{\boldsymbol{u}}_c) = \nabla \cdot \tau_c - \phi_c \nabla p_c + \phi_c \rho_c \boldsymbol{g} + \boldsymbol{M}_{dc} + \boldsymbol{M}^t_{dc} \tag{4.8}$$

The inter-phase momentum transfer term, $\boldsymbol{M}_{dc}$, and the term accounting for the turbulent fluctuations of the volumetric fraction $\boldsymbol{M}^t_{dc}$ are modelled as:

$$\boldsymbol{M}_{dc} = \frac{3}{4} \frac{\phi_d \rho_c}{d_d} C_D |\bar{\boldsymbol{u}}_d - \bar{\boldsymbol{u}}_c| \left(\bar{\boldsymbol{u}}_d - \bar{\boldsymbol{u}}_c\right) \tag{4.9}$$

$$\boldsymbol{M}^t_{dc} = \frac{3}{4} \frac{\phi_d \rho_c}{d_d} C_D |\bar{\boldsymbol{u}}_d - \bar{\boldsymbol{u}}_c| \left(\frac{\Gamma_d}{\sigma_t \phi_d} \nabla \phi_d - \frac{\Gamma_c}{\sigma_t \phi_c} \nabla \phi_c \right) \tag{4.10}$$

where the subscripts d and c refer to the dispersed and the continuous phase respectively, Γ is the turbulent diffusivity and σ_t is the turbulent Schmidt number, for which the standard value of 0.70 was always adopted.

For determining the droplet drag coefficient, C_D, the droplets were assumed to behave as rigid non-interacting spheres of fixed size rising in a stagnant liquid. For each impeller speed, the simulations were repeated considering the diameter of 50, 200 and 1000 μm for the purpose of assessing the effect of this parameter on the results. The C_D correction due to turbulence (Brucato et al. 1998b; Pinelli et al., 2001) was not effected in this case because of the small drop size and the relatively low agitation level. The mathematical closure of the problem was obtained by the standard $\kappa - \epsilon$ turbulence model. The general purpose CFD code Fluent 6.3 was adopted in this case too.

A liquid-liquid flat interface was assumed as the initial condition. The computational domain was divided into a structured hexahedral grid of about $5 \cdot 10^5$ cells over π. The Multiple Reference Frame method was selected for treating the interaction of the stationary baffles with the rotating impeller in a stationary fashion. The usually adopted numerical settings for RANS-based simulations of baffled stirred tanks were selected (e.g. Montante and Magelli, 2005; Montante et al., 2007).

The simulations were run at different impeller speeds varying from 2 s^{-1} up to 4.67 s^{-1} with a step size of 0.67 s^{-1}.

4.9 Results

4.9.1 Turbulent flow field and global parameters

The verification of the numerical uncertainties on the flow field predictions was started with the analysis of the predicted power number, N_p, that is one of the most important and representative global dimensionless parameters for a stirred vessel.

For all the simulations, the power consumption has been calculated from the predicted variables in two ways: in one case, it was estimated from the overall torque derived from the pressure and tangential stress distribution on the steady walls (baffles and tank) or on the moving surfaces (impeller and shaft); in the other case, the integral of the turbulent dissipation rate over the entire vessel volume was adopted. In the past, it has often been observed that the two methods lead to different N_p values, the second ($N_{p,\epsilon}$, based on ϵ) being usually lower than the former ($N_{p,torque}$, based on torque) due to underestimation of the turbulent quantities associated to the RANS $\kappa - \epsilon$ method (Middleton and Smith, 2004, Sommerfeld and Decker, 2004).

The results obtained with the three discretization schemes and Grid 1, that is the coarser grid, are summarised in Figure 4.6, where a dotted line giving the value computed following Rutherford et al. (1996) is also shown. The results confirm the wide discrepancy of N_p evaluation with the two methods, at least for the selected domain discretization: a realistic power number, close to the classic value of 5, results only when considering the power consumption obtained from the torque transferred from the moving walls to the fluid or from the fluid to the steady walls, while a much lower value is obtained with the second method. As expected, the first order discretization scheme is significantly less accurate than the other two: it leads to more severe underestimation of the volumetric ϵ integral and it does not even allow to reach an appropriate balance between the torque on steady and moving walls. The other two discretization schemes provide the same results. Therefore, in the subsequent simulations the second order upwind discretization for

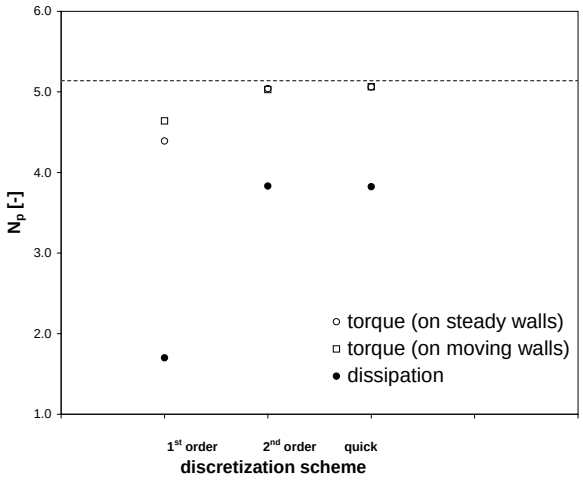

Figure 4.6: Effect of discretization scheme on the power number prediction. Grid 1. Open circle: $N_{p,torque}$ on steady walls; Open square: $N_{p,torque}$ on moving walls; Solid circle: $N_{p,\epsilon}$

the convective terms has been adopted, since apparently the higher order QUICK scheme does not improve further the results. The importance of an appropriate choice of the discretization scheme in the RANS simulations of turbulent stirred tanks was already observed by Aubin et al. (2004) and by Deglon and Meyer (2006).

The effect of the spatial discretization on the predicted power consumption is apparent from the results obtained with the four grids shown in Figure 4.7. As can be observed, the two N_p values are closer, the finer the grid is, thus showing that the severe $N_{p,\epsilon}$ underestimation almost disappears if the computational grid density is more than doubled with respect to the usually adopted resolution. Although the above quoted discrepancy between the two N_p values does not vanish entirely even with the finest grid, the effect of the spatial discretization on this important variable cannot be disregarded when evaluating the $\kappa - \epsilon$ model prediction capability.

A quantitative evaluation of the predicted N_p is better given by the relative difference between $N_{p,\epsilon}$ and $N_{p,torque}$ normalized with $N_{p,torque}$ shown in Figure 4.8. Appropriate selection of the discretization scheme and of spatial resolution leads to a decrease in the difference between the two calculated N_p values from very high values down to 7%. So far, similar reasonable RANS predictions of the global energy dissipation rate have been reported only by Delafosse at al. (2008), who adopted the same domain discretization for the RANS and LES simulations of a stirred tank of standard geometry.

As expected, the flow number, N_Q, which is another fundamental global di-

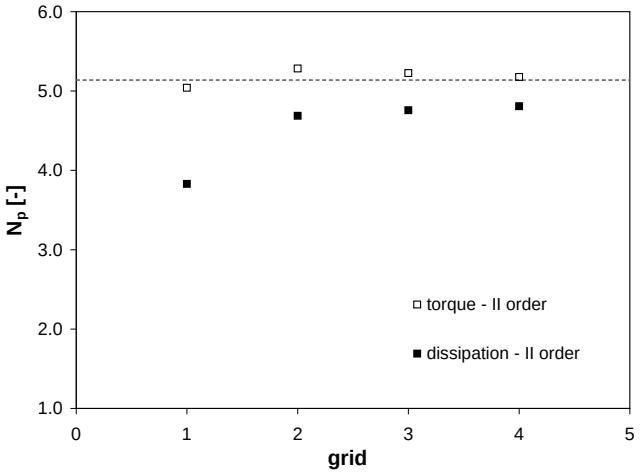

Figure 4.7: Effect of grid size on the power number prediction (2^{nd} order upwind). Open symbols: $N_{p,torque}$ on steady walls; solid symbols: $N_{p,\epsilon}$

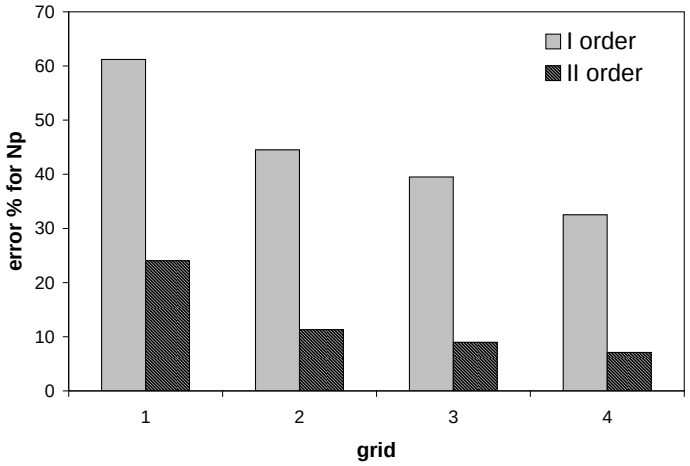

Figure 4.8: Discrepancy of N_p values obtained from torque and from the integral of ϵ for different grid densities and two discretization schemes. Error %=($N_{p,torque}$-$N_{p,\epsilon}$)/$N_{p,torque} \cdot 100$

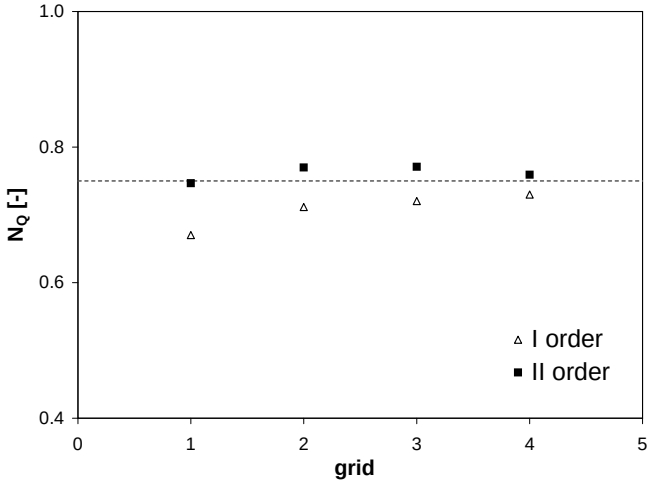

Figure 4.9: Effect of grid density and discretization scheme on the flow number predictions

mensionless parameter of fluid mixing, does not exhibit such a severe dependency on the same numerical issues: the simulation results shown in Figure 4.9 clearly suggest not to disregard the discretization order; however, if grid dependency were judged only on the basis of N_Q, the conclusion would be a weak dependency of the results in all cases. Indeed, a value of about 0.75 is found with the coarser grid and the second order discretization, that coincides with the design recommendation suggested by Revill (1982) (dotted line in Figure 4.9); a very limited variation smaller than the experimental uncertainty (Rutherford et al., 1996) is obtained moving from Grid 1 to Grid 2.

The grid convergence uncertainty parameters e and GCI based on N_Q are very small (of the order of about 3%) when passing from Grid 1 to Grid 2 and they practically vanish for the finer grids. On the contrary, the convergence indexes based on $N_{p,\epsilon}$ on Grid 1 and 2 rise to about 20% while they fall to a few percent for the finer grids. In any case, the values of e/GCI decrease from the coarser to the finer grid thus indicating grid convergence.

The analysis of the predictions based on the local variables fully confirms the above considerations. As an example, axial profiles of selected variables close to the blade tip and midway between two baffles are depicted in Figures 4.10, 4.11 and 4.12. As can be observed in Figure 4.10, grid independence of the radial velocity component is almost achieved with Grid 1 and reasonable agreement with experimental data relevant to a very similar stirred tank (Montante et al., 2006) is obtained provided that a second order discretization scheme is adopted. Instead, a finer grid (namely, Grid 2) is required to get grid independence when comparing

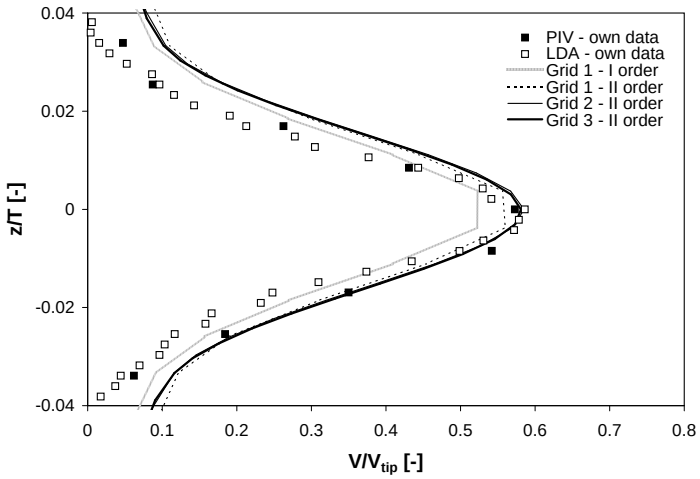

Figure 4.10: Local effect of grid density and discretization scheme on the prediction of radial velocity (axial profiles close to the blade tip: $r/T = 0.174$, $\theta = 45°$ from one baffle)

the κ and ϵ profiles, as shown in Figure 4.11 and 4.12, respectively.

Although experimental κ and ϵ data, obtained with advanced optical techniques for the specific geometrical configuration studied here, are not available, the difference between the κ profiles close to the impeller tip for impeller clearance $C = T/3$ and $C = T/2$ were found to be limited in previous studies (Ranade and Joshi, 1990; Kresta and Wood, 1991): therefore, the data of Wu and Patterson (1989) for κ and of Baldi and Yianneskis (2004) for ϵ both collected at C=T/3, are considered for this preliminary evaluation of the results (Figures 4.11 and 4.12, respectively). Though a strict quantitative estimate is not possible due to the mentioned difference in the geometrical configurations, the figures suggest that an increase in cell number increases the turbulence levels and, therefore, improves the predictions.

A further evaluation of the results is reported in Figures 4.13 and 4.14, where the turbulent intensity profiles of Ranade and Joshi (1989) and the turbulent dissipation rate values of Cutter (1966) are shown together with the corresponding predictions with different grid density. In most cases, significant underestimated κ and ϵ values were found as compared with experimental data in previous works, while in this case grid refinement goes towards an increase of the κ and ϵ levels: therefore, an improvement of the predictions at least on a qualitative ground is observed.

However, it has to be stressed that the intrinsic limitations of the $\kappa - \epsilon$ model prevent the results from strictly adhering to the real turbulent flow behaviour.

It is worth recalling that the requirement of a different level of domain dis-

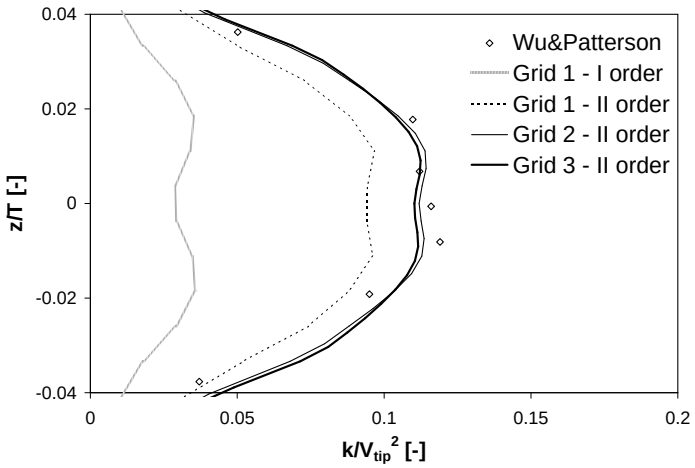

Figure 4.11: Local effect of grid density and discretization scheme on the prediction of dimensionless turbulent kinetic energy (axial profiles close to the blade tip: $r/T = 0.185$, $\theta = 45°$ from one baffle)

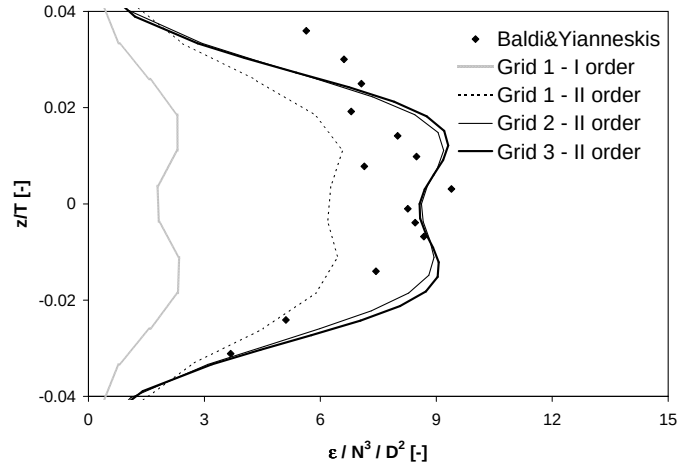

Figure 4.12: Local effect of grid density and discretization scheme on the prediction of dimensionless turbulent dissipation rate (axial profiles close to the blade tip: $r/T = 0.2$, $\theta = 45°$ from one baffle)

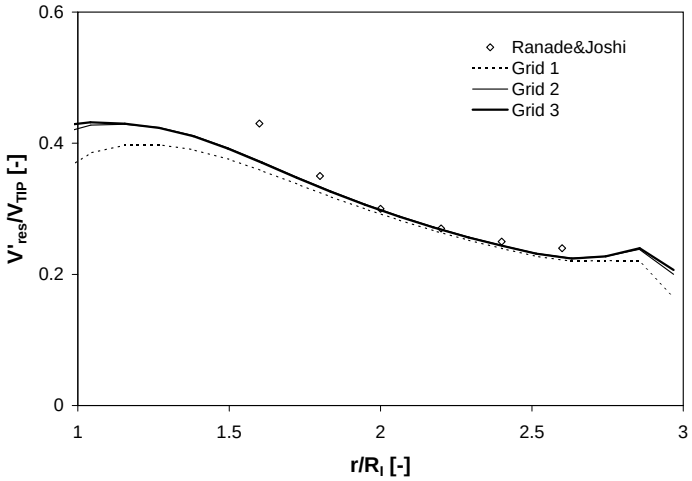

Figure 4.13: Local effect of grid density on the prediction of dimensionless turbulent intensity (radial profiles: $z/T = 1/2$, $\theta = 45°$ from one baffle, 2^{nd} order)

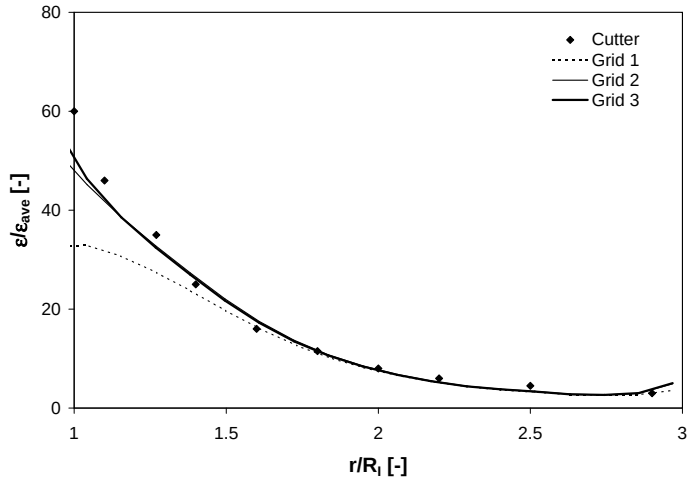

Figure 4.14: Local effect of grid density on the prediction of dimensionless turbulent dissipation rate (radial profiles: $z/T = 1/2$, $\theta = 45°$ from one baffle, 2^{nd} order)

cretization to achieve grid independence for the mean and turbulent variables was already noted by Sommerfeld and Decker (2004) and Deglon and Mayer (2006) and that the importance of grid sensitivity analysis has been pointed out by Wechsler et al. (1999) though these recommendations have rarely been taken into consideration. Indeed, typical computational grids for RANS simulations of stirred vessels are usually at least one order of magnitude coarser than those adopted for LES (van den Akker, 2006), thus encompassing much less than 1 million cells, and grid independence is still often based on very small grid refinements (e.g. Murthy and Joshi, 2008) or on mean variable predictions.

The possible improvement in κ and ϵ prediction due to the reduction of numerical uncertainties is particularly important if considering their impact on almost all the typical processes involving turbulent fluid mixing either in multiphase and/or reactive systems. A simple example is provided by the dynamic tracer homogenization process in a single phase stirred tank: indeed, in the Reynolds averaged approach this is affected by the capability to properly quantify the turbulent viscosity as shown in Equation 4.6. In the following section, the impact of the numerical issues identified above on the turbulent scalar transport as modelled in the RANS framework is discussed.

4.9.2 The dynamics of scalar transport

In the recent past, the ability of RANS methods to accurately follow the time evolution of a scalar concentration either in stirred tanks (e.g. Montante and Magelli, 2004) or in different mixing devices (Luo et al., 2007) was shown to be limited. The quantitative agreement with experimental data could often be obtained by significantly lowering to 0.2-0.1 the conventional value of the turbulent Schmidt number. The effect of σ_t in the RANS prediction of turbulent scalar transport has been identified as a critical feature also in other systems of engineering interest (Tominaga and Stathopoulos, 2007). Overall, the recourse to a turbulent Schmidt number lower than the conventional value of 0.7 may be regarded as an arbitrary way to compensate to the underestimation of turbulent diffusivity resulting from the underestimation of the turbulent viscosity. The dynamic trend of tracer homogenization obtained by the PLIF experiments provides a quantitative, indirect benchmark on the ability to reduce the prediction uncertainties by lowering the numerical approximation.

The dynamic evolution of the experimental coefficient of variation, CoV, and the CFD curves obtained with Grid 1 and Grid 2 are shown in Figure 4.15. Comparison of the results reveals that the increase in turbulent viscosity obtained by increasing the spatial discretization of the computational domain results in reasonable prediction of tracer dispersion dynamics, without the need of altering the conventional value of σ_t. In both calculated cases, the tracer injection time interval

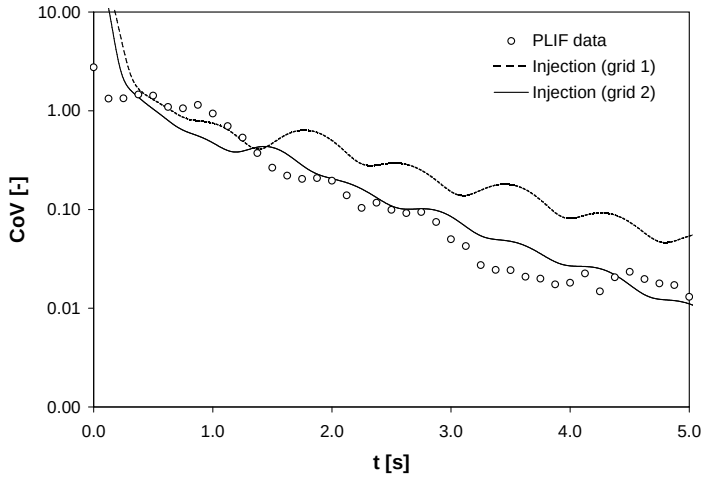

Figure 4.15: Comparison of CoV curves obtained with two different grid densities (2^{nd} order upwind scheme) and the corresponding experimental data obtained by the PLIF technique

was explicitly simulated by imposing a velocity inlet boundary condition on the injection tube uppermost surface for the same time duration of the experimental injection (i.e. 0.375 s). The improvement in the agreement obtained by grid refinement are apparent: the overestimation of the homogenization time and the periodic oscillation associated to the coarser grid are significantly reduced and the finer grid results are much closer to the experimental curve. Since the convective transport is most probably minimally affected by the grid size, as are the mean flow quantities, the underestimation of turbulent diffusion should be the sole reason for the poor quantitative prediction obtained with the coarser grid.

The physical explanation of the oscillatory patterns of the experimental and computed (with the finer grid) curves deals with the fact that the CoV is calculated only on a particular section of the vessel during the transient homogenization of a tracer plume. Both the PLIF and the CFD results present oscillatory patterns because in the measuring plane the plume covers different areas depending on its position, which varies periodically with time.

These results confirm that Reynolds averaging of the convection-diffusion equation is an acceptable approximation and it does not require any parameter adjustment for reliable prediction of the homogenisation time provided that the impact of numerical approximation on the turbulent variable estimation is reduced as much as possible.

Although the computational power required for the simulations with Grid 2 or a finer grid is affordable, the explicit simulation of the injection step with finer grids

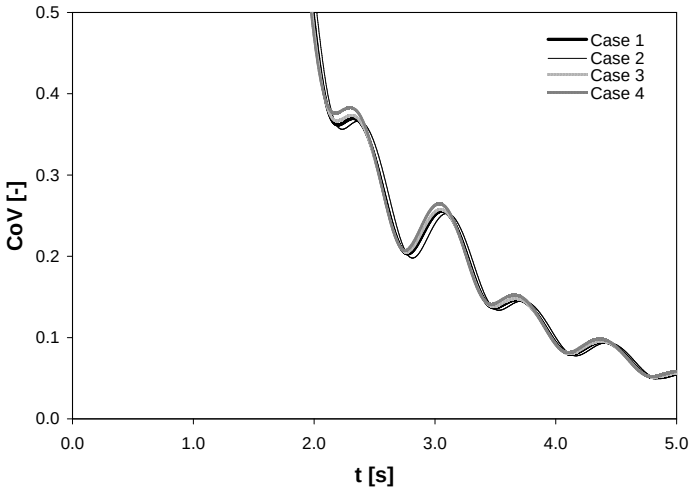

Figure 4.16: Temporal evolution of the coefficient of variation for various initial condition of the rhodamine solution inlet. Grid 1. Case 1: reference shape and velocity; Case 2: shorter and thicker shape, same velocity; Case 3: eccentric position, same shape and velocity; Case 4: same shape, doubled velocity

is very time consuming; therefore, the simpler method of instantaneously releasing the entire tracer quantity in the region above the injection tube was devised and its impact on the simulation accuracy was estimated. Before comparing the results obtained with the simpler and the accurate methods, the influence of the initial condition on the shape and velocity of the tracer was assessed, by using Grid 1 to reduce the computational time. As can be observed in Figure 4.16, the same results were obtained when significantly varying the way of spatial tracer distribution (cases 1, 2, 3) or even doubling the initial velocity vector (case 4). For cases 1 to 4, the initial velocity vector was assumed parallel to the tube axis and the radial and tangential components were assumed to be nil.

In order to assess the effect of this last assumption, a further simulation was run, in which a radial velocity component for the tracer initial condition was imposed (case 5), whose result is compared with the standard settings (case 1) in Figure 4.17: the difference between the two curves is notable, but not dramatic. This last check can be also regarded as a numerical test about the influence of geometrical (sparger position) and operational (injection duration) uncertainties in the experimental set-up on the measured tracer distribution. The curves obtained with the two methods have been finally compared and the results are shown in Figure 4.18: the assumption of instantaneous injection leads to a dynamic curve that is practically identical to that obtained by simulating the injection duration, provided that the time scale of the former is shifted forward by 0.375 s, that is the injection time

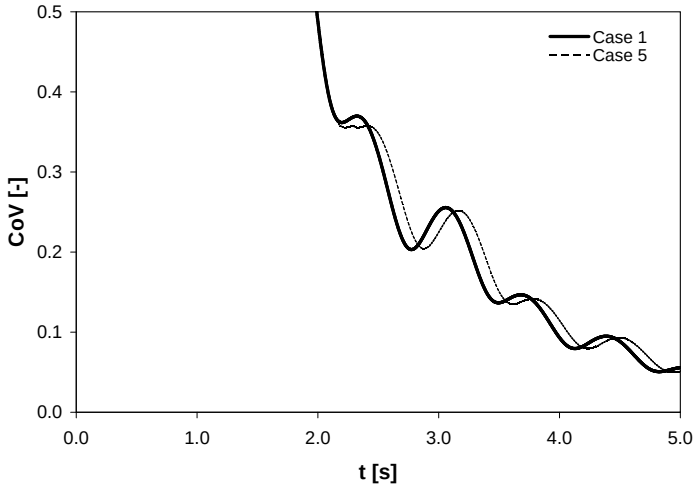

Figure 4.17: Effect of the inlet direction and position on the temporal evolution of the coefficient of variation. Grid 1. Case 1: reference shape and velocity (axial component only); Case 5: eccentric position and inlet velocity with a not-negligible radial component

length.

The qualitative agreement of the measured and predicted tracer concentration can also be observed in Figure 4.19, where the instantaneous PLIF pictures at the beginning of the injection as well as at two subsequent instants and the corresponding calculated tracer concentration maps are shown for case 1. Although the initial, assumed tracer concentration in the simplified simulation does not coincide with the experimental one, the subsequent predicted tracer distribution exhibits the main features of the actual dispersion evolution. As a result, it can be concluded that the simplified injection method coupled with sufficiently fine domain discretization in the realm of RANS based simulations is a satisfactory, fully predictive method for the homogenization dynamics in a stirred tank.

4.9.3 Immiscible liquid-liquid dispersions

Two typical experimental pictures of completely separated phases and initial liquid drawdown conditions in a portion of the vessel are shown in Figure 4.20.

At the lowest of the investigated impeller speeds and up to $N = 3\ s^{-1}$ some large oil droplets are entrained from the interface, but due to the action of the buoyancy force they do not reach the impeller discharge stream and quickly come back to the liquid-liquid interface. Above $N = 3\ s^{-1}$, that may be defined as the N_{id} condition, they reach the impeller and are broken into a number of small

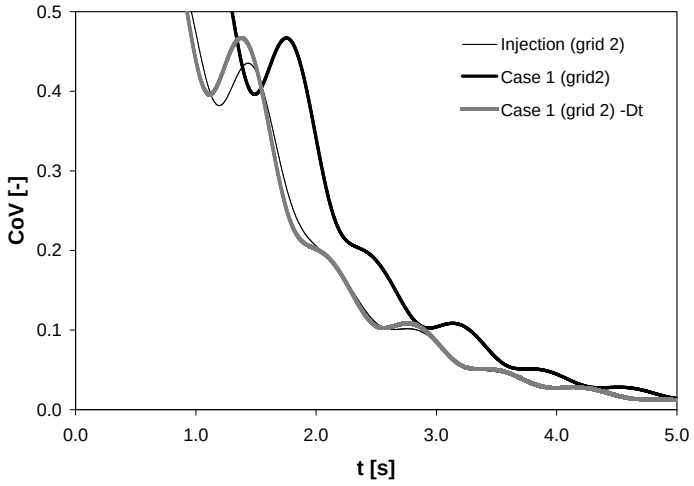

Figure 4.18: Temporal evolution of the coefficient of variation obtained from explicit simulation of the injection step extent or assuming it as instantaneous (fixed tracer concentration and velocity as initial condition). The shadowed curve is equal to the black curve, but the time scale is translated of Dt=0.375 s, that is the injection length

droplets that are dispersed either below and above the impeller.

At a further increase of N, the continuous oil layer thickness decreases until it entirely disappears at N equal to about 4.67 s^{-1}, that may defined as the N_{jd}.

The oil hold-up maps in a vertical plane midway between two baffles at $N = 3.33$ s^{-1} predicted at different droplet diameters, i.e. by assuming different droplet rising velocities, are shown in Figure 4.21. As can be observed, the effect of the droplet size is significant: when d_d is assumed to be equal to 1000 μm, the two liquids remain completely separated, while oil entrainment is predicted for the two lower size cases. For $d_d = 200$ μm, the oil is dispersed only in the upper half of the vessel, while with a further decrease down to 50 μm the droplets are present also below the impeller, thus matching the experimental observation more closely.

The simulation results relevant to the lower impeller speeds show the absence of droplets below the impeller in all cases but for $N = 2.67$ s^{-1} and $d_d = 50$ μm, at which the droplets start to appear though at a very low concentration. The predicted just-dispersed impeller speed is close to the value observed experimentally, $N = 4.67$ s^{-1}, only for $d_d = 50$ μm, while a thick oil layer is still present if the d_d was assumed to be equal to 200 μm, as can be clearly observed in Figure 4.22.

Overall, the simplified computational approach adopted in this work, which cannot account for the small scale phenomena contributing to the oil dispersion, can roughly predict the dispersion conditions. Clearly, the results are strictly dependent

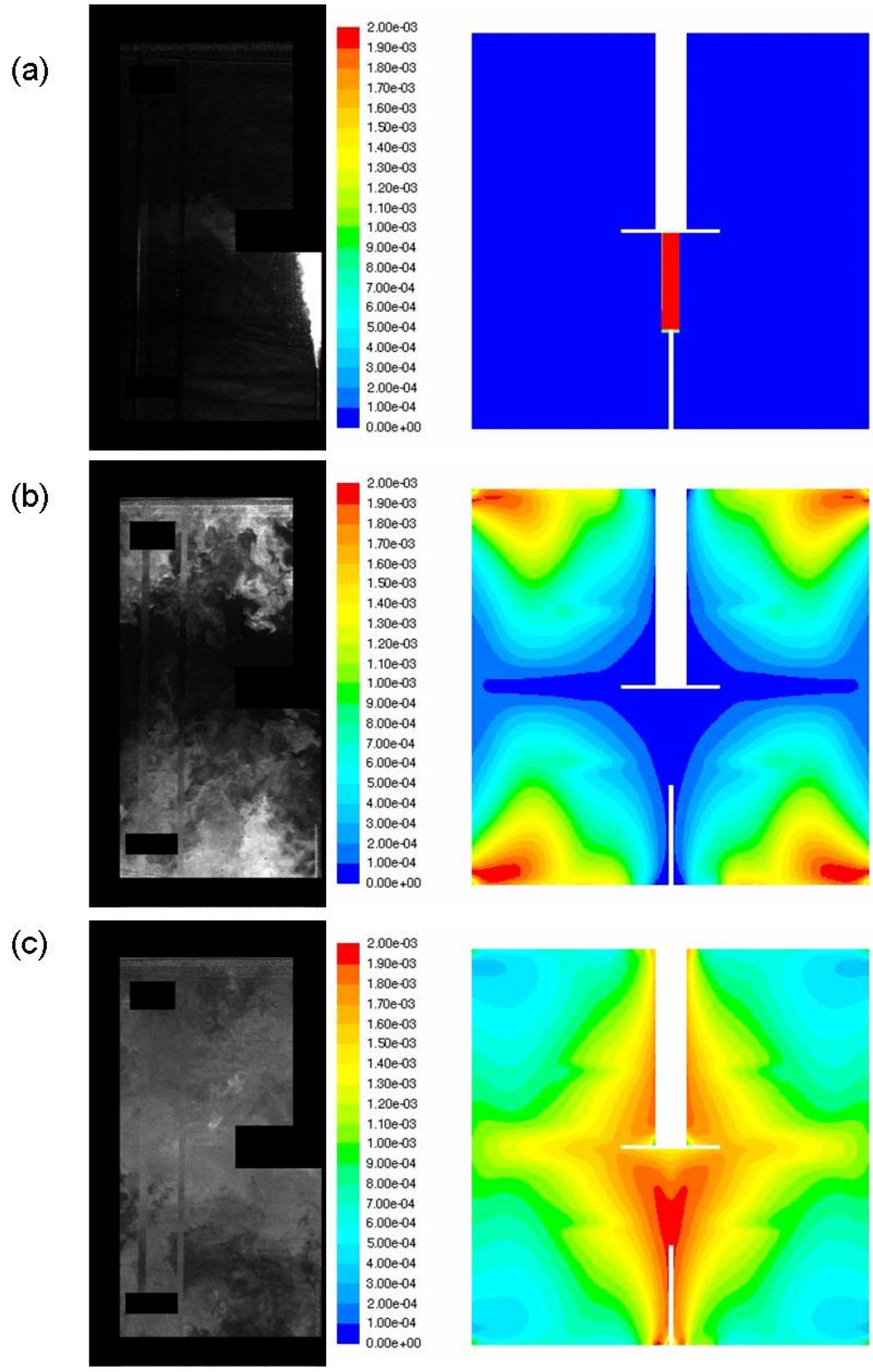

Figure 4.19: Instantaneous experimental (left) and computed (right) maps of tracer concentration: (a) $t = 0.0\ s$; (b) $t = 1.0\ s$; (c) $t = 1.6\ s$. CFD results obtained with Grid 2 and simplified tracer feed (Case 1)

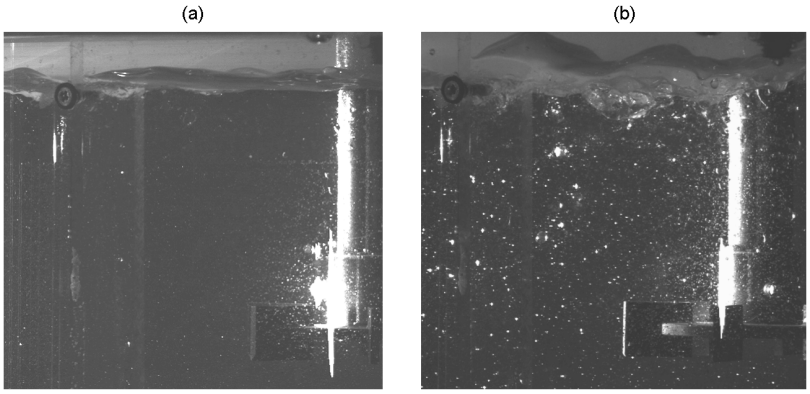

Figure 4.20: Picture of the experimental oil-water system close to the interface. (a) $N = 2.50\ s^{-1}$; (b) $N = 3.17\ s^{-1}$

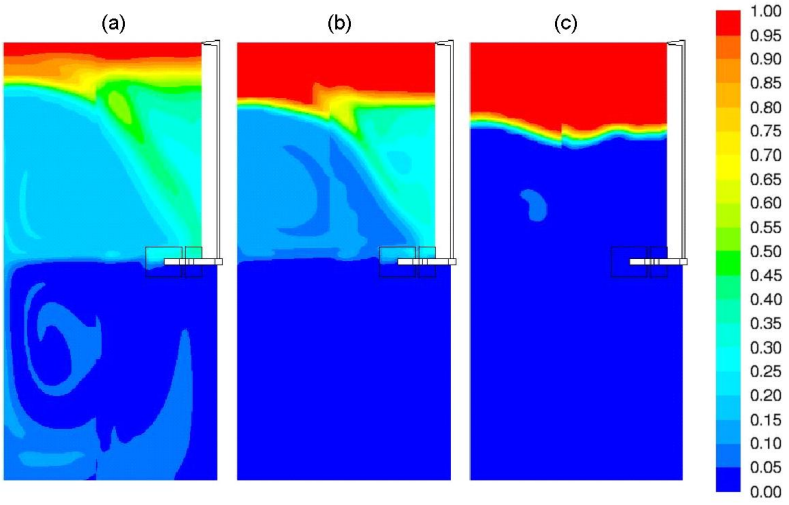

Figure 4.21: Maps of computed oil hold-up at $N = 3.33\ s^{-1}$. (a) $d_d = 50\ \mu m$; (b) $d_d = 200\ \mu m$; (c) $d_d = 1000\ \mu m$

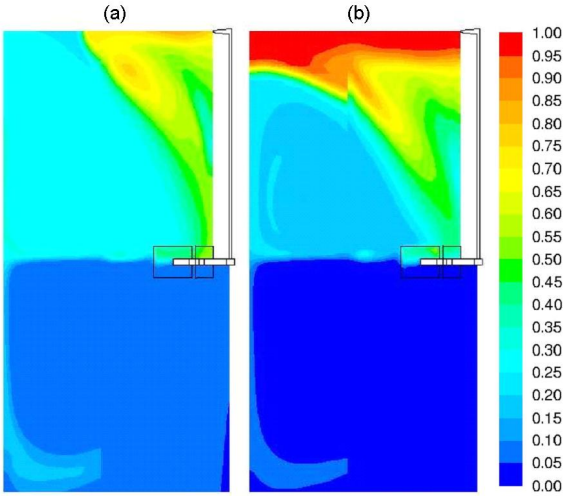

Figure 4.22: Maps of computed oil hold-up at $N = 4.67\ s^{-1}$. (a) $d_d = 50\ \mu m$; (b) $d_d = 200\ \mu m$

on the assumed droplet rising velocity, since the oil is allowed to go down only when its rising velocity is smaller than the local mean velocity in the upper part of the vessel.

4.10 Conclusions

RANS-based CFD simulations of fluid mixing in a single phase stirred tank of standard geometry have been carried out with different levels of spatial discretization of the computational domain and a number of other numerical options. The influence of these aspects on various fluid dynamic parameters as well as on the homogenization of a passive tracer has been investigated and the contribution of numerical errors to well-known limitations of the above-mentioned approach has been highlighted. Generally, the errors in the predictions of the turbulent quantities may be significantly reduced by preliminary verification on the numerical uncertainties, which is now possible thanks to the availability of increased computer power. Remarkably, the difference between the predicted power consumption evaluated from the overall torque on walls and the integral of the turbulent dissipation rate decreases significantly by reducing the spatial discretization size.

The numerical aspects were found to be critical also in the predictions of the tracer homogenization dynamics, that were compared with experimental curves obtained with the PLIF technique. The simulations were found to be accurate

even by adopting a simplified method for modelling the injection step, provided that a grid independent turbulent flow field was calculated before the injection, the major difference with respect to the coarser grid calculation being the increased level of turbulent viscosity.

Overall, much finer computational grids than those usually adopted for RANS simulations are required to reduce the numerical uncertainties to negligible values. Obviously, the inherent limitations of the turbulence closure model associated to the RANS simulations cannot allow a full and detailed description of turbulence fluid mixing in stirred tanks, especially energy dissipation and turbulence anisotropy.

The evolution of the oil dispersion in water has also been investigated. Starting from the condition of separate layers, the impeller speed was increased stepwise and the conditions of just drawdown and just dispersed speeds have been identified experimentally. A simplified RANS approach leads to a fair picture of the dispersion maps only when a suitable mean value of the droplet size that is required for estimating the droplet rise velocity, is selected. The present results suggest that improvements in the prediction capability might be expected by the modelling of the droplet size distribution and the possible effect of turbulence on the droplet rise velocity.

4.11 Notation

c:	concentration, $kg\ m^{-3}$
c_{pm}:	concentration at perfect mixing conditions, $kg\ m^{-3}$
$\overline{c}$:	mean concentration, $kg\ m^{-3}$
C:	impeller clearance, m
C_D:	drag coefficient, dimensionless
CoV:	coefficient of variation, dimensionless
D:	impeller diameter, m
D_m:	molecular diffusivity, $m^2 s^{-1}$
d_d:	droplet diameter, m
$\boldsymbol{g}$:	gravity acceleration, $m\ s^2$
h:	blade height, m
H:	vessel height, m
M_{dc}:	momentum transfer force, N
M_{dc}^t:	turbulent momentum transfer force, N
N:	agitation speed, s^{-1}
N_{id}:	onset of liquid dispersion agitation speed, s^{-1}
N_{jd}:	just dispersed agitation speed, s^{-1}
N_{pix}:	number of pixels
NG:	pixel grey level
$\overline{NG_{bg}}$:	mean background pixel grey level
$\overline{NG_{pm}}$:	pixel grey level at perfect mixing conditions
N_p:	power number, dimensionless
N_Q:	pumping number, dimensionless
p:	pressure, Pa
P:	power supplied to the impeller
Q:	impeller pumped flow rate
Re:	Reynolds number
r:	radial coordinate, m
T:	vessel diameter, m
t:	time, s
$\boldsymbol{u}$:	velocity vector, $m\ s^{-1}$
$\overline{\boldsymbol{u}}$:	mean velocity vector, $m\ s^1$
V:	radial velocity, $m\ s^{-1}$
V_{tip}:	impeller tip speed, $m\ s^{-1}$
w:	blade lenght, m
W:	impeller blade width, m
X:	number of pixel along x
x, y, z:	cartesian coordinate

Y:	number of pixel along y

Greek letters

ϵ:	turbulent dissipation, $m^2 s^{-3}$
ϕ:	volumetric fraction, dimensionless
Γ:	turbulent diffusivity, $m^2 s^{-1}$
κ:	turbulent kinetic energy, $m^2 s^{-2}$
μ:	dynamic viscosity, $Pa\ s$
μ_t:	turbulent viscosity, $Pa\ s$
ρ:	density, $kg\ m^3$
σ_t:	turbulent Schmidt number, dimensionless
τ:	stress tensor, $kg\ m^{-1} s^{-2}$
θ:	tangential coordinate

Subscripts

c:	continuous phase
d_i:	dispersed phase

4.12 Bibliography

Alopaeus, V., Koskinen, J., Keskinen, K.I., Majander, J., Simulation of the population balances for liquid-liquid systems in a nonideal stirred tank. Part 2-parameter fitting and the use of the multiblock model for dense dispersions (2002) Chem. Eng. Sci., 57, pp. 1815-1825;

Armenante, P.M., Huang, Y.-T., Experimental determination of the minimum agitation speed for complete liquid-liquid dispersion in mechanically agitated vessels (1992) Ind. Eng. Chem. Res., 31, pp. 1398-1406;

Aubin, J., Fletcher, D. F., Xuereb, C., Modeling turbulent flow in stirred tanks with CFD: The influence of the modeling approach, turbulence model and numerical scheme (2004) Exp. Therm. Fluid Sci., 28, pp. 431-445;

Bakker, A., Marshall, E. M., (2004) Computational fluid mixing, in: Paul, E.L., Atiemo-Obeng, V.A., Kresta, S.M., (Eds.) Handbook of Industrial Mixing, Wiley-Interscience: Hoboken, New Jersey, pp. 257-344;

Baldi, S., Yianneskis, M., On the quantification of energy dissipation in the impeller stream of a stirred vessel from fluctuating velocity gradient measurements (2004) Chem. Eng. Sci., 59, pp. 2659-2671;

Baldyga, J., Bourne, J.R., Drop breakup and intermittent turbulence (1993) J. Chem. Eng. Japan, 26, pp. 738-741;

Baldyga, J., Bourne, J.R., Pacek, A.W., Amanullah, A., Nienow, A.W., Effects of agitation and scale-up on drop size in turbulent dispersions: allowance for intermittency (2001) Chem. Eng. Sci., 56, pp. 3377-3385;

Baldyga, J., Podgrska, W., Drop break-up in intermittent turbulence: maximum stable and transient sizes of drops (1998) Can. J. Chem. Eng., 76, pp. 456-470;

Bartels, C., Breuer, M., Wechsler, K., Durst, F., Computational fluid dynamics application on parallel-vector computers: computations of stirred vessel flows (2001) Comput. Fluids, 30, pp. 69-97;

Brucato, A., Ciofalo, M., Grisafi, F., Micale, G., Complete numerical simulation of flow fields in baffled stirred vessels: the inner-outer approach (1994) IChemE Symp. Ser. No. 136, pp. 155-162;

Brucato, A., Ciofalo, M., Grisafi, F., Micale, G., Numerical prediction of flow fields in baffled stirred vessels: A comparison of alternative modelling approaches (1998a) Chem. Eng. Sci., 53, pp. 3653-3684;

Brucato, A., Grisafi, F., Montante, G., Particle drag coefficients in turbulent fluids (1998b) Chem. Eng. Sci., 53, pp. 3295-3314;

Bujalski, W., Jaworski, Z., Nienow, A.W., CFD study of homogenisation with dual Rushton turbines Comparison with experimental results. Part II: the Multiple Reference Frame (2002) Chem. Eng. Res. Des., 80, pp. 97-104;

Calabrese, R.V., Wang, C.Y., Bryner, N.P., Drop breakup in turbulent stirred-tank contactors. Part III: Correlations for mean size distribution (1986) AIChE J., 32, pp. 677-680;

Coleman, H. W., Stern, F., Uncertanties and CFD code validation (1997) J. Fluids Eng., 119, pp. 795-803;

Cutter L. A., Flow and turbulence in a stirred tank (1966) AiChE J., 12, pp. 35-45;

Deglon, D. A., Meyer, C. J., CFD modelling of stirred tanks: Numerical considerations (2006) Miner. Eng., 19, pp. 1059-1068;

Delafosse, A., Line, A., Morchain, J., Guiraud, P., LES and URANS simulations of hydrodynamics in mixing tank: Comparison to PIV experiments (2008) Chem. Eng. Res. Des., 86, pp. 1322-1330;

Derksen, J., Van den Akker, H. E. A., Large eddy simulations on the flow driven by a Rushton turbine (1999) AIChE Journal, 45, pp. 209-221;

Derksen, J.J., van den Akker, H. E. A., Multi-scale simulations of stirred liquid-liquid dispersions (2007) Chem. Eng. Res. Des., 85, pp. 697-702;

Eggels, J. G. M., Direct and large-eddy simulation of turbulent fluid flow using the lattice-Boltzmann scheme (1996) Int. J. Heat Fluid Flow, 17, pp. 307-323;

Fall, A., Lecoq, O., David, R., Characterisation of mixing in a stirred tank by planar laser induced fluorescence (P.L.I.F.) (2001) Chem. Eng. Res. Des., 79, pp. 876-882;

Ghadge, R. S., Patwardhan, A. W., Sawant, S. B., Joshi, J. B., Effect of flow pattern on cellulase deactivation in stirred tank bioreactors (2005) Chem. Eng. Sci. 60, pp. 1067-1083;

Giapos, A., Pachatouridis, C., Stamatoudis, M., Effect of the number of impeller blades on the drop sizes in agitated dispersions (2005) Chem. Eng. Res. Des., 83, pp. 1425-1430;

Guha, D., Ramachandran, P. A., Dudukovic, M. P., Derksen, J. J., Evaluation of large eddy simulation and euler-euler cfd models for solids flow dynamics in a stirred tank reactor (2008) AIChE J., 54, pp. 766-778;

Hall, J. F., Barigou, M., Simmons, M. J. H., Stitt, E. H., Mixing in unbaffled high-throughput experimentation reactors (2004) Ind. Eng. Chem. Res., 43, pp. 4149-4158;

Hartmann, H., Derksen, J. J., Montavon, C., Pearson, J., Hamill, I. S., van den Akker, H. E. A., Assessment of large eddy and RANS stirred tank simulations by means of LDA (2004) Chem. Eng. Sci., 59, pp. 2419-2432;

Hartmann, H., Derksen, J. J., Van den Akker, H. E. A., Mixing times in a turbulent stirred tank by means of LES (2006) AIChE J., 52, pp. 3696-3706;

Houcine, I., Vivier, H., Plasari, E., David, R., Villermaux, J., Planar laser induced fluorescence technique for measurements of concentration fields in continuous stirred tank reactors (1996) Exp. Fluids, 22, pp. 95-102;

Jahoda, M., Mostsk, M., Kukukova, A., Machon, V., CFD modelling of liquid homogenization in stirred tanks with one and two impellers using large eddy simulation (2007) Chem. Eng. Res. Des., 85, pp. 616-625;

Jahoda, M., Tomaskova, L., Mostek, M., CFD prediction of liquid homogenisation in a gas-liquid stirred tank (2009) Chem. Eng. Res. Des. 87, pp. 460-467;

Jaworski, Z., Bujalski, W., Otomo, N., Nienow, A. W., CFD study of homogenisation with dual Rushton turbines - Comparison with experimental results. Part I: Initial studies (2000) Chem. Eng. Res. Des., 78, pp. 327-333;

Khopkar, A. R., Tanguy, P. A., CFD simulation of gas-liquid flows in stirred vessel equipped with dual rushton turbines: influence of parallel, merging and diverging flow configurations (2008) Chem. Eng. Sci., 63, pp. 3810-3820;

Kresta S. M., Wood P., Prediction of the three-dimensional turbulent flow in stirred tanks (1991) AIChE J., 37, pp. 448-460;

Laborde-Boutet, C., Larachi, F., Dromard, N., Delsart, O., Schweich, D., CFD simulation of bubble column flows: Investigations on turbulence models in RANS approach (2009) Chem. Eng. Sci., 64, pp. 4399-4413;

Launder, B. E., Spalding, D. B., The numerical computation of turbulent flows (1974) Comput. Meth. Appl. Mech. Eng., 3, pp. 269-289;

Leng, D.E., Calabrese, R.V., Immiscible liquid-liquid systems (2004) Handbook of Industrial Mixing: Science and Practice, pp. 639-753., Paul E.L., Atiemo-Obeng V.A., and Kresta S.M. (Eds), Wiley-Interscience, Hoboken, NJ Chapter 12;

Luo, J. Y., Gosman, A. D., Issa, R. I., Middleton, J. C., Fitzgerald, M. K., Full flow field computation of mixing in baffled stirred vessels (1993) Chem. Eng. Res. Des., 71, pp. 342-344;

Luo, J. Y., Issa, R. I., Gosman, A. D., Prediction of impeller-induced flows in mixing vessels using multiple frames of reference (1994) IChemE Symp. Ser. No. 136, pp. 549-556;

Luo, P. C., Cheng, Y., Jin, Y., Yang, W.H., Ding, J.S., Fast liquid mixing by cross-flow impingement in millimeter channels (2007) Chem. Eng. Sci., 62, pp. 6178-6190;

Maaβ, S., Gabler, A., Zaccone, A., Paschedag, A. R., Kraume, M., Experimental investigations and modelling of breakage phenomena in stirred liquid-liquid systems (2007) Chem. Eng. Res. Des., 85, pp. 703-709;

Middleton, J. C., Smith, J. M. (2004). Gas-liquid mixing in turbulent systems, in: Paul, E.L., Atiemo-Obeng, V.A., Kresta, S.M. (Eds.), Handbook of Industrial Mixing, Wiley-Interscience: Hoboken, New Jersey, pp. 619-620;

Montante, G., Bakker, A., Paglianti, A., Magelli, F., Effect of the shaft eccentricity on the hydrodynamics of unbaffled stirred tanks (2006) Chem. Eng. Sci., 61, pp. 2807-2814;

Montante, G., Lee, K. C., Brucato, A., Yianneskis, M., Numerical simulations of the dependency of flow pattern on impeller clearance in stirred vessels (2001) Chem. Eng. Sci., 56, pp. 3751-3770;

Montante, G., Magelli, F., Liquid homogenization characteristics in vessels stirred with multiple Rushton turbines mounted at different spacings: CFD study and comparison with experimental data (2004) Chem. Eng. Res. and Des., 82, pp. 1179-1187;

Montante, G., Magelli, F., Modelling of solids distribution in stirred tanks: analysis of simulation strategies and comparison with experimental data (2005) Int. J. Comp. Fluid Dyn., 19, pp. 253-262;

Montante, G., Mostek, M., Jahoda, M., Magelli, F., CFD simulations and experimental validation of homogenisation curves and mixing time in stirred

Newtonian and pseudoplastic liquids (2005) Chem. Eng. Sci., 60, pp. 2427-2437;

Montante, G., Paglianti, A., Magelli, F., Experimental analysis and computational modelling of gas-liquid stirred vessels (2007) Chem. Eng. Res. Des., 85, pp. 647-653;

Murthy, B. N., Ghadge, R. S., Joshi, J. B., CFD simulations of gas-liquid-solid stirred reactor: Prediction of critical impeller speed for solid suspension (2007) Chem. Eng. Sci., 62, pp. 7184-7195;

Murthy, B. N., Joshi, J. B., Assessment of standard $\kappa-\epsilon$, RSM and LES turbulence models in a baffled stirred vessel agitated by various impeller designs (2008) Chem. Eng. Sci., 63, pp. 5468-5495;

Murthy, J. Y., Mathur, S. R., Choudhury, D., CFD simulation of flows in stirred tank reactors using a sliding mesh technique (1994) IChemE Symp. Ser. No. 136, pp. 341-348;

Ng, K., Fentiman N. J., Lee, K. C., Yianneskis. M. Assessment of sliding mesh CFD predictions and LDA measurements of the flow in a tank stirred by a Rushton impeller (1998) Chem. Eng. Res. Des., 76, pp. 737-747;

Ochieng, A., Onyango, M.S., Kumar, A., Kiriamiki, K., Musonge, P., Mixing in a tank stirred by a Rushton turbine at low clearance (2008) Chem. Eng. Process., 47, pp. 842-851;

Oshinowo, L., Jaworski, Z., Dyster, K. N., Marshall, E., Nienow, A. W., Predicting the tangential velocity field in stirred tanks using the Multiple Reference Frames (MRF) model with validation by LDA measurements (2000) Proc 10th European Conference on Mixing, Delft, 2-5 July, Elsevier, Amsterdam, pp. 281-288;

Pacek, A.W., Chamsart, S., Nienow, A.W., Bakker, A., The influence of impeller type on mean drop size and drop size distribution in an agitated vessel (1999) Chem. Eng. Sci., 54, pp. 4211-4222;

Pinelli, D., Nocentini, M., Magelli, F., Solids distribution in stirred slurry reactors: influence of some mixer configurations and limits to the applicability of a simple model for predictions (2001) Chem. Eng. Comm., 188, pp. 91-107;

Pope, S. B., Ten questions concerning the large-eddy simulation of turbulent flows (2004) New J. Phys., 6, 35;

Ranade, V. V., Joshi, J. B., Flow generated by a disk turbine: part I experimental (1990) Chem. Eng. Res. Des., 68, pp. 19-33;

Ranade, V. V., Joshi, J.B. Flow generated by a disk turbine: part I experimental (1990) Chem. Eng. Res. Des., 68, pp. 19-33;

Ranade, V. V., Tayalia, Y., Krishnan, H., CFD predictions of flow near impeller blades in baffled stirred vessels: Assessment of computational snapshot approach (2002) Chem. Eng. Commun., 189, pp. 895-922;

Revill, B.K., Pumping capacity of disc turbine agitators - a literature review (1982) Proc. 4th European Conference on Mixing, Noordwijkerhout, The Netherlands, April 27-29, pp. 11-24;

Revstedt, J., Fuchs, L., Tragardh, C., Large eddy simulations of the turbulent flow in a stirred reactor (1998) Chem. Eng. Sci., 53, pp. 4041-4053;

Roache, P.J., Perspective: a method for uniform reporting of grid refinement studies (1994) J. Fluids Eng., 116, pp. 405-413;

Rutherford, K., Mahmoudi, S. M. S., Lee, K. C., Yianneskis, M., The influence of rushton impeller blade and disk thickness on the mixing characteristics of stirred vessels (1996) Chem. Eng. Res. Des., 74, pp. 369-378;

Sommerfeld, M., Decker, S., State of the art and future trends in CFD simulation of stirred vessel hydrodynamics (2004) Chem. Eng. Technol., 27, pp. 215-224;

Svensson, F. J. E., Rasmuson, A., PIV measurements in a liquid-liquid system at volume percentages up to 10% dispersed phase (2006) Exp. Fluids, 41, pp. 917-931;

Tominaga, Y., Stathopoulos, T., Turbulent Schmidt numbers for CFD analysis with various types of flowfield (2007) Atmos. Environ., 41, pp. 8091-8099;

van den Akker, H. E. A., The details of turbulent mixing process and their simulation (2006) Adv. Chem. Eng., 31, pp. 151-229., Marin G.B. (Ed), Academic Press;

Verzicco, R., Fatica, M., Iaccarino, G., Orlandi, P., Flow in an impeller-stirred tank using an immersed-boundary method (2004) AIChE J., 50, pp. 1109-1118;

Wechsler, K., Breuer, M., Durst, F., Steady and unsteady computations of turbulent flows induced by a 4/45° pitched-blade impeller (1999) J. Fluids Eng., Trans. ASME, 121, pp. 318-329;

Wu, H., Patterson G. K., Laser-Doppler measurements of turbulent-flow parameters in a stirred mixer (1989) Chem. Eng. Sci., 44, pp. 2207-2221;

Yeoh, S. L., Papadakis, G., Lee, K. C., Yianneskis, M., Large Eddy Simulation of turbulent flow in a Rushton impeller stirred reactor with sliding-deforming mesh methodology (2004b) Chem. Eng. Tech., 27, pp. 257-263;

Yeoh, S. L., Papadakis, G., Yianneskis, M., Determination of mixing time and degree of homogeneity in stirred vessels with large eddy simulation (2005) Chem. Eng. Sci., 60, pp. 2393-2302;

Yeoh, S. L., Papadakis, G., Yianneskis, M., Numerical simulation of turbulent flow characteristics in a stirred vessel using the LES and RANS approaches with the sliding/deforming mesh methodology (2004a) Chem. Eng. Res. Des., 82, pp. 834-848;

Zhou, G., Kresta, S. M., Evolution of drop size distribution in liquid-liquid dispersions for various impellers (1998) Chem. Eng. Sci., 53, pp. 2099-2113;

Zhou, G., Kresta, S.M., Correlation of mean drop size and minimum drop size with the turbulence energy dissipation and the flow in an agitated tank (1998) Chem. Eng. Sci., 53, pp. 2063-2079;

Chapter 5

Fluidized Beds

5.1 Abstract

In this work, an Eulerian-Eulerian fluid-dynamic model was used to simulate monodisperse suspensions of Geldart A Group particles fluidized by a Newtonian incompressible fluid as well as binary segregating fluidized beds of particles differing in size and density. An appropriate drag force based on the Richardson and Zaki (1954) empirical correlation, generalized for multidimensional applications (Mazzei and Lettieri, 2007), was implemented.

The effects of inter-particle forces between Geldart A particles were taken in account and built onto an hydrodynamic model. The steady-state expansion profiles of a gas-fluidized system was simulated for three different FCC catalysts fluidized with increasing temperatures and compared with experimental data (Lettieri et al., 2001 and 2002). The model reproduces both qualitatively and quantitatively the voidage profiles with increasing velocity and temperature for all the three FCC catalysts examined.

For what concerns segregating beds, the capability of a fully predictive computational fluid dynamics method was investigated. The numerical solution of the multi-phase fluid-dynamic model based on an Eulerian description is applied to both the continuous and the two dispersed phases and the kinetic theory of granular flows for modelling the inter-particle interactions is considered. The results obtained under a number of different operating conditions are compared with experimental data (Olivieri et al., 2004) and the effect of grid size, time step and discretization schemes for the convective terms on axial segregation is also discussed. The capability of the model to correctly predict the minimum fluid velocity at which the mixture becomes steadily fluidized and fully mixed is also tested. Calculations demonstrate that firm conclusions on the CFD model reliability in the prediction of the segregation dynamics in fluidized beds can be drawn only after

careful verification of numerical uncertainties at the operating conditions under investigation.

This work was carried out in collaboration with the Fluidization group of the University College London (UK).

5.2 Outline of the chapter

The present chapter is organised as follow:

- in paragraph 5.3 the research objectives of the analysis and modelling of fluidized beds are presented;
- than in paragraph 5.4 an introduction to CFD modelling of fluidized beds is highlighted;
- generalities on homogeneous bed expansion and on segregating beds are discussed respectively in paragraphs 5.5 and 5.6;
- in paragraphs 5.7 and 5.8 details about the investigated operating conditions and about the models used in this work are presented;
- then in paragraph 5.9 numerical details are described;
- all the results are presented in paragraph 5.10 and conclusions are summarized in paragraph 5.11.

5.3 Research objectives

While in the overwhelming majority of papers in the literature on mono-disperse fluidized beds, bubbling or turbulent fluidization are simulated and analysed, very few works deal with homogeneous gas-fluidization. In the homogeneous regime the mixing is contained and the dynamics are not chaotic. Owing to its simplicity, CFD has been explicitly applied to homogeneous gas-fluidization in only a small number of cases, even if it may provide an opportunity to evaluate alternative CFD approaches. The goal of the work on homogeneous beds consists in finding a model able to reproduce experimental findings on the behaviour of homogeneous expansion of FCC catalysts. The model has to reproduce trend of voidage with velocity and temperature for three different FCC catalysts.

The work on segregating beds focuses on the contribution of numerical issues to the accuracy of the most widespread multi-fluid simulation method for fluidized beds. The spatial and temporal discretization influence on the accuracy of the

predicted segregation profiles for bidisperse mixtures of particles differing in size and density in a wide range of velocities and compositions will be investigated. Simulations in two-dimensional rectangular Cartesian coordinates, ignoring front and rear effects, will be run, since three-dimensional simulations of fluidized beds of bi-disperse mixtures are out of reach with current computational power.

5.4 CFD and fluidized beds

Fluidized beds are widely used in the chemical and process industry because of their good heat and mass transfer characteristics and excellent solid mixing, but their modelling is challenging because of the complex fluid dynamic behaviour of dense multi-phase systems. To date, a variety of mathematical models have been used and the application of computational fluid dynamics to gas-fluidized beds has gained considerable attention (Lettieri and Mazzei, 2009; van Wachem and Almstedt, 2003). The application of CFD methods to fluidization appears to have potential to be useful for design and development of fluidized beds of industrial interest, alleviating the need for extensive experiments, provided that the validity of the predictions is checked for a broad variety of situations. For this reason, further model development and validation is required, in particular for the case of segregating beds and homogeneous bed expansion, which have not been extensively investigated by CFD so far.

Two different modelling approaches are typically used for fluidized beds. In all cases for the continuous gas phase an Eulerian formulation is adopted while the dispersed solid phase is treated by either a discrete model or a continuum model. In the former case, namely the Eulerian-Lagrangian approach, the equations of motion for each particle are solved taking into account the forces acting on the particle and the particle-particle collisions (Pan et al., 2002), while with the continuum model, referred to as Eulerian-Eulerian approach, the solids are considered as fully interpenetrating continua subject to continuity and momentum equations (Anderson and Jackson, 1967).

The Eulerian-Lagrangian approach is a powerful tool, because it permits to obtain detailed information on the motion of particles and it may be used to develop or test constitutive relations for particle-particle interactions. However, this is also an expensive tool, because the computational time step has to be set close to the time scale of the particle-particle interactions, which is much less than the macroscopic flow time scale. Also the limitations, due to computational power requirements, on the particle number make the Lagrangian approach unsuitable for the simulation of dense gas-solid systems. For these reasons, the computational time necessary in Eulerian-Lagrangian simulations can be orders of magnitude higher than that needed for Eulerian-Eulerian ones. In any case, researchers adopted both the dis-

crete and continuum approaches for fluidized bed simulation with a certain degree of success; for example, Hoomans et al. (2001), Limtrakul et al. (2003), Feng et al. (2004), Bokkers et al. (2004), Dahl and Hrenya et al. (2005), Beetstra et al. (2007) used a discrete approach, while, among others, van Wachem et al. (2001a), Huilin et al. (2003a), Gera et al. (2004), Cooper and Coronella (2005), Mazzei et al. (2010) used the continuum one.

To model dense gas-solid flows, the continuum multi-fluid model is coupled with the kinetic theory of granular flow, which comes from the theory for non-uniform dense gases (Chapman and Cowling, 1970). This theory was developed by Ding and Gidaspow (1990), Peirano et al. (2002) and Patil et al. (2005) for particles of the same density and size and then extended to binary granular mixtures with unequal granular temperatures by Gidaspow et al. (1996).

5.5 Homogeneous bed expansion

The behaviour of a fluidized bed depends on the particles' characteristics. Geldart (1973) classified powders into four different groups, based on both particle density and diameter (see Figure 5.1). A fluidized bed of Group B powders starts bubbling as soon as the minimum fluidization velocity is reached without showing any homogeneous fluidization; whereas a bed of Group A powders shows a distinct region of homogeneous fluidization with significant bed expansion before the onset of bubbling. This characteristic behaviour has been studied both theoretically and experimentally. On the basis of the concept of bed elasticity introduced by Wallis (1969), Verloop and Heertjes (1970) and later Foscolo and Gibilaro (1984) were able to predict the stable behaviour of spherical mono-size Group A materials, based only on hydrodynamic forces.

Walliss idea (1969) was also used by Rietema et al. (1973, 1993) and Rietema and Piepers (1990), but according to them the bed elasticity is due to the existence of interparticle forces among the bed particles. According to Mutsers and Rietema (1977) particles contact forces between cohering particles give rise to a powder structure with a certain mechanical strength even in the expanded state of homogeneous fluidization. Their theory was experimentally demonstrated by Rietema and Piepers (1990) and Tsinontides and Jackson (1993), who concluded that the interparticle forces are responsible for the bed stabilization. Tsinontides and Jackson (1993), in particular, analysed the structure of the homogeneous bed and recognised the presence of particles contact forces because of the existence of yield stresses throughout the range of stable behaviour.

Agbim et al. (1971), Seville and Clift (1984), McLaughlin and Rhodes (2001), and Rhodes et al. (2001) showed that homogeneous fluidization and bed expansion can also be observed in a bed of Group B powders, if artificial interparticle forces

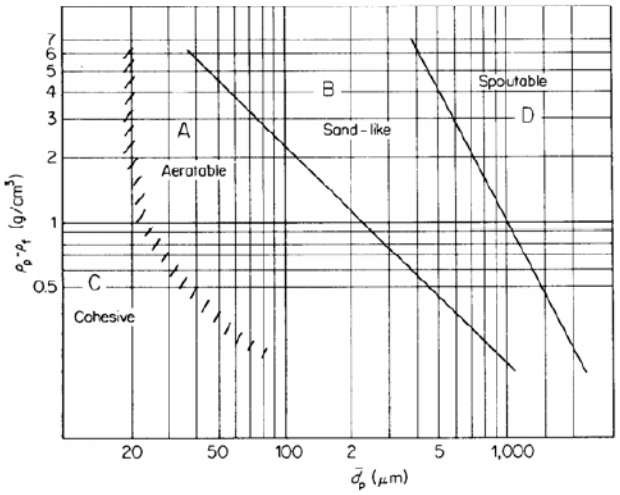

Figure 5.1: Fluid-particle system classification for air at ambient temperature (Geldart, 1973)

are introduced, highlighting the importance of cohesive interparticle forces in homogeneous fluidization. The importance of naturally occurring interparticle forces in determining the behaviour of a fluidized bed was also demonstrated by Molerus (1982), Geldart et al. (1984) and Chaouki et al. (1985).

It is commonly accepted that, for Geldart B particles, the hydrodynamic forces completely dominate over the interparticle forces, while for Geldart C particles the interparticle forces significantly dominate over the hydrodynamic forces. For Group A particles, the hydrodynamic and interparticle forces can both have a significant role on the fluidization behaviour. The balance between the two types of forces can change as a function of the operating conditions. Thus, in theory, some Group A particles probably behave in fluidization like either Group B or Group C particles as a result of variations in the balance between hydrodynamic and interparticle forces and changing fluidization factors.

The fact that the dynamic variables of fluidization (such as the minimum fluidization voidage and velocity, the minimum bubbling velocity, dense phase voidage, and even settled bed voidage) change as the temperature changes, undoubtedly indicates that interparticle forces have an effect on fluidization hydrodynamics, and their importance compared to hydrodynamic forces changes as the temperature changes. In particular, the fact that the settled bed voidage increases with increasing temperature for a wide range of particles from Geldart A to B, has been explained as being due to the role of the interparticle forces becoming more significant with increasing bed temperature (Formisani et al., 1998). Therefore, it was concluded that the contribution of the interparticle forces cannot be ruled out

in the prediction of fluidization dynamics using classic hydrodynamic theories (Xie and Geldart, 1995; Formisani et al., 1998; Lettieri et al., 2001). However, the interparticle forces are rather complex and poorly understood and there is no agreement as to how the interparticle forces change as the temperature increases.

The homogeneous expansion of Group A powders has also been described using the Richardson and Zaki (1954) equation:

$$u = u_t \epsilon^n \tag{5.1}$$

where u is the liquid velocity of the suspension, ϵ is the bed voidage and n is the slope of the line in the $\ln \epsilon - \ln u$ plot. The intercept on the $\ln u$ axis corresponding to $\epsilon = 1$ was found to coincide with the particle terminal velocity, u_t. The parameter n depends on the free falling particle Reynolds number, Re_t, and, normally, has values between 4.65 (viscous regime) and 2.4 (turbulent regime). This formulation was developed to describe the fluidization and sedimentation with liquid of uniformly sized particles, with diameters greater than 100 μm.

Various authors have made bed expansion experiments in gas fluidized beds with Group A powders and found that the relationship between the fluidizing velocity u and bed voidage ϵ could be expressed in the form of the Richardson-Zaki equation. However, the values of the index n for all powders tested were found to be higher than those predicted for uniform spheres fluidized by a liquid. Values of n between 5 and 8 were found by Godard and Richardson (1968), between 5.4 and 7 by Massimilla et al. (1972). The former found highest n values for some Phenolic resins, the latter for the finer and non-sieved materials. In the case of cohesive powders, Avidan and Yerushalmi (1982) reported values of n around 14, while Geldart and Wong (1984, 1985), for small particle size and high degrees of cohesiveness, found n values in the range between 4 and 60. They also studied the expansion mechanism of Group A powders and observed that in non-cohesive system, the terminal fall velocity, calculated using Stokes equation, is close to the velocity extrapolated from the Richardson-Zaki equation at $\epsilon = 1$.

Godard and Richardson (1968) found that the values of the terminal velocity obtained by extrapolation of the logarithmic voidage-velocity curves were generally somewhat higher than the terminal fall velocity of the particles u_t. For velocity above the velocity for minimum bubbling,u_{mb}, Avidan and Yerushalmi (1982) found extrapolated terminal fall velocity greater by almost two orders of magnitude than the free-fall velocity of a single median particle. This latter result supported their concept of presence of clusters in the dense phase, with the effective terminal velocity taken to represent the size and density of the clusters.

In any case, theories based on interparticle forces are very difficult to apply, as it proves difficult to determine the magnitude of interparticle forces and their relationship with the macroscopic physical properties of the bed. In this regard, in

recent years numerical simulation techniques have been increasingly used for studying gas-particle systems and different modelling approaches have been proposed.

5.6 Segregating beds

In several cases, industrial gas-fluidized beds treat polydisperse mixtures of particles characterised by broad distributions of size and/or density (e.g. fluidized-bed combustors, titania synthesis, production of acrylonitrile, pharmaceutical granulation, etc.). These mixtures of particles segregate (de-mix) over a wide range of superficial velocities greater than the minimum fluidization velocity. Some particles sink towards the gas distributor and are referred to as jetsam, while others rise towards the fluidized bed surface and are referred to as flotsam. This phenomenon is important in classifiers (Olivieri et al., 2009), but needs to be avoided in applications where an intimate particle mixing is necessary. In either case, we need to understand and to be able to predict segregation, because this influences chemical reaction, bed expansion and various mass and heat transfer properties.

Researchers have thoroughly studied experimentally how fluidized beds segregate, and we know that segregation depends on the differences in particle density and size of the particles, as well as on the fluid velocity. When particles have the same density, the smaller ones tend to concentrate near the bed surface while the larger fall to the bottom (Wu and Baeyens, 1998; Goldschmidt et al, 2003). Segregation increases as the gas velocity approaches the minimum fluidization velocity of the smaller particles (Geldart et al., 1981). For systems of particles having same size and different density, denser particles tend to fall to the bottom of the bed, segregation being more pronounced for intermediate compositions and less at low and high jetsam concentrations (Joseph et al., 2007). At low gas velocities, systems of particles differing only in size or density tend to segregate considerably (Olivieri et al., 2004).

In recent years, several research groups conducted CFD modelling of fluidization with polydisperse particles. Mathiesen et al. (1999), for example, predicted the volume fractions and velocities for two types of particles differing in size in a CFB riser. Goldschmidt et al. (2001), through a multi-fluid model, examined the effect of coefficient of restitution on segregation in dense gas-fluidized beds. Van Wachem et al. (2001b) predicted the flow behaviour of gas-fluidized beds with a bimodal particle mixture model. Huilin et al. (2003b), using kinetic theory of dense gases, derived a model for binary mixtures and simulated their flow behaviour in a bubbling fluidized bed. Balance equations and constitutive relations for a granular mixture with various sizes and densities were derived by Rahaman et al. (2003). Gera et al. (2004) simulated solids segregation in a dense fluidized bed, extending a two-fluid gas-solid model to a multi-fluid model by adding constitutive equations

for the particle-particle drag and the maximum particle packing. Chiesa et al. (2005) obtained flow patterns results comparable with experimental ones, computing for a ternary mixture the behaviour of a two-dimensional fluidized bed through a discrete particle method (DPM) and a multi-fluid model. Iddir et al. (2005) developed a model based on kinetic theory of dense gases from variant particle mechanical properties, obtaining non-equipartition energy and stresses of a binary granular mixture. Cooper and Coronella (2005) were able to observe segregating jump in a specific point of the bed, while modelling a gas fluidized bed of a binary mixture.
Moreover Sun and Battaglia (2006) computed the behaviour of a bidispersed bubbling gas-fluidized bed using a multi-fluid Eulerian model. In their simulations, they studied the effect of particle rotation on segregation phenomena and concluded that particle rotation and slight friction permit to the multi-fluid model to better capture the bubble dynamics and time-averaged bed behaviour. Huilin et al. (2007) successfully applied an Eulerian-Lagrangian hard-sphere discrete model and a multi-fluid CFD model with kinetic theory of granular flow to a fluidized bed of a binary mixture of particles differing in density or diameter. Leboreiro et al. (2008) used a hybrid model between the continuum and discrete approaches, demonstrating that the drag law treatment plays a crucial role in the qualitative and quantitative nature of segregation predictions at low gas velocities and may lead to qualitative differences in bubble dynamics.
Eulerian models have generally been able to provide good qualitative results and reasonable quantitative agreement with limited experimental findings. However, the computational codes have not yet reached the stage where they can be used with confidence for design and scale-up of fluidized bed reactors (Cornelissen et al., 2007). There is a need to validate the models in a proper way (Grace and Taghipour, 2003) examining the effect of every assumption on the capability of the code in predicting fluidized bed behaviour. Prediction uncertainties and errors are usually attributed to modelling deficiencies only, although the contribution of numerical errors is not to be disregarded in the verification process (Coleman and Stern, 1997). The numerical dependency of CFD results as applied to the simulation of bidisperse fluidized beds has been systematically conducted only in few cases. It is finally worth stressing that in most cases hardware constraints do not allow to fully investigate the numerical uncertainties due to the spatial and temporal discretization. As a matter of fact, the chaotic nature of dense gas-solid fluidized beds requires time-dependent simulations and, as a consequence, a great computational effort (Busciglio et al., 2009).

Table 5.1: Particle physical properties

Material	d_d $[\mu m]$	ρ_d $[kg\ m^{-3}]$	F_{45} [%]	σ/d_{50} [-]
FCC1 (fresh)	71	1420	5	0.34
FCC2 (fresh)	57	1420	16	0.58
FCC3 (fresh)	49	1420	25	0.61

5.7 Details of the investigated cases

Homogeneous bed expansion

Homogeneous bed simulations investigated in this work refer to experimental observations (Lettieri et al. 2001, 2002) on the homogeneous expansion of three FCC catalysts fluidized with nitrogen from ambient up to 650°C. These catalysts are all characterized by a wide particle size distribution and by non-perfectly spherical particles. Their mean diameters, d_d, density, ρ_d, fines content, F_{45}, and relative diameter spread, σ/d_{50}, are reported in Table 5.1.

The Richardson-Zaki equation is used to describe the homogeneous expansion of these catalysts. Values of n and u_t are predicted respectively by the Richardson-Zaki $n = n(Re_t)$ correlations employed for liquids and by the drag equation for the settling of an individual particle, using the Stokes law. These parameters are also estimated from experimental data as a function of temperature (values of n and u_t obtained from expansion profiles are marked with an asterisk, i.e. n^* and u_t^*). Predicted values of n are about 4.8 for all FCC catalysts, while n^* values are found to be within the range 6.4-9.6 in all cases (see Table 5.2), with higher values at lower temperatures. Thus, if high values of n are indicative of the presence of interparticle forces, as reported by Geldart and Wong (1984, 1985) and Avidan and Yerushalmi (1982), then their effect on the homogeneous expansion of these FCC catalysts is stronger at low temperatures.

Values of u_t^* are also found to be greater than the calculated ones, especially at ambient temperature. The discrepancy decreases from a factor of 10 to about a factor of 3 with increasing temperature (see Table 5.3). Following the approach of Avidan and Yerushalmi (1982) the discrepancy between u_t and u_t^* values obtained for the FCC catalysts may be explained assuming that the dense phase of these materials is characterized by the presence of clusters or of fluid dynamic interactions. The effective terminal velocity u_t^* can be considered to be representative of the size and density of the clusters. If this assumption is true, the diameters of such clusters, d_d^*, can be back-calculated from the u_t^* values. For all FCC catalysts, values of d_d^* with increasing temperature are reported in Table 5.4, where the

Table 5.2: Experimental (n) and calculated (n^*) values of the Richardson-Zaki parameter n for all FCC catalysts

T [°C]	FCC1		FCC2		FCC3	
	n	n^*	n	n^*	n	n^*
20	4.6	9.6	4.7	9.0	4.8	8.2
100	4.5	7.9	4.8	8.6	4.8	6.9
200	4.4	6.8	4.8	7.6	4.8	6.4
300	4.4	7.0	4.8	7.1	4.8	6.7
400	4.8	6.6	4.8	7.1	4.8	6.6
500	4.8	6.8	4.8	7.7	4.8	7.1
650	4.8	7.4	4.8	7.5	4.8	7.4

Table 5.3: Experimental (u_t) and calculated (u_t^*) values of the Richardson-Zaki parameter u_t for all FCC catalysts

T [°C]	FCC1		FCC2		FCC3	
	u_t $[cms^{-1}]$	u_t^* $[cms^{-1}]$	u_t $[cms^{-1}]$	u_t^* $[cms^{-1}]$	u_t $[cms^{-1}]$	u_t^* $[cms^{-1}]$
20	19.5	254.4	13.8	116.6	9.7	92.4
100	17.0	66.3	11.8	66.7	8.7	28.4
200	14.7	27.9	10.6	31.1	7.3	16.7
300	12.9	27.7	9.2	21.2	6.3	20.6
400	12.2	20.6	8.3	20.2	5.7	16.5
500	11.2	21.3	7.6	25.2	5.2	19.5
650	10.0	27.1	6.8	21.9	4.7	20.9

considerable diameter difference between low and high temperatures is evident.

Avidan and Yerushalmi (1982) also stressed the great influence that the particle size distribution may have on the values of u_t^*. They found lower u_t^* values for those catalysts characterized by higher content of fines. This is in agreement with Lettieri et al. (2001, 2002) results, where values obtained for FCC3, which contained 25% of fines, were lower than those obtained for FCC1 and FCC2, which contained, respectively, 5% and 16% of fines.

Thermo-gravimetric analyses (TGA) showed that capillary forces due to adsorption of water vapours on the surface or pores of the micro-porous silica-alumina FCC catalysts may be responsible for the high values of n^* and u_t^* found at low temperature. In which case, the adhesion force between two particles depends on them coming close enough together for the adsorbed layers to overlap.

Table 5.4: Mean particle diameter d_d^* back-calculated form u_t^* values for all FCC catalysts

T[° C]	FCC1 d_d^* [μm]	FCC2 d_d^* [μm]	FCC3 d_d^* [μm]
20	474	238	200
100	134	135	88
200	95	100	73
300	102	89	88
400	92	92	83
500	98	107	94
650	117	105	100

Rumpf (1962) reported that presence of adsorbed layers may contribute to the cohesion of the particles either by virtue of hydrogen bonding or other chemical forces, or by reducing their interparticle separation, so that the adsorption layer thickness could be added to the particle diameter.

Segregated fluidized beds

In the part of work referred to segregated fluidized beds, one of the systems experimentally investigated by Olivieri et al. (2004) was studied. The experimental apparatus consists of a vessel 120 mm wide and 1 500 mm high, whose lower part is made up of an assembly of cylindrical segments that permit to divide the bed in six control volumes in which it is possible to measure the mixture composition.

The bed is fluidized by air at ambient pressure and temperature and is composed of two Geldart B group particle phases differing in size and density (System 1 in Olivieri et al., 2004). The first phase (jetsam) has particle of a mean diameter of 125 μm and density of 2 600 kgm^{-3}, while the second one (flotsam) has a mean diameter of 375 μm and density of 600 kgm^{-3}.

It is worth observing that a preliminary knowledge on which material will act as jetsam or floatsam is possible for a two-component binary system, following appropriate rules (Yang, 2003). As stated by Olivieri et al. (2004), in the selected system the heavier phase acts as jetsam, which behavior is in agreement with the know features that density differences usually overtake size differences (Chiba et al., 1980) and with the rule suggested by Yang (2003).

Our CFD simulations reproduce type B experiments reported in Olivieri et al. (2004), i.e. in the initial state, the bed is packed and completely mixed, 144 mm high and with a fluid volume fraction equal to 0.4, then the gas superficial velocity is suddenly raised from zero to a preset value, and the bed is kept fluidized until

the steady state is reached. In the experiments, after the preset fluidization time elapsed, the bed was "frozen" by suddenly cutting off the fluidizing gas supply. The cylindrical segments were then disassembled one at a time to obtain the axial distributions of solids.

5.8 The model equations

The CFD simulation approach adopted in this work is based on an Eulerian multi-fluid model, which equations are written under incompressible, isothermal, time-dependent and laminar flow conditions, while the effect of possible local turbulent conditions is ignored (Cornelissen et al., 2007). With this approach, the continuity and momentum equations are solved for each phase, thus obtaining separate flow field solutions for the continuous and the dispersed phases simultaneously.

In the present section, equations considering two dispersed phases will be presented. Obviously, proper simplifications arise when only one dispersed phase is present in the system.

The continuity equation for a generic phase k $(= c, d_1, d_2)$, based on the Eulerian treatment, is:

$$\frac{\partial \phi_k}{\partial t} + \nabla \cdot (\phi_k \boldsymbol{u}_k) \tag{5.2}$$

where ϕ is the volumetric fraction and $\boldsymbol{u}$ is the velocity vector.

Momentum equations for the continuous phase

The momentum equation for the gas phase is expressed as:

$$\rho_c \frac{\partial}{\partial t}(\phi_c \boldsymbol{u}_c) + \rho_c \nabla \cdot (\phi_c \boldsymbol{u}_c \boldsymbol{u}_c) = -\phi_c \nabla p + \nabla \cdot \overline{\overline{\tau}}_c + \phi_c \rho_c \boldsymbol{g} - \sum_{d_i} \beta_i (\boldsymbol{u}_c - \boldsymbol{u}_{d_i}) \tag{5.3}$$

where the single gas phase viscous stress tensor with the bulk viscosity set to zero is adopted for $\overline{\overline{\tau}}_c$, the product of the slip velocity between the fluid and the two dispersed phases and a momentum transfer coefficient, β_i, represents the drag force and all the other symbols have the usual meaning. For β_i the closure relationship of Mazzei and Lettieri (2007), based on the empirical equation of Richardson and Zaki (1954) is implemented in the following form:

$$\beta_i = \frac{3}{4} C_D (Re_i) \frac{\rho_c ||\boldsymbol{u}_c - \boldsymbol{u}_{d_i}|| \phi_c \phi_{d_i}}{d_{d_i}} \phi_c^{-\psi(\phi_c Re_i)} \tag{5.4}$$

and only the drag is assumed to be responsible for the inter-phase momentum transfer between gas and solid phases, since the virtual mass force is not significant

when the dispersed phase density is much larger than that of the continuous phase, while the contribution of the lift force was evaluated only in one simulation and it was found to be negligible.

When cohesive powders are taken in consideration, the drag coefficient $C_D(Re)$ is described in the following form, as given by Dallavalle (1948):

$$C_D(Re_i) = \left(0.63 + 4.80 Re_i^{-1/2}\right)^2 \tag{5.5}$$

$$Re_i = \frac{\rho_{d_i}}{\mu_c}\epsilon||\boldsymbol{u}_c - \boldsymbol{u}_{d_i}||d^*_{d_i} \tag{5.6}$$

where d^*_d is the clusters diameter. It is assumed here that the powders behave like clusters of particles with a diameter $d^*_d > d_d$. The diameter of the cluster d^*_d was back-calculated from the experimental terminal velocity, u^*_t, and was used as the particles diameter. The analytical expression of ψ is:

$$\psi(\epsilon, Re_i) = -\frac{\ln \varphi(\epsilon, Re_i)}{\ln \epsilon} \tag{5.7}$$

with:

$$\varphi(\epsilon, Re_i) = -\frac{C^*_D(\epsilon, Re_i)}{C_D(Re_i)}\epsilon^{2(1-n)} \tag{5.8}$$

where

$$C^*_D(Re^*_i) = \left(0.63 + 4.80 Re_i^{*-1/2}\right)^2 \tag{5.9}$$

$$Re^*(\epsilon, Re_i) = \frac{Re_i}{\epsilon^n} \tag{5.10}$$

and n is the Richardson-Zaki equation parameter.

For non-cohesive powders, it is possible to calculate the exponent n through the empirical relation of Rowe (1987):

$$n(Re^*_i) = \frac{4.80 + 2.40 \cdot 0.175 Re_i^{*3/4}}{1 + 0.175 Re_i^{*3/4}} \tag{5.11}$$

while in the case of cohesive powders this exponent need to be obtained from experiments. In the study of homogeneous bed expansion, it is calculated from experiments of Lettieri et al. (2002) and was taken equal to n^*. In this way,

both the gas-particle and the particle-particle interaction forces are introduced in the model through the drag force term. This term is modelled as reported by Mazzei and Lettieri (2007), with a slight modification in order to take in account for the particular behaviour of Geldart A group particles. As a result, the presence of clusters in the system is simulated using particles with the same diameter of clusters, while the remaining interaction force between clusters is introduced using a n value equal to the experimental one. In this way, the model of homogeneous bed expansion is based on hydrodynamics only, but interparticle forces and clusters' formation are taken in account by using the appropriate n and d_d values.

Values of d_d^* different from the real particle diameter and of n different from the classic value are used only in the simulations of homogeneous bed expansion, while segregating fluidized beds are simulated in a fully predictive way introducing the real particle diameter d_d and values of n calculated with the empirical relation of Rowe (1987).

real values are used for the modelling of segregating fluidized beds, which in this way are simulated in a fully predictive way.

Momentum equations for the dispersed phases

When collisions dominate the particle motion, as in the case of the fluidized bed considered in this work, concepts from gas kinetic theory can be used to describe the effective stresses in the solid phase resulting from particle collisional contribution (Chapman and Cowling, 1970). As a result, the following formulation of the momentum equation for each solid phase is considered:

$$\rho_{d_i} \frac{\partial}{\partial t} \left(\phi_{d_i} \boldsymbol{u}_{d_i} \right) + \rho_{d_i} \nabla \cdot \left(\phi_{d_i} \boldsymbol{u}_{d_i} \boldsymbol{u}_{d_i} \right) = \\ = -\phi_{d_i} \nabla p + \nabla \cdot \boldsymbol{p}_{d_i} + \phi_{d_i} \rho_{d_i} \boldsymbol{g} + \beta_i \left(\boldsymbol{u}_c - \boldsymbol{u}_{d_i} \right) + \zeta_{ij} \left(\boldsymbol{u}_{d_j} - \boldsymbol{u}_{d_i} \right) \quad (5.12)$$

The interaction force between particles of different phases is described using the constitutive equation of Syamlal (1987):

$$\zeta_{ij} = \frac{3}{4} \left(1 + e_{ij} \right) \left(1 + \frac{\pi}{4} F_{ij} \right) \frac{\rho_{d_i} \rho_{d_j} \phi_{d_i} \phi_{d_j} g_{ij} \left(d_{d_i} + d_{d_j} \right)^2}{\rho_{d_i} d_{d_i}^3 + \rho_{d_j} d_{d_j}^3} ||\boldsymbol{d_j} - \boldsymbol{d_i}|| \quad (5.13)$$

where e_{ij} is the coefficient of restitution and accounts for the non-ideal collisions or inelasticity of the solids taken equal to 0.90 and F_{ij} is the coefficient of friction between the d_i-th and d_j-the solid phase particles. The radial distribution coefficient g_{ij} represents a correction factor that modifies the probability of collisions between grains when the solid granular phase becomes dense. This quantity governs the transition from the condition with the overall solid volume fraction $\phi < \phi_{max}$ where the spacing between the solid particles can continue to decrease,

to the incompressible condition with $\phi = \phi_{max}$, where no further decrease in the spacing can occur. It takes into account the probability of particles colliding with each other when the granular phase becomes densely packed. It can be obtained by combining the radial distribution functions g_i and g_j of the d_i-th and d_j-th particle phases, respectively in the following way:

$$g_{ij} = \frac{d_{d_i} g_j + d_{d_j} g_i}{d_{d_i} + d_{d_j}} \tag{5.14}$$

where g_i can be expressed as:

$$g_i = \frac{d_{d_i}}{2} \sum_{k=1}^{2} \frac{\phi_{d_i}}{d_{d_i}} + \left[1 - \left(\frac{\phi}{\phi_{max}}\right)^{1/3}\right]^{-1} \tag{5.15}$$

Here ϕ is the total volume fraction of the solids, and ϕ_{max} is the maximum packing limit. For a binary mixture the maximum packing limit is a function of the powder composition and can be determined by using the empirical expression of Fedors and Landel (1979) with $d_{d_i} \geq d_{d_j}$ for :

$$\omega_{d_i} \leq \frac{\phi^i_{max}}{\phi^i_{max} + \left(1 - \phi^i_{max}\right) \phi^j_{max}} \tag{5.16}$$

$$\phi_{max} = \phi^j_{max} + \left[\left(\phi^i_{max} - \phi^j_{max}\right) + \left(1 - \xi_{ij}\right)\left(1 - \phi^j_{max}\right)\right] \left[\phi^i_{max} + \left(1 - \phi^i_{max}\right) \phi^j_{max}\right] \frac{\omega_{d_i}}{\phi^i_{max}} \tag{5.17}$$

or otherwise:

$$\phi_{max} = \phi^i_{max} + \left(1 - \xi_{ij}\right)\left[\phi^i_{max} + \left(1 - \phi^i_{max}\right) \phi^j_{max}\right]\left(1 - \omega_{d_i}\right) \tag{5.18}$$

where $\omega_{d_i} = \frac{\phi_{d_i}}{\phi}$ and $\xi_{ij} = \left(\frac{d_{d_j}}{d_{d_i}}\right)^{1/2}$. Moreover, ϕ^i_{max} and ϕ^j_{max} are the particle volume fractions at maximum packing for the phases d_i and d_j, respectively, taken always equal to 0.63. The solid phase pressure tensor, $\boldsymbol{p}_{d_i}$, is modelled following the kinetic theory of granular gases (Gidaspow, 1994) as:

$$\boldsymbol{p}_{d_i} = \left(-p_{d_i} + \phi_{d_i} \lambda_{d_i} \nabla \cdot \boldsymbol{u}_{d_i}\right) \overline{\overline{\boldsymbol{I}}} + \phi_{d_i} \mu_{d_i} \left[\nabla \boldsymbol{u}_{d_i} + \left(\nabla \boldsymbol{u_{d_i}}^T - \frac{2}{3}\left(\nabla \cdot \boldsymbol{u}_{d_i}\right) \overline{\overline{\boldsymbol{I}}}\right)\right] \tag{5.19}$$

The models for the explicit formulation of solid pressure, p_d, and solid dilatation viscosity, λ_d, adopted in this work are due to Lun et al. (1984), while particle phase viscosity, μ_d, adopted is due to Gidaspow et al. (1992). The solids pressure

represents the normal solid-phase forces due to particle-particle interactions and is composed of a kinetic term and of a second term due to particle collisions (Lun et al., 1984). The kinetic part physically represents the momentum transferred through the system by particles moving across imaginary shear layers in the flow, while the collisional part denotes the momentum transferred by direct collisions. The resulting equation is:

$$p_{d_i} = \left[1 + 2\sum_{k=1}^{2}\left(\frac{d_{d_i} + d_{d_j}}{2d_{d_i}}\right)^3 (1 + e_{ij})\,\phi_{d_j} g_{ij}\right] \phi_{d_i} \rho_{d_i} \Theta_{d_i} \tag{5.20}$$

The solid dilatation viscosity describes the resistance of the particle suspension to compression or expansion and can be expressed in the following way (Lun et al., 1984):

$$\lambda_{d_i} = \frac{4}{3}\phi_{d_i} d_{d_i} d_{d_i} g_i\,(1 + e_{ij})\sqrt{\frac{\Theta_{d_i}}{\pi}} \tag{5.21}$$

The solid shear viscosity contains shear viscosity arising from particle momentum exchange due to collision, translation and friction.

$$\mu_{d_i} = \mu_{d_i,coll} + \mu_{d_i,kin} + \mu_{d_i,fr} \tag{5.22}$$

The collisional and kinetic parts of the shear viscosity are modelled as (Gidaspow et al., 1992):

$$\mu_{d_i,coll} = \frac{4}{5}\phi_{d_i} \rho_{d_i} d_{d_i} g_i\,(1 + e_{ij})\sqrt{\frac{\Theta_{d_i}}{\pi}} \tag{5.23}$$

$$\mu_{d_i,kin} = \frac{10\rho_{d_i} d_{d_i}\sqrt{\Theta_{d_i}\pi}}{96\phi_{d_i}\,(1 + e_{ij})\,g_i}\left[1 + \frac{4}{5} g_i \phi_{d_i}\,(1 + e_{ij})\right]^2 \tag{5.24}$$

A frictional component of viscosity was also included to account for the viscous-plastic transition that occurs when the volume fraction for the solid phase reaches the maximum solid volume fraction and the generation of stress is mainly due to friction between particles. The expression of Schaeffer (1987) was used:

$$\mu_{d_i,fr} = \frac{p_{d_i} \sin\theta_i}{2\sqrt{I_{2D}}} \tag{5.25}$$

where θ_i is the angle of internal friction of the d_i-th granular phase, always taken to be equal to 30°, and I_{2D} is the second invariant of the rate of deformation tensor D_{d_i}.

Kinetic theory of granular flow

Analogous to the thermodynamic temperature for gases, the granular temperature, Θ_{d_i}, represents a measure of the particle velocity fluctuations of the d_i-th solid phase. Since the solid-phase stress depends on the magnitude of these particle-velocity fluctuations, a balance of the granular energy $(3/2)\Theta_{d_i}$ associated with these particle-velocity fluctuations is required to supplement the continuity and momentum balance for both phases. The transport equation of the granular temperature is derived from the kinetic theory and takes the following form (Ding and Gidaspow, 1990):

$$\frac{3}{2}\left[\rho_{d_i}\frac{\partial}{\partial t}\left(\phi_{d_i}\Theta_{d_i}\right)+\rho_{d_i}\nabla\cdot\left(\phi_{d_i}\boldsymbol{u}_{d_i}\Theta_{d_i}\right)\right]= \\ =\boldsymbol{p}_{d_i}:\nabla\boldsymbol{u}_{d_i}+\nabla\cdot\left(k_{\Theta_{d_i}}\nabla\Theta_{d_i}\right)-\gamma_{\Theta_{d_i}}-3\beta_i\Theta_{d_i} \quad (5.26)$$

where the first term at the right hand side represents the generation of fluctuating energy due to shear in the d_i-th particle phase, the second the diffusion fluctuating energy due to gradients of Θ_{d_i}, the third the collisional dissipation of fluctuating energy and the last one is the fluctuating energy exchange between the fluid phase and the d_i-th solid phase. In all the simulations, the complete granular energy balance was solved, without any assumption on the steady state and local dissipation of the granular energy or on the convection and diffusion. The diffusion coefficient, k_{Θ_i}, for the granular energy is given by Gidaspow et al. (1992) as follows:

$$k_{\Theta_{d_i}}=\frac{150\rho_{d_i}d_{d_i}\sqrt{\Theta_{d_i}\pi}}{384\left(1+e_{ij}\right)g_i}\left[1+\frac{6}{5}\phi_{d_i}g_i\left(1+e_{ij}\right)\right]^2+2\rho_{d_i}\phi_{d_i}^2d_{d_i}\left(1+e_{ij}\right)g_i\sqrt{\frac{\Theta_{d_i}}{\pi}} \quad (5.27)$$

The collisional dissipation of energy, $\gamma_{\Theta_{d_i}}$, represents the rate of energy dissipation within the solid phase due to collisions between particles. This term is represented by the expression derived by Lun et al. (1984) in the following way:

$$\gamma_{\Theta_{d_i}}=\frac{12\left(1-e_{ij}^2\right)g_i}{d_{d_i}\sqrt{\pi}}\rho_{d_i}\phi_{d_i}^2\Theta_{d_i}^{3/2} \quad (5.28)$$

5.9 Simulation details

5.9.1 Homogeneous bed simulation details

Numerical schemes and techniques A two-dimensional geometry was created for a vessel 140 mm large and 1 000 mm high and a structured computational grid of 5 $mm\times$ 5 mm was used, consisting of a total of 5 600 computational cells. The

resulting set of equations was solved running the finite volume general purpose CFD code Fluent 12 (Ansys Inc.). For the present case of 2D two-phase flow, the model solves eight equations in as many unknowns: the two volumetric fractions, the four velocity components, the pressure and the granular temperature. To account for the fluid-particle interaction force term a routine developed by Mazzei and Lettieri (2008) was suitably modified and implemented into the code. The continuity, momentum and granular temperature equations as implemented in the code were numerically solved in a Cartesian coordinate system. The conservation equations were integrated in space and time and this integration was performed using first order upwind differencing in space and fully implicit in time. The SIMPLE algorithm was used to couple pressure and velocity. The timestep was chosen equal to $10^{-2}s$, as smaller ones do not give better accuracy, as already pointed out by Mazzei and Lettieri (2008). For each time step, a number of internal iterations ensuring constant values of residuals of all variables were performed. Thereby, the number of internal iterations ranged between a minimum of 100 and a maximum of 250. Stationary solution was considered reached when unchanged value of the bed height and voidage were obtained. Under-relaxation factors equal to 0.20 were adopted for all of the flow quantities.

Working and initial conditions No-slip boundary conditions were applied to the left and right walls for both phases. A pressure of $1.015 \cdot 10^5$ Pa was set at the domain upper boundary and a uniform inlet velocity was specified at the bottom of the bed for the gas phase. The solid mass fluxes are set to zero on all boundaries. Front and rear boundary planes were considered symmetry planes.

In its initial state, the bed is fixed, 500 mm high and with a voidage equal to 0.5, which is the average experimental minimum fluidization voidage. At time $t = 0$ the superficial velocity u is increased stepwise from zero to the final operating value, which is sufficient to fluidize the system and to bring it to homogeneous operating conditions.

All the simulations were run at ambient pressure and with temperature from ambient up to 650°C. Fluidizing gas was nitrogen and the three different FCC catalysts, previously described, were simulated. The working conditions adopted in the simulations are the same as in experiments, except from the particles diameter, which was chosen as that one giving the same experimental terminal velocity, u_t^*. In the following, the numerical results will be compared with the available experimental data (Lettieri et al., 2001 and 2002) for a quantitative analysis and evaluation of the simulation strategy.

5.9.2 Segregating bed simulation details

Numerical schemes and techniques For the vessel under investigation, a two-dimensional geometry (120 mm wide and 1 000 mm high) and three structured computational grids with cells of 5 $mm \times 5$ mm, 2.5 $mm \times 2.5$ mm and 1.25 $mm \times 1.25$ mm, consisting of a total of 4 800, 19 200 and 76 800 computational cells, respectively, were defined. Apart from the 2D approximation, a further saving of computational effort was obtained by limiting the height of the domain with respect the reference experimental bed. This limitation was possible, since in any case at the selected working conditions the dispersed phases could never reach elevation higher than 500 mm.

The continuity, momentum and granular temperature equations as implemented in the finite volume general purpose CFD code Fluent 6.3 (Ansys Inc.) were numerically solved in a Cartesian coordinate system. For the present case of 2D three-phase flow, the model includes twelve equations in as many unknowns: the three volume fractions, the six velocity components, the pressure and the two granular temperatures. To account for the fluid-particle interaction force term (Eq. 5.4), a routine developed by Mazzei and Lettieri (2008) was implemented into the code.

The conservation equations were integrated in space using two different discretization schemes for the convective terms, namely first order upwind and the higher order QUICK schemes; while the integration in time was performed using a fully implicit scheme. In order to couple pressure and velocity, the SIMPLE algorithm was used. Different simulations were performed using a time step of $10^{-2}s$, $10^{-3}s$ and $10^{-4}s$. In a specific case a time step of $7 \cdot 10^{-3}$ s was also used. For each time step, a number of internal iterations ensuring constant values of residuals of all variables were performed. Thereby, the number of internal iterations ranged between a minimum of 100 and a maximum of 250.

Stationary solution was considered reached when unchanged values of the jetsam volume fraction was reached in each layer of the bed. Under relaxation factors equal to 0.20 for all of the flow quantities were adopted.

All simulations were run in serial mode on a Dell Precision 690 workstation with two Quad-core processors Intel Xeon at 2.33 GHz and 8 Gbytes RAM. Typical computing times for a grid of 5 $mm \times 5$ mm and a time step of $10^{-3}s$ were about 4.33 computational hours every 1 s of simulation.

It is important to point out that, in unsteady-state problems, the numerical solution of the model equations in each time step is obtained in an iterative way, until a specified convergence criterion is reached. However, if the time step is too small compared to the time scale of the property variation, the predicted change of a cell property between a time step and the next one may become smaller than the fixed convergence criterion, resulting in a larger overall error. On the other hand, too large time step can result in a sharp change of a cell property between a time

step and the next one, leading to less accurate results (Cornelissen et al., 2007).

The prediction of a cell property also depends on the cell size and on the coupling between mesh size, time step and convergence criteria. With smaller cell dimensions, the fluid traverses fewer cells in each time step, resulting in a smaller cell property change between a time step and the next one.

The dimensionless Courant number N_C gives an idea of the portion of a cell traversed by the fluid in one time step , relating time step, Δt, grid size in the direction of the flow, Δx, and the gas velocity, U. It is defined in the following way:

$$N_C = u\frac{\Delta t}{\Delta x} \tag{5.29}$$

It is worth observing that although an implicit time integration method is adopted here, which ensures the computation stability at any Courant number, it has been demonstrated that for Courant number exceeding certain values a rapid loss of accuracy can be found (Hirsh, 2007).

Keeping the Courant number low improves accuracy, decreases oscillations and numerical dispersion. Gobin et al. (2001) proposed a maximum Courant number of 0.3. However, Cornelissen et al. (2007) state that also a smaller time step increases the relative error and therefore low Courant numbers also give inaccurate results (for a given convergence criterion). Therefore, for mono-disperse liquid-fluidized suspensions Cornelissen et al. (2007) proposed to adopt a Courant number between 0.03 and 0.3. In this work, it was ranged between 0.0036 and 1.2, since the same grid size at different time step and the same time step for different grid sizes at different inlet gas velocities were simulated.

Working, boundary and initial conditions No-slip boundary conditions were applied to the left and right walls for each phase, a pressure of $1.01 \cdot 10^5 Pa$ was set at the domain upper boundary and a uniform inlet velocity was specified at the bottom of the bed for the gas phase. The fluid distribution at the inlet, which was experimentally performed by a brass distributor, was treated as perfectly uniform (all fluid entering at the superficial velocity), since the distributor geometry could not be described in detail. In any case the distributor geometry was shown not to greatly affect the steady state overall bed voidage predictions (Cornelissen et al., 2007). The solid mass fluxes are set to zero on all boundaries. Front and rear boundary planes were considered symmetry planes.

All the simulations were run at ambient pressure and temperature, and all the working conditions adopted in the simulations were the same as in the experiments. As in the type B experiments of Olivieri et al., in the CFD simulations, at the beginning the bed is fixed and completely mixed, then the gas velocity is increased instantaneously at a pre-set value and the bed is kept fluidized for the

time necessary to reach a steady state condition. In the simulation there is no need to defluidize the bed, because the axial distribution can be directly calculated.

To determine the time-dependent jetsam volume fraction in each layer, a purposely written routine was used. It calculates at each time step the bed height and divides the bed in six layers, then it calculates the average jetsam volume fraction in each layer and saves it.

Simulations were run for different bed compositions, in particular the jetsam volume fraction on a fluid-free basis (that is, not accounting for the interparticle voidage) was varied in the range from 0.1 to 0.8, and the inlet gas velocities from 3.9 $cm\ s^{-1}$ to 21.5 $cm\ s^{-1}$. Table 5.5 summarizes all the different simulation runs for different operating conditions (named cases) and numerical set-ups (named simulation numbers), ordered for increasing jetsam volume fraction and gas velocity.

Calculated results are compared with available experimental data from Olivieri et al. (2004) for a quantitative analysis and evaluation of the simulation strategy.

5.10 Results and discussion

5.10.1 Homogeneous beds

CFD simulations were carried out for the three FCC catalysts at different temperature and gas velocity. Bed height and voidage were monitored over time and stationary solution was considered reached when unchanged value of the bed height and voidage were obtained. The time t_e required for the system to attain a steady state (u, h) starting from conditions of minimum fluidization (which can be assumed to be reached instantaneously from packed-bed conditions, if the superficial velocity is changed stepwise from zero to u) can be estimated through the relation of Mazzei and Lettieri (2008):

$$t_e = 3\frac{h - h_{mf}}{u - u_{mf}} \tag{5.30}$$

The time needed to reach the stationary solution in the present system ranges between 50 s and 130 s, depending on the temperature and gas velocity.

Figure 5.2 shows the plot of the averaged bed height versus time for FCC3 catalysts at 650°C and at 0.4 cms^{-1}, which is one of the cases with longer transient condition.

For the first FCC catalysts, FCC1, at 20°C, different types of simulations were run. First of all, some simulations were run using the most well-known expressions advanced to model the drag force for fluidized systems of uniformly dispersed particles. The model of Wen and Yu (1966) and the Gidaspow model (Gidaspow et

Table 5.5: Simulated test cases of the segregating bed

Case	X_{j0} [-]	u $[cms^{-1}]$	Simulation number	Δx $[mm]$	Δt $[s]$	Discretization order	N_C [-]
A	0.1	14	2	5	10^{-3}	1^{st}	0.028
	0.1	14	5	2.5	10^{-3}	1^{st}	0.056
B	0.1	18	2	5	10^{-3}	1^{st}	0.036
	0.1	18	5	2.5	10^{-3}	1^{st}	0.072
C	0.1	21.5	2	5	10^{-3}	1^{st}	0.043
D	0.2	3.9	2	5	10^{-3}	1^{st}	0.0078
	0.2	3.9	5	2.5	10^{-3}	1^{st}	0.016
E	0.2	15.2	1	5	10^{-2}	1^{st}	0.30
	0.2	15.2	2	5	10^{-3}	1^{st}	0.030
	0.2	15.2	3	5	10^{-2}	quick	0.30
	0.2	15.2	4	2.5	10^{-2}	1^{st}	0.61
	0.2	15.2	5	2.5	10^{-3}	1^{st}	0.061
	0.2	15.2	7	1.25	10^{-2}	1^{st}	1.2
	0.2	15.2	8	1.25	10^{-3}	1^{st}	0.12
	0.2	15.2	9	5	$7 \cdot 10^{-3}$	1^{st}	0.21
F	0.2	16.5	2	5	10^{-3}	1^{st}	0.033
G	0.2	20	1	5	10^{-2}	1^{st}	0.40
	0.2	20	2	5	10^{-3}	1^{st}	0.040
	0.2	20	3	5	10^{-2}	quick	0.40
	0.2	20	4	2.5	10^{-2}	1^{st}	0.80
H	0.5	9	2	5	10^{-3}	1^{st}	0.018
	0.5	9	4	2.5	10^{-2}	1^{st}	0.36
	0.5	9	5	2.5	10^{-3}	1^{st}	0.036
	0.5	9	6	2.5	10^{-4}	1^{st}	0.0036
	0.5	9	8	1.25	10^{-3}	1^{st}	0.072
I	0.5	13	2	5	10^{-3}	1^{st}	0.026
	0.5	13	5	2.5	10^{-3}	1^{st}	0.052
	0.5	13	8	1.25	10^{-3}	1^{st}	0.10
J	0.8	4.4	2	5	10^{-3}	1^{st}	0.0088
	0.8	4.4	5	2.5	10^{-3}	1^{st}	0.018
	0.8	4.4	8	1.25	10^{-3}	1^{st}	0.035
K	0.8	6.5	2	5	10^{-3}	1^{st}	0.013
	0.8	6.5	5	2.5	10^{-3}	1^{st}	0.026
	0.8	6.5	8	1.25	10^{-3}	1^{st}	0.052

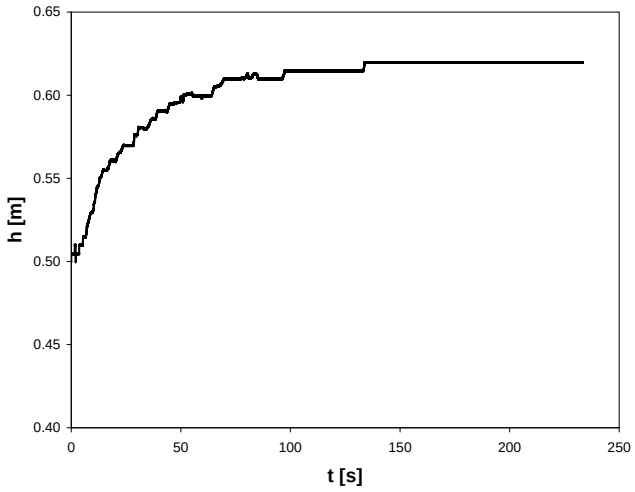

Figure 5.2: Bed height variation of a particulate system that, starting from packed-bed conditions, becomes homogeneously fluidized (FCC3, $T = 650$ °C, $u = 0.4$ $cm\ s^{-1}$)

al., 1992), which is a combination of the Wen and Yu (1966) model and the Ergun equation (Ergun, 1952), were used. These simulations were run using the real particle diameter, d_d. Then simulations were run using the closure of Mazzei and Lettieri (2007) with either the real particle diameter, d_d, and the n value calculated from Eq. 5.11, or the experimental parameters, d_d^* and n^*. The stationary values of the bed voidage for all the simulations were then compared with experimental bed voidage. Results are reported in Figure 5.3, where it is evident that it is necessary to use the Richardson and Zaki equation with experimental parameters in order to match the experimental trend of bed voidage with velocity. As a matter of fact, the experimental value of the Richardson-Zaki parameters n^*, for FCC1 at 20°C, is equal to 9.6, and only the present model is able to predict its value, which is found to be 9.53. Values of 4.60, 4.07 and 4.55 are found with the Wen&Yu model, the Gidaspow model and the Richardson-Zaki model with theoretical parameters, respectively.

All the other results reported in the present paper refers to simulations run using the Mazzei and Lettieri (2007) closure with experimental Richardson and Zaki parameters. In particular in Figure 5.4, a parity plot of the predicted and experimental bed voidage for all the three different FCC catalysts, at different temperature and velocity is presented. The agreement with experimental data is apparent, since all the points are in the 4% interval of confidence.

In Table 5.6 computational bed voidage for all three FCC catalysts at different temperature and velocity is reported. As a result, the model is capable of predict-

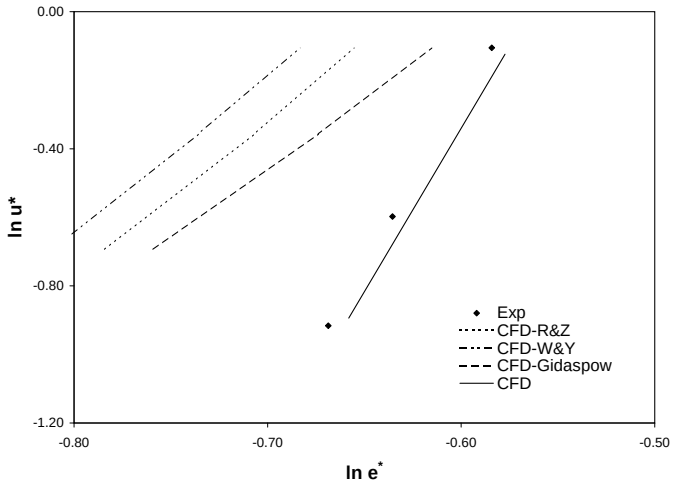

Figure 5.3: Voidage versus velocity for FCC1 at 20°C from experiments (Exp), from computations with experimental (CFD) and theoretical (CFD-R&Z) values of the Richardson-Zaki equation parameters, from computations using the Wen & Yu (CFD-W&Y) and the Gidaspow (CFD-Gidaspow) model.

ing the bed expansion for all the three FCC catalysts at the different simulated operating conditions.

In Figure 5.5, it is reported the computational and experimental voidage versus velocity for FCC3 catalyst at 20°C, 200°C, 400°C and 650°C. Simulations are able to predict the trend of the voidage with velocity at different temperatures, although a small over-prediction of the bed voidage is present. The same type of plot was obtained for FCC1 and FCC2 catalysts.

Once the trend of bed voidage with velocity is obtained, it is possible to calculate the computational Richardson-Zaki parameters, u_t^* and n^*, at each temperature and for each FCC catalysts. These values are reported in Table 5.7.

Computational terminal velocity is obtained extrapolating in the $\ln u - \ln \epsilon$ plot the computed lines till the value of $\epsilon = 1$. A small variation in the computational bed voidage produces a bigger one in the calculation of the terminal velocity because of the amplifying effect of the extrapolation operation. In any case, the model is able to predict this parameter with a 20% interval of confidence (see Figure 5.6).

The Richardson-Zaki parameter n represents the slope of the line in the $\ln u - \ln \epsilon$ plot and computational values are close to experimental ones, as it is possible to observe in Figure 5.7. All the values are within the 4% interval of confidence. This means that the model is able to predict fairly well trend of bed voidage with velocity in all the simulated cases in the operating conditions typical of homogeneous fluidization. The bigger interval of confidence for the terminal velocity come from

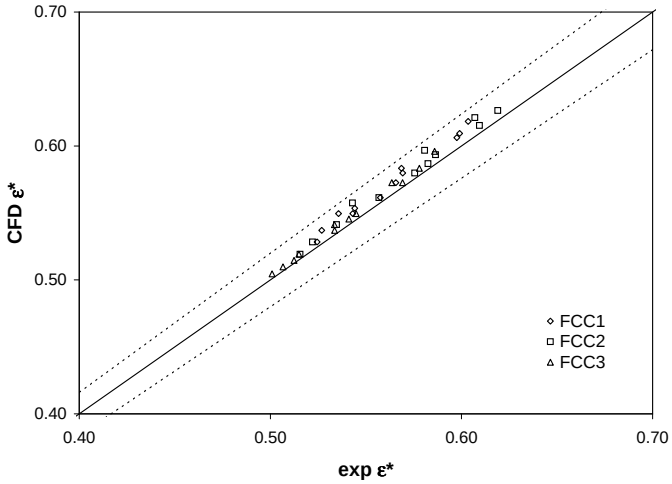

Figure 5.4: Comparison between computational and experimental bed voidage for all FCC catalysts at different temperature and velocity (dashed lines represents 4% interval confidence).

Table 5.6: Computational values of voidage for all FCC catalysts at different temperature and velocity

T	FCC1		FCC2		FCC3	
	u $[cm\ s^{-1}]$	ϵ^* [-]	u $[cm\ s^{-1}]$	ϵ^* [-]	u $[cm\ s^{-1}]$	ϵ^* [-]
20	0.5	0.528	0.3	0.519	0.35	0.510
	0.7	0.550	0.6	0.561	0.4	0.519
	0.9	0.561	0.9	0.587	0.6	0.545
200	0.4	0.550	0.3	0.557	0.2	0.505
	0.6	0.583	0.5	0.597	0.3	0.537
	0.9	0.618	0.7	0.621	0.5	0.583
400	0.3	0.537	0.2	0.528	0.2	0.515
	0.5	0.580	0.4	0.580	0.3	0.550
	0.7	0.609	0.6	0.615	0.4	0.573
650	0.3	0.554	0.2	0.541	0.2	0.541
	0.4	0.573	0.4	0.593	0.3	0.573
	0.6	0.606	0.6	0.626	0.4	0.596

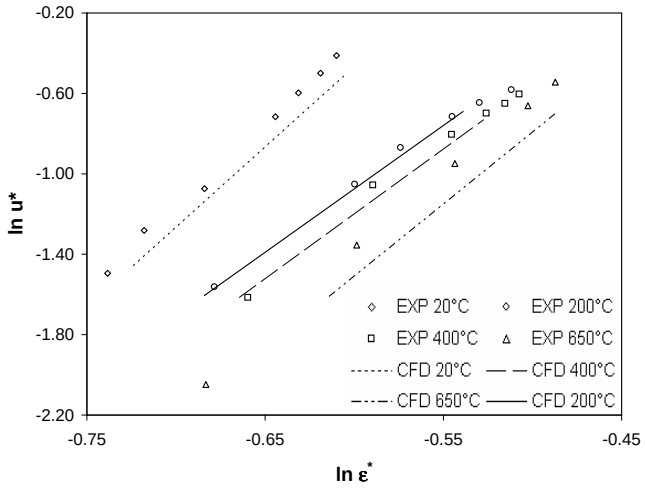

Figure 5.5: Computational and experimental voidage versus velocity for FCC3 at different temperature

Table 5.7: Computational values of n^* and u_t^*

T	FCC1		FCC2		FCC3	
	n^* [-]	u_t^* $[cm\ s^{-1}]$	n^* [-]	u_t^* $[cm\ s^{-1}]$	n^* [-]	u_t^* $[cm\ s^{-1}]$
20	9.528	216.2	8.965	106.8	8.024	77.5
200	6.878	24.5	7.802	28.5	6.304	15.0
400	6.700	19.3	7.222	20.2	6.450	14.5
650	7.564	26.6	7.515	20.2	7.199	16.6

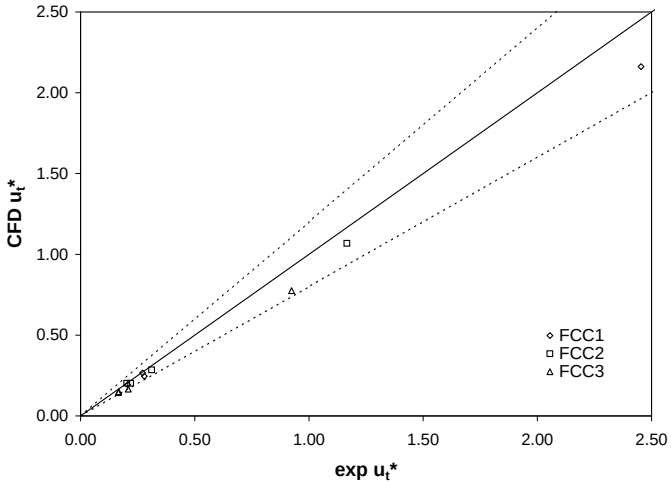

Figure 5.6: Comparison between computational and experimental terminal velocity values for all FCC catalysts at different temperature and velocity (dashed lines represents 20% interval confidence).

the small over-prediction of the bed voidage, which is amplified in the extrapolation operation by the small difference in the lines' slope. It means that with higher bed voidage, i.e. higher velocity, Richardson and Zaki equation with experimental parameters does not match the experimental extrapolated line as good as at lower velocity. However, at higher velocity the bed is not homogeneously fluidized any more and bubbling effects are present. This means that other phenomena takes place in the system and both experimental and computational bed voidage cannot be described any more by the Richardson and Zaki equation with the same parameters. Moreover, it is important to notice that, since the present model solves equation of change for each phase, bubbling conditions can be described by the present model without any changes, since the formation of bubbles is fully predictive.

The trend of the computational Richardson and Zaki parameters with temperature is also compared with experimental values. In Figures 5.8 and 5.9, trend of n^* and u_t^* with temperature is reported for FCC1 catalyst (similar plots are obtained for FCC2 and FCC3). Since simulations were run only at 20°C, 200°C, 400°C and 650°C, only four computational points for each FCC catalyst are present, while the values at all different temperature experimentally examined are reported. The agreement with experimental trend is apparent.

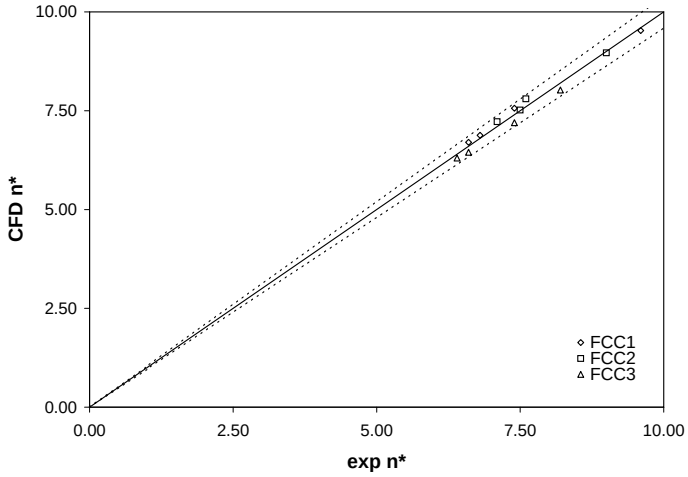

Figure 5.7: Comparison between computational and experimental n values for all FCC catalysts at different temperature and velocity (dashed lines represents 4% interval confidence).

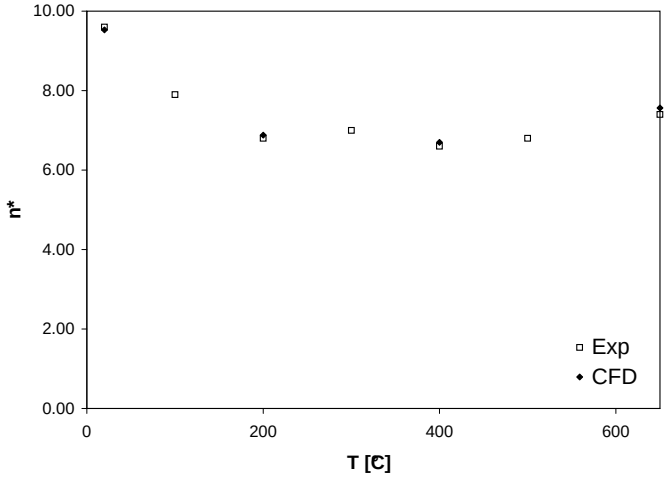

Figure 5.8: Effect of temperature on experimental and calculated n^* values for FCC1.

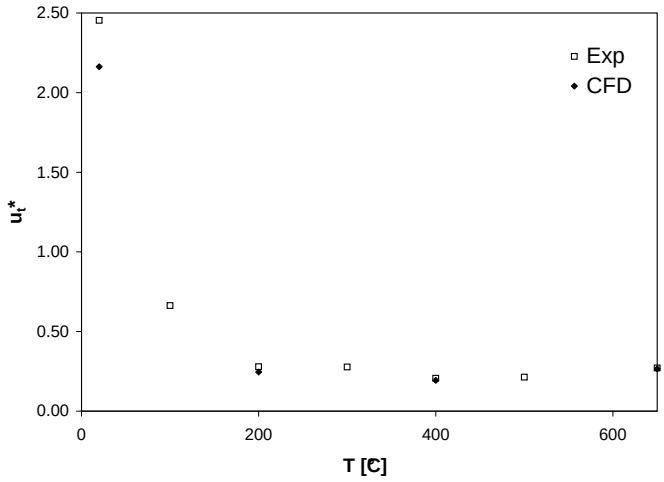

Figure 5.9: Effect of temperature on experimental and calculated u_t^* values for FCC1.

5.10.2 Segregating beds

Segregation profiles and dynamic results

The verification of the numerical uncertainties of the simulations was started with the analysis of the case of bed filled with a mixture at jetsam volume fraction X_{j0}=0.2 and fluidized at a gas velocity equal to 20 $cm\ s^{-1}$, at which conditions experimental results report a completely mixed bed (case G in Table 5.5). At these operating conditions the simulations were repeated changing the grid size, the time step and the order of discretization of the convective terms (see Table 5.5). Simulation 1 refers to a grid with cell size of 5 $mm \times 5\ mm$, a time step of $10^{-2}s$ and a first order discretization scheme, while simulation 2 is different only for the time step taken equal to $10^{-3}s$; in simulation 3 a QUICK order discretization scheme was used, while simulation 4 has a different grid, with a cell size halved in the two directions. The jetsam volume fractions on a fluid-free basis along the bed obtained from these four types of simulations are reported in Figure 5.10 together with the experimental data. As it is possible to observe, the coarser grid combined with the bigger time step (simulation 1) gives results really far from the completely mixed state. Simulation 3 and 4 give larger results, but the best agreement with experimental data is obtained through simulation number 2, for which the Courant number is 0.040.

Numerical set-up of simulation number 2 (cell size of $5mm \times 5mm$ and time step of $10^{-3}s$) was found to be a good set-up for mono-disperse gas-fluidized suspensions by Busciglio et al. (2009), who also demonstrated the negligible difference with a

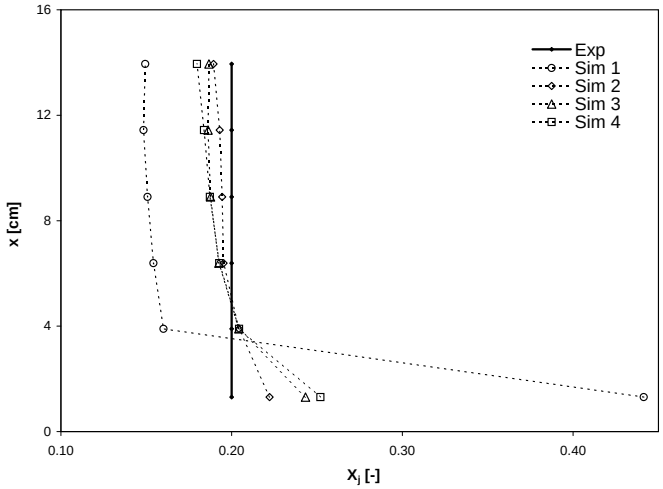

Figure 5.10: Jetsam volume fraction on a fluid-free basis along the bed at $X_{j0} = 0.2$ and $u = 20\ cm\ s^{-1}$ (case G).

3D simulation, a smaller grid size and time step. The same numerical set-up gave good results also to Taghipour et al. (2005) and Goldschmidt et al. (2004) for a mono-disperse gas-solid bed.

From Figure 5.10 it is also possible to observe that increasing the order of discretization, in this case, can be sufficient to improve the result accuracy while maintaining coarser grid and time step.

The same simulations choices were then adopted for simulating a condition in which the bed is not completely mixed, i.e. $X_{j0} = 0.2$ and the gas velocity is equal to 15.2 $cm\ s^{-1}$ (case E). In Figures 5.11, 5.12, 5.13 and 5.14 the change with time of jetsam volume fraction in the top and bottom layers is reported for the different simulations. As it is possible to observe, in all cases at the initial condition the bed is completely mixed and the jetsam volume fraction is equal to 0.2 in both the top and bottom layers, but significant differences can be observed in the calculated dynamic trends depending on the numerical settings. In particular, in simulation 1the steady composition of the top and bottom layer, which is attained after about 25 s, is approximately equal to 0.1 and 0.75, respectively, while the corresponding experimental data are equal to 0.17 and 0.25 respectively. The improvement of the results obtained with simulations 3 and 4, with respect to simulation 1, is absolutely not sufficient, while a good agreement between the computed and experimental steady solids composition at the selected locations is obtained only with simulation 2. Also, the time needed to reach the steady state is quite different for the four simulations, being for simulation 3 and 4 much longer than for the other two simulations. However, no direct comparison is performed between the time required

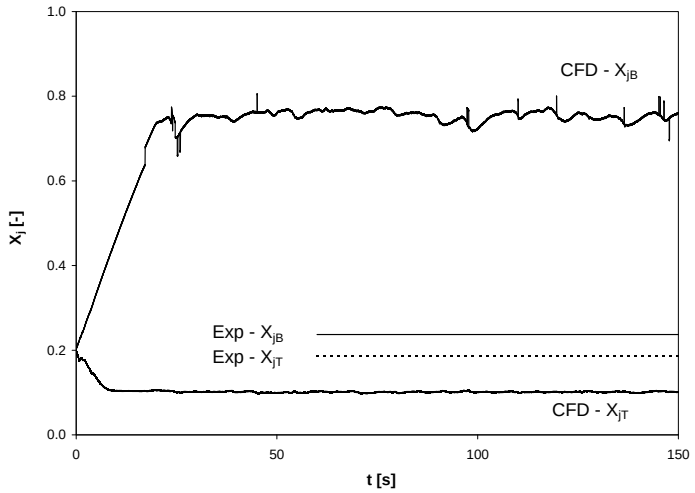

Figure 5.11: Jetsam volume fraction on a fluid-free basis of the top and bottom layers during time at $X_{j0} = 0.2$ and $u = 15.2\ cm\ s^{-1}$ (case E) for simulation number 1.

to reach a steady state condition and the corresponding experimental value, due to the lack of precise information relevant to each of the selected simulated cases.

In this case, the discretization order was found to have a small influence. For gas-solid fluidized beds, the difference between first and second order schemes has mainly been discussed with reference to the boundaries of gas bubbles (Hulme et al., 2005), with the second-order discretization scheme giving much sharper boundaries, while in liquid-solid fluidized bed Cornelissen et al. (2007) found small differences between first and second order discretizations. In this work a general statement on the influence of the discretization order cannot be identified because it depends on operating conditions. At the same operating conditions (case E), simulation number 5, 7, 8 and 9 were also run. In particular, simulation 5 refers to a grid size of 2.5 $mm \times 2.5\ mm$ with a time step of $10^{-3}\ s$, simulation 7 to a grid size of 1.25 $mm \times 1.25\ mm$ with a time step of $10^{-2}\ s$, simulation 8 to a grid size of 1.25 $mm \times 1.25\ mm$ with a time step of $10^{-3}\ s$, and simulation 9 to a grid size of 5 $mm \times 5\ mm$ with a time step of $7 \cdot 10^{-3}\ s$. Results show that only a time step size of $10^{-3}\ s$ (simulation 2, 5 and 8) seems to be able to reproduce experimental data, independently of grid size and discretization order, while in all the other cases the simulations give results far from experimental data (see Figure 5.15), in spite of what it has been shown for case G.

The average absolute errors (calculated as an average between the absolute error at the bottom and at the top of the bed of the jetsam volume fraction) obtained with simulations of case E are plotted versus the Courant number in Figure 5.16.

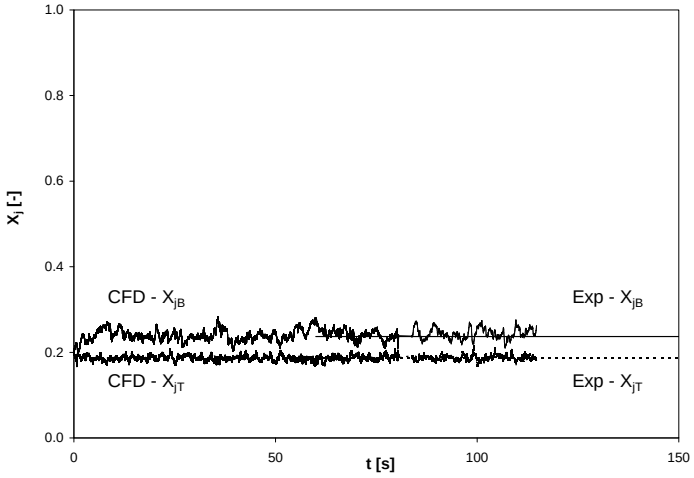

Figure 5.12: Jetsam volume fraction on a fluid-free basis of the top and bottom layers during time at $X_{j0} = 0.2$ and $u = 15.2\ cm\ s^{-1}$ (case E) for simulation number 2.

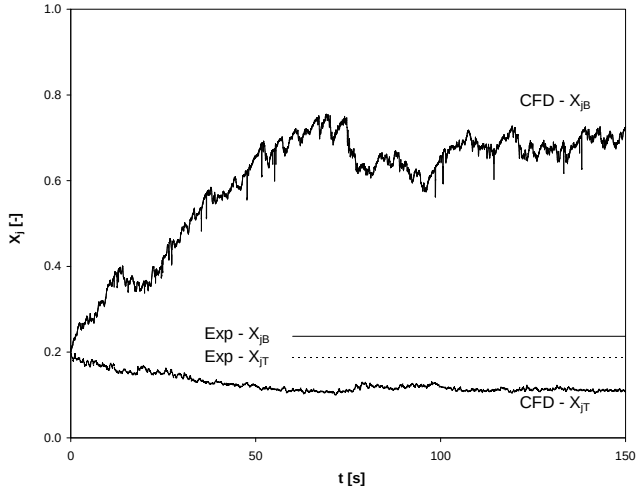

Figure 5.13: Jetsam volume fraction on a fluid-free basis of the top and bottom layers during time at $X_{j0} = 0.2$ and $u = 15.2\ cm\ s^{-1}$ (case E) for simulation number 3.

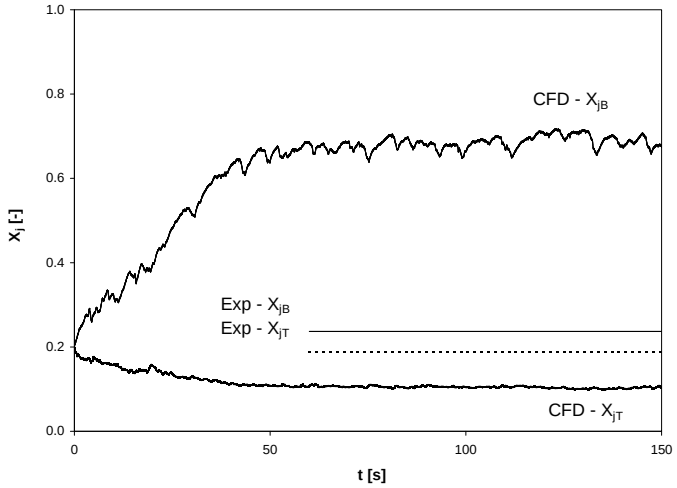

Figure 5.14: Jetsam volume fraction on a fluid-free basis of the top and bottom layers during time at $X_{j0} = 0.2$ and $u = 15.2\ cm\ s^{-1}$ (case E) for simulation number 4.

These results show that there is a threshold value above which simulations give errors higher than 20%.

For the same initial jetsam volume fraction ($X_{j0} = 0.2$), simulation number 2 was also run at two different inlet gas velocities: 3.9 $cm\ s^{-1}$ and 16.5 $cm\ s^{-1}$ (cases D and F). The first velocity is slightly higher than the flotsam minimum fluidization velocity (Olivieri et al., 2004), while the last one is equal to the minimum velocity at which the bed is completely mixed at the jetsam volume fraction under consideration. Results are reported in Figures 5.17 and 5.18. At the higher velocity the calculated bed is completely mixed as in the experiments (Figure 5.17), while at the lowest velocity the bed results quite segregated in both experiments and calculations (figure 5.18). Simulation results are in fair agreement with the experimental data and the difference in the jetsam volume fraction that is more pronounced at the bottom of the bed can be due to model uncertainties rather than to numerical issues, since the same results were found also reducing grid size (simulation 5).

Simulations were also run for an initial jetsam volume fraction X_{j0} equal to 0.1. At this composition, the bed behaviour at a gas inlet velocity equal to 14 $cm\ s^{-1}$ (case A), 18 $cm\ s^{-1}$ (case B) and 21.5 $cm\ s^{-1}$ (case C) was investigated and simulation 2 gives an average absolute error of 3.5%, 2.6% and 0.2%, respectively. For cases A and B, simulation 5 was also run and an average absolute error of 2.7% and 2.2% was found, respectively.

In agreement with previous findings, for cases A, B, C, D, E, F and G the

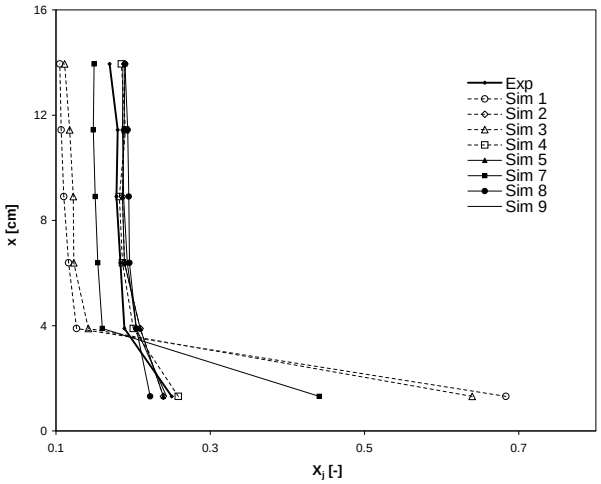

Figure 5.15: Jetsam volume fraction on a fluid-free basis along the bed at $X_{j0} = 0.2$ and $u = 15.2\ cm\ s^{-1}$ (case E).

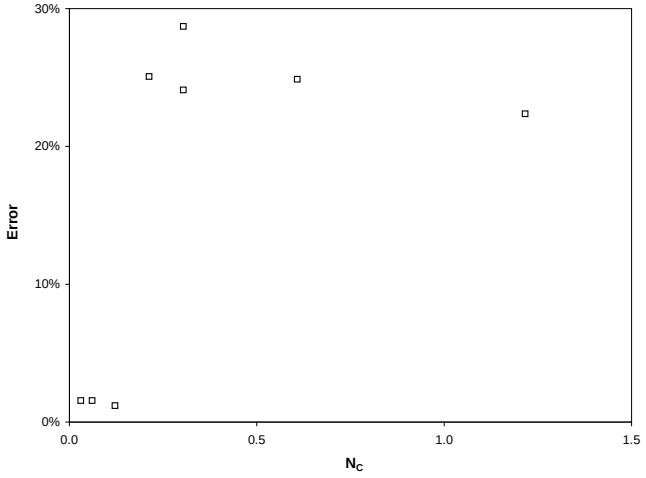

Figure 5.16: Average absolute error vs. Courant number for case E.

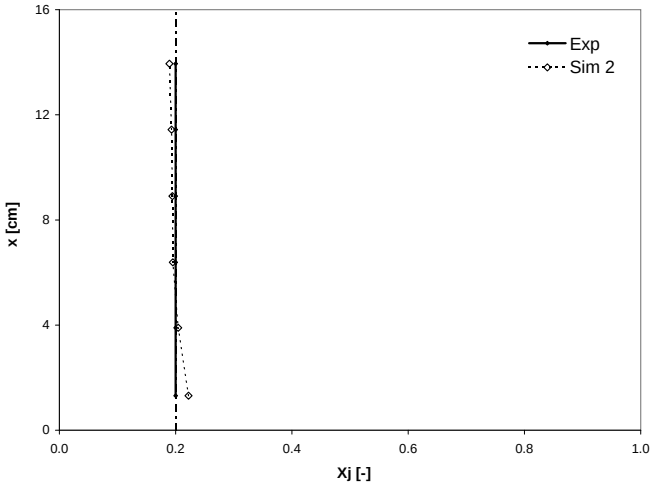

Figure 5.17: Jetsam volume fraction on a fluid-free basis along the bed at $X_{j0} = 0.2$ and $u = 16.5\ cm\ s^{-1}$ (case F).

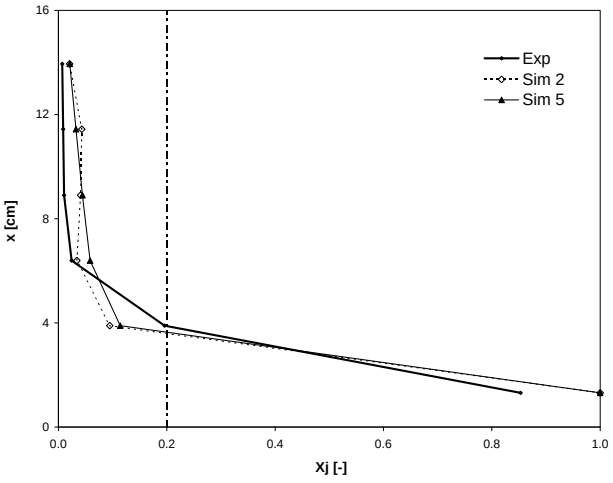

Figure 5.18: Jetsam volume fraction on a fluid-free basis along the bed at $X_{j0} = 0.2$ and $u = 3.9\ cm\ s^{-1}$ (case D).

numerical set up of simulation number 2 ($\Delta x = 5\ mm$, $\Delta t = 10^{-3}\ s$) was found to provide reasonably accurate results for conditions going from the completely segregated to steadily fluidized and completely mixed bed.

Grid size and time step sensitivity analysis

In order to more deeply address the effective influence of grid size on simulation results, the values of X_{jB} and X_{jT} for case E ($X_{j0} = 0.2$, $u = 15.2\ cm\ s^{-1}$) and a time step of $10^{-3}\ s$ at different cell sizes are shown in Figure 5.19. The grid density has only a negligible influence on the simulation results at these operating conditions (the average absolute error ranges between 1.2% and 1.6%). This is not true at different air inlet velocity and jetsam volume fraction, for example in case H, which refers to a jetsam volume fraction equal to 0.5 and an inlet gas velocity equal to 9 $cm\ s^{-1}$, which is intermediate between the flotsam minimum fluidization velocity and the minimum velocity at which the bed is completely mixed at the present composition. In this case, passing from a grid size of 5 $mm \times 5\ mm$ to 2.5 $mm \times 2.5\ mm$, the jetsam volume fraction at the top and at the bottom of the bed shows a substantial change (see Figure 5.20), which improves the accuracy of the results (the average absolute error changes from 38.7% to 9.1%). A further improvement is achieved with a smaller grid size (the average absolute error reaches the value of 4.7%). It is worthwhile noticing that the greatest accuracy of the prediction was obtained with the greatest Courant number. These results clearly show how at these operating conditions the range of grid size used is not small enough to know if simulation 8 is grid independent. Actually, with these three grids, we can only state that the simulation run on the coarser grid (simulation 2) is out of the asymptotic range of grid convergence (Coleman and Stern, 1997). Similar results are found for case I, which refers to the same initial jetsam volume fraction ($X_{j0} = 0.5$) and a different gas inlet velocity ($u = 13\ cms^{-1}$).

Simulations with the same numerical set up were run also for case J ($X_{j0} = 0.8$, $u = 4.4\ cm\ s^{-1}$) and K ($X_{j0} = 0.8$, $u = 6.5\ cm\ s^{-1}$). In case J, the gas inlet velocity is intermediate between the flotsam minimum fluidization velocity and the minimum velocity at which the bed is completely mixed at the present composition, while in case K it is similar to the velocity at which the bed is completely mixed. In these two cases, a different behaviour with respect to case H is observed (see Figure 5.21 relative to case J). No clear differences occur between simulations 2 and 5 (the average absolute error changes from 37.1% to 37.6%): these grids are too coarse in this case. However, an improvement of the results was found with simulation 8, which gave an average absolute error of 10.1%.

The accuracy of simulation 8 is quite good for case E, with an average absolute error of 1.2%, worse in case H, with an average absolute error of 4.7%, and even worse in case J, where the error increases to 10.1%. These results clearly show

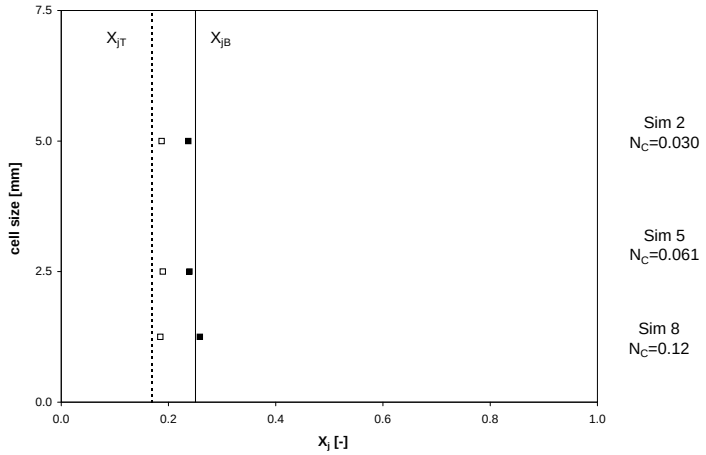

Figure 5.19: Calculated jetsam volume fraction at the top (open symbols) and the bottom (solid symbols) of the bed with a time step equal to $10^{-3}s$ and different cell size at $X_{j0} = 0.2$ and $u = 15.2\ cm\ s^{-1}$ (case E). Dashed and continuum lines represents experimental jetsam volume fraction at the top and bottom of the bed, respectively.

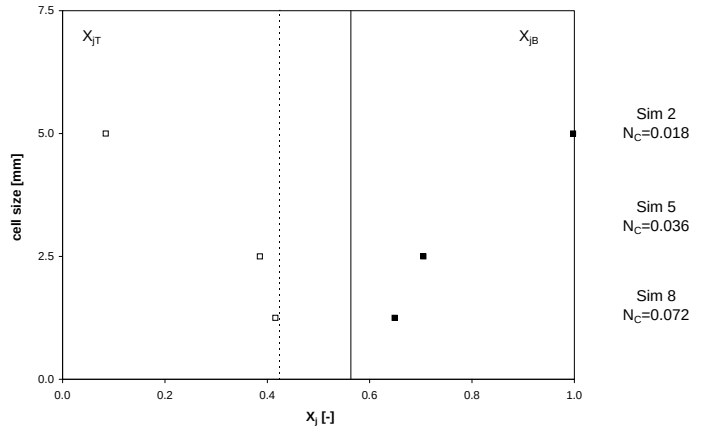

Figure 5.20: Calculated jetsam volume fraction at the top (open symbols) and the bottom (solid symbols) of the bed with a time step equal to $10^{-3}s$ and different cell size at $X_{j0} = 0.5$ and $u = 9\ cm\ s^{-1}$ (case H). Dashed and continuum lines represents experimental jetsam volume fraction at the top and bottom of the bed, respectively.

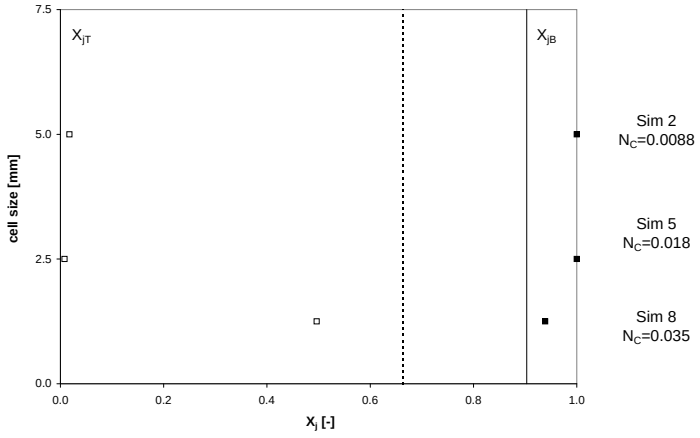

Figure 5.21: Calculated jetsam volume fraction at the top (open symbols) and the bottom (solid symbols) of the bed with a time step equal to $10^{-3}s$ and different cell size at $X_{j0} = 0.8$ and $u = 4.4\ cm\ s^{-1}$, (case J). Dashed and continuum lines represents experimental jetsam volume fraction at the top and bottom of the bed, respectively.

that the simulation accuracy depends on the operating conditions, since the same numerical set up can give an error ranging from 1.2% to 10.1%. A particular numerical set-up can reproduce quite well the behaviour of the system in some operating conditions, but a higher spatial and temporal resolution is necessary at different conditions.

A study on the influence of the time step on simulation results was also run for case H. In Figure 5.22, simulation results at different time step for the same grid size are compared with the experimental data. In particular, simulations for a grid size of 2.5 mm × 2.5 mm and a time step of $10^{-2}s$, $10^{-3}s$ and $10^{-4}s$ are reported. Increasing the time resolution, the accuracy of the results increases (the average absolute error ranges between 41.1% and 4.7%). In this case too, it would be necessary a further time step refinement respect to simulation 6 in order to state if these results are absolutely independent from the time step. However these simulations were not affordable with the currently available computational resources.

Possible guidelines for the time step and grid size choice

Due to the importance of the numerical choices, it is critical to identify the operating conditions that need a better grid and time resolution, and to test the numerical

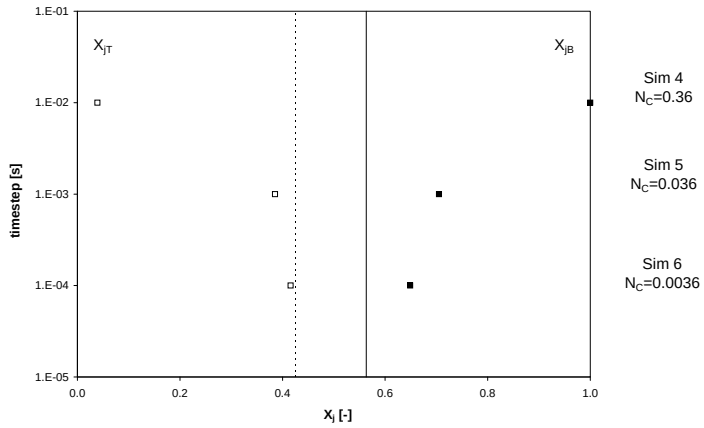

Figure 5.22: Calculated jetsam volume fraction at the top (open symbols) and the bottom (solid symbols) of the bed at $X_{j0} = 0.5$ and $u = 9\ cm\ s^{-1}$ (case H) for different time step with a cell size equal to 2.5 mm. Dashed and continuum lines represents experimental jetsam volume fraction at the top and bottom of the bed, respectively.

set-up in each particular case. Only after a careful selection of the numerical parameters for each specific operating condition the influence of different geometrical configurations and models can be evaluated.

A parameter that can be used is the Courant number, defined in Eq. 5.29. The Courant number for case H and for simulations 4, 5 and 6 is 0.36, 0.036 and 0.0036, respectively (see Figure 5.22). In this case a Courant number smaller than 0.3, which is the upper limit value proposed by Gobin et al. (2001) and by Cornelissen et al. (2007), seems to be a good choice in order to produce accurate results. However, the study of the influence of grid size in case H (see Figure 5.20) shows that the Courant number has to be larger than 0.03, as proposed by Cornelissen et al. (2007), in contrast with the results of simulation 6, which have shown that the better accuracy of the CFD simulation is obtained with a Courant number of 0.0036 (<0.03), with an average absolute error of 4.72%. These results seem to suggest that the Courant number alone does not provide a guideline for identifying the appropriate numerical settings for the solution of the model equations.

Figure 5.23 reports the average absolute error versus the Courant number for all the different simulations. For simulations with a gas inlet velocity in the range between the minimum fluidization velocity and the minimum velocity at which the bed is steadily fluidized and mixed (i.e. excluding case G), Courant numbers larger than approximately 0.15 always give results with an error larger than 20% (the

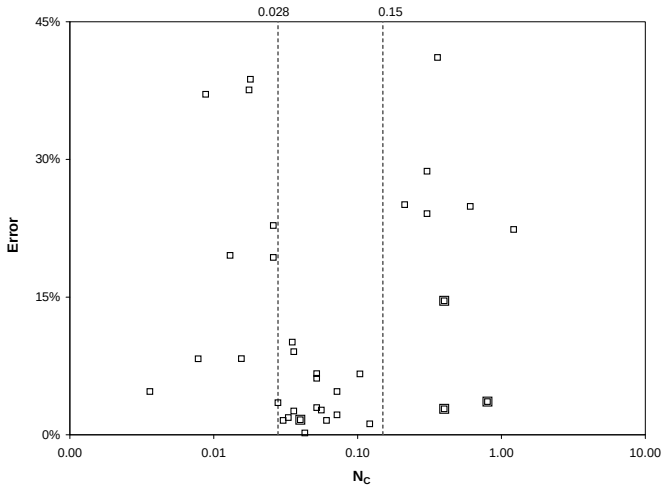

Figure 5.23: Average absolute error vs. Courant number for all the simulated test cases. Double squares represent case G.

average absolute error ranges from 22.4% to 41.1%), while the error is lower (in the range 2.83% - 14.6%) when segregation is not present and there is a complete mixing (case G). However, it is possible to recognize a range of Courant number (between 0.028 and 0.15) in which error is always lower than 10 %. The range is close to that already identified for a mono-disperse liquid-fluidized suspension by Cornelissen et al. (2007), who proposed to adopt a Courant number in the range between 0.03 and 0.3. Actually, in order to obtain accurate results, it is important to work with appropriate grid resolutions and time step sizes and since the Courant number takes into account the ratio between the grid size and the time step, it results that it has to vary in a particular range. However, simulation results also show that imposing limits to the variation of the Courant number is a sufficient condition but not a necessary condition.

For this reason a new parameter was introduced:

$$G = \Delta x \Delta t \frac{X_{j0}}{u} \tag{5.31}$$

It is a global parameter which takes into account not only the grid size and the time step, but also the operating conditions of the bed. This parameter takes into account the fact that smaller grid size and time step usually permit to reach the asymptotic range of convergence and are necessary when the bed operates at higher jetsam volume fractions and smaller air inlet velocities. Figure 5.24 reports the average absolute error versus the previously introduced global parameter: the smaller is G, the smaller is the average absolute error. This plot clearly shows what

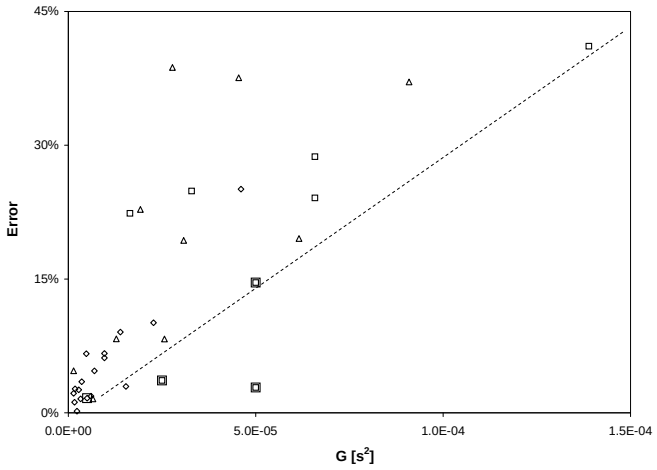

Figure 5.24: Average absolute error vs. global parameter for all the simulated test cases (Triangles: $N_C \leq 0.028$; Diamonds: $0.028 < N_C < 0.15$; Squares: $N_C \geq 0.15$). Double squares represents case G.

it was previously found about the influence of the operating conditions on result accuracy and what it is commonly known about the increasing of accuracy with the decrease of grid size and time step. When segregation occurs (i.e. excluding case G), at higher G values it is not possible to reach low error values. This means that given the operating conditions, it is possible to know the lower reachable error with a certain time step and grid size.

As a result working with a gas inlet velocity between the minimum fluidization velocity and the minimum velocity at which the bed is completely mixed and steadily fluidized, it is possible to obtain an indication of the numerical setup necessary for the operating conditions under study from Figures 5.23 and 5.24. By defining the operating conditions and the maximum acceptable average absolute error, a limit on the product of the grid size and the time step is produced. The limit on the higher Courant number gives in turn another limit, this time on the ratio between grid size and time step. These two conditions permit to have an idea of the grid size and the time step necessary to produce results with approximately the maximum acceptable average absolute error. However, while widely varying the operating conditions, a single binary solid mixture was considered in this work, therefore more extensive tests on a wider range of solid mixtures physical properties would be beneficial for assessing the general validity of the proposed method.

In any case, it is always necessary to run grid and time step convergence studies, in order to understand when results are in the asymptotic range of convergence, but the conditions previously found can give a good first guideline.

5.11 Conclusions

In this work, a first attempt to simulate numerically the homogeneous bed expansion of Geldart A Group particle powders has been presented. The importance of performing CFD simulations taking in account real Richardson-Zaki parameters is demonstrated. The model is able to reproduce trend of bed voidage with temperature and velocity for all the three FCC catalysts examined, and it is also capable to reproduce trend of n^* and u_t^* with temperature.

Moreover the behaviour of a bi-disperse gas-solid fluidized bed was studied in a fully predictive way with special attention to the influence of numerical set-up on the predicted bed segregation. Results clearly show that the difficulty in matching experimental findings, and in particular axial segregation and minimum mixing velocity, can be associated not only with the model limitation but also to numerical errors. The criticality of numerical issues was demonstrated to depend also from the particular operating condition investigated. This means that it is important to be careful when studying the dependency of the results from grid size and time step, because the magnitude of numerical errors changes with the composition of the mixture and was found to be higher at higher jetsam volume fractions and at lower inlet gas velocities. This behaviour will be also checked in future work for different systems, starting from mixtures of particles differing only in size or only in density. A global parameter, which takes into account both the operating conditions and the spatial and temporal resolutions, was found to be correlated with the average absolute error. As a result, given the operating conditions, the preliminary knowledge of the flotsam and the jetsam particle behaviour and the maximum acceptable error, it is possible to calculate the grid size and the time step to be used as a first attempt in a grid and time step convergence study.

5.12 Notation

C_D:	particle drag coefficient, dimensionless
C_D^*:	particle drag coefficient, dimensionless
d_d:	particle diameter, m
d_d^*:	cluster diameter, m
e_{ij}:	coefficient of restitution, dimensionless
F_{45}:	fraction of particles with diameter$< 45\mu m$, dimensionless
G:	global parameter, s^2
$\boldsymbol{g}$:	gravitational acceleration, $m\ s^{-2}$
g_i:	radial distribution function, dimensionless
g_{ij}:	constitutive function, dimensionless
h:	bed height, m
h_{mf}:	minimum fluidization bed height, m
$\overline{\overline{\boldsymbol{I}}}$:	identity tensor, dimensionless
I_{2D}:	second invariant of the deviatoric stress tensor, dimensionless
k_{Θ_p}:	diffusion coefficient for the granular temperature, $kg\ s^{-1}m{-}1$
N_C:	Courant number, dimensionless
n:	theoretical Richardson-Zaki exponent, dimensionless
n^*:	experimental Richardson-Zaki exponent, dimensionless
p:	pressure, $kgm^{-1}s^{-2}$
Re_i:	particle Reynolds number, dimensionless
Re_i^*:	particle Reynolds number, dimensionless
Re_t:	terminal particle Reynolds number, dimensionless
t:	time, s
t_e:	characteristic response time, s
u:	superficial fluid velocity magnitude, $m\ s^{-1}$
$\boldsymbol{u}$:	velocity vector, $m\ s^{-1}$
u_{mf}:	minimum fluidization superficial velocity magnitude, ms^{-1}
u_t:	theoretical terminal velocity magnitude, ms^{-1}
u_t^*:	experimental terminal velocity magnitude, ms^{-1}
X_{j0}:	jetsam volumetric fraction on a fluid-free basis at $t = 0$, dimensionless
X_{jB}:	jetsam volumetric fraction on a fluid-free basis at the bottom of the bed, dimensionless
X_{jT}:	jetsam volumetric fraction on a fluid-free basis at the top of the bed, dimensionless
x:	axial coordinate, m

Greek letters

α_{Θ_p}:	fluctuating energy exchange, $kg\ m^{-1}s^{-3}$
β_i:	drag force coefficient, $kg\ m^{-3}s^{-1}$
Δt:	time step, s
Δx:	grid size, m
ϵ:	fluid volume fraction, dimensionless
ϵ^*:	experimental fluid volume fraction, dimensionless
ϕ:	volume fraction, dimensionless
φ:	drag force corrective function, dimensionless
$\gamma_{\Theta_{d_i}}$:	collisional dissipation of fluctuating energy, $kg\ m^{-1}s^{-3}$
λ:	dilatation viscosity, $kg\ m^{-1}s^{-1}$
μ:	shear viscosity, $kg\ m^{-1}s^{-1}$
μ_{coll}:	collisional solid shear viscosity, $kg\ m^{-1}s^{-1}$
μ_{kin}:	kinetic solid shear viscosity, $kg\ m^{-1}s^{-1}$
μ_{fr}:	friction solid shear viscosity, $kg\ m^{-1}s^{-1}$
θ:	angle of internal friction, dimensionless
$\overline{\overline{\tau}}$:	viscous stress tensor, $kg\ m^{-1}s^{-2}$
Θ:	granular temperature, m^2s^{-2}
ρ:	density, $kg\ m^{-3}$
ω:	mass fraction of the solid phase on fluid-free basis, dimensionless
ξ_{ij}:	constitutive function, dimensionless
ψ:	drag force corrective function exponent, dimensionless
σ/d_{50}:	relative diameter spread, dimensionless
ζ_{ij}:	drag force coefficient, $kg\ m^{-3}s^{-1}$

Subscripts

c:	continuous phase
i, j:	generic solid phase
k:	generic phase

5.13 Bibliography

Agbim, J. A., Nienow, A. W., Rowe, P. N., Inter-particle forces that suppress bubbling in gas fluidised beds (1971) Chem. Eng. Sci., 26, pp. 1293-1294;

Anderson, T. B., Jackson, R., A fluid mechanical description of fluidized beds. Equations of motion (1967) Ind. Eng. Chem. Fundam., 6, pp. 527-539;

Avidan, A. A., Yerushalmi, J., Bed expansion in high velocity fluidization (1982) Powder Technol., 32, pp. 223-232;

Beetstra, R., van der Hoef, M. A., Kuipers, J. A. M., Numerical study of segregation using a new drag force correlation for polydisperse systems derived from lattice-Boltzmann simulations (2007) Chem. Eng. Sci. 62, pp. 246255;

Bokkers, G. A., Annaland, M. V. S., Kuipers, J. A. M., Mixing and segregation in a bidisperse gassolid fluidised bed: a numerical and experimental study (2004) Powder Technol. 140, pp. 176-186;

Busciglio, A., Vella, G., Micale, G., Rizzuti, L., Analysis of the bubbling behaviour of 2D gas solid fluidized beds: Part II. Comparison between experiments and numerical simulations via Digital Image Analysis Technique (2009) Chem. Eng. J., 148, pp. 145-163;

Chaouki, J., Chavarie, C., Klvana, D., Pajonk, G., Effect of interparticle forces on the hydrodynamic behaviour of fluidized aerogels (1985) Powder Technology, 43, pp. 117-125;

Chapman, S., Cowling, T.G. (1970) The Mathematical Theory of Non-uniform gases. Cambridge University Press, Cambridge, England;

Chiba, S., Nienow, A.W., Chiba, T., Kobayashi, H. (1980) Fluidised binary mixtures in which the denser component may be flotsam. Powder Technology 26, pp.1-10;

Chiesa, M., Mathiesen, V., Melheim, J. A., Halvorsen, B., Numerical simulation of particulate flow by the EulerianLagrangian and the EulerianEulerian approach with application to a fluidized bed (2005) Comput. Chem. Eng., 29, pp. 291-304;

Coleman, H. W., Stern, F., Uncertainties and CFD code validation (1997) J. Fluids Eng., Trans. ASME, 119, pp. 795-803;

Cooper, S., Coronella, C. J., CFD simulations of particle mixing in a binary fluidized bed (2005) Powder Technol., 151, pp. 27-36;

Cornelissen, J. T., Taghipour, F., Escudie, R., Ellis, N., Grace, J. R., CFD modelling of a liquid-solid fluidized bed (2007) Chem. Eng. Sci., 62, pp. 6334-6348;

Dahl, S. R., Hrenya, C.M., Size segregation in gassolid fluidized beds with continuous size distributions (2005) Chem. Eng. Sci., 60, pp. 6658-6673;

Dallavalle, J. M. (1948) Micromeritics. Pitman, London;

Ding, J., Gidaspow, D., A bubbling fluidization model using kinetic theory of granular flow (1990) AIChE J., 36, pp. 523-538;

Ergun, S., Fluid Flow through Packed Columns (1952) Chem. Eng. Prog., 48, pp. 89-94;

Fedors, R. F., Landel, R. F., An Empirical Method of Estimating the Void Fraction in Mixtures of Uniform Particles of Different Size (1979) Powder Technol., 23, pp. 225-231;

Feng, Y. Q., Xu, B. H., Zhang, S. J., Yu, A. B., Zulli, P., Discrete particle simulation of gas fluidization of particle mixtures (2004) AIChE J., 50, pp. 1713-1728;

Formisani, B., Girimonte, R., Mancuso, L., Analysis of the fluidization process of particle beds at high temperature (1998) Chem. Eng. Sci., 53, pp. 951-961;

Foscolo, P. U., Gibilaro, L. G., A fully predictive criterion for the transition between particulate and aggregate fluidization (1984) Chem. Eng. Sci. 39, pp. 1667-1675;

Geldart, D., Baeyens, J., Pope, D. J., Vandewijer, P., Segregation in beds of large particles at high velocities (1981) Powder Technol. 30, pp. 195-205;

Geldart, D., Harnby, N., Wong, A.C., Fluidization of cohesive powders (1984) Powder Technol., 37, pp. 25-37;

Geldart, D., Types of fluidization (1973) Powder Technol., 7, 285-292;

Geldart, D., Wong, A. C. Y., Fluidization of powders showing degrees of cohesiveness - I. Bed expansion (1984) Chem. Eng. Sci., 39, pp. 1481-1488;

Geldart, D., Wong, A. C. Y., Fluidization of powders showing degrees of cohesiveness - II. Experiments on rates of de-aeration (1985) Chem. Eng. Sci., 40, pp. 653-661;

Gera, D., Syamlal, M., O'Brien, T. J., Hydrodynamics of particle segregation in fluidized beds (2004) Int. J. Multiph. Flow, 30, pp. 419-428;

Gidaspow, D. (1994) Multiphase Flow and Fluidization: Continuum and Kinetic Theory Descriptions. Academic Press, Boston;

Gidaspow, D., Bezburuah, R., Ding, J., Hydrodynamics of Circulating Fluidized Beds, Kinetic Theory Approach (1992) In Fluidization VII, Proc. 7th Engineering Foundation Conference on Fluidization, pp. 75-82;

Gidaspow, D., Huilin, L., Mangar, E., Kinetic theory of multiphase flow and fluidization: validation and extension to binaries (1996) Proc.19th International Congress of Theoretical and Applied Mechanics, Japan;

Gobin, A., Neau, H., Simonin, O., Llinas, J., Reiling, V., Selo, J., In Numerical simulations of a gas-phase polymerization reactor (2001) Proc. European Congress on Computational Methods in Applied Sciences and Engineering, Wales;

Godard, K. M. S., Richardson, J. F. The behaviour of bubble-free fluidised beds (1968) IChemE Symp. Ser. 30, pp. 126-135;

Goldschmidt, M. J. V., Beetstra, R., Kuipers, J. A. M., Hydrodynamic modelling of dense gas-fluidised beds: comparison and validation of 3D discrete particle and continuum models (2004) Powder Technol., 142, pp. 23-47;

Goldschmidt, M. J. V., Kuipers, J. A. M., van Swaaij, W. P. M., Hydrodynamic modelling of dense gas-fluidized bed using the kinetic theory of granular flow (2001) Chem. Eng. Sci., 56, pp. 571-578;

Goldschmidt, M. J. V., Link, J. M., Mellema, S., Kuipers, J. A. M., Digital image analysis measurements of bed expansion and segregation dynamics in dense gas-fluidised beds (2003) Powder Technol., 138, pp. 135159;

Grace, J. R., Taghipour, F., Verification and validation of CFD models and dynamic similarity for fluidized beds (2003) Powder Technol., 139, pp. 99-110;

Hirsch, C. (2007) Numerical Computation of Internal & External Flows 1st Vol. Butterworth-Heinemann, 2nd Ed.

Hoomans, B. P. B., Kuipers, J. A. M., Salleh, M. A. M., Stein, M., Seville, J. P. K., Experimental validation of granular dynamics simulations of gas-fluidised beds with homogenous in-flow conditions using positron emission particle tracking (2001) Powder Technol., 116, pp. 166-177;

Huilin, L., Gidaspow, D., Hydrodynamics of binary fluidization in a riser: CFD simulation using two granular temperatures (2003a) Chem. Eng. Sci., 58, pp.3777-3792;

Huilin, L., Yunhua, Z., Ding, J., Gidaspow, D., Wei, L., Investigation of mixing/segregation of mixture particles in gassolid fluidized beds (2007) Chem. Eng. Sci., 62, pp. 301-317;

Huilin, L., Yurong, H., Gidaspow, D., Lidan, Y., Yukun, Q., Size segregation of binary mixture of solids in bubbling fluidized beds (2003b) Powder Technol., 134, pp. 86-97;

Hulme, I., Clavelle, E., van der Lee, L., Kantzas, A., CFD modeling and validation of bubble properties for a bubbling fluidized bed (2005) Ind. Eng. Chem. Res., 44, pp. 4254-4266;

Iddir, H., Arastoopour, H., Hrenya, C.M., Analysis of binary and ternary granular mixtures behavior using the kinetic theory approach (2005) Powder Technol., 151, pp. 117-125;

Joseph, G. G., Leboreiro, J., Hrenya, C. M., Stevens, A. R., Experimental segregation profiles in bubbling gas-fluidized beds (2007) AIChE J,. 53, pp. 2804-2813;

Leboreiro, J., Joseph, G. G., Hrenya, C. M., Snider, D. M., Banerjee, S. S., Galvin, J. E., The influence of binary drag laws on simulations of species segregation in gas-fluidized beds (2008) Powder Technol., 184, pp. 275-290;

Lettieri, P., Brandani, S., Yates, J. G., Newton, D., A generalization of the Foscolo and Gibilaro particle-bed model to predict the fluid bed stability of some fresh FCC catalysts at elevated temperatures (2001) Chem. Eng. Sci., 56, pp. 5401-5412;

Lettieri, P., Mazzei, L., Challenges and issues on the CFD modelling of fluidized beds: A review (2009) The J. Comput. Multiphase Flows, 2, pp. 83-131;

Lettieri, P., Newton, D., Yates, J. G., Homogeneous bed expansion of FCC catalysts, influence of temperature on the parameters of the RichardsonZaki equation (2002) Powder Technol., 123, pp. 221-231;

Limtrakul, S., Chalermwattanatai, A., Unggurawirote, K., Tsuji, Y., Kawaguchi, T., Tanthapanichakoon, W., Discrete particle simulation of solids motion in a gassolid fluidized bed (2003) Chem. Eng. Sci., 58, pp. 915-921;

Lun, C. K. K., Savage, S. B., Jerey, D. J., Chepurniy, N., Kinetic Theories for Granular Flow: Inelastic Particles in Couette Flow and Slightly Inelastic Particles in a General Flow Field (1984) J. Fluid Mech., 140, pp. 223-256;

Massimilla, L., Dons, G., Zucchini, C., The structure of bubble-free gas fluidized beds of fine fluid cracking catalyst particles (1972) Chem. Eng. Sci., 27, pp. 2005-2015;

Mathiesen, V., Solberg, T., Arastoopour, H., Hjertager, B.H., Experimental and computational study of multiphase gas/particle flow in a CFB riser (1999) AIChE J., 45, pp. 2503-2518;

Mazzei, L., Casillo, A., Lettieri, P., Salatino, P., CFD simulations of segregating fluidized bidisperse mixtures of particles differing in size (2010) Chem. Eng. J., 156, pp. 432-445;

Mazzei, L., Lettieri P., A drag force closure for uniformly dispersed fluidized suspensions (2007) Chem. Eng. Sci., 62, pp. 6129-6142;

Mazzei, L., Lettieri, P., CFD simulations of expanding/contracting homogeneous fluidized beds and their transition to bubbling (2008) Chem. Eng. Sci., 63, pp. 5831-5847;

McLaughlin, L. J., Rhodes, M. J., Prediction of fluidized bed behaviour in the presence of liquid bridges (2201) Powder Technol., 114, pp. 213-223;

Molerus, O., Interpretation of Geldart's type A, B, C and D powders by taking into account interparticle cohesion forces (1982) Powder Technol., 33, pp. 81-87;

Mutsers, S. M. P., Rietema K., The effect of interparticle forces on the expansion of a homogeneous gas-fluidized bed (1977) Powder Technol., 18, pp. 239-248;

Olivieri, G., Marzocchella, A., Salatino, P., A fluid-bed continuous classifier of polydisperse granular solids (2009) J. Taiwan Inst. Chem. Eng, 40, pp. 638-644;

Olivieri, G., Marzocchella, A., Salatino, P., Segregation of fluidized binary mixtures of granular solids (2004) AIChE J., 50, pp. 3095-3106;

Pan, T. W., Joseph, D. D., Bai, R., Glowinski, R., Sarin, V., Fluidization of 1204 spheres: simulation and experiments (2002) J. Fluid Mech., 451, pp. 169-191;

Patil, D. J., van Sint Annaland, M., Kuipers, J. A. M., Critical comparison of hydrodynamic models for gassolid fluidized beds - Part I: bubbling gassolid fluidized beds operated with a jet (2005) Chem. Eng. Sci., 60, pp. 57-72;

Peirano, E., Delloume, V., Johnsson, F., Leckner, B., Simonin, O., Numerical simulation of the fluid dynamics of a freely bubbling fluidized bed: influence of the air supply system (2002) Powder Technol. 122, pp. 69-82;

Rahaman, M. F., Naser, J., Witt, P. J., An unequal granular temperature kinetic theory: description of granular flow with multiple particle classes (2003) Powder Technol., 138, pp. 82-92;

Rhodes, M. J., Wang, X. S., Forsyth, A. J., Gan, K. S., Phadtajaphan, S., Use of a magnetic fluidized bed in studying Geldart Group B to A transition (2001) Chem. Eng. Sci., 56, pp. 5429-5436;

Richardson, J. F., Zaki, W. N., Sedimentation and fluidisation. Part 1 (1954) Trans. Inst. Chem. Eng., 32, pp. 35-53;

Rietema, K., Cottaar, E. J. E., Piepers, H. W., The effects of interparticle forces on the stability of gas-fluidized beds - II. Theoretical derivation of bed elasticity on the basis of van der Waals forces between powder particles (1993) Chem. Eng. Sci., 48, pp. 1687-1697;

Rietema, K., Piepers, H. W., The effect of interparticle forces on the stability of gas-fluidized beds - I. Experimental evidence (1990) Chem. Eng. Sci., 45, pp. 1627-1639;

Rietema, K., The effect of interparticle forces on the expansion of a homogeneous gas-fluidised bed (1973) Chem. Eng. Sci., 28, pp. 1493-1497;

Rowe, P.N., A convenient empirical equation for estimation of the Richardson & Zaki exponent (1987) Chem. Eng. Sci., 42, pp. 2795-2796;

Rumpf, H. (1962) The strength of granules and agglomerates. In W. Knepper (Ed.), Agglomeration. New York: Interscience Publishers;

Savage, S. B., Jeffrey, D. J., The stress tensor in a granular flow at high shear rates (1981) J. Fluid Mech, 110, pp. 255-272;

Schaeffer, D. G., Instability in the Evolution Equations Describing Incompressible Granular Flow (1987) J. Diff. Eq., 66, pp. 19-50;

Seville, J. P. K., Clift R., The effect of thin liquid layers on fluidisation characteristics (1984) Powder Technol., 37, pp. 117-129;

Sun, J., Battaglia, F., Hydrodynamic modeling of particle rotation for segregation in bubbling gas-fluidized beds (2006) Chem. Eng. Sci., 61, pp. 1470-1479;

Syamlal, M. (1987) The particle-particle drag term in a multiparticle model of fluidization. National Technical Information Service, Springfield, VA;

Taghipour, F., Ellis, N., Wong, C., Experimental and computational study of gassolid fluidized bed hydrodynamics (2005) Chem. Eng. Sci., 60, pp. 6857-6867;

Tsinontides, S. C., Jackson, R., The mechanics of gas fluidized beds with an interval of stable fluidization (1993) J. Fluid Mech., 255, pp. 237-274;

van Wachem, B. G. M., Almstedt, A. E., Methods for multiphase computational fluid dynamics (2003) Chem. Eng. J., 96, pp. 81-98;

van Wachem, B. G. M., Schouten, J. C., Bleek van den, C. M., Krishna, R., Sinclair, L. L., Comparative analysis of CFD models of dense gassolid systems (2001b) AIChE J., 47, pp. 1035-1051;

van Wachem, B. G. M., Schouten, J. C., van den Bleek, C. M., Krishna, R., Sinclair, J. L., CFD modeling of gas-fluidized beds with a bimodal particle mixture (2001a) AIChE J., 47, pp. 1292-1302;

Verloop, J., Heertjes, P. M., Shock waves as a criterion for the transition from homogeneous to heterogeneous fluidization (1970) Chem. Eng. Sci., 25, pp. 825-832;

Wallis, G. B. (1969) One Dimensional Two Phase Flow. McGraw-Hill, New York;

Wen, C. Y., Yu, Y. H., Mechanics of Fluidization (1966) Chem. Eng. Prog. Symp. Ser., 62, pp. 100-111;

Wu, S. Y., Baeyens, J., Segregation by size difference in gas fluidized beds (1998) Powder Technol., 98, pp. 139-150;

Xie, H. Y., Geldart, D., Fluidization of FCC powders in the bubble-free regime: effect of types of gases and temperature (1995) Powder Technol., 82, pp. 269-277;

Zhang, D. Z., Prosperetti, A., Averaged equations for inviscid disperse two-phase flow (1994) J. of Fluid Mech., 267, pp. 185-219;

Yang, W. C. (2003) Handbook of Fluidization and Fluid-Particle Systems. Siemens Westinghouse Power Corporation, Pennsylvania, USA.

Chapter 6

Conclusions

The objective of the work presented in this PhD thesis was to contribute to the identification of reliable fully predictive Computational Fluid Dynamics methods for the numerical simulation of equipment typically adopted in the chemical and process industries.

The apparatuses selected for the investigation were characterised by a different and often complex fluid dynamic behaviour: they treated single phase flows (membrane modules and stirred tanks) or multiphase mixtures (stirred tanks and fluidized beds), the prevalent flow regime was laminar in some cases (membrane modules and fluidized beds) and turbulent in others (membrane modules and stirred tank). Moreover, in some of the equipment the momentum transfer phenomena were coupled with mass transfer (gas species transport across the membrane and homogenization of a tracer in stirred tanks) or by complex multiphase interactions (solid-gas and solid-solid-gas systems in fluidized beds and liquid-liquid systems in stirred tanks).

Overall, in all the investigated cases, the CFD approaches, which have been originally developed or just suitably selected, were proved to be able to predict the experimental behaviour of the equipments at different accuracy levels. In any case, the reliability of the computational results strictly depends on a preliminary physical analysis of the selected problem. Subsequently, besides the check on the numerical uncertainties, before performing a CFD simulation the most appropriate models have to be identified or purposely developed, in order to avoid the risk to give to CFD the meaning Colourful Fluid Dynamics.

The results obtained in the present thesis can be regarded as a further contribution to assess that, if properly adopted, CFD simulations are a valuable tool for helping the researchers to describe the physical phenomena occurring in the equipment by fully predictive models based on local parameters, thus avoiding to adopt empirical equations fitting the experimental data.

A clear example of the superiority of CFD methods over other simplified ap-

proaches, which can lead to severe errors, can be found in the analysis of the behaviour of Pd-Ag membrane modules for hydrogen separation from gaseous mixtures of other species. In the past, in order to fit the experimental data of permeation through the membrane, the arbitrary change of the exponent of the Sieverts' law was suggested. Instead, the CFD analysis has shown that for predicting the experimental behaviour of the equipment, all the mass transfer resistances taking place in the membrane modules have to be taken into account, while the modification of the Sieverts' law exponent was a wrong way for compensating the absence of the convective resistance modelling. The importance of CFD approaches in the field of membrane module for gas mixture separation is apparent, particularly for the case of highly permeable membranes. In these cases, large errors can be made if the presence of the convective mass transfer resistances is neglected.

The spread of CFD applications is nowadays growing together with computer power resources availability. Nevertheless, the full simulations of the complex geometrical and physical features of some equipment is not affordable or extremely time consuming; as a result the researchers have to identify a strategy for simplifying problems while still obtaining acceptable level of results' accuracy. An example of this specific issue faced in the present work is provided by the tracer homogenization simulations: the dynamic evolution of a tracer in the stirred tank was accurately simulated with a significant computational time saving releasing the tracer instantaneously as a plume, thus cutting the tracer injection simulation time.

The results obtained in the present thesis have also contributed to highlight that the reduction of numerical uncertainties is an important aspect, which is nowadays possible not to disregard thanks to the increasing computer power, resulting in improved predictions of important phenomena of special impact in the industrial chemical equipment considered in this work, e.g. mixing time and tracer homogenization in single phase stirred tanks and segregation in fluidized beds. Comprehensive grid and time step independency studies are often difficult to perform due to computational power limitations and these numerical parameters are often selected on empirical bases. In the present work, an original procedure to be applied to the case of segregating fluidized beds has been suggested for identifying the grid size and time step depending on the maximum acceptable error on the solid hold-up prediction.

However, it is not always easy to define the variables that a researcher has to check for identifying the accuracy of the CFD results. For instance, if the attention is limited to the mean velocity in a turbulent flow field, proper predictions can be expected by the solution of the RANS equations and a suitable turbulence closure model, while great errors are obtained for the turbulent variables. In the present work this conclusion was shown to be strongly dependent on the spatial discretization of the computational domain. Therefore, a clear identification of the

limits of the RANS approach can be obtained only separating the effect of the numerical uncertainties from the intrinsic approximation of the models.

The different problems tackled in this work have always evidenced that the adoption of any commercial CFD software as a black box (although strongly encouraged from the main software houses) is particularly dangerous and often meaningless, since, unless all the simulation steps are strictly and deeply monitored, it is very easy to fall into the mistake of assuming that any converged calculation is the right prediction.

The main specific results achieved in the thesis are summarized in the following.

- Membrane separation modules:

  - A CFD approach has been developed, which was demonstrated to be a reliable tool for the description and the prediction of the behaviour of membrane modules for gas mixtures separation.
  - The effect of several different operating conditions, such as temperature, feed flow rate, pressure and composition of the feed stream in binary and ternary mixtures, on the separation performances has been accurately predicted, since a strict comparison with experimental permeation data was performed.
  - The accuracy of the CFD simulations for investigating the non ideal flow of membrane separation modules was tested by comparison of the simulation results with original PIV data.
  - The definite decrease of H_2 permeate flux, when mixtures are fed instead of pure gases, has been successfully modelled, confirming the ability of the CFD approach to investigate the flow dynamics of the module and its influence on the membrane separation efficiency.
  - The presence of the concentration polarisation effect has been highlighted.
  - The simulations considering the case of membrane inhibition, that have been accounted for in the model by implementing a literature equation, have allowed to estimate the relative importance of concentration polarization and inhibition.
  - The effect on separation performances of geometrical details, such as fittings and inlet/outlet tube, has been highlighted.
  - The effect of perforated plates and of purposely designed baffles has been assessed.

  - The novel baffles permit to avoid complete mixing and to reduce the concentration polarization, increasing the driving force.

- Stirred vessels:

  - The contribution of numerical errors to well-known limitations of the RANS-based CFD approach has been highlighted.
  - Much finer computational grids than those usually adopted for RANS simulations are required to reduce the numerical uncertainties to negligible values.
  - The difference between the predicted power consumption evaluated from the overall torque on walls and the integral of the turbulent dissipation rate decreases significantly by reducing the spatial discretization size.
  - The numerical aspects were found to be critical also in the predictions of the tracer homogenization dynamics, that were compared with experimental curves obtained with the PLIF technique.
  - The simulations were found to be accurate even by adopting a simplified method for modelling the injection step.
  - The conditions of just drawdown and just dispersed speeds for the water-oil system have been identified, through a simplified RANS approach, only when a suitable mean value of the droplet size is selected.

- Fluidized beds:

  - Trend of experimental bed voidage with temperature and velocity in the homogeneous bed expansion of Geldart A Group particle powders can be reproduced taking in account real Richardson-Zaki parameters.
  - In bi-disperse gas-solid fluidized bed, the difficulty in matching experimental findings, and in particular axial segregation and minimum mixing velocity, can be associated not only with the model limitation, but also to numerical errors.
  - The criticality of numerical issues was demonstrated to depend also from the particular operating condition investigated, being the magnitude of numerical errors higher at higher jetsam volume fractions and at lower inlet gas velocities.
  - A global parameter, which takes into account both the operating conditions and the spatial and temporal resolutions, was found to be correlated with the average absolute error.

- It is possible to calculate the grid size and the time step to be used as a first attempt in a grid and time step convergence study, given the operating conditions and the maximum acceptable error.

List of Publications

Papers on international journals (with referee)

Coroneo, M., Montante, G., Giacinti Baschetti, M., Paglianti, A., CFD modelling of inorganic membrane modules for gas mixture separation (2009) Chemical Engineering Science, 64, pp. 1085-1094;

Laurenzi, F., Coroneo, M., Montante, G., Paglianti, A., Magelli, F., Experimental and computational analysis of immiscible liquid-liquid dispersions in stirred vessels (2009) Chemical Engineering Research and Design, 87, pp. 507-514;

Coroneo, M., Montante, G., Catalano, J., Paglianti, A., Modelling the effect of operating conditions on hydrodynamics and mass transfer in a Pd-Ag membrane module for H_2 purification (2009) Journal of Membrane Science, 343, pp. 34-41;

Coroneo, M., Montante, G., Paglianti, A., Numerical and experimental fluid-dynamic analysis to improve the mass transfer performances of Pd-Ag membrane modules for hydrogen purification (2010) Industrial and Engineering Chemistry Research, 49, pp. 9300-9309;

Coroneo, M., Montante, G., Paglianti, A., Magelli, F., CFD Prediction of fluid flow and mixing in stirred tanks: numerical issues about the RANS simulations (2010) Computers and Chemical Engineering, doi:10.1016/j.compchemeng.2010.12.007.

Submitted papers

Coroneo, M., Mazzei, L., Lettieri, P., Paglianti, A., Montante, G., CFD prediction of segregating fluidized bidisperse mixtures in gas-solid fluidized beds (2010) Chemical Engineering Science, submitted.

Papers in congress preceedings (with referee)

Coroneo, M., Catalano, J., Montante, G., Giacinti Baschetti, M., Paglianti, A., Sarti, G.C., Experimental and CFD modelling of membranes for hydrogen separation. GPE-EPIC 2009, Venice, 14 - 17 Jun 2009;

Laurenzi, F., Coroneo, M., Montante, G., Paglianti, A., Magelli, F., Hydrodynamics of immiscible liquid-liquid dispersions in stirred vessels. 13th European Conference on Mixing, London, 14 - 17 April 2009.

Other papers in congress preceedings

Coroneo, M., Montante, G., Giacinti Baschetti, M., Paglianti, A., Modellazione CFD di moduli a membrana per la purificazione di H2. Convegno GRICU 2008, Le Castella (KR), 14-17 Sep 2008.

Abstracts of oral presentations and posters

Coroneo, M., Catalano, J., Giacinti Baschetti, M., Montante, G., Paglianti, A., CFD modelling of fluid dynamics and mass transfer in membrane modules for gas mixture separation Oral presentation at AIChE 2008, 16 - 21 Nov 2008, Philadelphia, PA, USA;

Catalano, J., Coroneo, M., Giacinti Baschetti, M., Montante, G., Paglianti, A., Sarti, G.C., Hydrogen permeation in thin palladium silver membranes: comparison between experimental data and model calculations. ICOM 2008, 12 - 18 Jul 2008, Honolulu, Hawaii, USA.